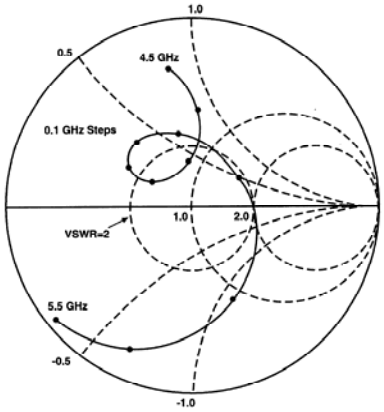

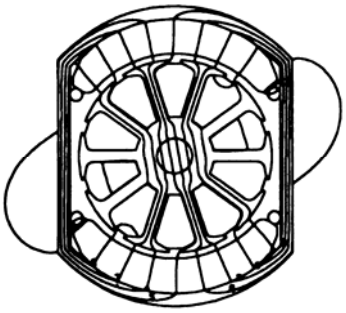

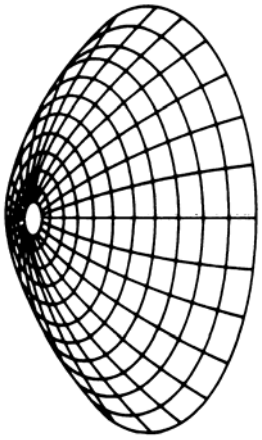

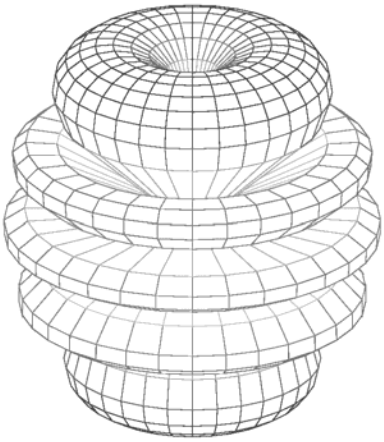

Applied Computational Electromagnetics Society Journal

Editor-in-Chief
Atef Z. Elsherbeni

November 2007
Vol. 22 No. 3
ISSN 1054-4887

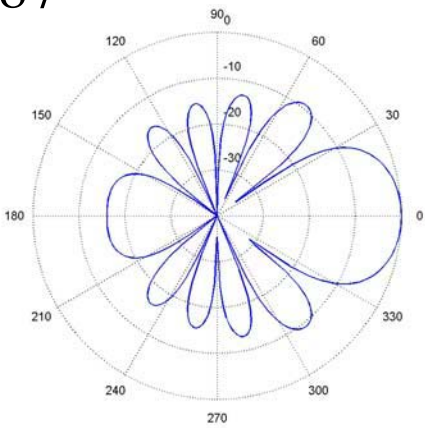

GENERAL PURPOSE AND SCOPE: The Applied Computational Electromagnetics Society ***(ACES)*** Journal hereinafter known as the ***ACES Journal*** is devoted to the exchange of information in computational electromagnetics, to the advancement of the state-of-the art, and the promotion of related technical activities. A primary objective of the information exchange is the elimination of the need to "re-invent the wheel" to solve a previously-solved computational problem in electrical engineering, physics, or related fields of study. The technical activities promoted by this publication include code validation, performance analysis, and input/output standardization; code or technique optimization and error minimization; innovations in solution technique or in data input/output; identification of new applications for electromagnetics modeling codes and techniques; integration of computational electromagnetics techniques with new computer architectures; and correlation of computational parameters with physical mechanisms.

SUBMISSIONS: The ***ACES Journal*** welcomes original, previously unpublished papers, relating to applied computational electromagnetics. Typical papers will represent the computational electromagnetics aspects of research in electrical engineering, physics, or related disciplines. However, papers which represent research in applied computational electromagnetics itself are equally acceptable.

Manuscripts are to be submitted through the upload system of ***ACES*** web site http://aces.ee.olemiss.edu See "Information for Authors" on inside of back cover and at ***ACES*** web site. For additional information contact the Editor-in-Chief:

Dr. Atef Elsherbeni
Department of Electrical Engineering
The University of Mississippi
University, MS 386377 USA
Phone: 662-915-5382 Fax: 662-915-7231
Email: atef@olemis.edu

SUBSCRIPTIONS: All members of the Applied Computational Electromagnetics Society who have paid their subscription fees are entitled to receive the ***ACES Journal*** with a minimum of three issues per calendar year and are entitled to download any published journal article available at http://aces.ee.olemiss.edu.

Back issues, when available, are $15 each. Subscriptions to ***ACES*** is through the web site. Orders for back issues of the ***ACES Journal*** and changes of addresses should be sent directly to ***ACES*** Executive Officer:

Dr. Richard W. Adler
ECE Department, Code ECAB
Naval Postgraduate School
833 Dyer Road, Room 437
Monterey, CA 93943-5121 USA
Fax: 831-649-0300
Email: *rwa@attglobal.net*

Allow four week's advance notice for change of address. Claims for missing issues will not be honored because of insufficient notice or address change or loss in mail unless the Executive Officer is notified within 60 days for USA and Canadian subscribers or 90 days for subscribers in other countries, from the last day of the month of publication. For information regarding reprints of individual papers or other materials, see "Information for Authors".

LIABILITY. Neither ***ACES***, nor the ***ACES Journal*** editors, are responsible for any consequence of misinformation or claims, express or implied, in any published material in an ***ACES Journal*** issue. This also applies to advertising, for which only camera-ready copies are accepted. Authors are responsible for information contained in their papers. If any material submitted for publication includes material which has already been published elsewhere, it is the author's responsibility to obtain written permission to reproduce such material.

APPLIED COMPUTATIONAL ELECTROMAGNETICS SOCIETY JOURNAL

Editor-in-Chief
Atef Z. Elsherbeni

November 2007
Vol. 22 No. 3
ISSN 1054-4887

The ACES Journal is abstracted in INSPEC, in Engineering Index, DTIC, Science Citation Index Expanded, the Research Alert, and to Current Contents/Engineering, Computing & Technology.

The first, fourth, and sixth illustrations on the front cover have been obtained from the Department of Electrical Engineering at the University of Mississippi.

The third and fifth illustrations on the front cover have been obtained from Lawrence Livermore National Laboratory.

The second illustration on the front cover has been obtained from FLUX2D software, CEDRAT S.S. France, MAGSOFT Corporation, New York.

THE APPLIED COMPUTATIONAL ELECTROMAGNETICS SOCIETY
http//:aces.ee.olemiss.edu

ACES JOURNAL EDITORS

ACES JOURNAL ASSOCIATE EDITORS

NOVEMBER 2007 REVIEWERS

Fan Yang
Ercument Arvas
Mohamed Al-Sharkawy
Malcolm Bibby
William A. Davis
Mohamed H. Bakr
Fernando Las-Heras
Michiko Kuroda
Yasushi Kanai
Masoud Kahrizi
Naftali (Tuli) Herscovici
John H. Beggs
Veysel Demir
Alan Taflove
Andy Harrison
Sami Barmada
Andrew F. Peterson
Michael A. Morgan
James Rautio
Darko Kajfez
Eric Michielssen

THE APPLIED COMPUTATIONAL ELECTROMAGNETICS SOCIETY

JOURNAL

Vol. 22 No. 3 November 2007

TABLE OF CONTENTS

Eliminating Interface Reflections in Hybrid Low-Dispersion FDTD Algorithms

Mohammed F. Hadi[1] **and Rabie K. Dib**[2]

[1]Electrical Engineering Dept., Kuwait University, P. O. Box 5969, Safat 13060, Kuwait
[2]College of Technological Studies, PAAET, P. O. Box 4196, Hawalli 32072, Kuwait

Abstract — The numerical phase mismatch across FDTD lattice layers with different sets of update equations has been investigated. A predictive equation of numerical reflections across high-order/low-order layers has been derived. Based on this equation the standard Yee (S_{22}) update equations have been modified to allow their implementation around PEC boundaries and other special situations in an otherwise global high-order implementation, while keeping spurious reflections at the hybrid interface to a practical minimum and independent of the traversing wave direction. S_{22} Phase matching has been developed and verified in both S_{24} and M24 high-order hybrid algorithms.

Keywords — FDTD, Numerical Dispersion, High-Order Schemes, Phase-Matching, Electrically Large Structures.

I. INTRODUCTION

SEVERAL FDTD algorithms have been developed over the past decade to minimize the loss of phase coherency in wave solutions due to numerical dispersion. Shlager and Schneider [1] compared some of the more prominent low-dispersion algorithms and compared their phase coherency for both single-frequency and wideband use. While some of the analyzed algorithms that restricted their stencils to a single Yee cell did extremely well for single-frequency use [2] and [3], it was the two-dimensional extended-stencil M24 algorithm [4] that excelled in both single-frequency and wideband suitability. The M24 algorithm utilizes multiple weighted Ampere's and Faraday's loop integrals over extended FDTD stencils as demonstrated in Fig. 1. In comparison, the S_{24} algorithm (second-order in time and fourth-order in space finite differences) which will also be discussed in this present work is a special case of the M24 algorithm when the outermost loop integral in Fig. 1 is omitted and K_1 is set to $-1/8$.

The main challenge to such extended-stencil algorithms, however, is porting the wealth of FDTD tools that were developed over the decades for the standard single-cell Yee algorithm (S_{22} for second-order differencing in both time and space). It was suggested in [4] that this challenge could be simply resolved by introducing minimal S_{22} buffer zones where needed in an otherwise global M24 implementation. Haussmann in [5], however, demonstrated experimentally that such an approach would cause measurable reflections at the interface between the high-order and low-order zones. Another approach pursued by Georgakopoulos *et al.* in [6] was using a fine-meshed S_{22} buffer zone that would better match its dispersion characteristics to a coarsely-meshed S_{24} zone. Both works, however, left open the questions as to the extent of interface reflections at oblique wave incidence angles as well as to the optimum mesh size ratio between the high-order and low-order zones.

Recently, Celuch-Marcysiak and Rudnicki [7] and [8] developed a methodology for predicting numerical reflections at normal and oblique angles of incidence across dissimilarly gridded homogeneous zones and went on to validate them using FDTD simulations. In this present work this same methodology will be applied to derive appropriate equations to predict the reflection coefficient across similarly gridded homogeneous zones but with varying differencing schemes (in particular, S_{24}/S_{22} and $M24/S_{22}$ interfaces) and quantify the limitations of using S_{22} buffer zones within high-order FDTD implementations. As in [8], the effect of nonorthogonality of wave polarization to propagation direction (wavenumber vector) [9] will be accounted for. Furthermore, new update equations for the S_{22} buffer zone will be developed and validated that will utilize single-cell depth normal to the interface plane and extended-cell depth tangentially to eliminate cross-interface reflections while still being usable near PEC boundaries and other special situations. In effect, realizing optimum phase matching (minimal interface reflections) without the need for S_{22} subgridding.

II. FDTD RENDITION OF PLANE WAVES

When an FDTD algorithm attempts to propagate a plane wave it introduces two types of numerical dispersion-related errors that are of interest to us here. The first is the error in the rendered numerical

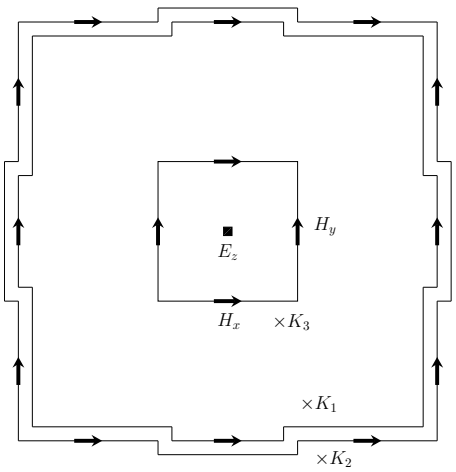

Fig. 1. Multiple weighted Ampere's loops for updating a centered E_z node in the M24 algorithm. A uniform $\Delta x = \Delta y = h$ is assumed and $K_3 = 1 - K_1 - K_2$.

wavenumber that causes the accumulation of phase error as the wave traverses the numerical domain. This error is a function of the propagation angle and resolution factor (number of FDTD cells per wavelength, R) and is well documented in the literature. The other type of error is the one that affects the polarization of the propagating wave. It was demonstrated in [9] and [10] that as the wave bounces around in the FDTD lattice the orthogonal $\bar{E}$ and $\bar{H}$ vectors form a numerical Poynting vector that is not parallel to the propagation direction

$$\bar{\beta} = \bar{a}_x \beta_x + \bar{a}_y \beta_y + \bar{a}_z \beta_z \tag{1}$$

but rather to

$$\bar{P} = \bar{a}_x D_x + \bar{a}_y D_y + \bar{a}_z D_z, \tag{2}$$

where D_x, D_y and D_z are discrete operators dictated by the FDTD algorithm of interest, and β_x, β_y and β_z are the numerically rendered wavenumber components that can be derived from the algorithm's dispersion relation.

A. Discrete Operators

The standard S_{22} algorithm in 2–D implementations has the discrete operators

$$D_x = \frac{\sin\frac{\beta_x h}{2}}{h/2} \quad \text{and} \quad D_y = \frac{\sin\frac{\beta_y h}{2}}{h/2}. \tag{3}$$

The M24 algorithm, on the other hand, has the update equations [4] (see Fig. 1)

$$\begin{aligned}
\epsilon\frac{\partial E_z}{\partial t} &= \frac{K_1}{3h}\begin{pmatrix} H_x|_{j-\frac{3}{2}} - H_x|_{j+\frac{3}{2}} \\ +H_y|_{i+\frac{3}{2}} - H_y|_{i-\frac{3}{2}} \end{pmatrix} \\
&\quad + \frac{K_2}{6h}\begin{pmatrix} H_x|_{i-1,j-\frac{3}{2}} + H_x|_{i+1,j-\frac{3}{2}} \\ -H_x|_{i-1,j+\frac{3}{2}} - H_x|_{i+1,j+\frac{3}{2}} \\ +H_y|_{i+\frac{3}{2},j-1} + H_y|_{i+\frac{3}{2},j+1} \\ -H_y|_{i-\frac{3}{2},j-1} - H_y|_{i-\frac{3}{2},j+1} \end{pmatrix} \\
&\quad + \frac{K_3}{h}\begin{pmatrix} H_x|_{j-\frac{1}{2}} - H_x|_{j+\frac{1}{2}} \\ +H_y|_{i+\frac{1}{2}} - H_y|_{i-\frac{1}{2}} \end{pmatrix}, \qquad (4) \\
\mu\frac{\partial H_x}{\partial t} &= \frac{K_1}{3h}\left(E_z|_{j-\frac{3}{2}} - E_z|_{j+\frac{3}{2}}\right) \\
&\quad + \frac{1-K_1}{h}\left(E_z|_{j-\frac{1}{2}} - E_z|_{j+\frac{1}{2}}\right), \qquad (5) \\
\mu\frac{\partial H_y}{\partial t} &= \frac{K_1}{3h}\left(E_z|_{i+\frac{3}{2}} - E_z|_{i-\frac{3}{2}}\right) \\
&\quad + \frac{1-K_1}{h}\left(E_z|_{i+\frac{1}{2}} - E_z|_{i-\frac{1}{2}}\right) \qquad (6)
\end{aligned}$$

where non-staggered indices are omitted for cleaner notation and $K_3 = 1 - K_1 - K_2$. These K parameters are chosen through an optimization routine that will ensure minimal dispersion error across all angles of propagation in the numerical lattice. The corresponding discrete operators are given by

$$\begin{aligned}
D_x^y &= K_3\frac{\sin\frac{\beta_x h}{2}}{h/2} \\
&\quad + (K_1 + K_2\cos\beta_y h)\frac{\sin\frac{3\beta_x h}{2}}{3h/2}, \qquad (7) \\
D_x^z &= (1-K_1)\frac{\sin\frac{\beta_x h}{2}}{h/2} + K_1\frac{\sin\frac{3\beta_x h}{2}}{3h/2}, \qquad (8) \\
D_y^x &= K_3\frac{\sin\frac{\beta_y h}{2}}{h/2} \\
&\quad + (K_1 + K_2\cos\beta_x h)\frac{\sin\frac{3\beta_y h}{2}}{3h/2}, \qquad (9) \\
D_y^z &= (1-K_1)\frac{\sin\frac{\beta_y h}{2}}{h/2} + K_1\frac{\sin\frac{3\beta_y h}{2}}{3h/2}. \qquad (10)
\end{aligned}$$

The operator notation for the M24 algorithm is slightly different than that of the S_{22}'s as an x, y or z superscript on the discrete operator denotes its restricted applicability to that particular field component. On the other hand, the S_{22} operators are linear; $D_x^y = D_x^z = D_x$ and $D_y^x = D_y^z = D_y$.

When K_1 and K_2 are substituted with $-1/8$ and zero, respectively, equations (4) to (10) produce the corresponding update equations and discrete operators for the S_{24} algorithm. In particular, the latter will be linear;

$$\begin{aligned}
D_x &= \frac{9}{8}\frac{\sin\frac{\beta_x h}{2}}{h/2} - \frac{1}{8}\frac{\sin\frac{3\beta_x h}{2}}{3h/2}, \qquad (11) \\
D_y &= \frac{9}{8}\frac{\sin\frac{\beta_y h}{2}}{h/2} - \frac{1}{8}\frac{\sin\frac{3\beta_y h}{2}}{3h/2}. \qquad (12)
\end{aligned}$$

B. Dispersion Relations

The generalized dispersion relation for FDTD algorithms can be conveniently written in the form [5]

$$\mu\epsilon D_t^2 = D_x^y D_x^z + D_y^x D_y^z + D_z^x D_z^y \tag{13}$$

with

$$D_t = -\frac{\sin\frac{\omega\Delta t}{2}}{\Delta t/2}, \tag{14}$$

provided that

$$D_y^z D_z^x D_x^y = D_z^y D_x^z D_y^x. \tag{15}$$

This latter condition is not a problem for 2-D algorithms with nonlinear operators as is the case with the M24 algorithm since $D_z^x = D_z^y = 0$. For linear-operator algorithms (S_{22} and S_{24}), equation (13) can be reduced to

$$\mu\epsilon D_t^2 = D_x^2 + D_y^2 + D_z^2. \tag{16}$$

Direct substitutions of equations (3) and (11) to (12) into (16), and equations (7) to (10) into (13) will produce the dispersion relations for the S_{22}, S_{24} and M24 algorithms.

C. Stability Criteria

The maximum allowable time step before the onset of numerical instability for FDTD algorithms with linear discrete operators and second-order differencing in time is given by,

$$\Delta t \le \frac{2\sqrt{\mu\epsilon}}{\sqrt{(D_x^2 + D_y^2 + D_z^2)_{\max}}} \tag{17}$$

while for 2-D such algorithms with nonlinear operators it is given by,

$$\Delta t \le \frac{2\sqrt{\mu\epsilon}}{\sqrt{\left(D_x^y D_x^z + D_y^x D_y^z\right)_{\max}}} \tag{18}$$

where the "max" condition exists at $\beta_x h = \beta_y h = \pi$ or its odd multiples. These two inequalities will provide the well known S_{22} and S_{24} stability criteria,

$$\Delta t_{S22} \le \frac{h}{c\sqrt{2}} \quad \text{and} \quad \Delta t_{S24} \le \frac{(6/7)h}{c\sqrt{2}} \tag{19}$$

as well as

$$\Delta t_{M24} \le \frac{h}{c\sqrt{2}} \frac{3}{\sqrt{(3-4K_1)(3-4K_1-2K_2)}}. \tag{20}$$

In hybrid S_{24}/S_{22} or M24/S_{22} implementations the corresponding S_{24} or M24 time steps need to be used to avoid instability since they would be slightly smaller than the S_{22}'s maximum time step. Finally, it should be mentioned here that $\sqrt{-1}$ factors have been omitted from all the discrete operators since they would eventually cancel out for our purposes here.

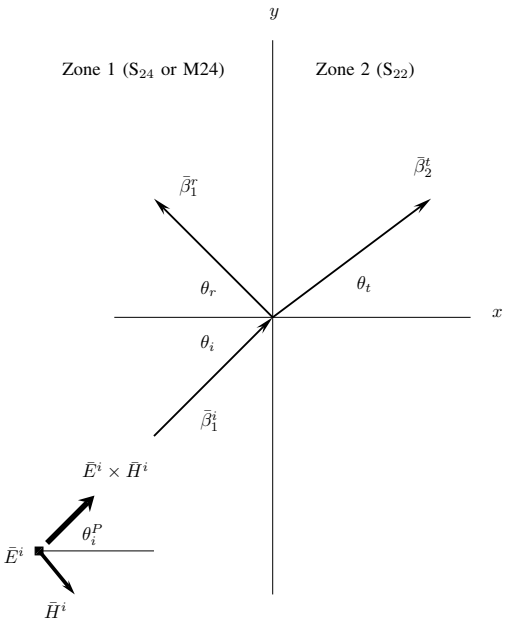

Fig. 2. Interpretation of a plane wave interaction with a planar interface separating two similarly gridded homogeneous zones with different FDTD schemes. Field nodes on the y-axis are assumed part of zone 2.

III. NUMERICAL REFLECTION COEFFICIENT

Let us assume a planar interface in a standard FDTD lattice is being traversed at an oblique angle of incidence from left to right with the medium at both sides of the interface being free space (see Fig. 2). Let us also assume that S_{22} update equations are used in the right zone including field nodes coinciding with the planar interface itself. In the left zone we will be using the update equations of the algorithm under study (S_{24} or M24). In either zone of this FDTD lattice the relationship between the direction of propagation and wavenumber is governed by,

$$\bar{\beta} = \bar{a}_x\beta_x + \bar{a}_y\beta_y = \bar{a}_x\beta\cos\theta + \bar{a}_y\beta\sin\theta \tag{21}$$

where θ could be θ_i, θ_r or θ_t (incidence, reflection or transmission angles) and β could be β_1 or β_2, the numerical wavenumbers which are the solutions of the dispersion relations corresponding to either zonal algorithm. From equation (2) we can write

$$\bar{P} = \bar{a}_x P\cos\theta^P + \bar{a}_y P\sin\theta^P \tag{22}$$

where, again, θ^P could be θ_i^P, θ_r^P or θ_t^P and is calculated from

$$\theta^P = \tan^{-1}\frac{D_y}{D_x}. \tag{23}$$

A $\theta = \theta^P = 0$ means both propagation and Poynting

vectors are normal to the interface. Since we are using uniform space meshing in both zones we can assume that $\theta_r = \theta_i$ and $\theta_r^P = \theta_i^P$, with the latter being due to numerical dispersion symmetry around $\theta = 0$. Also, at the planar interface ($x = 0$), boundary conditions will force

$$\beta_{1y} = \beta_{2y} \tag{24}$$

since both zonal algorithms share the same field nodes at the interface and the incident, transmitted and possibly reflected field amplitudes are related by $E_{1o}^i + E_{1o}^r = E_{2o}^t$. We will also be using $E_{1o}^r = \Gamma E_{1o}^i$ where Γ is the desired numerical reflection coefficient.

The S_{22} update equation for the E_z field node at the interface (say, at the $x = 0$ and $y = 0$ location) is

$$E_z|_{0,0}^{n+\frac{1}{2}} - E_z|_{0,0}^{n-\frac{1}{2}} = \frac{\Delta t}{\epsilon h} \begin{pmatrix} H_y|_{\frac{1}{2},0}^n - H_y|_{-\frac{1}{2},0}^n \\ -H_x|_{0,\frac{1}{2}}^n + H_x|_{0,-\frac{1}{2}}^n \end{pmatrix}. \tag{25}$$

Assuming that each of the above field nodes has the form $e^{j(\omega t - \beta_x x - \beta_y y)}$ we can replace them, each (after eliminating common terms) with

$$E_z|_{0,0}^{n\pm\frac{1}{2}} \rightarrow (1+\Gamma) E_{1o}^i e^{\pm j\omega\Delta t/2}, \tag{26}$$

$$H_y|_{\frac{1}{2},0}^n \rightarrow -\frac{(1+\Gamma)E_{1o}^i}{\eta} \cos\theta_t^P e^{-j\beta_{2x}h/2}, \tag{27}$$

$$H_y|_{-\frac{1}{2},0}^n \rightarrow -\frac{E_{1o}^i}{\eta} \cos\theta_i^P e^{j\beta_{1x}h/2} + \frac{\Gamma E_{1o}^i}{\eta} \cos\theta_i^P e^{-j\beta_{1x}h/2}, \tag{28}$$

$$H_x|_{0,\frac{1}{2}}^n \rightarrow \frac{E_{1o}^i}{\eta} \sin\theta_i^P e^{-j\beta_{1y}h/2} + \frac{\Gamma E_{1o}^i}{\eta} \sin\theta_i^P e^{-j\beta_{1y}h/2}, \tag{29}$$

$$H_x|_{0,-\frac{1}{2}}^n \rightarrow \frac{E_{1o}^i}{\eta} \sin\theta_i^P e^{j\beta_{1y}h/2} + \frac{\Gamma E_{1o}^i}{\eta} \sin\theta_i^P e^{j\beta_{1y}h/2} \tag{30}$$

where η is the dispersion-immune intrinsic wave impedance [9]. Assembling these substitutions into equation (25) and simplifying we get

$$\begin{aligned} \frac{j2h(1+\Gamma)}{c\Delta t} \sin(\omega\Delta t/2) \;=\; & -(1+\Gamma)\cos\theta_t^P e^{-j\beta_{2x}h/2} \\ & + \cos\theta_i^P \left(e^{j\beta_{1x}h/2} - \Gamma e^{-j\beta_{1x}h/2} \right) \\ & + j2(1+\Gamma)\sin\theta_i^P \sin(\beta_{1y}h/2). \end{aligned} \tag{31}$$

Splitting the reflection coefficient into its real and imaginary parts ($\Gamma = \Gamma_r + j\Gamma_i$) and decoupling the complex equation we can write,

$$\begin{bmatrix} -(1+\Gamma_r)\cos\theta_t^P \cos\frac{\beta_{2x}h}{2} \\ +(1-\Gamma_r)\cos\theta_i^P \cos\frac{\beta_{1x}h}{2} \end{bmatrix} = \Gamma_i \begin{bmatrix} -\frac{2h}{c\Delta t}\sin\frac{\omega\Delta t}{2} + \cos\theta_t^P \sin\frac{\beta_{2x}h}{2} \\ +\cos\theta_i^P \left(\cos\frac{\beta_{1x}h}{2} + \sin\frac{\beta_{1x}h}{2} \right) \end{bmatrix} \tag{32}$$

and

$$\Gamma_i \left[\cos\theta_t^P \sin\frac{\beta_{2x}h}{2} + \cos\theta_i^P \cos\frac{\beta_{1x}h}{2} \right] = (1+\Gamma_r) \begin{bmatrix} -\frac{2h}{c\Delta t}\sin\frac{\omega\Delta t}{2} + 2\sin\theta_i^P \sin\frac{\beta_{1y}h}{2} \\ +\cos\theta_t^P \sin\frac{\beta_{2x}h}{2} + \cos\theta_i^P \sin\frac{\beta_{1x}h}{2} \end{bmatrix}. \tag{33}$$

Equations (32) and (33) are satisfied by a real-valued Γ which reduces (32) (when $\Gamma_i = 0$) to

$$(1-\Gamma_r)\cos\theta_i^P \cos\frac{\beta_{1x}h}{2} - (1+\Gamma_r)\cos\theta_t^P \cos\frac{\beta_{2x}h}{2} = 0 \tag{34}$$

from which the closed-form expression of the numerical reflection coefficient can be written as,

$$\Gamma = \frac{1-\kappa}{1+\kappa} \qquad \text{with} \qquad \kappa = \frac{\cos\theta_t^P \cos\frac{\beta_{2x}h}{2}}{\cos\theta_i^P \cos\frac{\beta_{1x}h}{2}}. \tag{35}$$

For any incidence angle θ_i, β_{1x} and β_{1y} are obtained from the left zonal dispersion relation. β_{2x} is then calculated from the right zonal dispersion relation after setting $\beta_{2y} = \beta_{1y}$, which would also yield θ_t. This is followed by finding θ_i^P and θ_t^P using equation (23), then finally Γ is calculated from equation (35).

IV. S_{24}/S_{22} HYBRID ALGORITHM IN 2-D

Starting with the hybrid S_{24}/S_{22} algorithm let us first observe the deviations of the polarization angle from the propagation angle, $\theta^P - \theta$, as a function of the incidence angle θ_i in both zones (Fig. 3). As shown, grid symmetry aligns both angles when the incidence angle is either zero or $\pi/4$. At other angles, however, the deviation in the S_{22} zone reaches as high as 25 times that in the S_{24} zone at the uniform resolution of $R = 10$ cells per wavelength. Furthermore, as $\theta_i \rightarrow \pi/2$ the boundary condition (24) forces an exaggerated error in both transmission angles, θ_t and θ_t^P as shown in Figs. 3 and 4. Figure 5 compares the numerical reflection coefficient at different resolution factors versus angle of incidence (solid lines). It is clear from the figure that spurious reflections can become problematic as the incidence angle goes beyond 80° unless fine meshing is used which negates the computational efficiency advantage of the high-order S_{24} algorithm.

To solve this problem of increasing reflections near grazing angles, the S_{22} algorithm in the right zone is modified so that second order differencing is maintained for $\partial/\partial x$ and a fourth order differencing is applied to $\partial/\partial y$ as demonstrated in Fig. 6. This approach

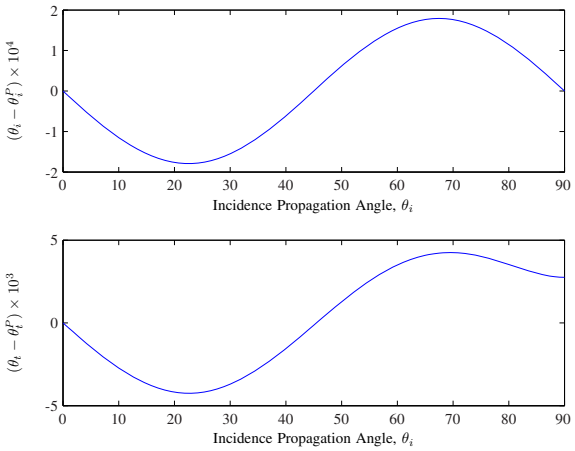

Fig. 3. Deviation between propagation and polarization angles in both incidence and transmission zones. $R = 10$ cells per wavelength.

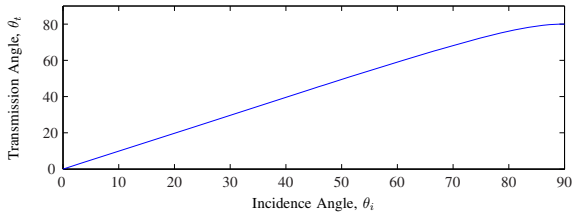

Fig. 4. Effect of boundary conditions at the $x = 0$ interface on the transmission angle. $R = 10$ cells per wavelength.

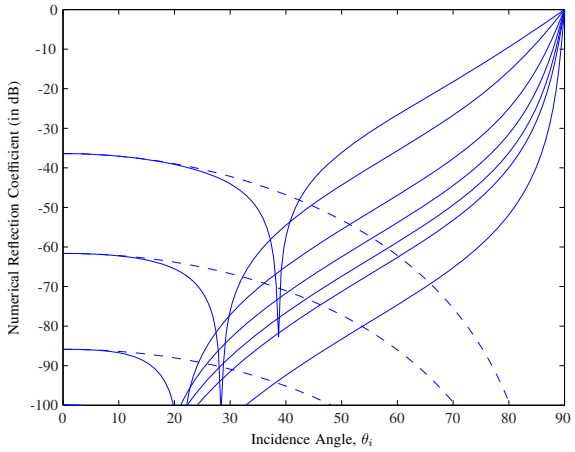

Fig. 5. Numerical reflection coefficient vs. θ_i across an S_{24}/S_{22} hybrid algorithm interface before (solid) and after (dashed) tangential phase matching at the resolution factors (from top to bottom), $R = 5, 10, 20, 30, 40, 50, 100$.

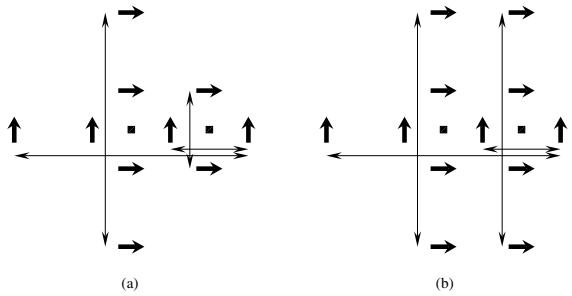

Fig. 6. FDTD stencil extents at the S_{24}/S_{22} interface before (a) and after (b) tangential stretching in the S_{22} zone for phase matching purposes.

has the advantage of single-cell interface-normal depth for modeling physical discontinuities and an extended interface-tangential cell that matches the numerical wavenumbers along that direction. The corresponding update equations for the $y-$stretched algorithm in zone 2 are given by,

$$\begin{aligned}
\epsilon\frac{\partial E_z}{\partial t} &= \frac{H_y|_{i+\frac{1}{2}} - H_y|_{i-\frac{1}{2}}}{h} \\
&\quad -\frac{27(H_x|_{j+\frac{1}{2}} - H_x|_{j-\frac{1}{2}})}{24h} \\
&\quad +\frac{H_x|_{j+\frac{3}{2}} - H_x|_{j-\frac{3}{2}}}{24h} \\
\mu\frac{\partial H_y}{\partial t} &= \frac{E_z|_{i+\frac{1}{2}} - E_z|_{i-\frac{1}{2}}}{h} \\
\mu\frac{\partial H_x}{\partial t} &= -\frac{27(E_z|_{j+\frac{1}{2}} - E_z|_{j-\frac{1}{2}})}{24h} \\
&\quad +\frac{E_z|_{j+\frac{3}{2}} - E_z|_{j-\frac{3}{2}}}{24h}
\end{aligned} \tag{36}$$

and the discrete operators which would replace those of equation (3) are

$$D_x = \frac{\sin\frac{\beta_x h}{2}}{h/2}, \tag{37}$$

$$D_y = \frac{9}{8}\frac{\sin\frac{\beta_y h}{2}}{h/2} - \frac{1}{8}\frac{\sin\frac{3\beta_y h}{2}}{3h/2}. \tag{38}$$

The corresponding dispersion relation is obtainable from equation (16) and the stability limit is governed by,

$$\Delta t \leq \frac{h}{c\sqrt{2}}\sqrt{\frac{72}{85}} \tag{39}$$

a slightly more relaxed condition than that of the left zone's S_{24} algorithm ensuring stability when the latter is enforced. Figure 5 (dashed lines) demonstrates the advantage gained in the form of vanishing reflections at near-grazing incidence angles.

It must be remembered that the numerical reflection coefficient (35) was derived using the S_{22} update equation (25) at the interface. The corresponding expression

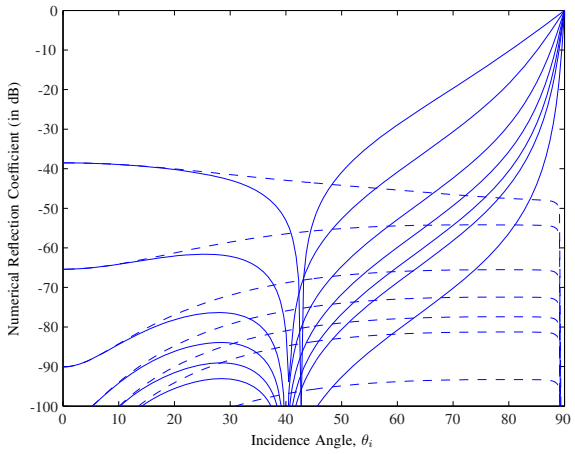

Fig. 7. Numerical reflection coefficient vs. θ_i across an M24/S_{22} hybrid algorithm interface before (solid) and after (dashed) tangential phase matching at the resolution factors (from top to bottom) $R = 5, 10, 20, 30, 40, 50, 100$.

for the above phase-matched S_{24}/S_{22} interface must be derived from,

$$E_z|_{0,0}^{n+\frac{1}{2}} = E_z|_{0,0}^{n-\frac{1}{2}} + \frac{\Delta t}{\epsilon h}\left(H_y|_{\frac{1}{2},0}^{n} - H_y|_{-\frac{1}{2},0}^{n}\right) - \frac{\Delta t}{24\epsilon h}\begin{pmatrix} 27H_x|_{0,\frac{1}{2}}^{n} - 27H_x|_{0,-\frac{1}{2}}^{n} \\ -H_x|_{0,\frac{3}{2}}^{n} + H_x|_{0,-\frac{3}{2}}^{n} \end{pmatrix} \quad (40)$$

which necessitates an additional substitution to equations (26) to (30);

$$H_x|_{0,\pm\frac{3}{2}}^{n} \rightarrow \frac{(1+\Gamma)E_{1o}^{i}}{\eta}\sin\theta_i^P e^{\mp j3\beta_{1y}h/2}. \quad (41)$$

Completing the substitutions into equation (40) will only affect the term containing β_{1y} in (31), leaving (32) and the Γ_i term in (33) intact and in a manner that maintains equation's (35) validity for predicting the numerical reflection coefficient across the interface in the present case.

V. M24/S_{22} HYBRID ALGORITHM

As in the case of the S_{24}/S_{22} interface, variations in the M24 algorithm's dispersion behavior versus propagation angle compared to those of the S_{22} algorithm cause serious spurious numerical reflections at near grazing angles at the interface as demonstrated in Fig. 7 (solid lines). To remedy these high reflections the S_{22} algorithm in the right zone needs to be replaced by one that maintains single cell normal depth but has matching tangential dispersion characteristics to the left zone M24 algorithm. A logical choice would be to apply the M24 development methodology using concentric flat (one cell depth along the x-axis) Ampere's and Faraday's loops. However, such an approach would be an overkill and is unnecessary, considering that in real applications the right zone would be only one cell deep negating the need for low dispersion for all propagation angles save for the tangential direction to the interface. A simpler and more practical scheme is to use again an elongated S_{22} algorithm as in the previous case, except that a tuning parameter is introduced to be used for phase matching with the left M24 zone,

$$\begin{aligned} \epsilon\frac{\partial E_z}{\partial t} &= \frac{H_y|_{i+\frac{1}{2}} - H_y|_{i-\frac{1}{2}}}{h} \\ &\quad + \frac{K^b}{3h}(H_x|_{j-\frac{3}{2}} - H_x|_{j+\frac{3}{2}}) \\ &\quad + \frac{1-K^b}{h}(H_x|_{j-\frac{1}{2}} - H_x|_{j+\frac{1}{2}}) \\ \mu\frac{\partial H_y}{\partial t} &= \frac{E_z|_{i+\frac{1}{2}} - E_z|_{i-\frac{1}{2}}}{h} \\ \mu\frac{\partial H_x}{\partial t} &= \frac{K^b}{3h}(E_z|_{j-\frac{3}{2}} - E_z|_{j+\frac{3}{2}}) \\ &\quad + \frac{1-K^b}{h}(E_z|_{j-\frac{1}{2}} - E_z|_{j+\frac{1}{2}}). \end{aligned} \quad (42)$$

The corresponding discrete operators are

$$D_x = \frac{\sin\frac{\beta_x h}{2}}{h/2}, \quad (43)$$

$$D_y = (1-K^b)\frac{\sin\frac{\beta_y h}{2}}{h/2} + K^b\frac{\sin\frac{3\beta_y h}{2}}{3h/2}, \quad (44)$$

with the dispersion relation obtainable from equation (16) and the stability limit governed by

$$\Delta t \le \frac{h}{c}\frac{1}{\sqrt{1+(1-4K^b/3)^2}}. \quad (45)$$

The choice for the tuning parameter K^b will be based on an optimization routine that will minimize the numerical reflection coefficient (equation (35) is valid for this case too) for the particular resolution factor R used in the simulation. Table 1 lists the K_1 and K_2 parameters for the left zone at several R values along with matching K^b values for the right zone that will eliminate spurious reflections at the interface as shown in Fig. 7 (dashed lines).

VI. NUMERICAL VALIDATION

To verify the effectiveness of the modified update equations (36) and (42) at eliminating reflections off the S_{24}/S_{22} and M24/S_{22} interfaces, FDTD simulations were performed where a point sinusoidal source was initiated very near the interfaces (4 cells away) to highlight near-grazing wave incidence. The simulations were run once with high-order update equations for the left zone and S_{22} update equations for the right zone, and again with the former applied to both zones. Figure 8 highlights the absolute difference between the

Table 1. K_1 and K_2 values for the left zone M24 algorithm with corresponding K^b values for a phase-matched right zone S_{22} algorithm.

R	K_1	K_2	K^b
5	−0.144932	0.1020689	−0.0933211
10	−0.116193	0.0734445	−0.0793836
20	−0.110322	0.0678920	−0.0763555
30	−0.109283	0.0669205	−0.0758122
40	−0.108922	0.0665844	−0.0756233
50	−0.108756	0.0664296	−0.0755362
100	−0.108535	0.0662238	−0.0754201

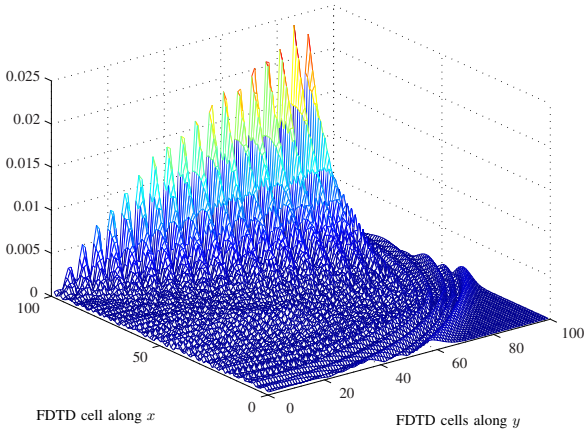

Fig. 8. Isolated numerical reflections at the interface of a typical hybrid S_{24}/S_{22} algorithm. $R = 10$ at 1 GHz.

two simulation runs for the S_{24}/S_{22} case isolating net numerical reflections off the interface.[1] Note in this figure the increasing reflection noise levels as the surface wave propagates further away from the source location along the interface. In comparison, Fig. 9 demonstrates the total absence of this interface hugging reflection noise due to the implementation of equations (36) in the right zone. Figures 10 and 11 demonstrate a similar accomplishment for the M24/S_{22} case. Table 2 summarizes a comparison between these measured after-modification reflections and those predicted in Figs. 5 and 7 showing reasonable agreements, especially in the M24/S_{22} case.

Finally, reflection noise levels could be further reduced by using a soft-start sinusoidal source. For example, using Furse *et al.*'s raised cosine ramp function [11],

$$r(t) = \begin{cases} 0, & t < 0 \\ \frac{1}{2}\left(1 - \cos\frac{\omega t}{2\alpha}\right), & 0 \le t \le \alpha T \\ 1, & t > \alpha T \end{cases} \qquad (46)$$

[1]Only the upper-left quadrant data of Fig. 2 are shown as the reflections were symmetric across the x-axis.

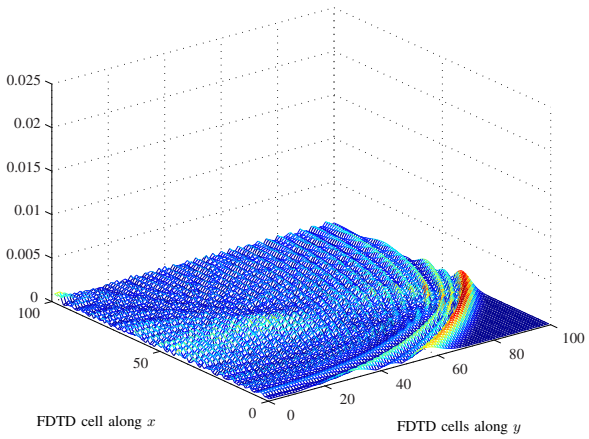

Fig. 9. Elimination of tangential reflections due to S_{22} phase-matching with the S_{24} scheme in a hybrid S_{24}/S_{22} algorithm. $R = 10$ at 1 GHz.

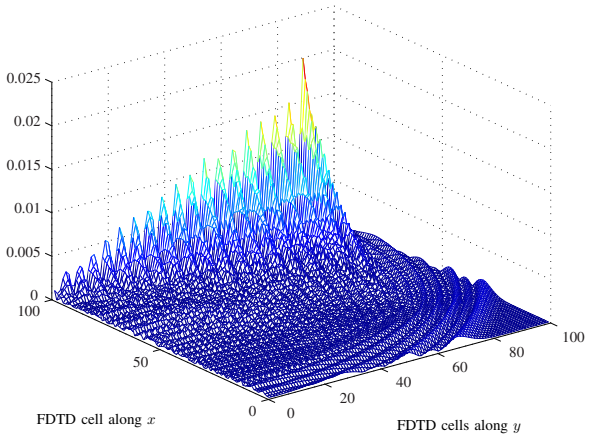

Fig. 10. Isolated numerical reflections at the interface of a typical hybrid M24/S_{22} algorithm. $R = 10$ at 1 GHz.

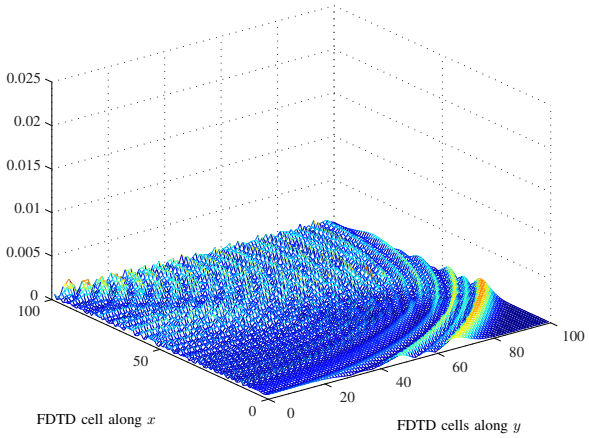

Fig. 11. Elimination of tangential reflections due to S_{22} phase-matching with the M24 scheme in a hybrid M24/S_{22} algorithm. $R = 10$ at 1 GHz.

Table 2. Comparison of predicted and measured numerical reflections after phase-matching the high-order and low-order schemes in the hybrid algorithms discussed in this work. $R = 10$ at 1 GHz.

Algorithm	Predicted $\Gamma_{\max}$	Measured $\Gamma_{\max}$
S_{24}/S_{22}	-62 dB	-55 dB
$M24/S_{22}$	-54 dB	-57 dB

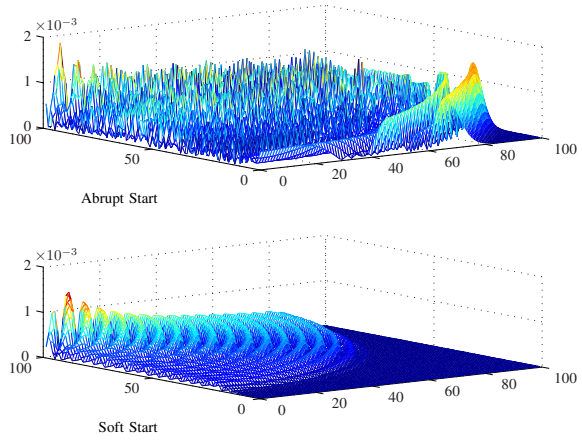

Fig. 12. Filtering out high-frequency content of the reflection noise in the phase-matched hybrid $M24/S_{22}$ algorithm by replacing the abruptly-starting sine source with a smooth-starting ramped-cosine source.

with $T = 2\pi/\omega$ and α chosen as 1.5, we can replace the $\sin(\omega t)$ source in the FDTD simulations with $r(t)\cos(\omega t)$. Such a substitution would effectively filter out the high frequency content of the reflection noise as demonstrated in Fig 12.

VII. CONCLUSION

The phase velocity mismatches across hybrid high-order/low-order FDTD implementations cause unacceptably growing reflections across the hybrid interface when the traversing wave is at near grazing incidence angles. A predictive equation of the ensuing numerical reflections has been derived, investigated and used along with the dispersion relations of both the high-order and low-order schemes to modify the latter and match its tangential (to the interface) phase velocity to that of the former. Numerical experiments have demonstrated that this modification has completely eliminated the excessive interface-hugging reflection noises and reduced them to the same level as the axial reflection noises. These experiments have been performed for the S_{24}/S_{22} and $M24/S_{22}$ hybrid algorithms with good agreement between predicted and measured reflections after the phase-matching algorithm modifications. In practical applications this innovation allows efficient use of thin (one cell deep) S_{22} buffer zones where needed in an otherwise global high-order implementation for modeling electrically large structures with high phase accuracy.

REFERENCES

[1] K. L. Shlager and J. B. Schneider, "Comparison of the dispersion properties of several low-dispersion finite-difference time-domain algorithms," *IEEE Trans. Antennas Propagat.*, vol. 51, no. 3, pp. 642–653, Mar. 2003.

[2] E. A. Forgy and W. C. Chew, "A time-domain method with isotropic dispersion and increased stability on an overlapped lattice," *IEEE Trans. Antennas Propagat.*, vol. 50, no. 7, pp. 983–996, July 2002.

[3] J. B. Cole, "A high-accuracy realization of the Yee algorithm using non-standard finite differences," *IEEE Trans. Microwave Theory Tech.*, vol. 45, no. 6, pp. 991–996, June 1997.

[4] M. F. Hadi and M. Piket-May, "A modified FDTD (2,4) scheme for modeling electrically large structures with high-phase accuracy," *IEEE Trans. Antennas Propagat.*, vol. 45, no. 2, pp. 254–264, Feb. 1997.

[5] G. J. Haussmann, "A dispersion optimized three-dimensional finite-difference time-domain method for electromagnetic analysis," Ph.D. dissertation, University of Colorado at Boulder, Boulder, CO, 1998.

[6] S. V. Georgakopoulos, R. A. Renaut, C. A. Balanis, and C. R. Birtcher, "A hybrid fourth-order FDTD utilizing a second-order FDTD subgrid," *IEEE Microwave Wireless Compon. Lett.*, vol. 11, no. 11, pp. 462–464, Nov. 2001.

[7] M. Celuch-Marcysiak, "Extended study of poynting theorem and reciprocity on nonuniform fdtd meshes," *IEE Proc.-Sci. Meas. Technol.*, vol. 151, no. 6, pp. 452–455, Nov. 2004.

[8] M. Celuch-Marcysiak and J. Rudnicki, "A study of numerical reflections caused by fdtd mesh refinements in 1d and 2d," *15th Ann. Conf. Microwave Radar Wireless Comm., Warsaw, Poland*, pp. 626–629, May 2004.

[9] M. Celuch-Marcysiak and W. K. Gwarek, "On the nature of solutions produced by finite difference schemes in time domain," *Int. J. Numerical Modelling: Electronic Networks, Devices and Fields*, vol. 12, no. 1–2, pp. 23–40, Jan.–Apr. 1999.

[10] J. B. Schneider, "Plane waves in FDTD simulations and a nearly perfect total-field/scattered-field boundary," *IEEE Trans. Antennas Propagat.*, vol. 52, no. 12, pp. 3280–3287, Dec. 2004.

[11] C. M. Furse, D. H. Roper, D. N. Buechler, D. A. Christensen, and C. H. Durney, "The problem and treatment of DC offsets in FDTD simulations," *IEEE Trans. Antennas Propagat.*, vol. 48, no. 58, pp. 1198–1201, Aug. 2000.

Mohammed Hadi was born in 1965. He received his B.S. degree in electrical engineering from Kuwait University in 1988 and his M.S. and Ph.D. degrees from the University of Colorado at Boulder in 1992 and 1996. From his position as an Assistant Professor at the Department of Electrical Engineering of Kuwait University, Dr. Hadi kept himself busy for the last decade in governmental work and consultations in the areas of engineering training, higher education planning and Kuwait's labour profile studies. Dr. Hadi is currently a Visiting Research Scholar at Duke University, North Carolina.

Rabie Dib was born in 1977. He received his B.S. and M.S. degrees in electrical engineering from Kuwait University in 1999 and 2002. Mr. Dib worked as a Teaching Assistant and operated the Electromagnetic Compatibility Lab. at Kuwait University from 2000 to 2006 during which he participated in several intra-industry training programs. Mr. Dib is currently an Instructor with the College of Technological Studies at Kuwait's Public Authority of Applied Education and Training.

Finite Difference Time Domain Method for the Analysis of Transient Grounding Resistance of Buried Thin Wires

[1] Md. Osman Goni, [2] Eiji Kaneko, and [3] Akihiro Ametani

[1] Faculty of Engineering, Khulna University of Engineering & Technology, Bangladesh
[2] Faculty of Engineering, University of the Ryukyus, Japan
[3] Department of Electrical Engineering, Doshisha University, Japan

Abstract – For the analysis of grounding resistance with the finite-difference time-domain (FDTD) method for solving Maxwell's equations, an equivalent radius of a naked thin wire in a lossy medium is derived by means of the static field approximation, proposed for derivation of that of an aerial thin wire. It is 0.23 times the size of each cell employed, which is the same as that of an aerial thin wire. The validity is tested by comparing the grounding-resistance values obtained through FDTD simulation on simple buried structures with the theoretical values.

Key words – FDTD method, grounding electrode, grounding resistance, thin wire, and conductor.

I. INTRODUCTION

The role of grounding electrodes is to dissipate fault currents effectively into the soil, and thereby to prevent damage of insulations in power systems. Thus, the performance of power systems is influenced by proper functioning of grounding systems.

No formulas of impedance and admittance have been derived even for simple vertical or horizontal naked conductor buried in a homogeneous ground. Hence, transient characteristics of grounding electrodes have been investigated by experiments and recently numerical electromagnetic analyses [1 - 4] based on the method of moments (MoM), the finite element method (FEM), or the finite-difference time-domain (FDTD) method [5 - 6]. Numerical electromagnetic analyses can be performed assuming well-profiled condition that the values of conductivity and permittivity of a ground are known or set arbitrarily. Such results are useful in understanding the phenomena as well as in confirming measured results.

Numerical electromagnetic analyses based on the FDTD method are effective to analyze the transient response of a large solid conductor or electrode. The accuracy of this method, in the case of being applied to such analysis, has been fully investigated in comparison with an experiment and shown to be satisfactory [7]. As this method requires long computation time and large capacity of memory, the analysis is restricted to a rather small space. A transient analysis of a large system or a system composed of various elements still need to be performed by such tools like Electromagnetic Transients Program (EMTP) [8]. One reasonable process of study, therefore, is to investigate the physical characteristics of a grounding electrode by a numerical electromagnetic analysis, and then to represent the obtained characteristics by an equivalent circuit model or to determine the values of its parameters [3].

So far in most of the FDTD analyses of transient and steady-state grounding resistance, large solid electrodes [6], [7], which can be decomposed into small cubic cells, have been chosen and thin-wire electrodes have not been dealt with. This is because an equivalent radius of a thin wire in a lossy medium has not been made clear. In [9], a rigorous method has been shown for determining the effective radius of a single axial field component, E_x or H_x, in a two-dimensional (2-D) TM_x or TE_x FDTD grid. The method is based upon matching FDTD results for a filamentary field source with the analytical Green's function in two dimensions. It is therefore, essential to clarify the equivalent radius of a buried thin wire for more general analyses of grounding systems. In the present paper, an equivalent radius of a thin wire in lossy medium is derived with the help of the concept proposed for derivation of that of an aerial thin wire [10]. Then its validity is tested by comparing the grounding-resistance values obtained through FDTD simulations on simple buried structures with the theoretical values.

II. METHOD OF ANALYSIS

The FDTD method employs a simple way to discretize a differential form of Maxwell's equations. In the Cartesian coordinate system, it generally requires the entire space of interest to be divided into small rectangular cells and calculates the electric and magnetic fields of the cells using the discretize Maxwell's equations. As the material constant of each cell can be specified arbitrarily, a complex inhomogeneous medium can be easily analyzed. To analyze fields in an open space, an absorbing boundary has to be set on each plane which limits the space to be analyzed, so as to avoid reflection there. In the present analysis, the second-order Mur's method [11] is employed to represent absorbing planes.

III. DERIVATION OF EQUIVALENT RADIUS OF BURIED THIN WIRE

In [8], it has been shown that an aerial thin wire has some equivalent radius in the case that the electric-field elements along the thin wire are set to zero in an orthogonal and uniform-spacing Cartesian grid. When the size of cubic cells employed is Δs, the equivalent radius is 0.23Δs. In the present paper, an equivalent radius of a naked thin wire in a lossy medium is derived. Note that in [10] an equivalent radius of an aerial thin wire has been shown to be 0.135Δs. In a quasi-steady state, however, 0.23Δs is more appropriate than 0.135Δs as an equivalent radius [8] which is very close to the effective radius 0.2Δs [7].

Figure 1 illustrates the cross section of a long thin wire surrounded by a cylindrical sheath conductor. The radii of the thin wire and the sheath are a and b, respectively. The conductivity and the relative permittivity of a medium between the thin wire and sheath conductor are assumed to be σ and ε_s, respectively. In this condition, the conductance G and the susceptance B between the thin wire and the sheath are given as follows,

$$G = \frac{2\pi\sigma}{\ln(b/a)}, \quad B = \frac{2\pi\varepsilon_0\varepsilon_s\omega}{\ln(b/a)}. \tag{1}$$

Note that ε_0 is the permittivity of vacuum and ω is the angular frequency. Therefore, the conductance becomes equal to the susceptance when the frequency f is

$$f_0 = \sigma/(2\pi\varepsilon_0\varepsilon_s). \tag{2}$$

For instance, f_0 is 1.5 or 7.5 MHz for a medium of ε_s = 12 and σ = 1 mS/m or 5 mS/m, respectively.

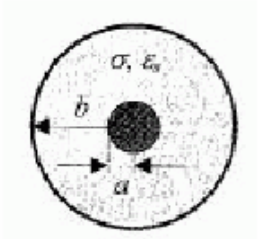

Fig. 1. Cross section of a thin wire surrounded by a cylindrical sheath.

Figure 2 shows the cross section of a thin wire surrounded by a rectangular sheath conductor for an FDTD simulation. Both the thin wire core and the sheath are perfectly conducting. The cross-sectional area of the sheath is 2.5 X 2.5 m^2 and the length is 25 m. The conductor system is represented with cubic cells whose side Δs is 0.25 m. A voltage, which has a rise-time of 20 ns and a magnitude of 100 V, is applied between the thin wire and the sheath at its one end. The other end is open. The response is calculated up to 10 μs with a time increment of 0.4 ns.

Figure 3 shows the time-variations of the ratios of E_1, E_2 and E_3 to E_2 which are radial electric fields calculated for 0.5Δs, 1.5Δs, and 2.5Δs, at 12.5 m from the ends of the conductor. It is found that the ratios settle down after 100 ns or so, and they are almost equal to those calculated for a thin wire in air [10]: 2.21, 1.00 and 0.59. This is natural because both the conductance and the susceptance of a thin wire follow similar expressions as shown in equation (1). Furthermore, the ratios change a little even if a different conductivity such as 0.2 or 10 mS/m is employed and a different time increment 0.25 or 0.48 ns is used. Thus electric field around the thin wire can also be approximated by the following function [10],

$$E = 3\Delta s/(2x). \tag{3}$$

Note that x is the distance from the centre of the thin wire. In this function, the electric field $\boldsymbol{E}$ is normalized so that $\boldsymbol{E}$ should be unity at x =1.5 Δs. Figure 4 shows the radial electric fields calculated by this function and those obtained by the FDTD simulation.

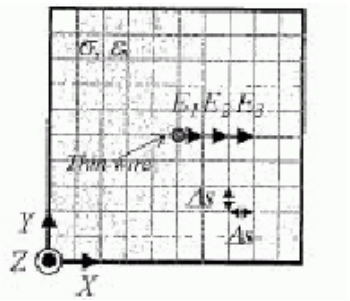

Fig. 2. Electric field around a thin wire in a rectangular sheath to be used for an FDTD simulation.

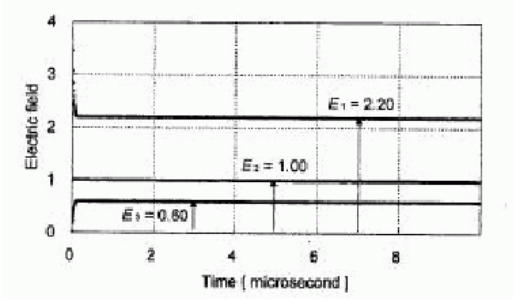

Fig. 3. Time-variation of the ratios of E_1, E_2 and E_3 to E_2 calculated by the FDTD method in the case of σ = 5 mS/m and ε_s = 12.

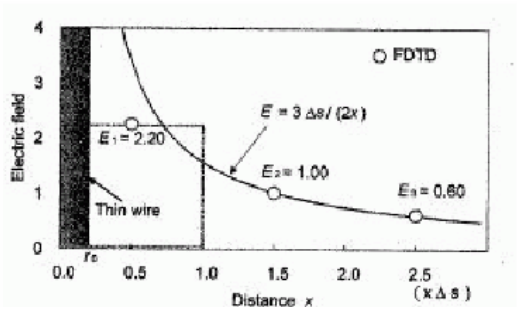

Fig. 4. Radial electric fields around the thin wire.

If the equivalent radius of the thin wire now in question is assumed to be r_0 and the electric field is assumed to follow the above function, the potential difference between $x = r_0$ and $x = \Delta s$ is given as follows,

$$\int_{r_0}^{\Delta s} \mathrm{E}\ \mathrm{dx} = \frac{3\Delta \mathrm{s}}{2} \ln \frac{\Delta s}{r_0}. \quad (4)$$

If the above expression is equated to 2.2 Δs, which is the potential difference obtained by the FDTD simulation, the equivalent radius r_0 is given as,

$$r_0 = 0.23\,\Delta s. \quad (5)$$

This is an equivalent radius of a naked thin wire in a lossy medium.

IV. COMPARISON WITH SUNDE'S FORMULA ON GROUNDING RESISTANCE

A. Models for Analysis

Figure 5 shows a side view of an analysis model, which is composed of two naked vertical thin wires and an overhead horizontal thin wire. The buried portion of vertical thin wires is 3 or 5 m. The horizontal thin wire is 30 m long and 1 m high over the surface of a homogeneous ground. The conductor system is excited by a voltage source at a connection point between the horizontal wire and one of the buried vertical wires. The voltage source produces a steep-front wave having a rise-time of 10 ns, after which it maintains a magnitude of 100 V, [12 - 16].

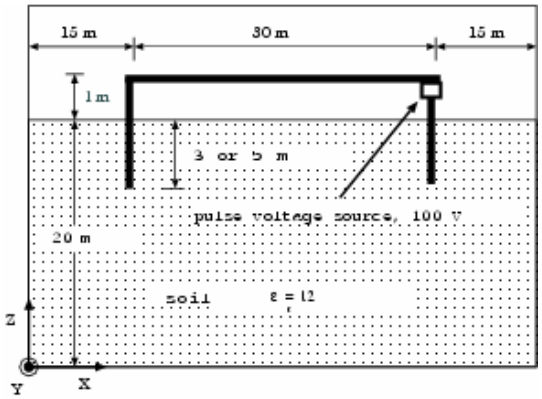

Fig. 5. Two buried vertical thin wires connected by an overhead horizontal wire to be analyzed by the FDTD method.

The conductivity of the homogeneous ground σ is set to 0.2 mS/m, 1.0 mS/m, and 5 mS/m in order to visualize the moisture contained in the soil, where the conductors are buried. The thickness and relative permittivity (ε_s) of the ground are set to 20 m and 12, respectively. For the FDTD simulation, the conductor system shown in Fig. 5 is accommodated by a large rectangular analysis space of 80 ×120 × 60 m^3 with space length Δs = 0.5 m. The voltage in the gap which exists between the horizontal wire and one of the buried vertical wires represents conductor-top voltage. The gap length is maintained as the space length of the conductor system. The time-step was determined by equation (14) found in [10] with α = 0.01, and all the six boundaries of the cell were treated as the second-order Liao's absorbing boundary.

It may be believed that the FDTD method is a time-consuming method. However, the progress of computers in terms of speed and memory is considerable, and even a personal computer can be used for the FDTD calculation. In fact, the simulation presented in this paper were performed by a personal computer with Intel Pentium 4, 2.80 GHz CPU and 512 MB RAM. Responses are calculated up to 1.5 μs with a time increment of 0.9 ns. Therefore, the computation time for one case is about 3 hours.

B. Analyzed Results

Figures 6 and 7 show both voltage and current waveforms at the vertical conductor-top, respectively, i.e., at the injection point calculated for the model of Fig. 5 in case of the vertical thin wires are buried up to 3 m and 5 m with different conductivity of the earth soil. Tables I and II summarizes the values of transient grounding resistance R_{GV} of the 3-m and 5-m vertical thin wires evaluated at 1.5 μs for Figs. 6 and 7. They are simply calculated from the following relation: $I_s = V_s / R_{GV}$. Note that V_s is the magnitude of the voltage and I_s is the current of the circuit.

Figure 8 shows the propagation of the current at different heights of the 6 m-vertical electrodes, which are buried up to 5 m and with different conductivity. These currents are simulated at 5.5 m, 2.5 m and at the bottom of the electrode in which the source is applied and thus treated as upper, middle and lower currents. It is noted that the middle and lower currents are characterized by the ground parameters. The magnitudes of current waveforms are increasing with the increase of the conductivity and thus the time required to settle down the currents is increasing. It is also noted that as the conductivity gets higher, the wavefronts of voltage and current become less steep. The waveform of a voltage of the buried naked conductor is not similar to that of a current, particularly around the injection point. If the buried conductor is insulated, the waveform of a voltage is almost identical to that of a current just, as if it is a coaxial cable [17].

C. Discussion

The wavelength of an electromagnetic field, which corresponds to the evaluation time (1.5 μs), is several hundred meters. It is ten times longer than the length of the conductor system shown in Fig. 5. Hence, it is considered that the transient-resistance value at 1.5 μs is close to the resistance in the steady state. Sunde [18] has

derived a theoretical formula for the DC resistance of a vertical conductor buried in a homogeneous ground. It is expressed as

$$R_{GV_{SUNDE}} = \frac{1}{2\pi\sigma d}(\ln\frac{4d}{r} - 1), \qquad (6)$$

where, d is the length and r is the radius of the electrode. The values of grounding resistance calculated by this theoretical formula are also included in Tables I and II. The values of the transient grounding resistance obtained by the FDTD simulation are only 8 % lower than those calculated by Sunde's formula regardless of the ground conductivity.

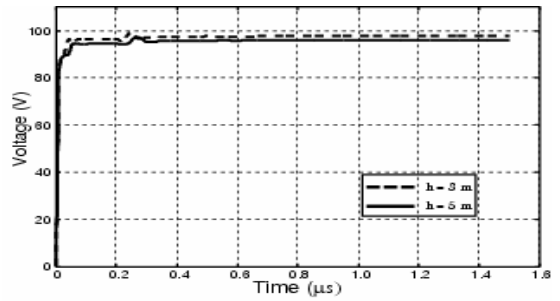

(a) σ = 0.2 mS/m.

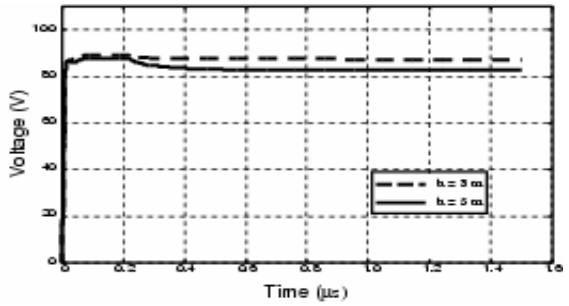

(b) σ = 1 mS/m.

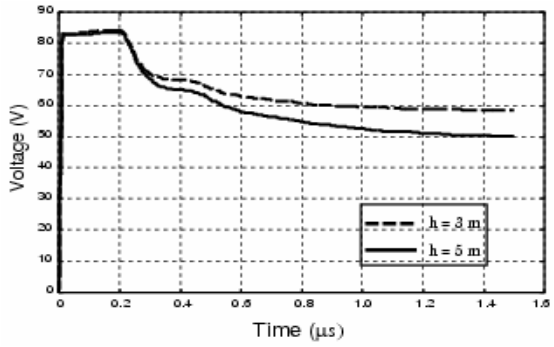

(c) σ = 5 mS/m.

Fig. 6. Voltages evaluated at the injection point of vertical thin electrodes of Fig. 5 buried up to 3 m and 5 m with different ground conductivity.

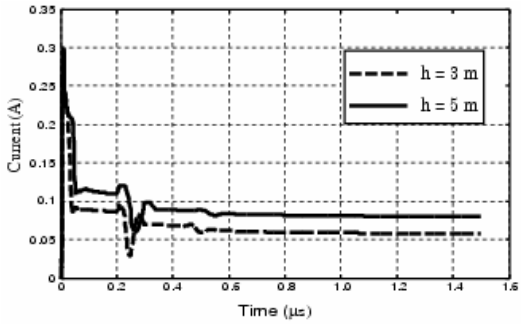

(a) σ = 0.2 mS/m.

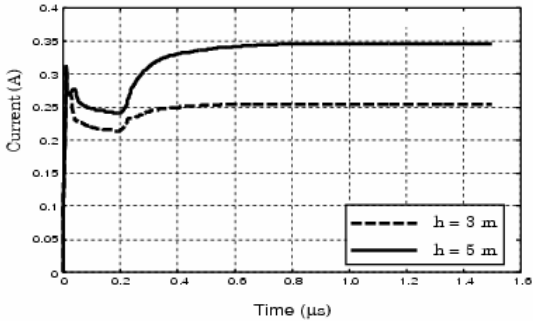

(b) σ = 1 mS/m.

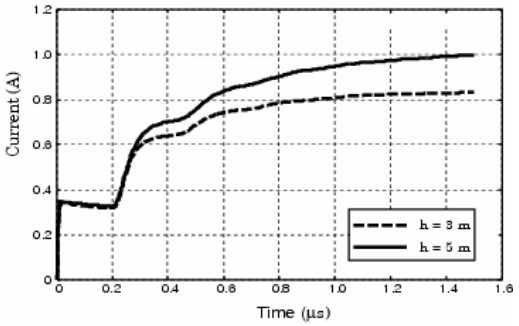

(c) σ = 5 mS/m.

Fig. 7. Calculated current waveforms at the injection point of the model of Fig. 5 with different conductivity in the case that the vertical thin wires are buried up to 3 and 5 m.

Table I. Transient grounding resistance of a 3-m vertical electrode obtained by the FDTD analysis and the DC resistance calculated by Sunde's formula.

	σ=0.2mS/m	*σ=1mS/m*	*σ=5 mS/m*
FDTD	900	178	36
Theory	967	193	38.7
Difference	6.9%	7.7%	7%

Table II. Transient grounding resistance of a 5-m vertical electrode obtained by the FDTD analysis and the DC resistance calculated by Sunde's formula.

	σ=0.2mS/m	*σ=1mS/m*	*σ=5 mS/m*
FDTD	615	121	21.5
Theory	661	131	26.5
Difference	7%	8%	7.5%

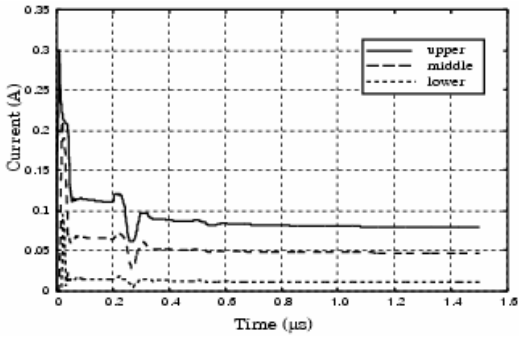

(a) σ = 0.2 mS/m.

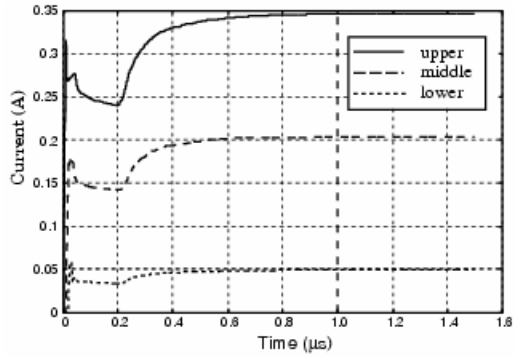

(b) σ = 1 mS/m.

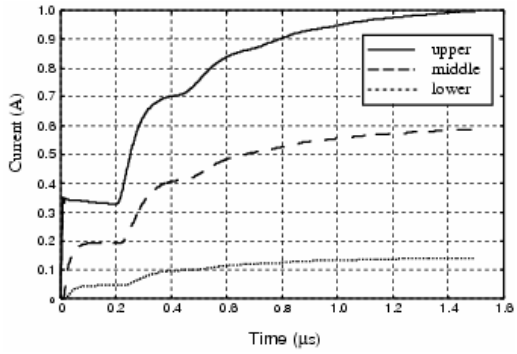

(c) σ = 5 mS/m.

Fig. 8. Propagating current observed at a different height of the vertical thin wire with different conductivity (5 m buried vertical thin wires).

When the length of the overhead horizontal thin wire is shortened or enlarged from 30 m to 20 m or 40 m, the transient resistance decreases only by 0.5 Ω (1.7\ %) or increases by 0.4 Ω (1.3\ %) for a 5-m buried vertical thin wire in a ground having the conductivity of 5 mS/m, as shown in Table III. Therefore, it is clear that the influence of the 30-m distance between the two electrodes is insignificant than the properties and the depth of the lossy ground.

As a consequence, it has become clear that the 0.23 Δs is valid as the equivalent radius of a thin wire buried in a lossy ground. Note that Sunde has proposed a theoretical formula of resistance also for a horizontal cylindrical electrode [18]. As it is a function of the natural logarithm of the square root of ***r***, the resistance value of a horizontal thin electrode is not so sensitive to the radius of the electrode. This is the reason why a horizontal electrode is not employed for comparison.

Table III. Dependency of the transient grounding resistance of a 5-m vertical electrode, calculated by the FDTD analysis on the distant two electrodes.

Distance	20 m	30 m	40 m
Resistance	25.8	26.5	27.7

V. CONCLUSIONS

In the present paper, for the analysis of grounding resistance with the FDTD method, an equivalent radius of a naked vertical thin wire in a lossy medium has been investigated with the help of the static-field concept proposed for an aerial thin wire. It is 0.23 times the side of cells employed, which is the same as that of the aerial thin wire. The validity has also been examined by comparing the grounding-resistance value obtained through FDTD simulations on simple buried structures with the theoretical values, and are shown to be satisfactory.

VI. ACKNOWLEDGMENT

The authors are indebted to T. Noda and Y. Baba for their technical support and providing useful information.

REFERENCES

[1] L. Grcev and F. Dawalibi, "An electromagnetic model for transients in grounding systems," *IEEE Trans. Power Delivery*, PWRD, vol. 5, no. 4, pp. 1773-1781, 1990.

[2] Y. Liu, M. Zitnik, and R. Thottappillil, "A time domain transmission line model of grounding systems," *Proc. Int. Symp. High Voltage Engineering*, pp. 154 -157, 2001.

[3] Y. Liu, M. Zitnik, and R. Thottappillil, "A time domain transmission line model of grounding systems," *Proc. Int. Symp. High Voltage Engineering,* pp. 154 -157, 2001.

[4] Y. Baba and M. Ishii, "Numerical electromagnetic field analysis on lightning surge response of tower with shield wire," *IEEE Trans. Power Delivery*, PWRD, vol. 15, pp. 1010 - 1015, no. 3, Jul. 2000.

[5] Y. Baba, M. Nayel, N. Nagaoka, A. Ametani, and S. Sekioka, "Numerical analysis of wave propagation characteristics on a buried horizontal conductor by FDTD method," *Journal of IEE*, vol. 123, no. 11, pp. 1319 - 1327, 2003.

[6] A. Taflove and S. C. Hugness, *Computational Electrodynamics: The Finite-Difference Time-*

Domain Method, 3rd edition, Boston: Artech House, 2005.

[7] K. Tanabe, A. Asakawa, T. Noda, M. Sakae, M. Wada, and H. Sugimoto, "Varifying the novel method for analyzing transient grounding resistance based on the FD-TD method through comparison with experimental results," *CRIEPI Report,* no. 99043, 2000. (in Japenese)

[8] W. Scott-Meyer, *EMTP Rule Book*, B.P.A, 1977.

[9] G. Waldschmidt and A. Taflove, "The determination of the effective radius of a filamentary source in the FDTD mesh," *IEEE Microwave and Guided Wave Letters*, vol. 10, pp. 217 - 219, June 2000.

[10] T. Noda and S. Yokoyama, "Thin wire representation in finite difference time domain surge simulation," *IEEE Trans. Power Delivery*, PWRD, vol. 17, no. 3, pp. 840 - 847, 2002.

[11] G. Mur, "Absorbing boundary conditions for the finite-difference approximation of the time-domain electromagnetic-field equation," *IEEE Trans. Electromagnetic Compatibility,* EMC, vol. 23, no. 4, pp. 377 - 382, 1981.

[12] M. O. Goni, P. T. Cheng, and H. Takahashi, "Theoretical and experimental investigations of the surge response of a vertical conductor," *Proc. IEEE Power Engineering Society Int'n Conf.*, vol. 2, pp. 699 -704, 2002.

[13] M. O. Goni and H. Takahashi, "Theoretical and experimental investigations of the surge response of a vertical conductor," *ACES Journal,* vol. 18, no. 1, Mar. 2003.

[14] M. O. Goni and H. Takahashi, "Thin wire representation of the vertical conductor in surge simulation," *ACES Journal*, vol. 19, no. 1a, Mar. 2004.

[15] M. O. Goni, M. F. Hossain, M. M. Rahman, M. S. U. Yusuf, E. Kaneko, and H. Takahashi, " Simulation and experimental analyses of electromagnetic transient behaviours of lightning surge on vertical conductors," *IEEE Trans. on Power Delivery*, PWRD, vol. 21, no. 4, Oct. 2006.

[16] K. R. Umashankar, A. Taflov, and B. Beker, "Calculation and experimental validation of induced currents on coupled wires in an arbitrary shaped cavity," *IEEE Trans. Antennas and Propagation*, vol. 17, no. 11, pp. 1248 - 1257, 1987.

[17] Y. Baba, M. Nayel, N. Nagaoka, A. Ametani, and S. Sekioka, "Numerical analysis of wave propagation characteristics on a buried horizontal conductor by FDTD method," *Journal of IEE*, vol. 123, no. 11, pp. 1319 - 1327, 2003.

[18] E. D. Sunde, *Earth Conduction Effects in Transmission Systems*, Dover, New York 1968.

Md. Osman Goni was born in Bangladesh on February, 1971. He received his B.S. degree in electrical and electronic engineering from Bangladesh Institute of Technology, Khulna in 1993. He joined the Institute in 1994. He received M.S. degree and D. Eng. degree from the University of the Ryukyus, Japan in 2001 and 2004 respectively. He is currently an assistant professor and has been engaged in teaching and research in digital signal and image processing, electric power and energy system, electromagnetic energy engineering, electromagnetic theory, electromagnetic fields computation, transient phenomena, lightning and EMP effects on power and telecommunication networks, FDTD method, MoM, NEC-2, lightning surge analysis, vertical conductor problems, EMTP etc. He is the author or co-author of about 20 scientific papers presented at international conferences and published in reviewed journals.

Dr. Goni is the Director of the Lightning Research Group of Khulna University of Engineering and Technology, Bangladesh. He is a member of IEEE, ACES, IEE of Japan, IEB and AGU.

Eiji Kaneko was born in Japan, on September 16, 1952. He received M.S. degree from Nagoya University in 1977. He joined in Toshiba Corporation in April 1977 and engaged in research and development of vacuum interrupter and discharge. He received D. Eng. degree from Nagoya University in 1989. He is now professor of University of the Ryukyus. He has been engaged in teaching and research on electric power and energy system engineering, electromagnetic energy engineering etc. Dr. Kaneko is a member of IEEE and IEE of Japan.

Akihiro Ametani received the B.S. and M.S. degrees from Doshisha University, Kyoto, Japan, in 1966 and 1968, respectively, and the Ph.D. degree from the University of Manchester Institute of Technology (UMIST), Manchester, U.K., in 1973. He was with Doshisha University from 1968 to 1971, UMIST from 1971 to 1974, and the Bonneville Power Administration, Portland, OR, for the summers of 1976 to 1981. He has been a Professor at Doshisha University since 1985. He was the Director of the Institute of Science and Engineering of Doshisha University from 1997 to 1998 and the Dean of the Library and Computer/Information Center from 1998 to 2001. Dr. Ametani is a Chartered Engineer in the U.K., a Distinguished Member of CIGRE, and a Fellow of the IEE. He has been a Vice President of the IEE of Japan since 2004.

Accelerated GRECO Based on a GPU

[1] Yang ZhengLong, [1] Jin Lin, and [2] Li WeiQing

[1] Nanjing Research Institute of Electronics Technology, China
[2] Computer Science and Tech. Institute, Nanjing University of Science. and Technology, China

Abstract – For obtaining the electromagnetic scattering characteristic of a complex target efficiently, GRECO (Graphical Electromagnetic COmputing) is implemented by a programmable pipeline of a modern GPU (Graphics Processing Unit). The speed of the simulation can be improved up to 20 times compared with the raw GRECO. The ray tracing algorithm based on a GPU is implemented to obtain the multiple reflection contribution of a target with concave structure. This approach will redound to research works such as radar target identification and Inverse Synthetic Aperture Radar (ISAR) imaging.

Key words – EM scattering, GRECO, and GPU.

I. INTRODUCTION

GRECO (GRaphics Electromagnetic COmputing) is an effective method for computing the high-frequency radar cross section (RCS) of complex targets based on physical optics (PO), and physical theory of diffraction (PTD) [1]. In this paper, an accelerated version of the GRECO method is implemented by the programmable pipeline of a modern GPU (Graphics Processing Unit), the speed of the simulation can be improved up to 20 times compared with the base GRECO. Furthermore, the ray tracing algorithm based on the GPU is implemented to obtain the contribution of multiple reflection of a target.

Compared with the raw GRECO, the GPU accelerated GRECO has higher efficiency and enhanced ability to simulate the multiple reflection of a complex target with concave structure.

With the development of GPU and the creation of the new feature of programmability, researchers begin to transfer some of the processing stages in the graphics output pipeline or some graphics algorithms from the CPU (Central Processing Unit) to the GPU. Except for those graphics-only applications, GPU finds applications in general purpose computations in other fields, and it has become a hot topic for research in recent years. In the electromagnetics filed, the FDTD method has been implemented based on the GPU for higher efficiency [2].

In some applications such as computational electromagnetics and signal processing, the speed of the CPU can not meet the requirement of efficiency. One can use other high-speed processing unit like DSP (Digital Signal Processing) or HPC (High Performance Cluster) system, but DSP or HPC system is very expensive and limited in application. By contrast with a general CPU, a GPU consists of higher-bandwidth memory and more floating-point hardware units. For example, current GPU such as the Nvidia 6800 Ultra has a peak performance of 40 Gflops and a memory bandwidth of 35.2 Gbytes per second, compared to 6.8 Gflops and 6 Gbytes per second for a 3-GHz Pentium 4 CPU. Furthermore, GPU performance for graphics applications throughput has been increased from 2 to 2.5 times a year. This growth rate is faster than Moores law as it applies to CPUs, which corresponds to about 1.5 times a year. In a GPU, there are several vertex pipelines using MIMD (Multiple Instructions Multiple Data), and fragment pipelines using SIMD (Single Instruction Multiple Data) to provide the ability for high-speed parallel data processing. So the GPU can be treated as a parallel vector machine that is suitable for some kinds of numerical computations [3], [4].

The function of the fixed pipeline of graphics hardware used in raw GRECO is to obtain the shadow of different parts of a complex target in the rendering process. Based on the raw GRECO, the programmable pipeline of a GPU can be applied to implement GRECO method without a rendering process. The customized vertex and fragment shaders for RCS computing can be compiled and linked into the GPU pipeline to substitute some functions of the fixed-pipeline [5]. Since most of the time-consuming computation in raw GRECO is used to obtain the scattering contribution of the small facets represented by the pixels on the screen, thus it can be implemented by the parallel fragment shader to accelerate the simulation. In this paper, the vertex and fragment shaders are applied to the raw GRECO method based on prior work to obtain the mono and bistatic RCS of complex targets [6]. The GPU-based ray tracing algorithm is implemented to obtain the contribution of multiple reflection of a target with concave structure. The paper is focused on the combination of GRECO and GPU programming, the GRECO and related techniques will not be discussed here, its details can be found in [1] and [7].

Compared with the raw GRECO, the main advantages of GPU-based GRECO are:

1) Higher efficiency, where the speed can be improved

up to 20 times compared with the raw GRECO.
2) Ability to simulate multiple reflection of the complex targets (see section II.***C***), this feature is not involved in raw GRECO.

The development of GPU-based GRECO is part of the work for the target echo simulation for radar target identification and Inverse Synthetic Aperture Radar (ISAR) imaging. High speed simulation is required for obtaining the wide-band and wide-angle scattering response of many complex targets, it is the main motivation of the work.

II. METHODOLOGY

In GRECO, the procedures of RCS prediction are:
1) Read the 3D model files created by CAD software.
2) Render the 3D model in the frame-buffer of a graphics card.
3) Obtain the depth information of each pixel.
4) Obtain the surface normal of each pixel using two different lighting configurations.
5) Map the depth information to the real depth of the target.
6) Obtain the scattering contribution of each pixel using PO/PTD.
7) Obtain the total scattering contribution by accumulating the contribution of each pixel coherently.

In the procedures mentioned above, normal vector computation, depth mapping, scattering simulation of each pixel, and final accumulating are done in the CPU. There are three massive data exchanges between main memory and video memory: two for color information of two different lighting configurations and one for depth information. In the CPU, massive floating point operations are needed for computing the normal vector and scattering contribution of each pixel on the target surface based on serial processing mechanism, that is, many loop operations are needed in the raw GRECO. Using the programmable pipeline of the GPU, the normal vector and depth can be accessed directly by using built-in variables of shading languages such as Cg (C for Graphics, released by Nvidia) and GLSL (Graphics Library Shading Language) [8], so the two different lighting configurations and depth mapping are needless. Thus scattering contribution of each pixel can be obtained rapidly based on parallel processing mechanism of fragment shader, and the final total scattering contribution can be obtained by a parallel reduction process in the GPU [9]. The detailed procedures are explained as follows.

A. PO Simulation by Shader

Figure 1 represents the procedures of the GPU's fixed-pipeline (solid line) and the programmable pipeline (dashed line). Some functions of the fixed-pipeline can be replaced by the programmable pipeline using vertex shaders and fragment shaders. Vertex shaders can be used to specify a general sequence of operations to be applied to each vertex and its associated data, and the fragment shaders can be used to specify the operations on fragment values and its associated data.

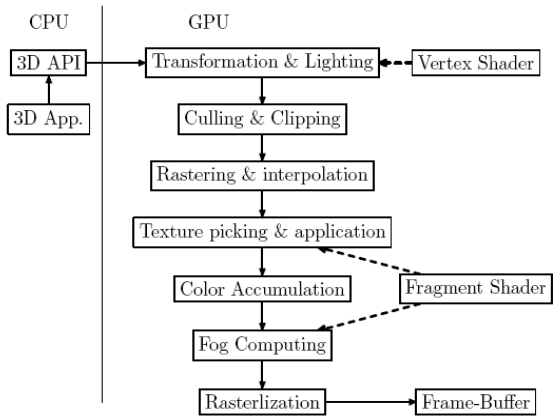

Fig.1. GPU pipeline.

In GRECO, the main time for the RCS prediction is spent on the electromagnetic computation, while the geometric model manipulations are left to the graphics hardware. Raster element is applied to discrete the target surface natively, and automatic culling technique is used to remove the shadowed parts of the target. With the rapid development of graphics hardware especially the programmable pipeline of the GPU, GRECO can be implemented entirely in the GPU. The key procedures of GPU accelerated GRECO are:
1) Write the user-defined vertex shaders and fragment shaders for RCS computation based on PO/PTD.
2) Compile and link the shaders, and then embed the shaders to the GPU pipeline.
3) Start up the general drawing process and store the scattering results of each pixel in the frame buffer.
4) Obtain total scattering contribution by the reduction technique that will be described in section II.***D***.

For GPU accelerated GRECO, the 3D geometrical transformation, including normal transformation can be implemented in a vertex shader. The scattering results of each pixel can be obtained directly in a fragment shader by equation (5) in [1], then it can be written into the R component and G component of RGB (Red, Green, Blue) by render-to-texture technique, where R and G components represent the real part and imagery part, respectively. Finally, the reduction technique can be applied to obtain the total scattering contribution.

B. Diffraction of Edge

In [1], the Element Edge Wave (EEW) is applied

to obtain the edge diffraction contribution. The geometrical parameters such as the normal vectors of two facets that construct the edge, edge inner angle and the direction of the edge should be obtained correctly. The method used in [1] can obtain the edge information on the condition that two facets are all illuminable. It will fail when one of the facets that construct the edge is shadowed.

In [10] and [11], the complete edge information is obtained from the model information stored in the 3D model file based on some principles of computer graphics. It is found that the edge diffraction can be obtained by the GPU programming. The primary issue is how to obtain the edge information with the shadow between model and edges must be considered, and the second issue is how to pass the edge information to the fragment shader for diffraction computation using PTD or ILDC (Incremental Length Diffraction Coefficient) [7].

The 3D facet model is constructed by a number of triangles with a certain topological relationship. For a regular 3D model, the common edge exists in the adjacent facets. If the angle between two normal vectors of two facets is larger than the predefined threshold, the common edge needs to be considered for diffraction; otherwise, the two facets are treated as locating on the smooth surface. This is similar to normal averaging in computer graphics [8].

Through the preprocessing of the model information, edge information such as normal vectors, edge direction, and inner angle of each edge can be obtained for edge diffraction computation later. These parameters are dependent, the edge direction and inner angle can be obtained by the cross product and dot product of two normal vectors respectively. The normal vector of one illuminable facet, edge direction and inner angle are sufficient for edge diffraction computation. In paper [11], three display lists [8] are used to store the normal vector, edge direction and inner angle respectively. In order to eliminate the shadowed edge, the "dark" model (r,g,b=0,0,0) can be rendered with lighting disabled before the edges are rendered. In this paper, only one display list is used to store the three parameters for edge diffraction by eliminating the shadowed edges and pass this edge information to the fragment shader.

In OpenGL, the main color and secondary color can be assigned for each vertex of a 3D model and each color has four components named RGBA (Red, Green, Blue, and Alpha). In the rendering procedure of an edge, the RGBA of the main color can be used to store the normal vector $\boldsymbol{n}$ of illuminated facet and the inner angle α, that is, R = $\boldsymbol{n}$.x, G = $\boldsymbol{n}$.y, B = $\boldsymbol{n}$.z, and A = α, while the RGB of the secondary color can store the edge direction. Eliminating the shadowed edges can be implemented by the "dark" model mentioned above.

Figure 2 illustrates the rendering result of a missile model with shadowed edges that are eliminated. The smooth part of the model, such as the fuselage and wings, is full dark as the background, while the edges of the wings are rendered with the geometrical parameters passed to the fragment shader by main color and secondary color for diffraction computation. When all information for diffraction computation is available, the EEW method can be implemented in the fragment shader for edge diffraction.

Fig. 2. Rendering result of edges.

C. *Multiple Reflections*

Multiple reflections play an important role in the scattering of complex targets. The Shooting and Bouncing Ray (SBR) technique has been developed for RCS prediction for a target with concave structure [12]. The software Xpatch based on SBR has been released by ASIC Inc. Ray tracing is the core algorithm of SBR. In order to obtain multiple reflection contribution, the ray propagation paths of incident wave and reflected wave need to be recorded to obtain the amplitude and phase of each ray that bounced between different parts of the target surface. All contributions from scattering and iterative multiple reflection should be accumulated in the direction in which the receiver is located.

Conventional ray tracing algorithm computes light intensity and color components of the scene. The coherence of light is not considered in conventional ray tracing because the phase of the light is not important for rendering scene in computer graphics. However, it is as important as the amplitude in the EM scattering of complex targets. Thus the modifications should be applied to conventional ray tracing algorithm for obtaining the multiple reflections' contribution. The differences between conventional ray tracing and SBR in EM scattering are:

1) Conventional ray tracing calculates the amplitude of light. As for the EM scattering, both the amplitude and phase are to be calculated.

2) The light amplitude in a conventional ray tracing is obtained by the Phong lighting model, while the amplitude and phase of the EM scattering are obtained by physical optics, geometrical optics, and PTD.

3) Refraction must be considered in conventional ray tracing while there is no refraction contribution from metal target surface for EM scattering computation.

To obtain the multiple reflections' contribution, the propagation paths bounced between different parts of the complex target should be recorded including the sequences of the intersections between the radar beam and the facets of the target. It is very time-consuming because massive intersection tests are needed to be computed.

In order to accelerate the ray tracing by GPU, Purcell mapped the vertices of the complex model to three textures and constructed a texture representing the linked list which stores the triangles of the model surface [13]. Thus, the ray tracing algorithm can be implemented by the GPU. The GPU accelerated ray tracing for EM scattering is implemented in the fragment shader based on Purcell's work in this paper. The algorithm flow chart is shown in Fig. 3.

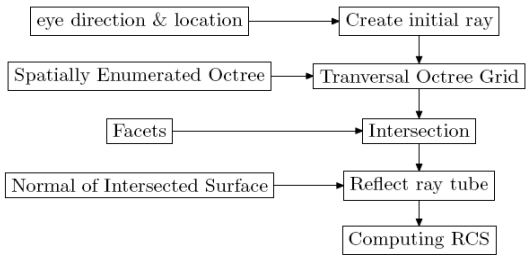

Fig. 3. Ray tracing for multiple reflection.

The algorithm can be divided into five parts and implemented by fragment shader, except the ray tube initialization is preprocessed in the CPU. The method provided by Didier Badouel is applied to obtain fast ray-polygon intersection [14] and the Proximity Clouds algorithm is applied to scene traversal [15]. The performance of the 3D traversal is important to the efficiency of the algorithm. BSP (Binary Space Partition) tree, Adaptive octree, KD tree, and SEADS (Spatially Enumerated Auxiliary Data Structure) [16] etc., can be adopted to store the 3D scene data for acceleration of traversal [17]. In this paper, the SEADS method is applied to fast traversal due to the following reasons:

1) It is simple for parallel processing.
2) The time for each data access is constant and with linear time complexity.
3) Easy code for hardware implementation.

The ray tracing algorithm is very complicated; it is a hot topic in computer graphics, the detailed procedures of the ray tracing accelerated by the GPU is not described here. It should be noted that if the depth of tracing is reduced to 1, the algorithm degenerates to GRECO.

D. Reduction

When shaders for PO/PTD and multiple reflections are applied to scattering computing, the contribution of each pixel is stored in RG components of the current texture and has to be accumulated to obtain the total scattering contribution. Traditionally, the RGB components can be read back to the main memory and then accumulated by CPU. It is time-consuming because of long time loop operations for accumulation and massive data exchanges between video memory and main memory, for example, if the viewport is 1024 by 1024, this means that there is 1024×1024 = 1048576 accumulation operations that are needed to obtain the final total contribution. Additionally, it is slow to read the RGB components from video memory to main memory. If the accumulation can be implemented in GPU without the massive data exchanges and loop operations, higher execution efficiency will be obtained.

After investigating the parallel mechanism of the fragment shader, it is found that the parallel reduction technique is suitable for acceleration of accumulation [9] in GPU. After several reduction processes, only one complex number that represents the total contribution is needed to be read back to the main memory resulting in no massive data exchange.

In computer graphics, reduction technique is mainly applied to obtain the maximum value or accumulation of the floating point numbers stored in texture. Here, texture can be treated as a 2D array that stores the scattering contribution of each pixel. The maximum value in a 2D array can be obtained by the procedure shown in Fig. 4.

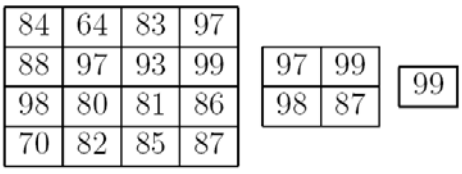

Fig. 4. Reduction for obtaining the maximum.

For obtaining the maximum of the 4 by 4 array, the maximums of 4 subregions with the elements {84, 64, 88, 97}, {83, 97, 93, 99}, {98, 80, 70, 82}, and {81, 86, 85, 87} should be first obtained, and then a new array can be created with the elements {97, 99, 98, 87} that are the maximums of 4 subregions.

The same procedure can be applied to the new array for obtaining the final maximum of the array, that is, 99. For obtaining the accumulation result of the array, similar procedure can be applied.

In the implementation of reduction by the GPU, the accumulation can be applied to a 2 by 2 subregion of the texture, then a new texture can be constructed

with 1/4 the size of the current texture. Iteratively, the final accumulated result can be obtained. This operation limits the size of the texture to the integer number that is power of 2 but it is suitable for parallel processing in fragment shader. In this paper, the size of the texture is set to 2^{10} = 1024, only 10 reduction operations are needed to obtain the total contribution without massive data exchanges from video memory to main memory and large amount of loop operations (up to 1048576).

Jinwook Kim provided a reduction example on the web and helped us to implement the reduction easily [18]. The reduction procedure for computing the RCS of a missile model is illustrated as shown in Fig. 5.

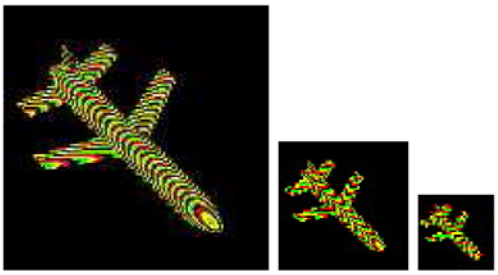

Fig. 5. Reduction for RCS accumulation.

The R and G components of the images in Fig. 5 represent the real and imaginary parts of the scattering contribution of each pixel, respectively. The size of the first image is 1024×1024. After one reduction operation, the size of the image is reduced to 512×512 and the accumulation results of each 2 by 2 subregion are obtained. The final accumulation result is obtained after 10 iterative reduction operations and stored in a 1×1 array.

III. EXAMPLES

In order to compare the simulation speed, the RCS of a scaled missile model (1:8) is simulated by raw GRECO and the GPU accelerated GRECO. The view port for computing is 1024 by 1024, f = 10GHz, aspect angle is from 0◦ to 360◦ with an angle step of 0.25◦, that is, 1441 RCS results are calculated. The CPU in our platform is an Intel Pentium 4 with clock frequency 2.8 GHz and the GPU is provided by Nvidia GeForce 6600 GT graphics card. The time for raw GRECO is 390 s and that for GPU accelerated GRECO is only 19 s. The speed of the simulation is improved up to 20 times. The RCS of the model is also measured by CATR (Compact Antenna Test Range) system and the results that are smoothed by 10-point adjacent average are shown in Fig. 6.

For illustration of multiple reflection contributions, the RCS of a dihedral constructed with two 1m × 1m metal planes is simulated with the depth of tracing set to 2. The result shown in Fig. 7 agrees well with that shown in [7]. The time for computing the RCS in the aspect angle range [-60◦, 60◦] with step 1◦ is about 100s.

Furthermore, the wide-band, wide-angle scattering data of complex targets are simulated by the GPU accelerated GRECO to obtain the high resolution range profile and ISAR image. Figure 8 is the turntable ISAR image of a Boeing 737 model obtained by the simulated data at X-band with bandwidth 300 MHz.

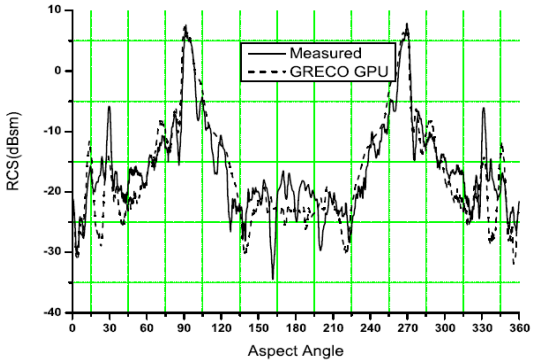

Fig. 6. Measured and simulated RCS of the missile model.

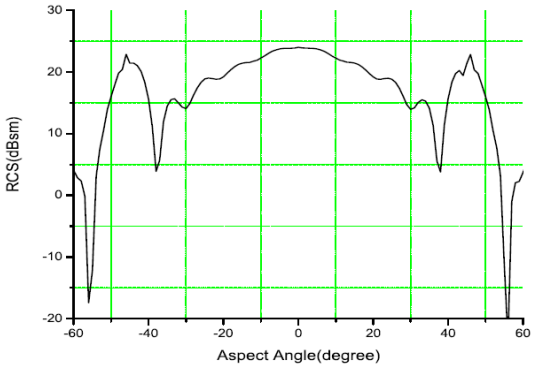

Fig. 7. Simulated RCS of dihedral.

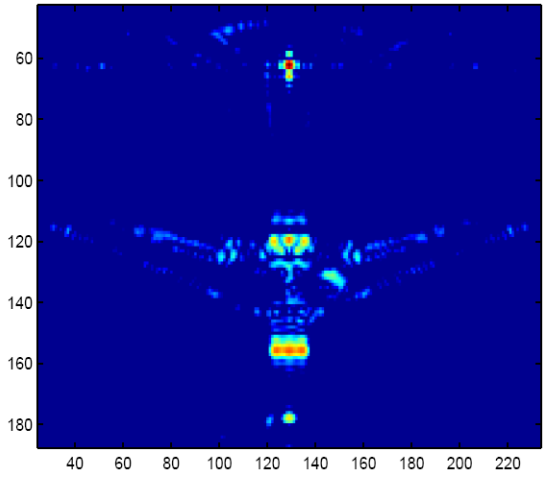

Fig. 8. Turntable ISAR image of a Boeing 737 model.

IV. CONCLUSION

The programmable pipeline of a modern GPU is applied successfully to the implementation of a GPU accelerated GRECO method with multiple reflection contribution included. The speed of simulation is improved up to 20 times compared with the raw GRECO. The GPU accelerated GRECO method has been used to simulate radar echo for different radar systems and the wide-band wide-angle scattering data of different targets for constructing the database for the radar target identification. Further improvement on simulation speed can be obtained by a more powerful GPU and better algorithms with the rapid development of computer graphics.

REFERENCES

[1] J. M. Rius, M. Ferrando, and L. Jofre, "High - frequency RCS of complex radar targets in real-time," *IEEE Trans. on Antennas and Propagat*., vol. 41, no.9, pp. 1308–1318, Sep. 1993.

[2] M. M. Okoniewski, S. E. Krakiwsky, L. E. Turner, "Graphics processor unit (GPU) acceleration of finite-difference time-domain (FDTD) algorithm," *ISCAS 2004, IEEE*, pp. 265–268, 2004.

[3] D. Goddeke, *GPGPU–basic math tutorial*, Technical report, FB Mathematik, Universitat Dortmund, http://www.mathematik/ unidortmund. de/~goeddeke/gpgpu, Nov. 2005.

[4] W. Enhua, "State of the art and future challenge on general purpose computation by graphics processing unit," *Journal of Software*(In Chinese), vol. 15, no. 10, pp. 1493–1504, Oct. 2004.

[5] R. J. Rost, *OpenGL Shading Language*, Addison Wesley, 2004.

[6] Y. ZhengLong, J. Lin, N. JingLing, and F. Dagang, "Bistatic RCS calculation of complex target by Greco," *Journal of Electronics* (In Chinese), vol. 32, no. 6, pp. 1033–1035, June 2004.

[7] E. F. Knott, J. F. Shaeffer, and M. T. Tuley, *Radar Cross Section*, Artech House, 1985.

[8] R. S. Wright and Jr. B. Lipchak, *OpenGL Super Bible*, Third Edtion. Sams Publishing, 2005.

[9] R. Fernando, *GPU GEMS, Programming Techniques, Tips, and Tricks for Real-Time Graphics*, Pearson Education, Inc., 2005.

[10] Y. ZhengLong, F. DaGang, and L. TieJun, "Modification of software for computing EM scattering of complex targets," *System Engineering and Electronics* (In Chinese), vol. 24, no. 4, pp. 86–89, April 2002.

[11] Q. DeHua, W. BaoFa, and L. TieJun, "Improvements of edges detecting and diffraction field computing in GRECO," *Journal of Electronics* (In Chinese), vol. 31, no. 8, pp. 1160–1163, Aug. 2003.

[12] H. Ling and R. Bhalla, "Three-dimensional scattering center extraction using the shooting and bouncing ray technique," *IEEE Trans. on Antennas and Propagat*., vol. 44, no. 11, pp. 1445–1453, Nov. 1996.

[13] T. J. Purcell, I. Buck, W. R. Mark, and P. Hanrahan, "Ray tracing on programmable graphics hardware," *ACM Transactions on Graphics*, vol. 21, no. 3, pp. 703–712, July 2002.

[14] D. Badouel, *An Efficient Ray-Polygon Intersection*, Academic Press Professional, Inc., San Diego, CA, USA, pp. 390–393, 1990.

[15] D. Cohen and Z. Sheffer, "Proximity clouds-an acceleration technique for 3D grid traversal," *The Visual Computer*, vol. 11, no. 1, pp. 27–38, 1994.

[16] A. Fujimoto, T. Tanaka, and K. Iwata, "Arts: Accelerated ray-tracing systems," *IEEE Comput. Graph*., vol. 6, no. 4, pp. 16–26, 1986.

[17] D. F. Rogers, *Prodedural Elements for Computer Graphics*, 2nd Edition. McGraw-Hill Press, 1998.

[18] J. Kim, *GPGPU reduction example*, http://web. imrc. kist.re.kr/~jwkim/GLSL/reduction.zip, 2005.

Yang ZhengLong was born in Gansu province, China. He received Ph.D. in electromagnetics and microwave technology at Nanjing University of Science and Technology (NUST) in 2002, then joined Nanjing Research Institute of Electronics Technology. His main research interests are computational electromagnetics and radar imaging.

Jin Lin was born in Jiangxi province, China. He received the master degree and Ph.D. in electronic engineering at Beijing University of Aeronautics and Astronautics (BUAA) in 1989 and 2003, respectively. He is the supervisor of R&D Center of Nanjing Research Institute of Electronics Technology and the member of IEEE and senior member of CIE (Chinese Institute of Electronics). His main research interests are radar system and microwave antenna.

Li WeiQing was born in Hebei province, China. He received Ph.D. in Computer Sci. and Tech. Inst. at NUST. His main research interests are computer graphics, virtual reality and system simulation etc.

An Efficient Preconditioner (LESP) for Hybrid Matrices Arising in RF MEMS Switch Analysis

[1] Zhongde Wang, [2] John L. Volakis, [3] Katsuo Kurabayashi, and [3] Kazuhiro Saitou

[1] Anosft Corp., San Jose, California
[2] ElectroScience Lab, Electrical and Computer Engineering Dept., The Ohio State University
[3] Mechanical Engineering Dept., University of Michigan.

Abstract – The small dimensions of Radio Frequency Micro-ElectroMechanical Switches (RF MEMS) raise significant modeling challenges in terms of accuracy and solver efficiency. This paper introduces a practical RF MEMS switch analysis based on an extended finite element-boundary integral (EFE-BI) method with an iterative solver incorporating a new sparse-matrix preconditioner whose large eigenvalues are very close to those of the original matrix. This sparse preconditioner is key to successfully solving the ill-conditioned EFE-BI matrix. The smaller condition number and almost positive-definite eigenvalue spectrum after preconditioning leads to fast convergence. Specific RF MEMS simulations are presented to demonstrate the accuracy and effectiveness of the methodology and solution process.

I. INTRODUCTION

RF MEMS switches have demonstrated low on-state insertion loss, high off-state isolation, and very linear behavior over a broad frequency range [1] and [2]. Despite their excellent characteristics, they generally suffer from low power-handling capability, with most switches operating well below 1W [2]. This limitation is due to the complex interactions among electromagnetic losses, heat transfer, and mechanical deformations of the switch. To better understand the associated failures, a multiphysics model was proposed in [3]. However, the work in [3] employed an approximate two-dimensional modeling of the RF current though the switch. As such it was not sufficiently rigorous in characterizing the edge current behavior which is critical for the heat dissipation process. Toward the goal of developing a more accurate and reliable analysis of RF MEMS, we proposed in [4] and [5] a more robust and efficient analysis method referred to as the extended finite element-boundary integral (EFE-BI) method.

Of importance in our EFE-BI analysis was the treatment of very small features associated with the MEMS switches. For example, at 2 GHz, the beam length corresponds to an electrical size of $\lambda/1500$ to $\lambda/250$ and a gap of $\lambda/150{,}000$ to $\lambda/50{,}000$. Because of these small features, the resulting hybrid matrix system is highly ill-conditioned and the matrix entries (viz. the integrals defining the matrix entries) are difficult to be accurately evaluated. Standard implementations of the finite element (FEM) and moment methods (MoM) employ integrations based on the Gaussian quadrature formulae for evaluating the matrix entries. However, for the small RF MEMS dimensions, these standard integral treatments were found to lead to ill-conditioned matrices with erratic changes in the output of the observable quantities. In [6] we proposed a set of semi-analytic evaluations of the matrix entries for the resulting EFE-BI hybrid system. However, a good preconditioner is still needed to ensure convergence, especially for frequencies below *X* band (10 GHz).

Many authors have explored preconditioning matrices for ill-conditioned matrix systems [7], [8], and [9]. Although the standard diagonal (DP) and block-diagonal preconditioners (BDP) can partially overcome convergence issues, they are still not reliable for RF MEMS modeling. In this paper, we present a highly efficient and reliable analysis of RF MEMS systems based on a new preconditioner referred to as the Large-Eigenvalue-Sparse Preconditioner (LESP). This preconditioner is implemented within the Generalized Minimal Residual iterative solver (GMRES) and is shown to significantly reduce the condition number and lead to almost positive-definite preconditioned matrix for RF MEMS switches. The reader is referred to [4], [6] and [10] for details related to the formulation of the EFE-BI and the element evaluations. Here, we focus only on the preconditioning approach and the relevant results. The reader is also referred to [9] and [11] for a review of iterative solvers and pre-conditioners. Other preconditioners for RF applications are mentioned in [7] and [12]. However, our particular application relates to the unique issue of RF MEMS switches where the entire geometry is $\lambda/250$ or less in size.

II. PRECONDITIONING OF THE HYBRID MATRIX SYSTEM

A simplified RF MEMS switch is illustrated in Fig.1. As it is well known, the RF MEMS switch beam experiences shape deformation during its dynamic operation. The conventional FE-BI [13] with rectangular gridding cannot track this deformation with sufficient

geometrical accuracy. For this purpose in [4], we introduced an extended FE-BI analysis method (EFE-BI) for RF MEMS switches. The EFE-BI employs the moment method to model the beam and the usual FE-BI for the substrate and conducting sections on the boundary of the same substrate. As a result, the beam mesh is separated from the FE-BI section of the model. It can therefore be readily re-meshed as the beam curves. This approach allows for full flexibility in modeling the deformed 3D surfaces while reducing the computational expense. The typical EFE-BI matrix takes the form [4] and [6]

$$\begin{bmatrix} \mathbf{A}^{FEM} + \mathbf{A}^{S_1S_1} & \mathbf{A}^{S_1S_2} \\ \mathbf{A}^{S_2S_1} & \mathbf{A}^{S_2S_2} \end{bmatrix} \begin{Bmatrix} \mathbf{E}_n^V \\ \mathbf{J}_n^{S_2} \end{Bmatrix} = \begin{Bmatrix} \mathbf{b}_m^V \\ \mathbf{0} \end{Bmatrix} \quad (1)$$

where $\mathbf{A}^{FEM}$ and $\mathbf{A}^{S_1S_1}$ represent the FE-BI system for the fixed volume V_1 enclosed by S_1 as shown in Fig. 1. As usual, $\mathbf{A}^{FEM}$ is a very sparse submatrix whereas $\mathbf{A}^{S_1S_1}$ is dense. Similarly, $\mathbf{A}^{S_1S_2}$ and $\mathbf{A}^{S_2S_1}$ are the dense matrices representing the interaction between the beam and the BI enclosing the substrate, whereas $\mathbf{A}^{S_2S_2}$ is a dense submatrix representing the discrete method of moments system. The small sizes discussed above lead to near-zone integrals in the various submatrices of equation (1). These integrals can be efficiently evaluated using the semi-analytic integrations [6]. However, the resulting matrices are still ill-conditioned (Fig. 2).

Given the small number of unknowns due to the electrically small size of RF MEMS switch, GMRES (without restart) [8] and [11] is a good choice for solving equation (1). A description of the GMRES algorithm is given in [11] and [14]. We also note that available commercial software typically converges rather slowly or never at frequencies below ~50 GHz due to the extremely small MEMS dimension. This highlights the need for a preconditioner, but also points to the need for improved methods to carry out a reliable analysis of RF MEMS switches. The next paragraphs describe the construction of the proposed LESP. We then proceed to demonstrate the solution effectiveness of the entire EFE-BI approach for RF MEMS analysis.

It is well known that a good preconditioner is sparse and should have eigenvalues close to the larger ones of the original matrix. This approach generates a preconditioner that is a highly sparse matrix, but incorporates the critical elements of the original matrix. A preconditioner A_{LESP} can be applied to equation (1) as

$$\mathbf{A}_{LESP}^{-1} \begin{bmatrix} \mathbf{A}^{FEM} + \mathbf{A}^{S_1S_1} & \mathbf{A}^{S_1S_2} \\ \mathbf{A}^{S_2S_1} & \mathbf{A}^{S_2S_2} \end{bmatrix} \begin{Bmatrix} \mathbf{E}_n^V \\ \mathbf{J}_n^{S_2} \end{Bmatrix} = \mathbf{A}_{LESP}^{-1} \begin{Bmatrix} \mathbf{b}_m^V \\ \mathbf{0} \end{Bmatrix} \quad (2)$$

with

$$\mathbf{A}_{LESP} = \begin{bmatrix} \mathbf{A}^{FEM} + \left(\mathbf{A}^{S_1S_1}\right)_{NZ1} & \left(\mathbf{A}^{S_1S_2}\right)_{NZ12} \\ \left(\mathbf{A}^{S_2S_1}\right)_{NZ21} & \left(\mathbf{A}^{S_2S_2}\right)_{NZ22} \end{bmatrix}. \quad (3)$$

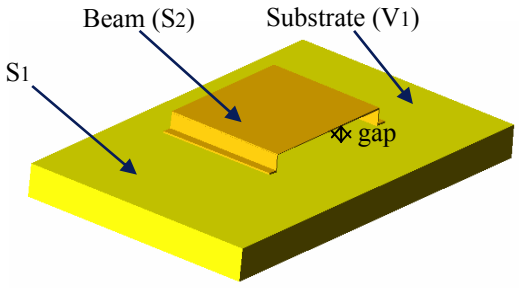

Fig. 1. RF-MEMS simplified model.

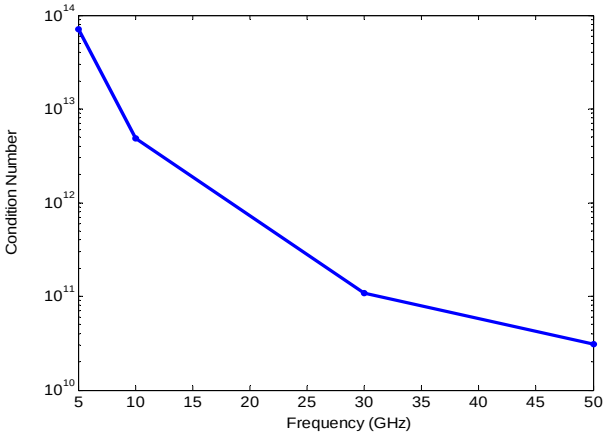

Fig. 2. Matrix condition number versus frequency (75*50*2 um).

In this, $\{\mathbf{A}^{S_1S_1}\}_{NZ1}$ contains an optimal number of the strongest coupling elements in each row of $\{\mathbf{A}^{S_1S_1}\}$. To actually generate $\{\mathbf{A}^{S_1S_1}\}_{NZ1}$, the matrix elements within each row of $\{\mathbf{A}^{S_1S_1}\}$ are sorted with respect to their modulus and the n_{NZ1} elements with the largest modulus are included to form the preconditioning matrix $\{\mathbf{A}^{S_1S_1}\}_{NZ1}$. Typically, most elements of $\{\mathbf{A}^{S_1S_1}\}_{NZ1}$ are located in a band around the main diagonal, but edge numbering can make some of the large elements distributed over the entire extent of the square matrix. A similar procedure is applied to submatrices $\mathbf{A}^{S_1S_2}$, $\mathbf{A}^{S_2S_1}$, and $\mathbf{A}^{S_2S_2}$. Unlike the conventional preconditioners, our approach includes the high modulus elements from the submatrices $\mathbf{A}^{S_1S_2}$ and $\mathbf{A}^{S_2S_1}$. For simplicity, in this paper, the same NZ from each row of the original matrix

is selected to construct the preconditioner matrix, and an optimal NZ is found to achieve the best compromise between convergence versus CPU cost.

III. NUMERICAL APPLICATION

In this section, we present examples that demonstrate the efficiency of the LESP preconditioner. As a solver we used the general minimal residual algorithm (GMRES) with Krylov subspace methods [13] because it converges monotonically and (generally) gives the smallest residual errors among other Krylov subspace methods. The dimensions of the considered example are given in Fig. 3, and we note that the glass substrate was meshed using brick elements to reduce the number of unknowns. However, triangular surface (S2) elements were used to model the MEMS beam to accurately represent of the deformed beam surface. Beam thickness and conductivity were modeled using the resistive sheet model [13].

Figure 4 shows the construction of LESP. Specifically the original EFE-BI matrix is shown at the top of the figure with the corresponding preconditioner given at the bottom. We also remark that the elements in the beam are all in the near zone with respect to each other and are therefore strongly coupled. Thus, we found it necessary to include the entire BI matrix (marked in black in Fig. 4 (b)) to construct the preconditioner. This process was later found to ensure convergence in all cases.

A convergence rate comparison using different preconditioners with GMRES is shown in Fig. 5. We observe that the matrix condition number is very high (3.694×10^{10}) and therefore LESP preconditioner is needed to obtain fast convergence.

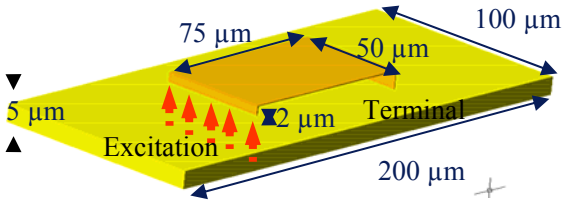

Fig. 3. RF-MEMS switch for our modeling.

From Fig. 5, it is seen that LESP leads to faster convergence as compared to the diagonal/block preconditioner. In addition, LESP has an optimized number of high-coupling terms which generate the best convergence (here NZ = 10 for the 50 GHz case). As can be expected, the value of NZ is dependent on the geometry. The mesh size and expansion function also affect the number of the near zone elements to be included in the preconditioner.

Figure 6 presents the convergence rate versus frequency. As seen, more iteration is needed to obtain the same convergence as the frequency is reduced. At the same time, the optimized NZ rises due to the much higher coupling among the matrix elements. It is also interesting to point out that the convergence rate is much better at the beginning of the iteration process. However, it reaches a relatively stable rate at lower frequencies. At higher frequencies, the convergence rate is slower at the start, but is more consistent and reaches the convergence criteria more quickly.

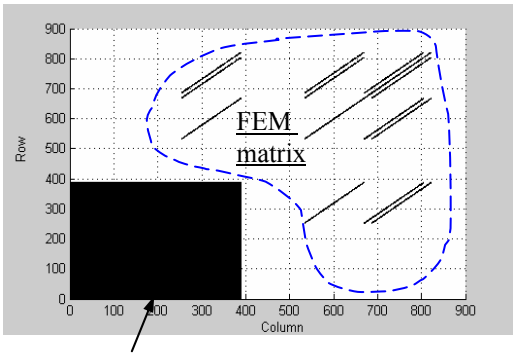

(a) Original EFE-BI matrix.

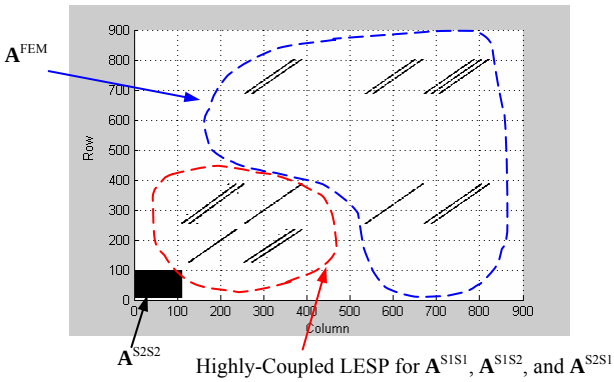

(b) Preconditioner.

Fig. 4. Profile of the EFE-BI and preconditioner matrices.

To better understand the preconditioner's influence on convergence, Fig. 7 shows the eigenvalue spectrum before and after preconditioning. Specifically, we show the spectrum when NZ = 1 (same as the diagonal preconditioner) and 15 (optimal) at 30 GHz. It is seen in Fig. 7 (a) that for NZ=15, most of the eigenvalues are closer to those of the original matrix. Nevertheless, of importance is that after preconditioning (Fig. 7 (b)): (1) the eigenvalue spectrum cluster becomes tighter and the convergence is faster since the condition number is proportional to the ratio of the maximum to minimum

eigenvalues (as compared to the NZ = 1 case); (2) the preconditioned matrix with the optimized LESP leads to an almost all-real and positive eigenvalue spectrum (implying an almost positive-definite system).

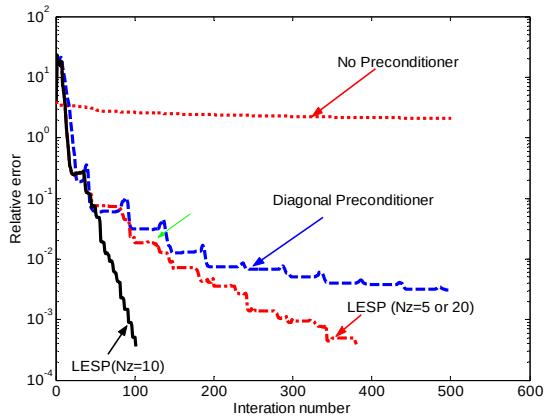

Fig. 5. Convergence versus iteration number for the preconditioned EFE-BI matrix.

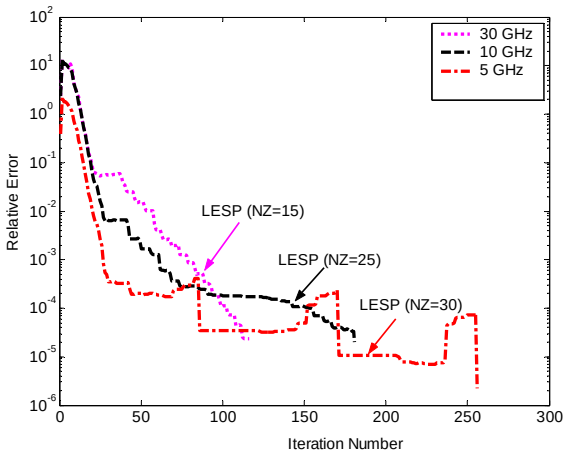

Fig. 6. Convergence versus frequency using an optimal number of non-zero rows (NZ is given in the parenthesis).

To compare the proposed LESP with the diagonal and block preconditioner, we repeated the example at 50 GHz (1241 unknowns) on an Intel Pentium-IV® [2-9]. It was found that at each iteration, LESP (NZ = 10) took 1.92 sec, whereas the diagonal preconditioner took about the same time of 1.914 sec. However, LESP (NZ = 10) was 4.2 times faster in reaching the normalized residual norm (set to 0.005) as compared to the diagonal preconditioner and 3 times faster as compared to the block preconditioner (NZ = 20) due to the fewer iterations. At the same time, the memory requirements were reduced dramatically since the needed storage per iteration rises linearly with the iteration count [15].

Using the preconditioner discussed above, we simulated the model in Fig. 3 at 5 GHz. The current is shown in Fig. 8. As seen, it compares well to the static approximation.

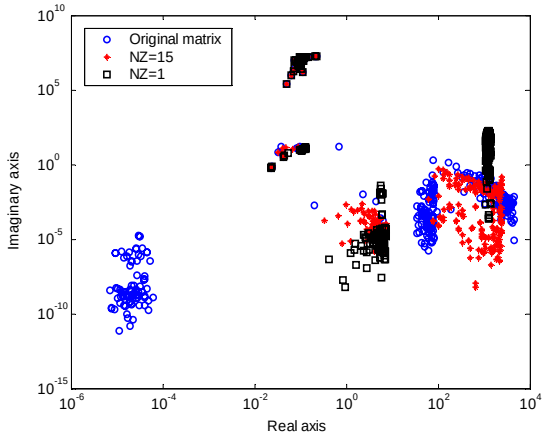

(a) Eigenvalues of the original and the preconditioning matrices with NZ = 1 and NZ = 15.

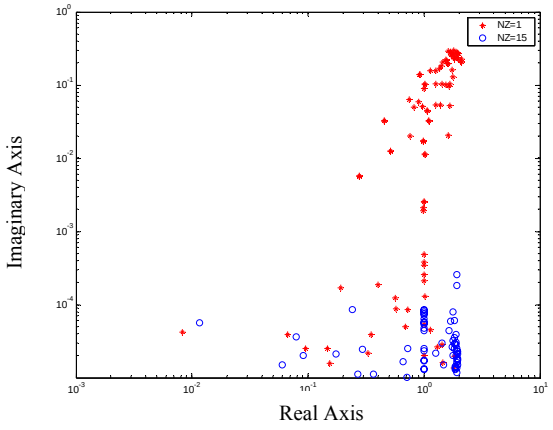

(b) Eigenvalues after preconditioning.

Fig.7. Eigenvalue spectrum distribution.

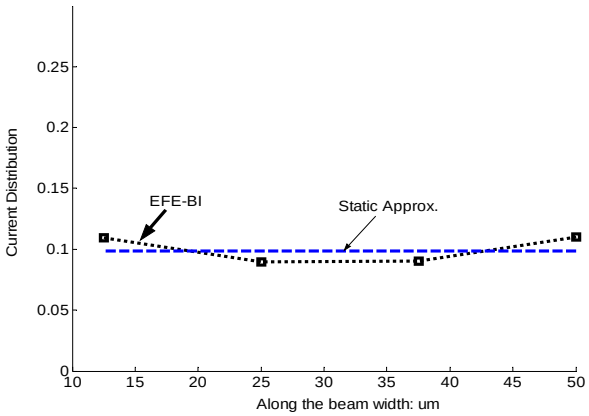

Fig. 8. Current density versus beam width (f = 5 GHz).

IV. CONCLUSION

The extremely small dimensions of RF MEMS switches inevitably lead to highly ill-conditioned matrix systems for RF analysis. Consequently, poor convergence is experienced when the RF MEMS switches are modeled via the conventional FE-BI method. In this paper, we presented a new preconditioner (LESP) to solve the matrix system generated via the extended FE-BI method. This new preconditioner preserves the matrix elements consisting of the largest eigenvalues associated with the original matrix. After preconditioning, the resulting system is almost positive-definite, implying fast and reliable convergence. Using the proposed preconditioner we were able to reliably predict the behavior of RF MEMS switches over a broad range of frequencies (500 MHz – 50 GHz).

ACKNOWLEDGEMENT

This work was supported in part by the National Science Foundation under grant no. ECS-01152222 and ECS-0330963.

REFERENCES

[1] J. J. Yao, "RF-MEMS from device perspective," *J. Micromech. and Microeng.,* vol. 10, pp. R8 - R38, 2000.

[2] G. M. Rebeiz and J. B. Muldavin, "RF MEMS switches and switch circuits," *IEEE Microwave Mag.,* vol. 2, no. 4, pp.59 – 71, Dec. 2001.

[3] B. D. Jensen, K. Saitou, J. L. Volakis, and K. Kurabayashi, "Fully integrated electrothermal multi-domain modeling of RF MEMS switches," *IEEE Microwave and Wireless Components Letters*, vol. 13, no. 9, pp. 364 - 366, 2003.

[4] Z. Wang, B. Jensen, L. Chow, J. Volakis, K. Saitou, and K. Kurabayashi, "Full-wave electromagnetic and thermal modeling for the prediction of heat-dissipation-induced RF MEMS switch failure," *J. Micromech. and Microeng.,* vol. 16, pp. 157 – 164, 2006.

[5] Z. Wang, B. Jensen, J. Volakis, K. Saitou, and K. Kurabayashi, "Analysis of RF-MEMS switches using finite element-boundary integration with moment method," *Proc. IEEE Society International Conference on Antennas and Propagation*, vol. 2, pp. 173 -176, June 22-27, 2003.

[6] Z. Wang, J. Volakis, K. Saitou, and K. Kurabayashi, "Comparison of semi-analytical formulations and Gaussian quadrature rules for quasi-static double surface potential integrals," *IEEE Antenna Prop. Magazine*, vol. 45, no. 6, pp. 96 - 102, 2003.

[7] J. Liu and J.-M. Jin, "A highly effective preconditioner for solving the finite element-boundary integral matrix equation of 3-D scattering," *IEEE Trans. on Antenna and Propagation*, vol. 50, no.9, pp.1212 - 1221, 2002.

[8] T. F. Eibert, "Iterative near-zone preconditioning of iterative method of moments electric field integral equation solutions," *IEEE Antennas and Wireless Propagation Letters*, vol.2, pp.101 - 102, 2003.

[9] J. L. Volakis, "Iterative algorithms for sparse systems," *IEEE Antenna Prop. Magazine*, vol. 37, no. 6, pp. 94 – 96, Dec. 1995.

[10] T. Eibert and V. Hansen, "Calculation of unbounded field problems in free space by a {3D} {FEM/BEM}-hybrid approach," *J. Electromagnetic Waves and Applications*, vol. 10, no.1, pp.61 - 78, 1996.

[11] Y. Saad, *Iterative Methods for Sparse Linear Systems*. Boston, MA: PWS, 1996.

[12] D.-K. Sun, J.-F. Lee, and Z. Cendes, "Construction of nearly orthogonal Nedelec bases for rapid convergence with multilevel preconditioned solvers," *SIAM J. Sci. Comput.*, vol. 23, no. 4, pp.1053 - 1076, 2001.

[13] J. L. Volakis, A. Chatterjee, and L. C. Kempel, *Finite Element Method of Electromagnetics*, New York, IEEE Press, 1998.

[14] Y. Saad and M. H Schultz, "GMRES: a generalized minimal residual algorithm for solving nonsymmetric linear systems," *SIAM Journal on Scientific and Statistical Computing*, vol. 7, no. 3, pp. 856 - 869, July 1986.

[15] J. Dongarra, I. Duff, D. Sorensen, and H. Van Der Vorst, *Solving Linear Systems on Vector and Shared Memory Computers*, Philadelphia, PA: *SIAM*, 1991.

Zhongde Wang received his Ph.D. from University of Michigan in 2005, and his M.S. from University of Waterloo, Canada in 2002, major in microwave/RF engineering. He joined Ansoft Corporation as an Application Engineer starting from January 2005. His research focuses on computational electromagnetics, Signal/Power Integrity, RF MEMS structures modeling, and various antenna designs and CMOS inductors/capacitors optimization.

Dr. Wang was awarded 'the 2nd Grade Prize for Significant Contribution to Radar Cross Section Modeling of Arbitrary 3D Geometry' by the Chinese Electrical Ministry in 1996. He has published about 30 academic papers in journals and conferences.

John L. Volakis was born on May 13, 1956 in Chios, Greece and immigrated to the U.S.A. in 1973. He obtained his B.E. Degree, summa cum laude, in 1978 from Youngstown State Univ., Youngstown, Ohio, the M.Sc. in 1979 from the Ohio State Univ., Columbus, Ohio and the Ph.D. degree in 1982, also from the Ohio State Univ.

From 1982-1984 he was with Rockwell International, Aircraft Division (now Boeing Phantom Works), Lakewood, CA and during 1978-1982 he was a Graduate Research Associate at the Ohio State University ElectroScience Laboratory. From January 2003 he is the Roy and Lois Chope Chair Professor of Engineering at the Ohio State University, Columbus, Ohio and also serves as the Director of the ElectroScience Laboratory. Prior to moving to the Ohio State Univ, he was a Professor in the Electrical Engineering and Computer Science Dept. at the University of Michigan, Ann Arbor, MI. (1984-2003). He also served as the Director of the Radiation Laboratory from 1998 to 2000. His primary research deals with antennas, computational methods, electromagnetic compatibility and interference, design of new RF materials, multi-physics engineering and bioelectromagnetics. Dr. Volakis published 230 articles in major refereed journal articles (9 of these have appeared in reprint volumes), nearly 350 conference papers and 10 book chapters. In addition, he co-authored 3 books: *Approximate Boundary Conditions in Electromagnetics* (Institution of Electrical Engineers, London,1995), *Finite Element Method for Electromagnetics* (IEEE Press, New York, 1998) and *Frequency Domain Hybrid Finite Element Methods in Electromagnetics* (Morgan & Claypool). He has also written two well-edited coursepacks on introductory and advanced numerical methods for electromagnetics, and has delivered short courses on numerical methods, antennas and frequency selective surfaces. In 1998 he received the University of Michigan (UM) College of Engineering Research Excellence award and in 2001 he received the UM, Dept. of Electrical Engineering and Computer Science Service Excellence Award. Dr. Volakis is listed by ISI among the top 250 most referenced authors (2004, 2005); He graduated/mentored over 45 Ph.D. students/post-docs, and co-authored with them 5 best paper awards at conferences.

Dr. Volakis served as an Associate Editor of the *IEEE Transactions on Antennas and Propagation* from 1988-1992, and as an Associate Editor of Radio Science from 1994-97. He chaired the 1993 IEEE Antennas and Propagation Society Symposium and Radio Science Meeting, and co-chaired the same Symposium in 2003. Dr. Volakis was a member of the AdCom for the IEEE Antennas and Propagation Society from 1995 to 1998 and served as the 2004 President of the IEEE Antennas and Propagation Society. He also serves as an associate editor for the *J. Electromagnetic Waves and Applications,* the *IEEE Antennas and Propagation Society Magazine*, and the URSI Bulletin. He was elected Fellow of the IEEE in 1996, and is a member of Commissions B and E of URSI.

Katsuo Kurabayashi (M'00) received his B.S. (1992) in Precision Engineering from the University of Tokyo, Japan and his M.S. (1994) and Ph.D. (1998) degrees in Materials Science and Engineering with Electrical Engineering minor from Stanford University, CA. His dissertation work focused on measurement and modeling of the thermal transport properties of electronic packaging and organic materials for integrated circuits under the contract with the Semiconductor Research Corporation (SRC). Upon completion of his Ph.D. program, he was hired as Research Associate with the Department of Mechanical Engineering at Stanford University for 12 months. In January 2000, he joined the faculty of the University of Michigan, Ann Arbor, where he is currently Associate Professor of Mechanical Engineering and Electrical Engineering and Computer Science. His group at Michigan studies multi-physics modeling and characterization of RF MEMS, biomolecular motor hybrid NEMS/MEMS technology, and polymer-on-silicon strain-tunable photonic devices.

Dr. Kurabayashi is a recipient of the Semiconductor Research Corporation (SRC) Best Paper Award (1998), the NSF CAREER Award (2001), and the University of Michigan Robert Caddell Memorial Award (2004).

Kazuhiro Saitou received the Ph.D. degree in mechanical engineering from the Massachusetts Institute of Technology (MIT), Cambridge, in 1996. From 1997 to 2003, he was an Assistant Professor with the Department of Mechanical Engineering, University of Michigan, Ann Arbor, where he is currently an Associate Professor. His research interests include design automation and optimization of mechanical systems, design for manufacture, assembly, robustness, environment, and modeling and optimization of micro electro-mechanical systems, and evolutionary computation in mechanical design.

Dr. Saitou is a member of American Society of Mechanical Engineers (ASME), Institute of Electrical and Electronics Engineers (IEEE), Society of Manufacturing Engineers (SME), Association for Computing Machinery (ACM), and Sigma Xi. He currently serves as an Associate Editor for the *IEEE Transactions on Automation Science and Engineering* and an editorial board member of the *International Journal of CAD/CAM*, and the *Genetic Programming and Evolvable Machines*. He was the recipient of the 1999 CAREER Award from the National Science Foundation, and of the Best Paper Award at the 5th International Symposium on Tools and Methods of Competitive Engineering in 2004.

A Parallelized Monte Carlo Algorithm for the Nonlinear Poisson-Boltzmann Equation in Two Dimensions

Kausik Chatterjee[1] and Jonathan Poggie[2]

[1]Department of Electrical and Computer Engineering, Cooper Union, New York, NY 10003-7185, USA, Email: chatte@cooper.edu, Phone: (212) 353-4333

[2]Computational Sciences Center, Air Force Research Laboratory, Wright-Patterson AFB, OH 45433-7512, USA

Abstract – This paper presents the parallelization of a previously-developed two-dimensional floating random walk (FRW) algorithm for the solution of the nonlinear Poisson-Boltzmann (NPB) equation. Historically, the FRW method has not been applied efficiently to the solution of the NPB equation which can be attributed to the absence of analytical expressions for volumetric Green's functions. Stochastic approaches to solving nonlinear equations (in particular the NPB equation) that have been suggested in literature involve an iterative solution of a series of linear problems. As a result, previous applications of the FRW method have examined only the linearized Poisson-Boltzmann equation. In our proposed approach, an approximate (yet accurate) expression for the Green's function for the nonlinear problem is obtained through perturbation theory, which gives rise to an integral formulation that is valid for the entire nonlinear problem. As a result, our algorithm does not have any iteration steps, and thus has a lower computational cost. A unique advantage of the FRW method is that it requires no discretization of either the volume or the surface of the problem domains. Furthermore, each random walk is independent, so that the computational procedure is highly parallelizable. In previously published work, we have presented the fundamentals of our algorithm and in this paper we report the parallelization of this algorithm in two dimensions. The solution of the NPB equation has many interesting applications, including the modeling of plasma discharges, semiconductor device modeling and the modeling of biomolecules.

Key words – Monte Carlo, random walk, stochastic algorithm, nonlinear Poisson-Boltzmann equation, modeling of plasma sheaths, semiconductor device modeling, and modeling of biomolecular structure and dynamics.

I. INTRODUCTION

The solution of the nonlinear Poisson-Boltzmann (NPB) equation has widespread applications in science and engineering. These applications include the modeling of plasma sheaths [1], semiconductor device modeling [2] and the modeling of biomolecular structures and dynamics [3]. In this paper, we address the parallelization of a two-dimensional floating random-walk (FRW) [4-6] algorithm (a sub-class of Monte Carlo algorithms) for the NPB equation, subject to Dirichlet boundary conditions.

The FRW method is based on probabilistic interpretations of deterministic equations. We consider a differential equation, with a differential operator L,

$$L[U(\mathbf{r})] = f(\mathbf{r}), \tag{1}$$

where the solution $U(\mathbf{r})$ is a function of the three-dimensional position vector $\mathbf{r}$. The function $f(\mathbf{r})$ is a source term. Using Green's integral representation [7] $U(\mathbf{r})$ can be written as

$$\begin{aligned} U(\mathrm{r_o}) = & \iiint_V dv G(\mathrm{r}\,|\,\mathrm{r_o})\, f(\mathrm{r}) \\ & - \oiint_S \left[d\mathbf{s}\cdot\nabla_{\mathrm{r}} U(\mathrm{r}) \right] \; G(\mathrm{r}|\mathrm{r_o}) \\ & + \oiint_S \left[d\mathbf{s}\cdot\nabla_{\mathrm{r}} G(\mathrm{r}|\mathrm{r_o}) \right] \; U(\mathrm{r}). \end{aligned} \tag{2}$$

The symbol $G(\mathbf{r}|\mathbf{r_o})$ is the volumetric Green's function [7] for equation (1) at $\mathbf{r}$ given an impulse function at $\mathbf{r_o}$ and is given by the solution of the equation $L[U(\mathbf{r})] = \delta(\mathbf{r}-\mathbf{r_o})$. $\nabla_{\mathbf{r}} G(\mathbf{r}\,|\,\mathbf{r_o})$, which on the other hand is called the surface Green's function [7]. The first term on the right hand side of equation (2) is a volume integral involving the source term in the entire volume V of interest. The second and third terms are vector surface integrals over the surface S enclosing V, where $d\mathbf{s}$ is a vector whose magnitude is equal to that of an infinitesimally small area unit on the surface S and directed normally outward from the center of the area

unit. The second integral on the right hand side of equation (2) corresponds to the Neumann [7] boundary condition, whereas the third integral corresponds to the Dirichlet [7] boundary condition.

Equation (2) forms the mathematical basis of the FRW method. To evaluate the solution of equation (1) at a particular point in the domain of interest, we consider maximal spheres, cubes, or any geometrical object for which the volumetric Green's function of equation (1) is known [4-6]. We then make random hops to the surface of that geometrical object based on any predefined probability density. The weights for such random hops are determined by sampling the various integrands in equation (2). For example, in the case of a Dirichlet problem with no source term [that is, $f(\mathbf{r}) = 0$], the problem reduces to a Monte Carlo integration of an infinite-dimensional integral, as given by [8],

$$U(\mathrm{r}_0) = \oint_{S_1} ds_1 K(\mathrm{r}_0 \mid \mathrm{r}_1) \times \oint_{S_2} ds_2 K(\mathrm{r}_1 \mid \mathrm{r}_2) \times \oint_{S_n} ds_n K(\mathrm{r}_{n-1} \mid \mathrm{r}_n) U(\mathrm{r}_n), \quad (3)$$

$$K(\mathrm{r}_{n-1} \mid \mathrm{r}_n) = \left| \nabla_{\mathrm{r}_n} G(\mathrm{r}_{n-1} \mid \mathrm{r}_n) \right| \cos(\gamma_{n-1,n}) \ ,$$

where $\gamma_{n-1,n}$ is the angle between $\nabla_{\mathbf{r_n}} G(\mathbf{r_{n-1}} \mid \mathbf{r_n})$ and $d\mathbf{s_n}$, being a vector whose magnitude (ds_n) is equal to that of an infinitesimally small area unit on the surface S_n and directed normally outward from the center of the area unit. The successive surface integrals in equation (3) relate to successive random hops across the problem domain and the weight factors of the form $K(\mathbf{r_{n-1}} \mid \mathbf{r_n})$ are derived from the third integral term on the right hand side of equation (2) that corresponds to the Dirichlet boundary condition. A particular random walk is terminated at the boundary, where the solution is known, and the samples of successive weight factors multiplied by the solution at the boundary yield a particular sample of the solution. A numerical solution of equation (1) is obtained by averaging over a statistically large number of such samples.

At this point, we note that this method does not require any discretization, as the solution can be evaluated at the point of origination of the random walks irrespective of the solution at any other point. In contrast, deterministic numerical methods require the discretization of either the volume or the surface of the problem domain. Methods such as the finite-difference [9] or the finite-element [10] are based on volume discretization, while methods such as the method of moments [11] require surface discretization. As a result, the FRW method has lower memory requirements compared to deterministic numerical methods.

We also note that this method is inherently parallelizable, since different random-walks can be performed in different processors, and inter-processor communication is required only during the final averaging of the contributions from different walks. As a result, one can obtain very close to linear rate of parallelization for a large number of processors, which is a very unique advantage that the FRW method enjoys over deterministic methods. In this paper, the superiority of the FRW method over the finite-difference method as regard to parallelization will be demonstrated.

In spite of these unique advantages, the FRW method has not being applied to the NPB equation and other important nonlinear equations. This can be attributed to the absence of analytical expressions for volumetric Green's functions of these equations. Early researchers in the area expressed the apprehension that the extension of the stochastic solution methodology to nonlinear problems might not be possible. In a 1954 paper [12], J. R. Curtiss wrote: "*So far as the author is aware, the extension of Monte Carlo methods to non-linear processes has not yet been accomplished and may be impossible*." Stochastic approaches to solving nonlinear equations (in particular the NPB equation) that have been suggested in literature [13], involve an iterative solution of a series of linear problems and as a result random-walk algorithms that have been presented in literature [14-15], involve prior linearization of the NPB equation. In our proposed approach, an approximate (yet accurate) expression for the Green's function for the nonlinear problem is obtained through perturbation theory, which gives rise to an integral formulation that is valid for the entire nonlinear problem. As a result, our algorithm does not have any iteration steps, and thus has a lower computational cost. The validity of such an integral expression is maintained by restricting the size of a random hop and increasing the order of perturbation in the Green's function would allow one to increase the hop size, thus increasing computational speed. An approach utilizing a perturbation-based Green's function was used to develop an FRW algorithm for the Helmholtz equation in heterogeneous problem domains (important for IC interconnect analysis at high frequencies) by Prof. K. Chatterjee in Ref. [16-17], where the idea of extending the approach to nonlinear problems was also proposed. Later that idea was extended to develop the fundamentals of a floating random-walk (FRW) algorithm for the NPB equation [18-20]. In this paper,

we present the results of parallelization of the FRW algorithm for the two-dimensional NPB equation.

II. FORMULATION OF THE ALGORITHM

The formulation of the two-dimensional algorithm is presented in detail in [19, 20], along with its validation with the help of finite-difference based benchmarks. In this section, we give a brief description of that formulation before presenting the details of the parallelization.

In our problem of interest, the dependent variable ϕ is governed by the NPB equation, given as

$$\nabla^2\phi = \frac{1}{c^2}\left(e^{k\phi(\mathbf{r})} - e^{-k\phi(\mathbf{r})}\right), \quad \mathbf{r} \in W, \tag{4}$$

where $\mathbf{r}(r,\theta)$ is the two-dimensional position coordinate, c and k are constants, while W is the two-dimensional problem domain. Dirichlet boundary conditions have been imposed,

$$\phi = g(\mathbf{r}), \quad \mathbf{r} \in \partial W \tag{5}$$

where ∂W is the boundary of the domain W. Equation (4) can be normalized to

$$\frac{1}{\hat{r}}\frac{\partial}{\partial \hat{r}}\left(\hat{r}\frac{\partial \hat{\phi}}{\partial \hat{r}}\right) + \frac{1}{\hat{r}^2}\frac{\partial^2 \hat{\phi}}{\partial \hat{\theta}^2} = e^{\hat{\phi}} - e^{-\hat{\phi}}, \tag{6}$$

where $\hat{r} = r/\lambda$, $\hat{\theta} = \theta$, $\hat{\phi} = k\phi$ and $\lambda = c/\sqrt{k}$. We further normalize the length scales to the radius R of a circular domain (the chosen geometry for random-walks) and substitute $\hat{\rho} = \hat{r}/R$ and $\hat{\rho}_o = \hat{r}_o/R$ in equation (6). The twice-normalized NPB equation is written as,

$$\frac{1}{\hat{\rho}}\frac{\partial}{\partial \hat{\rho}}\left(\hat{\rho}\frac{\partial \hat{\phi}}{\partial \hat{\rho}}\right) + \frac{1}{\hat{\rho}^2}\frac{\partial^2 \hat{\phi}}{\partial \hat{\theta}^2} = R^2\left(e^{\hat{\phi}} - e^{-\hat{\phi}}\right). \tag{7}$$

A volumetric Green's function of equation (7), $\hat{G}(\hat{\boldsymbol{\rho}} \mid \hat{\boldsymbol{\rho}}_{\mathbf{o}})$ at $\hat{\boldsymbol{\rho}}$, assuming a dirac-delta function at $\hat{\boldsymbol{\rho}}_{\mathbf{o}}$ inside the circular domain, is given as the solution of the equation

$$\frac{1}{\hat{\rho}}\frac{\partial}{\partial \hat{\rho}}\left(\hat{\rho}\frac{\partial \hat{G}}{\partial \hat{\rho}}\right) + \frac{1}{\hat{\rho}^2}\frac{\partial^2 \hat{G}}{\partial \hat{\theta}^2} - R^2\left(e^{\hat{G}} - e^{-\hat{G}}\right) = \delta\left(\hat{\rho} - \hat{\rho}_o\right). \tag{8}$$

A zero-order approximation (assuming homogeneous Dirichlet boundary conditions) for the volumetric Green's function, $\hat{G}^{(0)}(\hat{\boldsymbol{\rho}} \mid \hat{\boldsymbol{\rho}}_{\mathbf{o}})$ is the solution of equation

$$\frac{1}{\hat{\rho}}\frac{\partial}{\partial \hat{\rho}}\left(\hat{\rho}\frac{\partial \hat{G}^{(0)}}{\partial \hat{\rho}}\right) + \frac{1}{\hat{\rho}^2}\frac{\partial^2 \hat{G}^{(0)}}{\partial \hat{\theta}^2} = \delta\left(\hat{\rho} - \hat{\rho}_o\right) \tag{9}$$

and is given as [7]

$$\hat{G}^{(0)}\left(\hat{\rho} \mid \hat{\rho}_o\right) = \frac{1}{4\pi} \times \ln\left[\frac{\hat{\rho}^2 + \hat{\rho}_o^2 - 2\hat{\rho}\ \ \hat{\rho}_o\cos\left(\hat{\theta} - \hat{\theta}_o\right)}{1 + \hat{\rho}^2\hat{\rho}_o^2 - 2\hat{\rho}\ \ \hat{\rho}_o\cos\left(\hat{\theta} - \hat{\theta}_o\right)}\right]. \tag{10}$$

Equation (10) can be used to obtain a first-order approximation, $\hat{G}^{(1)}(\hat{\boldsymbol{\rho}} \mid \hat{\boldsymbol{\rho}}_{\mathbf{o}})$ to the volumetric Green's function and is given as a solution of the following equation,

$$\frac{1}{\hat{\rho}}\frac{\partial}{\partial \hat{\rho}}\left(\hat{\rho}\frac{\partial \hat{G}^{(1)}}{\partial \hat{\rho}}\right) + \frac{1}{\hat{\rho}^2}\frac{\partial^2 \hat{G}^{(1)}}{\partial \hat{\theta}^2} = \delta\left(\hat{\rho} - \hat{\rho}_o\right) + R^2\left(e^{G^{(0)}} - e^{-G^{(0)}}\right). \tag{11}$$

Based on equations (2), (10) and (11), $\hat{G}^{(1)}(\hat{\boldsymbol{\rho}} \mid \hat{\boldsymbol{\rho}}_{\mathbf{o}})$ is given by the following expression,

$$G^{(1)}\left(\hat{\boldsymbol{\rho}} \mid \hat{\boldsymbol{\rho}}_{\mathbf{o}}\right) = G^{(0)}\left(\hat{\boldsymbol{\rho}} \mid \hat{\boldsymbol{\rho}}_{\mathbf{o}}\right) + R^2\int_0^1\int_0^{2\pi}\left[d\hat{\rho}'\,d\hat{\theta}'\,\hat{\rho}'\,G^{(0)}\left(\hat{\boldsymbol{\rho}} \mid \hat{\boldsymbol{\rho}}'\right) \times f\{y\}\right], \tag{12}$$

where $f\{y\} = e^y - e^{-y}$ with $y = \hat{G}^{(0)}(\hat{\boldsymbol{\rho}} \mid \hat{\boldsymbol{\rho}}_{\mathbf{o}})$. It can again be noted that $\left\{G^{(1)}\left(\hat{\boldsymbol{\rho}} \mid \hat{\boldsymbol{\rho}}_{\mathbf{o}}\right)\right\}_{\hat{\rho}=1} = 0$ along the circumference of the circular domain. Based on this approximate expression for the volumetric Green's function and equation (2), an expression for normalized potential at a point $\hat{\boldsymbol{\rho}}_{\mathbf{o}}$ is given by a line integral over the circumference of the unit circle and is expressed as,

$$\hat{\phi}\left(\hat{\boldsymbol{\rho}}_{\mathbf{o}}\right) = \int_{\theta=0}^{2\pi} d\hat{\theta}\left[\frac{dG^{(1)}}{d\hat{\rho}}\right]_{\hat{\rho}=1}\hat{\phi}(1,\hat{\theta}). \tag{13}$$

For the development of the FRW algorithm, we need to estimate $\left[\frac{dG^{(1)}}{d\hat{\rho}}\right]_{\hat{\rho}=1}$ in equation (13). This estimate is obtained by differentiating equation (12), and in the zero-centered notation (i.e. $\hat{\rho}_o = 0$) is given by,

$$\left[\frac{dG}{d\hat{\rho}}\right]_{\hat{\rho}=1} = \frac{1}{2\pi} + \frac{R^2}{4\pi}\int_0^1\int_0^{2\pi} \hat{\rho}' d\hat{\rho}' d\theta' A \times B, \qquad (14)$$

where A and B are given by,

$$A = \left[\left(\hat{\rho}'\right)^{\frac{1}{2\pi}} - \left(\hat{\rho}'\right)^{-\frac{1}{2\pi}}\right],$$
$$B = \frac{2\left(1-\left(\hat{\rho}'\right)^2\right)}{1+\left(\hat{\rho}'\right)^2 - 2\hat{\rho}'\cos\left(\hat{\theta}-\hat{\theta}'\right)}. \qquad (15)$$

Equation (13) in conjunction with equations (14) and (15) is used to develop the FRW algorithm for the problem under consideration. In order to calculate the normalized potential at a point of interest, we start our random-walks at that point and hop to the circumference of a circle of radius R. The random-walks have to be restricted to a small fraction of the characteristic length λ in order to maintain the validity of the first-order approximation in the perturbation expression for the volumetric Green's function. For every hop there is a weight factor obtained by sampling the multi-dimensional integrand of equation (13) according to a pre-determined probability distribution for each of the variables. As explained in the previous section, a particular random-walk, consisting of several such random hops, is terminated on the boundary of the problem domain, where the value of the potential is known. The contribution from a particular random-walk is obtained by multiplying the overall weight factor (which is obtained by multiplying the weight factors of individual hops) with the boundary value. An estimate $\overline{\hat{\phi}}$ of the potential, at the point of origination of the hops is then obtained by averaging over a statistically large number of random-walks.

The error in the result has a deterministic component arising from the truncation of the perturbation-based Green's function in equation (12), which can be controlled by controlling the radius of the hop. The error also has a stochastic component, a measure of which is given by the "1-σ error σ_T" given by [21],

$$\sigma_T = \frac{\sigma_E}{\sqrt{N}}, \qquad (16)$$

where σ_E is the standard deviation of the contributions from different random-walks, N being the number of random-walks. As a result, the statistical error can be controlled by controlling the number of random-walks.
The FRW algorithm described previously was parallelized. Two levels of parallelism are inherent in an FRW algorithm. First, the solutions for different points in the domain (different origins for the random walks) are independent of each other. Second, for a given point of origin, each random walk is independent, and inter-processor communication is required only to sum up the contributions of the walks. For this initial parallel implementation, the test points in the domain were handled serially. The walks were distributed in groups across computer processors, with communication and a reduction operation at the completion of the walks. The FRW algorithm was implemented in C, and the serial version of the code was converted to parallel using the Message Passing Interface (MPI) library. The elegance and inherent parallelism of the FRW algorithm is demonstrated in the fact that the serial and parallel versions of the code differ by only four function calls, three of which are merely initialization routines. The results of this parallelization are given in the next section.

III. RESULTS

In our benchmark problem (Fig. 1) [20], a circle λ in diameter, is surrounded by a rectangle of dimensions $3\lambda \times 2\lambda$. The normalized potential is unity on the inner circle and zero on the outer rectangle. When run in a single processor, 20000 random-walks were performed per solution point, while the radii of the hops were restricted to two percent of the characteristic length λ to maintain the validity of the first-order approximation in the derivation of the volumetric Green's function in equation (12). For finite-difference calculations, a grid of 51×51 points, distributed over the first quadrant was used. The finite-difference calculations were carried out using a standard transformation from a curvilinear mesh in physical space to a uniform mesh in computational space, while maintaining second order accuracy. The results are shown in Table 1 and Fig. 2. Excellent agreement is observed between FRW and finite-difference based results.

It can also be observed that the absolute errors are consistently larger than the statistical errors, which can be attributed to the truncation of the perturbation-based Green's function in equation (12), and also to the truncation errors in the finite-difference based approach.

The parallelized algorithm was implemented on an IBM P4+ machine, running 1.7 GHz Power 4+ chips, with 2 Gigabytes RAM available per processor for as many as 64 processors. The timing results are shown in Fig. 3 for 100000 and 10000 random-walks per solution point. It can be observed that for 100000 random-walks per solution point the speed of computation increases perfectly linearly with the number of processors, particularly for a relatively smaller number of

processors. This can be attributed to the fact that the random-walks per processor needs to be high enough to ensure that the time spent in actual computation is large compared to the communication time between the various processors. For the same reason, the increase in the speed of computation is only sixteen fold for 32 processors with only 10000 random-walks per solution point. It should be borne in mind that the benchmark problems used for validation are relatively simple problems, and for more complicated problems one can expect to see even better scalability, stemming from the increased number of samples per processor. In comparison, the parallelization of the finite-difference algorithm (Fig. 4) for the same problem showed markedly inferior performance (compared to the case where N =100000) with increase in the number of processors. With 32 processors, the speed of computation is only 16 times higher than the speed with a single processor. It can also be concluded that as the finite-difference method (like other deterministic methods based on discretization) reduces the numerical solution of a differential equation to the numerical solution of a matrix equation, our newly-developed algorithm will exhibit superior efficiency of parallelization compared to other discretization-based deterministic methods as well.

Table 1. Statistical error and mean absolute error between FRW and finite-difference based results.

Benchmark Problem (20000 Random Walks per Solution Point)	***Mean Absolute Error***	***Statistical Error***
Along the centerline positive x-axis	0.0033	0.0028
Along the centerline positive y-axis	0.0067	0.0025

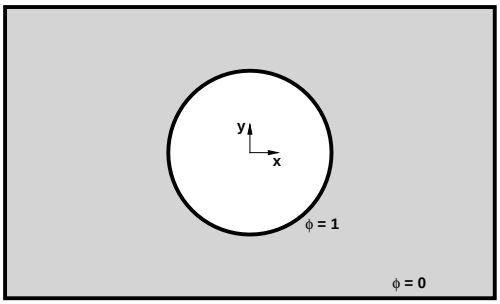

Fig. 1. The solution of the NPB equation in the region between a circle surrounded by a rectangular boundary. Problem dimension is $3\lambda \times 2\lambda$.

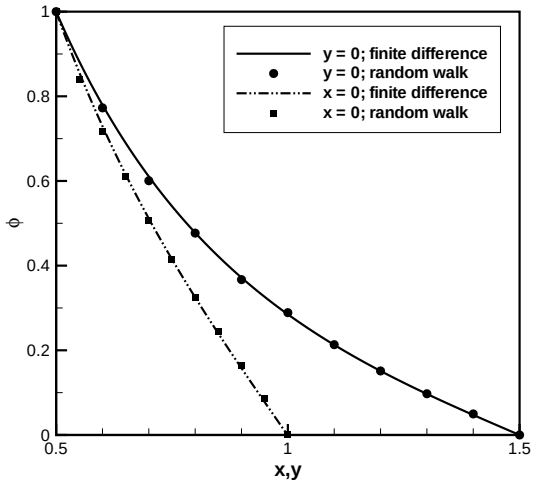

Fig. 2. Normalized potential plotted against position in normalized coordinates.

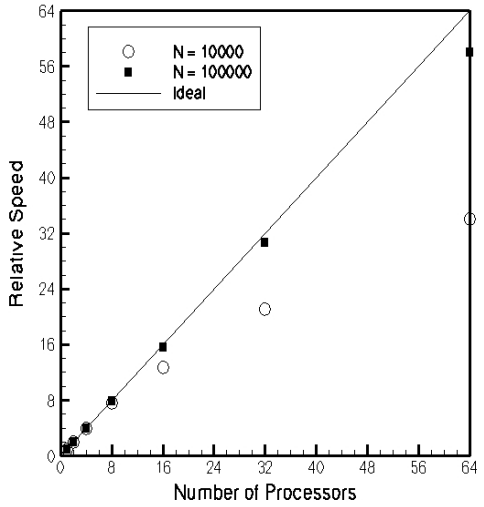

Fig.3. Parallelization results for the FRW algorithm.

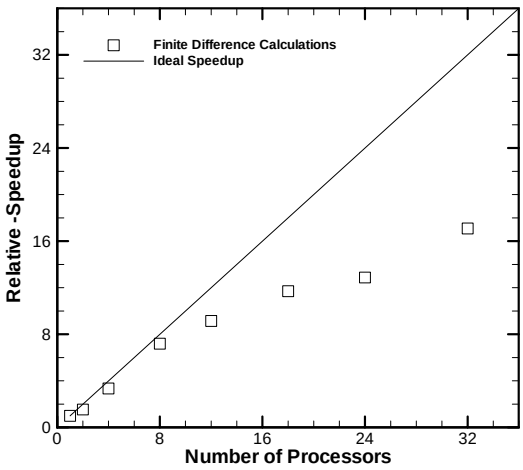

Fig. 4. Parallelization results for the finite-difference algorithm.

IV. CONCLUSION

In summary, we have parallelized a previously-developed FRW algorithm for the solution of the NPB equation in two dimensions. This algorithm is based on an approximate volumetric Green's function, derived using perturbation theory. Excellent agreement was found between the random walk and finite-difference results, while the FRW algorithm exhibited vastly superior (almost linear) efficiency of parallelization for a statistically significant number of random-walks per processor. The FRW algorithm also has the advantage of not requiring any discretization of the volume or the surface of problem domains. The approach is general, and can be applied to the numerical solution of other important nonlinear equations. Our work in the immediate future will involve the extension of this new FRW algorithm to Neumann and mixed boundary condition problems. The ultimate objective of this work is the extension of the perturbation-based approach to flow problems.

ACKNOWLEDGEMENTS

This research has been supported by the Air Force Office of Scientific Research through a grant (FA9550-06-1-0439) monitored by Dr. F. Fahroo. Additional support has been provided in the form of summer fellowships for Prof. K. Chatterjee at Air Force Research Laboratory, Wright Patterson Air Force Base (AFRL/WPAFB). We would also like to acknowledge valuable discussions with Dr. D. Gaitonde at AFRL/WPAFB.

REFERENCES

[1] M. Mitchner and C. H. Kruger, *Partially Ionized Gases*, John Wiley & Sons, New York, 1973.

[2] S. M. Sze, *Physics of Semiconductor Devices*, second edition, John Wiley & Sons: New York, pp. 366-368, 1999.

[3] M. E. Davis and J. A. McCammon, *Electrostatics in Biomolecular Structure and Dynamics*, Chemical Reviews, pp. 509-521, 1990.

[4] G. M. Brown, *Modern Mathematics for Engineers*, McGraw-Hill, New York, 1956.

[5] Y. L. Le Coz, H. J. Greub, and R. B. Iverson, "Performance of random walk capacitance extractors for IC interconnects: A numerical study," *Solid-State Electronics,* vol. 42, pp. 581-588, 1998.

[6] Y. L. Le Coz, R. B. Iverson, T. L. Sham, H. F. Tiersten, and M. S. Shepard, "Theory of a floating random walk algorithm for solving the steady-state heat equation in complex materially inhomogeneous rectilinear domains," *Numerical Heat Transfer, Part B: Fundamentals,* vol. 26, pp. 353-366, 1994.

[7] R. Haberman, *Elementary Applied Partial Differential Equations*, third edition, Prentice-Hall, Englewood Cliffs NJ, 1998.

[8] Y. L. Le Coz and R. B. Iverson, "A stochastic algorithm for high speed capacitance extraction in integrated circuits," *Solid-State Electronics,* vol. 35, pp. 1005-1012, 1992.

[9] K. S. Kunj and R. J. Lebbers, *The Finite Difference Time Domain Method for Electromagnetics*, CRC Press, Boca Raton, 1993.

[10] J. Jin, *The Finite Element Method in Electromagnetics*, John Wiley & Sons, New York, 1993.

[11] J. J. H. Wang, *Generalized Moment Methods in Electromagnetics*, John Wiley & Sons, New York, 1991.

[12] J. H. Curtiss, "Monte Carlo methods for the iteration of linear operators," *Journal of Mathematics and Physics*, vol. 32, pp. 209-232, 1954.

[13] K. K. Sabelfeld and N. A. Simonov, *Random Walks on Boundary for Solving PDEs*, VSP, Utrecht, The Netherlands, pp. 119-120, 1994.

[14] C.-O. Hwang and M. Mascagni, "Efficient modified 'walk on spheres' algorithm for the linearized poisson-boltzmann equation," *Applied Physics Lett.*, vol. 78, no. 6, pp. 787-789, 2001.

[15] M. Mascagni and N. A. Simonov, "Monte Carlo methods for calculating the electrostatic energy of a molecule," *Proceedings of the 2003 International Conference on Computational Science* (ICCS 2003).

[16] K. Chatterjee, "Development of a Floating Random walk Algorithm for Solving Maxwell's Equations in Complex IC-Interconnect Structures," Rensselaer Polytechnic Institute, May, 2002, UMI Dissertation Services, www.il.proquest.com.

[17] K. Chatterjee and Y. L. Le Coz, "A floating random-walk algorithm based on iterative perturbation theory: solution of the 2d vector-potential maxwell-helmholtz equation," Journal *of Applied Computational Electromagnetics Society*, vol. 18, no. 1, pp. 48-57, 2003.

[18] K. Chatterjee and J. Poggie, "A meshless stochastic algorithm for the solution of the nonlinear poisson-boltzmann equation in the context of plasma discharge modeling: 1d analytical benchmark," *Proceedings of the 17th AIAA Computational Fluid Dynamics Conference*, Toronto, Ontario, Canada, 6-9 June 2005.

[19] K. Chatterjee and J. Poggie, "A two-dimensional floating random-walk algorithm for the solution of the nonlinear poisson-boltzmann equation: application to the modeling of plasma sheaths,"

Proceedings of the 3rd MIT Conference on Computational Fluid and Solid Mechanics, Cambridge, MA, June 14-17, 2005.

[20] K. Chatterjee and J. Poggie, "A two-dimensional stochastic algorithm for the solution of the nonlinear poisson-boltzmann equation: validation with finite-difference benchmarks," *International Journal for Numerical Methods in Engineering*, vol. 66, no. 1, pp. 72-84, 2006.

[21] J. M. Hammersley and D. C. Handscomb, *Monte Carlo Methods*, John Wiley & Sons, New York, NY, pp. 50-54, 1964.

Kausik Chatterjee was born in India in 1969. In 1992, he received a Bachelor of Engineering degree in Electrical Engineering from Jadavpur University, Calcutta, India. Subsequently, in 1995, he received a Master of Technology degree in Nuclear Engineering from Indian Institute of Technology, Kanpur, India, and in 2002, he received his PhD degree in Electrical Engineering from Rensselaer Polytechnic Institute, Troy, New York. In 2002, he joined the faculty at California State University, Fresno as an Assistant Professor of Electrical and Computer Engineering, a position he held till 2005. He had been a visiting scientist at MIT Laboratory for Electromagnetic and Electronic Systems (2004-2005), held faculty fellowships at Air Force Research Laboratory at Wright-Patterson Air Force Base (2004, 2006) and NASA, Langley Research Center (2005) and held the position of a Junior Engineer at Durgapur Steel Plant, India (1992-1993). He is currently an Assistant Professor in the Department of Electrical and Computer Engineering at Cooper Union. His current research interests include the development of stochastic algorithms for important equations in nature and a theory for high temperature superconductors. He has been awarded a Government of India Fellowship at Indian Institute of Technology, Kanpur (1993-1995) and an Intel Doctoral Fellowship at Rensselaer Polytechnic Institute (2001-2002). He has also received the Charles M. Close Doctoral Prize at Rensselaer Polytechnic Institute (2002). He is a naturalized citizen of the United States.

Jonathan Poggie was born in the United States in 1966. He studied mechanical engineering at the University of Rhode Island, receiving a B.S. degree in 1988. He went on to obtain a Ph.D. degree in mechanical and aerospace engineering from Princeton University in 1995, specializing in fluid mechanics. Since then, he has worked at the U.S. Air Force Research Laboratory, focusing on physical problems associated high speed flight. His work has encompassed laminar/turbulent transition in hypersonic boundary layers, unsteadiness of shock waves in separated flow, and the control of ionized gas flow by electromagnetic means. Jonathan Poggie is a member of the American Physical Society and the American Society of Mechanical Engineers, and an associate fellow of the American Institute of Aeronautics and Astronautics.

Electromagnetic Scattering Computation Using a Hybrid Surface and Volume Integral Equation Formulation

Chong Luo and Cai-Cheng Lu

Electrical Computer Engineering Department, University of Kentucky
Lexington, Kentucky, USA

Abstract **–** This paper presents a hybrid integral equation formulation for computation of electromagnetic scattering by composite conducting and dielectric materials. In the hybrid formulation, multiple material regions in a scatterer are classified into two categories, one is the surface integral equation (SIE) region, and the other is the volume integral equation (VIE) region. For the SIE region, the boundary conditions for tangential E-field and tangential H-field are applied to formulate the surface integral equation for the equivalent surface currents. For the VIE region, the equivalent principle is applied to formulate the volume integral equation for the induced volume currents. The hybrid formulation takes the advantageous of both the SIE and VIE. The integral equations are cast into a set of linear equations using the method of moments. For regions that are electrically large, the multilevel fast multipole algorithm is applied to accelerate the matrix-vector multiplication needed by iterative solvers. Numerical results are provided to verify the accuracy and the application of the program developed from the hybrid formulation.

Key words **–** Scattering/RCS, method of moments, hybrid methods, and boundary integral equations.

I. INTRODUCTION

The integral equation approach has been used to model electromagnetic scattering by perfectly electrical conducting objects as well as dielectric materials. When this approach is used to solve an electromagnetic wave scattering problem involving piece-wise homogeneous electric and magnetic materials, there are two frequently used formulations: the surface integral equation (SIE) formulation [1-10] and the volume integral equation (VIE) formulation [11-16]. In SIE formulation, unknown equivalent electric current and magnetic current are assigned on the material surfaces, as well as the perfectly electrical conducting (PEC) surfaces. The boundary conditions of tangential E-field and tangential H-field across material surfaces are applied to formulate the SIE for the equivalent currents. In the VIE formulation, equivalent electric and magnetic volume currents are assigned to the volumes occupied by the materials. The field equivalence principle[1] is applied to formulate the volume integral equations for the volume currents. Both the SIE and VIE formulations have their own advantageous depending on the problem to be solved and on the way the discretized linear equation is solved. In general, the SIE formulation leads to less number of unknowns for electrically large material volume regions compared to that of the VIE formulation. If a problem consists of materials of electrically thin cylinders and thin slabs, it is expected that both SIE and VIE formulation will have comparable numbers of unknowns. However, If iterative solvers are used to solve the discretized linear equations, the VIE formulation will have higher converge rate (or need less number of iterations) because it is of the second kind [18]. Based on the above comparisons, we propose a hybrid SIE and VIE formulation. In this way, the material volumes are classified into two groups. The electrically large and bulk material volumes belong to one group for which the SIE formulation is applied (the SIE also applied to the perfectly electric conducting surfaces). The other group consists of material volumes that are electrically thin or small (such as the thin slabs and cylinders) for which the VIE formulation is applied. We call this approach the "SIE+VIE" approach. The purpose is to take the advantageous of the "SIE ONLY" and "VIE ONLY" approaches, and avoid the drawbacks of the two. It is difficult to draw a line on the use of VIE and SIE for a given material region. As a general guideline, large, thick, and homogeneous material regions are modeled by SIE, and small, thin and inhomogeneous material regions are modeled by VIE. In the following, we will present the hybrid formulation of the "SIE+VIE" approach, followed by numerical examples to verify the implementation. For a composite scatterer with piece-wise dielectric material, we can solve the problem using any one of the three approaches, i.e., the hybrid "SIE+VIE", the "SIE ONLY", and the "VIE ONLY". It must be emphasized that in all three approaches, SIE is applied to PEC surfaces. The distinction lies in the treatment of material. In the "SIE ONLY" approach, SIE is applied to all material surfaces (hence it can only deal with piece-wise homogeneous scatterers); in the "VIE ONLY" approach, VIE is applied to all material volumes; and in the hybrid "SIE+VIE" approach, part of the material region is modeled by SIE and the rest are modeled by VIE. The formulation is in frequency domain, and the time factor of $\exp\{-i\omega t\}$ is implied and suppressed in all the equations.

[1] A rigorous derivation of VIE can be found in a recent paper by M. Sencer *et al* in [17].

II. FORMULATION

A general scatterer usually consists of PEC surfaces and electric/magnetic materials regions, as shown in Fig. 1. In the "SIE+VIE" formulation, the volume integral equation is constructed for the small or inhomogeneous material regions, and the surface integral equation is constructed for PEC surfaces and the surfaces of large homogeneous material regions. Although pure SIE formulation (the "SIE ONLY") could be applied to all the piece-wise material regions, it can be inefficient if there are small and thin material volumes to which the VIE formulation is more efficient and will lead to a better conditioned system equation [18].

A. Integral Equations

To simplify the notation, we first define two operators, $\bar{\bar{L}}$ and $\bar{\bar{K}}$, such that,

$$\bar{\bar{L}}_j \cdot \vec{J} = \int_\Omega (\bar{\bar{I}} + \frac{1}{k_j^2}\nabla\nabla) G(\vec{r},\vec{r}',k_j)\cdot \vec{J}(\vec{r}')d\Omega, \qquad (1)$$

$$\bar{\bar{K}}_j \cdot \vec{M} = \nabla\times\int_\Omega G(\vec{r},\vec{r}',k_j)\vec{M}(\vec{r}')d\Omega, \qquad (2)$$

where the integral domain Ω could be either a surface or a volume, $G(\vec{r},\vec{r}',k_j)=\exp(ik_j|\vec{r}-\vec{r}'|)\ /(4\pi|\vec{r}-\vec{r}'|)$ is the 3-D scalar Green's function for unbounded homogeneous material space with constant wavenumber $k_j=\omega\sqrt{\varepsilon_j\mu_j}$, and $\bar{\bar{I}}$ is the identity dyad.

Before explaining the general scattering configurations, we first consider a few simple cases. The focus is on introducing the domains for a scattering configuration. The details of the equivalence problem and integral equation formulation will be discussed afterwards. To illustrate the configuration in general, we first consider several simple cases. (1) If a PEC sphere is in a free-space, then the configuration consists of one domain (the whole space) with one PEC body embedded within it. The domain boundary is S_∞ (a spherical surface of infinite radius). This surface S_∞ is implied for all infinite regions, and is ignored in all cases since no integral equation is formulated on it. In this case, one SIE is constructed on the PEC surface for the induced electric current. (2) If a dielectric body is in free-space and it is to be modeled by VIE, then the configuration has one domain, and the dielectric body is said to be embedded within this domain. One VIE is formulated for the dielectric volume (assuming non-magnetic case). (3) If a homogeneous material sphere resides in a free-space, and SIE is used to model the scattering of the material, then the configuration consists of two domains that are separated by a spherical surface (the interior domain R_1 and the exterior domain R_2). The spherical surface is named S_1 for R_1, and S_2 for R_2. Two SIEs are formulated on S_1, and two SIEs are formulated for S_2 (equation redundancy will be considered later). (4) Now we consider a two-layer dielectric sphere in free-space. There are two concentric spherical surfaces with radii a_1 and a_2 ($a_1<a_2$), respectively. If the hybrid "SIE+VIE" is applied to this problem, there are at least two possibilities. In one case, the spherical core is considered as embedded within a dielectric sphere of radius a_2, and it is modeled by VIE. In this case, the overall configuration has two domains, one (R_1) is interior to the larger sphere ($r\le a_2$, including the core region), and the other (R_2) is the exterior one ($r\ge a_2$). The two domains share the same spherical surface of radius a_2. This surface is named S_1 for R_1, and S_2 for R_2. Equivalent problem for R_2 leads to two SIEs on S_2, and the equivalent problem for R_1 leads to two SIEs on S_1, and one VIE for the embedded core volume. In the other case, the scatterer is considered as a thin layer of coating on a homogeneous sphere of radius a_1. The coating is modeled by VIE. In this case, the overall configuration has two domains as well, domain R_1 is the spherical space of $r\le a_1$, and domain R_2 is the rest of the whole space ($r\ge a_1$). The two domains share the same spherical surface $r=a_1$. This surface is named S_1 for R_1, and S_2 for R_2. The equivalent problem for R_1 leads to two SIEs on S_1, and the equivalent problem for R_2 leads to two SIEs on S_2, and one VIE for the embedded dielectric shell coating. Of the two cases, one is more efficient sometimes than the other depending on the relative sizes of each part. For example, case one will be more efficient if the dielectric core has radius much less than a wavelength, and case two is more efficient if the shell thickness (a_2-a_1) is much smaller than a wavelength.

With the above discussions, we consider the sketch of a general scatterer shown in Fig. 1. It consists of PEC bodies (denoted by $\sigma=\infty$), and a number of piece-wise homogeneous material domains $R_1,R_2,\cdots,R_n$ (with complex material parameters of ε_i,μ_i, $i=1,2,\cdots,n$), and a number of un-named material regions (shown by the dot-shaded regions in the figure) embedded within the existing domains. These embedded regions are not numbered and will be modeled by VIE. For instance, the region marked by $\vec{J}_{V2}$ is embedded within R_2. Let S_{ij} be the surface shared by domain R_i and R_j, and S_{pj} be the conducting surface that is exposed to domain R_j. In addition, we define S_i to be the boundary of domain R_i, it may be a union of several open surfaces. For example, S_3 is the boundary of R_3 and it is the union of $S_{31},S_{32},S_{34},$ and S_{3n} (highlighted by thick solid lines in Fig. 1), i.e., $S_3=\cup\{S_{13},S_{23},S_{34},S_{3n}\}$. If there are PEC regions embedded within R_3, then the conducting surfaces shall also be part of S_3.

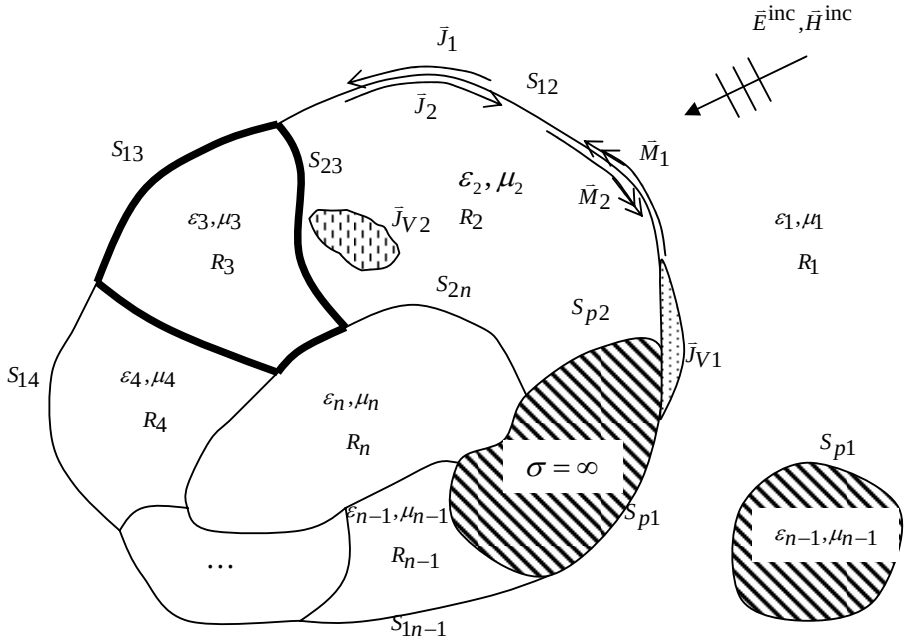

Fig. 1. A sketch of a general scatterer that is made of PEC bodies as well as multiple piece-wise homogeneous dielectric materials within which inhomogeneous materials may be embedded.

The equivalent problems for the domains are formed independently from each other. For example, the equivalent problem for R_1 is shown in Fig. 2. It is obtained by removing all materials exterior to boundary S_1 (highlighted by thick dotted line), all PEC bodies within S_1, and then filling the left over space with the same material as that of region R_1. The total electric field and magnetic field are set to zeros for the region exterior to S_1, and equivalent electric current $\bar{J}_1$ and magnetic current $\bar{M}_1$ are introduced on surface S_1.

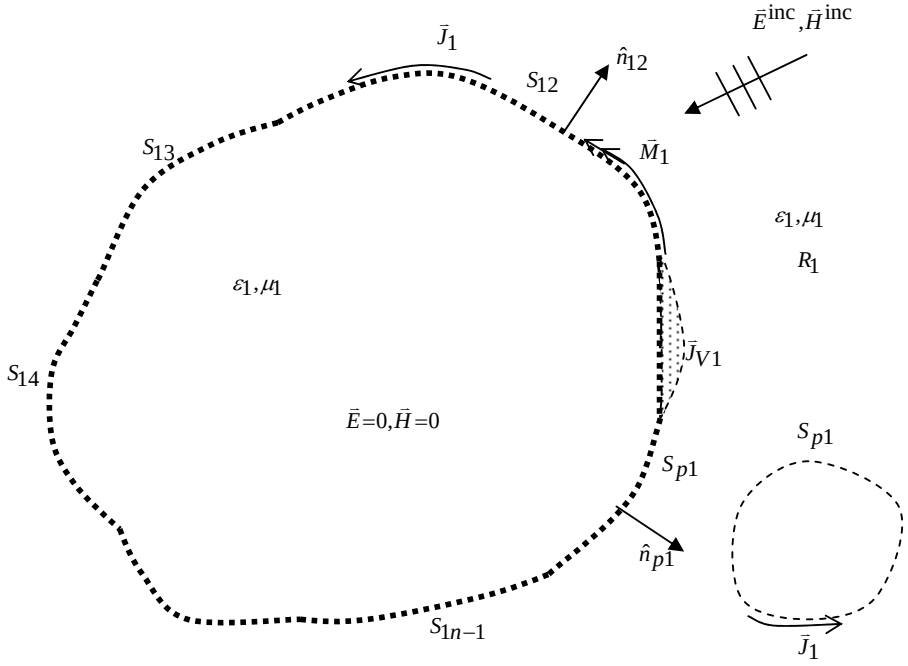

Fig. 2. Equivalent problem for region R_1.

Meanwhile, the material body embedded within R_1 is removed and the equivalent volume current $\bar{J}_{V1}$ is introduced for that volume. This is repeated for all such embedded material bodies (for simplicity of derivation, we will not consider embedded magnetic material in this paper. If embedded magnetic material presents, then additional volume integral equation for equivalent magnetic volume current shall be formulated in the same way).

Applying the boundary conditions of continuous tangential field components for the portion of S_1 that is originally the interface of materials, i.e., $S_{1i}\,(i=1,2,3,\ldots n)$ in R_1, electric field integral equation (EFIE) and magnetic field integral equation (MFIE) can be established as,

$$\hat{n}_{1i}\times\left(\vec{E}_1^{\,\mathrm{sca}}+\vec{E}_1^{\,\mathrm{inc}}\right)=-\vec{M}_1\,, \tag{3}$$

$$\hat{n}_{1i}\times\left(\vec{H}_1^{\,\mathrm{sca}}+\vec{H}_1^{\,\mathrm{inc}}\right)=\bar{J}_1\,, \tag{4}$$

where

$$\vec{E}_1^{\,\mathrm{sca}}=ik_1\eta_1\bar{\bar{L}}_1\cdot\bar{J}_1-\bar{\bar{K}}_1\cdot\vec{M}_1+ik_1\eta_1\bar{\bar{L}}_1\cdot\bar{J}_{V1}\,,$$
$$\vec{H}_1^{\,\mathrm{sca}}=\bar{\bar{K}}_1\cdot\bar{J}_1+ik_1\eta_1^{-1}\bar{\bar{L}}_1\cdot\vec{M}_1+\bar{\bar{K}}_1\cdot\bar{J}_{V1}\,.$$

The unit vector $\hat{n}_{1i}$ in equations (3) and (4) is the normal direction on surface S_{1i} that points in to R_1, and $\vec{E}_1^{\,\mathrm{inc}}$ is the primary field generated by sources in R_1 ($\vec{E}_1^{\,\mathrm{inc}}$ is calculated assuming that the sources in R_1 radiate into an unbounded homogeneous space of k_1). The EFIE on the PEC surface S_{p1}, is established using the vanishing tangential field boundary condition as

$$\hat{n}_{p1}\times\left(\vec{E}_1^{\,\mathrm{sca}}+\vec{E}_1^{\,\mathrm{inc}}\right)=0\,, \tag{5}$$

where $\hat{n}_{p1}$ is the normal direction of S_{p1} directed outward of the conductor.

In the volume material portion, the total electric field is the superposition of the incident and the scattered field. Based on this fact, VIE in domain R_1 is constructed as

$$\vec{E}_1^{\,\mathrm{sca}}-\vec{E}_1^{\,\mathrm{tot}}=-\vec{E}_1^{\,\mathrm{inc}}\,. \tag{6}$$

The volume electric current $\bar{J}_{V1}$ in equation (6) is related to the total electric field intensity by $\bar{J}_{V1}=i\omega(\varepsilon-\varepsilon_1)\vec{E}_1^{\,\mathrm{tot}}$, with ε being the position dependent permittivity for the material body embedded in V_1, and $\vec{E}_1^{\,\mathrm{tot}}=\vec{E}_1^{\,\mathrm{sca}}+\vec{E}_1^{\,\mathrm{inc}}$ is the total electric field within V_1. Thus, we have established a set of four integral equations, (3) to (6), for domain R_1. Moreover, if the conducting surface S_{p1} is a closed surface, the MFIE (magnetic field integral equation) or CFIE (combined field integral equation) can be used to replace equation (5). It should be pointed out that equation (5) will not appear for R_1 if S_1 does not contain any PEC surfaces, and equation (6) will not appear for R_1 if there are no embedded dielectric volumes in R_1.

Similarly, the equivalent problem of R_2 can be established as shown in Fig. 3.

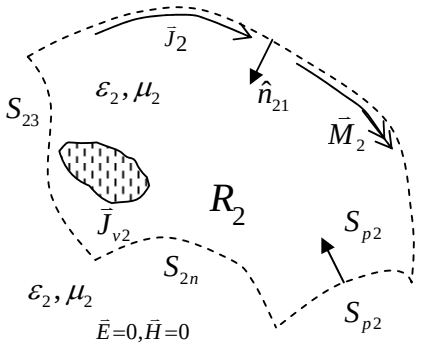

Fig. 3. Equivalent problem of domain R_2 for which the whole space (both interior and exterior to S_2) is filled with the same material of ε_2,μ_2.

The surface integral equations on the material surface S_2 (or $\cup S_{2i}$) are also based on the boundary conditions of tangential E and H fields, i.e.,

$$\hat{n}_{2i}\times\left(\vec{E}_2^{\,\mathrm{sca}}+\vec{E}_2^{\,\mathrm{inc}}\right)=-\vec{M}_2\,, \tag{7}$$

$$\hat{n}_{2i}\times\left(\vec{H}_2^{\,\mathrm{sca}}+\vec{H}_2^{\,\mathrm{inc}}\right)=\bar{J}_2\,, \tag{8}$$

where

$$\vec{E}_2^{\,\mathrm{sca}}=ik_2\eta_2\bar{\bar{L}}_2\cdot\bar{J}_2-\bar{\bar{K}}_2\cdot\vec{M}_2+ik_2\eta_2\bar{\bar{L}}_2\cdot\bar{J}_{V2}\,,$$
$$\vec{H}_2^{\,\mathrm{sca}}=\bar{\bar{K}}_2\cdot\bar{J}_2+ik_2\eta_2^{-1}\bar{\bar{L}}_2\cdot\vec{M}_2+\bar{\bar{K}}_2\cdot\bar{J}_{V2}\,.$$

The volume integral equation for V_2 is constructed in the same way as in equation (5). It is given by

$$\vec{E}_2^{\,\mathrm{sca}}-\vec{E}_2^{\,\mathrm{tot}}=-\vec{E}_2^{\,\mathrm{inc}}\,. \tag{9}$$

As stated previously, the vector $\vec{E}_2^{\,\mathrm{tot}}$ is related to the volume current by $\bar{J}_{V2}=i\omega(\varepsilon-\varepsilon_2)\vec{E}_2^{\,\mathrm{tot}}$.

Now we have established a set of three integral equations for domain R_2 (if there are PEC bodies within R_2, there would be one more surface integral equation for the PEC surfaces). This process can be repeated for all the remaining domains, $R_3,R_4,\cdots,R_n$. It is expected that for each domain, a set of two to four integral equations are established depending on whether PEC surfaces and embedded dielectric material exist in that domain. We have an overall of n sets of integral equations. It is observed that there are redundant unknown vectors assigned in the integral

equations. The redundancy is removed by using the fact that $\vec{J}$ and $\vec{M}$ on the two sides of any material interface are equal in magnitude and opposite in direction. For example, on interface S_{12} shared by domains R_1 and R_2, we have,

$$\hat{n}_{12} = -\hat{n}_{21},\ \vec{J}_1 = -\vec{J}_2 \text{ and } \vec{M}_1 = -\vec{M}_2 . \qquad (10)$$

In this way, we have only two unknown functions on each interface that is shared by two material domains. By utilizing the above relationships for $\vec{r} \in S_{12}$, we can add equations (7) to (3), and equations (8) to (4), to reduce the number of equations from four to two (this approach was proposed in a paper by Wu and Tsai [4] based on the earlier work of Poggio, Miller, Chang, Harrington, Wu, and Tsai, and hence the formulation is called PMCHWT). In this paper, the SIE applied to dielectric material surfaces refers to this PMCHWT formulation. It shall be noted that there are other ways to combine the integral equations leading to different SIE formulations.

B. Discretization of the Integral Equations

When all the integral equations are established, we apply the method of moments (MoM) to descritize the integral equations into a set of N linear algebra equations. Once again, the integral equations formulated for each domain are discretized before they are combined with those of the other domains to remove redundancy. To this end, the surfaces are modeled by a set of electrically small and nearly flat quadrangles, and the volumes are modeled by a set of electrically small hexahedron elements whose six faces are also nearly flat quadrangles. Basic requirements on the mesh are,

(a) All quadrangles are well connected (two quadrangles can share no more than two nodes, and if they share two nodes, then they must share an edge).

(b) All hexahedrons are well connected (two hexahedrons can share no more than four nodes, and if they share four nodes, then they must share a common face).

(c) All quadrangles and hexahedrons are also well connected. If the number of shared nodes between a quadrangle and a hexahedron is n, then (a) n must be 0,1,2,4 only; (b) if n = 2, they must share a common edge; (c) if n = 4, the quadrangle must overlap with a face of the hexahedron.

(d) All mesh nodes must be vertices of quadrangles and/or hexahedrons (no mesh nodes are allowed inside a mesh element or interior to the boundary of it.

Then surface roof-top basis functions are used to expand the surface vectors ($\vec{J}$ and $\vec{M}$), and the volume roof-top basis functions are used to expand the volume vector $\vec{J}_V$. A volume roof-top basis function is defined on two neighboring hexahedrons that share a common face (if a face of a hexahedron is not shared, a volume basis function is also assigned to this face [12], and this basis function is called a half basis). A surface roof-top basis function is defined on two or more neighbor quadrangles that share a common edge. If an edge is shared by more than two quadrangles, it is a junction edge [5] (no half basis is defined for surface mesh). There are several types of junctions that must be treated differently. Here we consider two simple types of junctions: (1) all quadrangles that share a common edge are material interfaces. In this case, one basis function is assigned to the junction; (2) Multiple material quadrangles are connected to an edge shared by two PEC quadrangles that on a PEC body of non-zero thickness. In this case, one basis function is assigned to the junction. Both the surface and volume basis functions can be written in the following form [18],

$$\vec{f}_i^{\,\Omega}(\vec{r}) = \frac{\pm 1}{\sqrt{g}} u \frac{\partial \vec{r}}{\partial u}, \quad \vec{r} \in \Omega, \quad \Omega = S_i \text{ or } V_i , \qquad (11)$$

where S_i (or V_i) is a surface (or volume) mesh element, $\sqrt{g}$ is the Jacobian of the transformation that maps a mesh element in (x,y,z) coordinate system into a unit element in the (u,v,w) coordinate system. In the (u,v,w) space, a unit quadrangle is a square defined by $0 \le u \le 1,$, $0 \le v \le 1,$ and $w = 0$, and a unit hexahedron is a cube defined by $0 \le u \le 1,$ $0 \le v \le 1,$ and $0 \le w \le 1$. More details on the discretization can be found in [12,18]. After discretization, we get a set of n matrix equations, one set for each domain, as follows,

$$\bar{\bar{A}}_i \cdot \bar{x}_i = \bar{b}_i , \quad i = 1,2,\cdots,n , \qquad (12)$$

where, $\bar{\bar{A}}_i$ is the impedance matrix of size $N_i \times N_i$ for the integral operators, $\bar{x}_i$ is a vector of length N_i whose components are the expansion coefficients for the unknown vectors, and $\bar{b}_i$ is the excitation vector of length N_i that is determined by the sources, all associated with domain R_i (if R_i does not contain any source, then $\bar{b}_i = 0$). If the matrix equations are to be solved by a direct solver, then the matrices $\bar{\bar{A}}_i$, $i = 1,2,\cdots,n$, must be combined to form the system matrix $\bar{\bar{A}}$ of dimension $N \times N$ using the relationships in equation (10), where N is the total number of independent unknowns. It shall be noted that N is not a simple summation of N_i , for $i = 1,2,\cdots,n$. In general, $N \le \sum_i N_i$. If fast solvers are utilized to speed-up the solution, the linear equations are not combined until the matrix-vector product for each domain, $\bar{\bar{A}}_i \cdot \bar{x}_i$, is completed. This is discussed in the next sub-section.

C. Solution using Multilevel Fast Multipole Algorithm

For many realistic scattering problems, the electrical size of certain or all domains can be very large, and direct solvers may not be feasible. In this case, fast iterative solvers are needed to reduce the computational complexity as well as memory requirement. In general, different fast solvers can be applied to different domains depending on the size and the shape of the domains. In this paper, we apply the multilevel fast multipole algorithm (MLFMA) for all domains that is electrically large. MLFMA has been discussed in detail in many publications such as [19, 20], we focus on the implementation for multi-region problems here. To this end, we first identify the regions for which fast solvers will be applied. This is done by calculating the maximum electrical dimension D_i / λ_i of each domain R_i. If $D_i / \lambda_i \geq 1.0$, then fast solver is applied for this region (this criteria depends on the implementation). For the rest domains that do not need the fast solvers, as well as the near-neighbor interaction of any fast-solver domain, the matrices are combined and stored into one sparse matrix $\bar{\bar{A}}_0$ and direct method is applied to perform $\bar{\bar{A}}_0 \cdot \bar{x}$. For a domain R_i that MLFMA is applied, then $\bar{\bar{A}}_i \cdot \bar{x}_i$ will be performed in the same way as in a single domain problem, and $N_i \log N_i$ floating point operations are needed. The overall operation count per iteration is then made of two parts, one part is $T_1 = O(N_0)$ (N_0 is the number of non-zero entries in $\bar{\bar{A}}_0$), and the other part is

$$T_2 = \sum_i C_i N_i \log N_i \tag{13}$$

where i runs over all the domains to which MLFMA are applied, and C_i is a constant determined by the MLFMA implementation.

As a summary, the procedure to perform a matrix-vector product $\bar{y} = \bar{\bar{A}} \cdot \bar{x}$ include the following steps:

(a) For a given trial vector $\bar{x}$ in any iteration, formulate $\bar{x}_i$ (using (10) for domain R_i to which MLFMA is applied).

(b) Perform $\bar{y}_i = \bar{\bar{A}}_i \cdot \bar{x}_i$ using MLFMA in R_i.

(c) Repeat steps (a) and (b) for all domains in which MLFMA are applied.

(d) Formation of $\bar{y}' = \bigcup_i \{\bar{y}_i\}$. The union operation uses the rule of equation (10).

(e) $\bar{y} = \bar{\bar{A}}_0 \cdot \bar{x} + \bar{y}'$.

Using the above processes, a test program is written for the case of $n=2$ and numerical results are generated and shown in the next section to validate the method and to demonstrate the applications.

III. NUMERICAL RESULTS

This section provides numerical examples using the program developed for the "SIE+VIE" method. The examples are designed to consider several typical application configurations that include,

(1) Spherical structure that can use Mie series to verify the results (example 1).

(2) A large homogeneous material with small and thin materials embedding (examples 1 and 3).

(3) Small or thin materials are outside a large homogeneous material region (example 4).

(4) Structures with flat faces and edges (example 3).

(5) Structures with curved faces and edges (examples 1, 2, and 4).

(6) Structures with bulk material for which VIE is inefficient (example 2).

For example 1, we use the exact solution as a comparison. For the rest of the examples, two approaches, "SIE+VIE", and "VIE ONLY", are applied to solve the problems and results are compared to each other. In both approaches, CFIE is used for the closed PEC surfaces. The difference of the two approaches lies in the treatment of the material regions. In the "SIE+VIE" approach that is introduced in this paper, part of the material regions (normally small or thin regions) are modeled by VIE, and the large and thick material regions are modeled by SIE. The results from this approach are labeled as "SIE+VIE" in the figures. It should be noted that the VIE modeled material can be inside (embedded in) or outside the SIE material surfaces. The second approach uses VIE to model all materials, and the results are labeled as "VIE ONLY" (The terms of "VIE ONLY", "VIE+SIE", and "SIE ONLY", are introduced to mark the results and they refer to the ways materials are handled. In all cases, the surface integral equation is applied to PEC surfaces, including "VIE ONLY" approach). The "VIE ONLY" modeling is used as a way of validating the numerical results of "SIE+VIE" approach. Hence the examples are designed so that both approaches can be applied. Because of this, the run time parameters are provided for reference only. They shall not be used to determine which approach is more efficient for certain examples. All calculations are performed on a HP Superdome computer with 1.5 GHz processor and 2GB of memory.

The first example is a layered spherical structure. It consists of a PEC core (radius 0.45 m) covered by two layers of dielectric materials. The inner layer has thickness 0.05 m with relative permittivity $\varepsilon_{r2} = 4.0$; The outer layer has thickness 0.3 m with $\varepsilon_{r1} = 2.0 + 0.1i$. In the "SIE+VIE" approach, the inner layer of the coating is considered as embedded within a shell of inner radius 0.45 m, and outer radius of 0.8 m. The PEC surface and the outermost spherical surface are modeled by a total of 5,592 quadrangles (1,536 for PEC surface, and 4,056 for the outermost spherical surface). The embedded material shell of thickness 0.05

m is modeled by 1,536 hexahedron element (VIE mesh). The total number of independent unknowns for the hybrid formulation of "SIE+VIE" is N = 25,440, and the memory used is M = 469 MB. Computed bi-static RCSs for $\theta^i=0^\circ$ incidence at 300MHz are plotted in Fig. 4. The exact solutions from Mie series are also plotted for comparison. If we use the RMS error defined as

$$\text{RMS ERROR} = \sqrt{\frac{1}{n}\sum_{i=0}^{n}(\sigma_i-\sigma_i^{\text{ref}})^2}$$

to measure the difference of our solution σ_i and reference solution σ_i^{ref}, for i=1,2,...,n=181 (angles), the errors are 0.5dB for V-V, and 0.23dB for H-H polarizations, respectively.

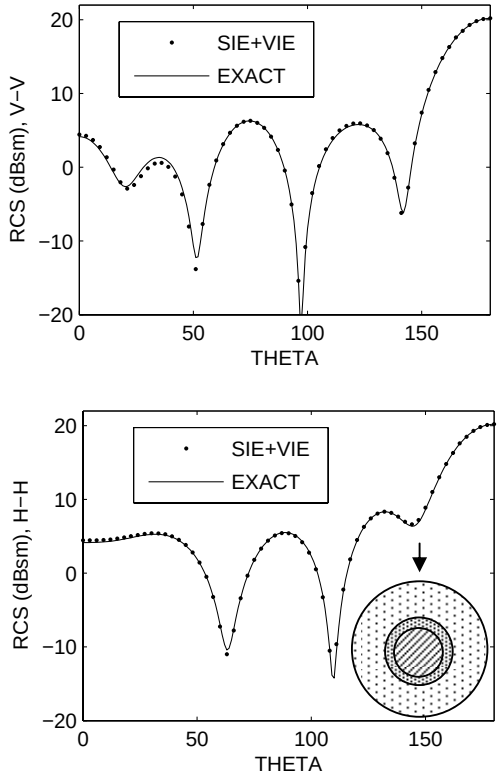

Fig. 4. Bi-static RCSs of a layered spherical scatterer for two polarizations: V-V (left) and H-H (right). The incident angle is $\theta^i=0^\circ$.

The second example is taken from [8]. It is made of two sections of circular cylinders, one PEC and one dielectric. The side view of the structure as well as the dimension parameters are shown in Fig. 5. The relative permittivity of the dielectric is 2.6, and the incident plane wave frequency is 3.0 GHz.

For the "SIE+VIE" modeling, SIE is applied to the material surface (no part of material is modeled with VIE for this example). The number of unknowns is N=6,672, CPU time is T = 35.8 s per incident angle, and total memory used is M = 113 MB. For "VIE ONLY" modeling, the run time parameters are N=17,280, T=92.05s, and M = 1,171 MB. It is seen that the "SIE+VIE" approach uses almost three times less number of unknowns compared to the "VIE ONLY" approach. The latter also uses more CPU time per incident angle (this is an example for which "VIE ONLY" approach is not efficient to apply). The computed mono-static RCSs by both approaches are shown in Fig. 6, from which, we can see good agreement between the two results.

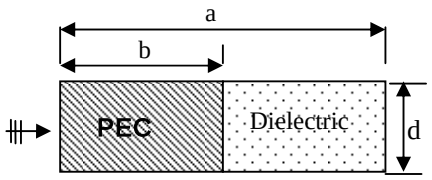

Fig. 5. The side view of a composite PEC and dielectric cylindrical scatterer of circular cross section (a = 15.24 cm, b = 10.16 cm, d = 7.62 cm). The incident $\theta^i=0$ is on PEC side of the axis (shown by the arrow in the figure).

The next example is a composite triangular plate that is made by two material regions and a PEC surface, as shown in Fig. 7. Material-2 (with permittivity ε_2) is considered as embedded within material-1 (with permittivity ε_1). For "SIE+VIE" modeling, N=17,959, CPU time is T = 76.7 per incident angle, total memory is 355 MB, and average iteration number per angle is $\bar{N}_{\text{itr}}$ = 41.9 (it equals the total iteration number for all incident angles divided by number of incident angles). For "VIE ONLY" modeling, the runtime parameters are N = 24,219, T = 8.6s, M = 427 MB, and $\bar{N}_{\text{itr}}$ =5.66. The numbers of iterations explain why the CPU time for the "SIE+VIE" approach is more than that of "VIE ONLY" approach. Because the overall thickness of the structure is thin ($0.4\lambda_0$), the "VIE ONLY" approach is more efficient to apply for this example. The two results are given in Fig. 8 and they agree well to each other.

In the last example, we consider a composite cylinder of finite length as shown in Fig. 9. The cross section of this cylinder is an ogive, and the two edges (parallel to z-axis) are coated by materials of $\varepsilon_{r1}=\varepsilon_{r2}=2.5+0.5i$. The width of the coating with ε_1 (in the +x side) is 0.236m, and that with ε_2 (in –x side) is 0.115m. For "SIE+VIE" modeling, N = 16,052, T = 110 s, and M = 196 MB. For "VIE ONLY" modeling, the runtime parameters are N = 19,446, T = 43.7 s, and M = 172.8 MB. The calculated RCSs at 1.0 GHz incidence are shown in Fig. 10.

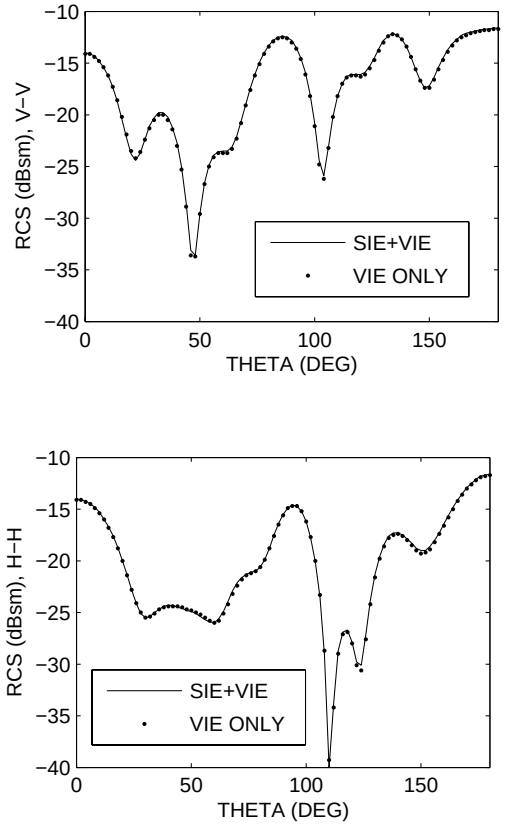

Fig. 6. Mono-static RCSs of a composite cylindrical scatterer for V-V polarization (left) and H-H polarization (the description of the cylinder is in Fig. 5).

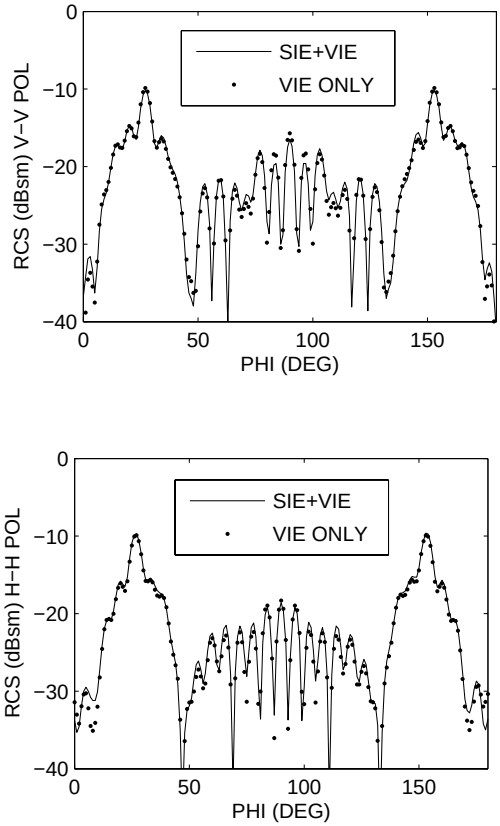

Fig. 8. The mono-static RCSs of the composite plate of Fig. 7. The incident wave frequency is 3.0 GHz, and the results are for the $\theta^i = 90^\circ$ plane.

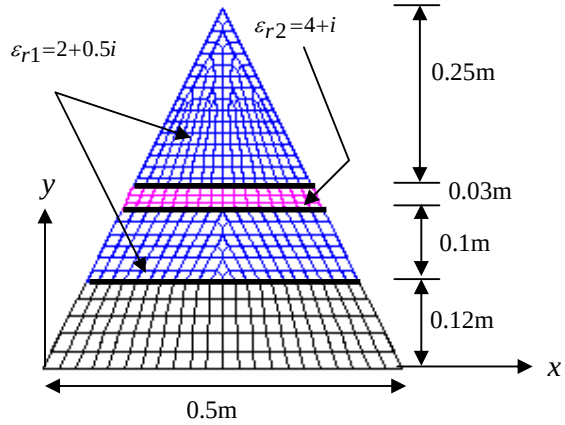

Fig. 7. The top view of a composite triangular plate that is made by 3 parts, a conducting part (bottom), and two dielectric regions. The middle dielectric (with ε_{r2}) is considered as embedded within the material of ε_{r1}. The thickness of the plate is 0.04 m.

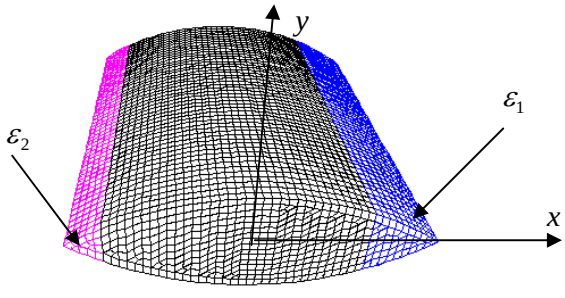

Fig. 9. A composite finite-length cylinder of ogive cross section is made of two dielectric materials and a PEC body. The sizes in x, y, and z-directions are 1.4 m, 0.36 m, and 1.44 m, respectively.

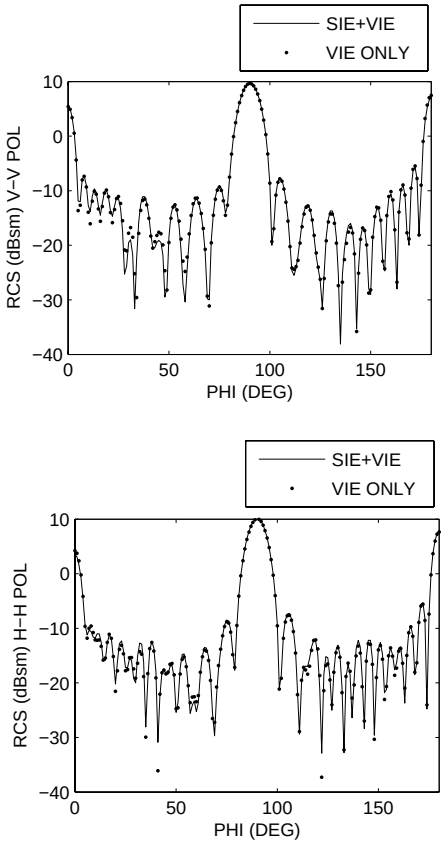

Fig. 10. The calculated RCSs for the ogive cylinder of Fig. 9 for V-V polarization (left) and H-H polarizations (right).

IV. CONCLUSIONS

In this work, we implemented a hybrid "SIE+VIE" formulation for computing the scattering by composite scattereres that made of larger conducting and dielectric materials. This formulation takes the advantage of SIE for large homogeneous material regions, and that of VIE for small and thin material regions. It is applicable to scattering problems with multiple material regions of different sizes and shapes. When a material region is electrically large, the MLFMA is applied to accelerate the matrix-vector multiplication in the iterative solution process. Numerical examples are presented that verified the solution accuracy of the hybrid formulation, and demonstrated its ability in solving large and complex scattering problems. This work applied one type of fast solver only (the MLFMA) which is not the best choice for all domains or for all problem configurations. In fact, based on domain shape and size, it is possible to use different types of fast solvers for different domains to achieve optimum performance. This remains to be a future implementation.

REFERENCES

[1] K. Umashankar, A. Taflove, and S. M. Rao, "Electromagnetic scattering by arbitrary shaped three-dimensional homogeneous lossy dielectric objects," *IEEE Trans. Antennas Propagat*., vol.34, no. 6, pp. 758-766, June 1986.

[2] R. F. Harrington, "boundary integral formulations for homogeneous material bodies," *J. Electromag. Waves Appl*., vol. 3, no. 1, pp. 1-15, 1989.

[3] S. M. Rao, D. R. Wilton, and A. W. Glisson, "Electromagnetic scattering by surfaces of arbitrary shape," *IEEE Trans. Antennas Propagat*., vol. 30, no. 3, pp. 409-418, May 1982.

[4] T. K. Wu and L. L. Tsai, "Scattering from arbitrarily-shape lossy dielectric bodies of revolution," *Radio Sci*., vol. 12, no.5, pp. 709-718, 1977.

[5] P. Yla-Oijala, M. Taskinen, and J. Sarvas, "Surface integral equation for general composite metallic and dielectric structures with junctions," *Progress In Electromagnetics Research*, PIER-52, pp. 81-108, 2005.

[6] E. Arvas, A. Rahhal-Arabo, A. Sadigh, and S. M. Rao, "Scattering from multiple conducting and dielectric bodies of arbitrary shape," *IEEE Trans. Antennas and Propagat*., vol. 33, no. 2, pp. 29-36, April 1991.

[7] P. L. Huddleston, N. Medgyesi-Mitschang, and J. M. Putnam, "Combined field integral equation formulation for scattering by dielectrically coated conducting bodies," *IEEE Trans. on Antennas and Propagat*., vol. 34, no. 4, pp. 510-520, April 1986.

[8] L. N. Medgyesi-Mitschang and J. M. Putnam, "Electromagnetic Scattering from Axially Inhomogeneous Bodies of Revolution," *IEEE Trans. Antennas Propagat*., vol. 32, no. 8, pp. 797-806, Aug. 1984.

[9] K. Donepudi, J. M. Jin, and W. C. Chew, "A higher order multilevel fast multiple algorithm for scattering from mixed conducting/dielectric bodies," *IEEE Trans. Antennas and Propagat*., vol. 51, no. 10, pp. 2814-2821, Oct. 2003.

[10] S. M. Rao and D. R. Wilton, "E-field, H-field, and combined field solution for arbitrarily shaped three-dimensional dielectric bodies," *Electromagnetics*, vol. 10, pp. 407-421, 1990.

[11] J. P. Kottmann and O. J. Martin, "Accurate solution of volume integral equation for high-permittivity scatterers," *IEEE Trans. on Antennas and Propagat*., vol. 48, no. 11, pp. 1719-1726, Nov. 2000.

[12] C. C. Lu and W. C. Chew, "A coupled surface-volume integral equation approach for the calculation of electromagnetic scattering from composite metallic and material targets," *IEEE Trans. Antennas Propagat*., vol. 48, no. 12, pp. 1866-1868, Dec. 2000.

[13] D. E. Livesay and K. M. Chen, "Electromagnetic fields induced inside arbitrary shaped biological

bodies," *IEEE Trans. Micro. Theory Tech.*, vol. 22, no. 12, pp. 1273-1280, Dec. 1974.

[14] D. H. Schaubert, D. R. Wilton, and A. W. Glisson, "A tetrahedral modeling method for electromagnetic scattering by arbitrary shaped inhomogeneous dielectric bodies," *IEEE Trans. Antennas Propagat.*, vol. 32, no. 1, pp. 77-85, Jan. 1984.

[15] S. Gedney and C. C. Lu**,** "High-order solution for the electromagnetic scattering by inhomogeneous dielectric bodies," *Radio Sci.*, vol. 38, no. 1, pp. 15-1 to 15-8, 2003.

[16] C. Yu and C. C. Lu, "Analysis of Finite and Curved Frequency Selective Surfaces Using the Hybrid Volume-Surface Integral Equation Approach," *Micro. Opt. Tech. Lett*., vol. 45, no. 2, pp. 107-112, April 2005.

[17] M. I. Sancer, K. Sertel, J. L. Volakis, and P. V. Alstine, "On volume integral equations", *IEEE Trans. Antennas Propagat.*, vol. 54, no. 5, pp. 1488-1495, May. 2006.

[18] C. C. Lu and C. Luo, "Comparison of iteration convergences of SIE and VSIE for solving electromagnetic scattering problems for coated objects", *Radio Sci.*, vol. 38, no. 2, pp. 11-1 to 11-9, 2003.

[19] R. Coifman, V. Rokhlin, and S. Wandzura, "The Fast Multipole Method for the Wave Equation: A Pedestrian Prescription," *IEEE Antennas and Propagat. Magazine*, vol. 35, no. 3, June 1993.

[20] J. M. Song and W. C. Chew, "Multlevel Fast-Multipole Algorithm for Solving Combined Field Integral Equations of Electromagnetic Scattering," *Microwave Opt. Tech. Lett.*, vol. 10, no. 1, Sep.1995.

Cai-Cheng Lu received the Ph.D. degree from University of Illinois at Urbana Champaign in 1995. He is now an associate professor in the Department of Electrical and Computer Engineering at the University of Kentucky. Priori to join University of Kentucky, He was with Science Application International, Inc., where he worked on a number of new features for the XPATCH code. His research interests are in wave scattering, microwave circuit simulation, and antenna modeling. He is especially experienced in fast algorithms for computational electromagnetics and is one of the authors for a CEM code FISC. He is a recipient of the 2000 Yong Investigator Award from the Office of Naval Research, and a CAREER Award from the National Science Foundation. Dr. Lu is a senior member of IEEE.

Chong Luo was born in Sichuan, China, in 1972. He received B.S. degree, in Electrical Engineering from Beijing University of Aeronautics and Astronautics, Beijing, China, in 1994, the M.S. and Ph.D. degrees in Electrical Engineering from University of Kentucky, Lexington, in May 2002 and December 2006. He is currently with the Electrical Engineering Department, University of Kentucky. His primary research interest is in computational electromagnetics. Dr. Luo is a member of IEEE.

Accurate Computational Algorithm for Calculation of Input Impedance of Antennas of Arbitrarily Shaped Conducting Surfaces

Khalid F. A. Hussein

Microwave Eng. Dept., Electronics Research Inst., Dokki, Cairo, Egypt

Abstract **–** In the present work, a Galerkin's electric field integral equation (EFIE) solution is applied to get the current flowing on a conducting surface of arbitrary shape when excited by a gap generator as well as when illuminated by an incident plane wave. The main objective of this work is to get a fast, accurate and efficient computer algorithm that optimizes the use of computer resources and reduces the computational time and to accurately evaluate the input impedance of conducting surface antennas. The singular integrals arising in such a Galerkin's formulation are accurately evaluated and obtained as analytic expressions. An efficient method is described for accurate evaluation of the input impedance for antennas of arbitrarily-shaped conducting surface. The efficiency of the applied Galerkin's algorithm is examined by calculating the input impedance of well known antennas of conducting surfaces such as the strip-dipole, bow-tie and planar equiangular spiral antennas. To investigate the accuracy of the applied technique the results concerning these antennas are presented and compared with some published results.

I. INTRODUCTION

Among the electromagnetic techniques used for treating the problems of scattering, antennas and discontinuities in waveguides, the integral equation is one of the most widely used techniques. In electromagnetic integral equation methods, the original boundary value problems for Maxwell equations are reformulated as integral equations over the boundary interfaces of homogeneous domains. If the object is inhomogeneous, integral equation over the entire volume of the object has to be considered.

One of the most powerful techniques used in the electromagnetic modeling of conducting bodies is based on the EFIE formulation of the Maxwell equations [1 - 7]. The EFIE solution for scattering from conducting surfaces of arbitrary shape was developed by Rao, Wilton and Glisson (RWG) in [8]. In the same paper, triangular basis functions, commonly known as RWG basis functions, were introduced for current expansion on the conducting surface. Since that time, this formulation of EFIE together with the triangular-patch surface modeling have become one of the most widely used techniques for solving electromagnetic scattering and radiation problems.

A point-matching method of moments (MoM) solution was applied in [8] to get the current on an arbitrary surface. This technique ensures the satisfaction of the boundary conditions (that yield the vanishing of the tangential electric field on the conducting surface) at the centroids of the triangular patches forming the conducting surface. However, residual errors remain at the other points of the surface.

In [9] and [10], the problems that arise when a Galerkin technique is applied for the formulation and solution of the EFIE for conducting surfaces are treated. Their main purpose was to evaluate accurately the singular integrals arising in such a Galerkin formulation rather than the description of a computational algorithm for the application of Galerkin's technique on an arbitrarily shaped conducting surface.

In the present work, the Galerkin solution is applied to the EFIE to get the current flowing on the conducting body surface in a way to get a complete description of a fast, accurate and efficient algorithm that optimizes the use of computer resources and reduces the computational time.

The singular integrals encountered when Galerkin's formulation is used are classified and evaluated analytically. The integrals involved are carried out on planar triangular patches and, hence, they can be evaluated by first transforming from the 3D Cartesian coordinates to the so-called simplex coordinates. The analytic expressions for the singular integrals provided in [11] are used here to accurately evaluate the singular integrals.

Three types of singular integrals appear in Galerkin's formulation. The first type results when the source and observation triangular patches are the same. The second type results when the two patches share a

common edge. The third type of such singular integrals results when the source and observation patches share a common vertex. These singular integrals are reduced to a standard form, which is evaluated analytically by the expressions provided in [11].

An efficient method is described for accurate evaluation of the input impedance for antennas of arbitrarily-shaped conducting surface. The efficiency of the applied Galerkin's algorithm is examined by calculating the input impedance of well known antennas of conducting surfaces such as the strip-dipole, bow-tie and planar equiangular spiral antennas. To investigate the accuracy of the applied technique the results concerning these antennas are presented and compared with some published results.

It may be worth noting that the characteristics of a conical equiangular spiral antenna were investigated in [12] using the EFIE. However, the work of [12] employs a point matching technique and not a Galerkin's one, which arrives at different singular integrals. The method presented here (section 5) for evaluating the input impedance was not included in [12]. Furthermore, the present work uses a method of calculating the singular integrals, which is more accurate than that used in [12].

II. FORMULATION OF GALERKIN'S EFIE

It is required to deduce the current flowing on a conducting surface due to an exciting source, which may be an incident wave or a generator attached to the conducting surface. The formulation of the EFIE that is to be solved for the current distribution on the conducting surface requires, first, modeling the scatterer or antenna surface by triangular patches. Then, the linear density of the current on the surface is expanded using the appropriate basis functions with unknown amplitudes. A Galerkin's testing procedure is then applied to get the unknown amplitudes.

A. Modeling the Surface of the Scatterer

As shown in Fig. 1-a, the surface is divided into a number of triangular patches. Each patch has three edges; an edge which belongs to only one triangular patch is called a *boundary edge*. Such an edge exists only on the rim of an open surface and hence, it has no electric current component flowing normal to it. As shown in Fig. 1-b, an edge which belongs to two adjacent triangular patches is called a *non-boundary edge*. Only non-boundary edges can have electric current components flowing normal to them.

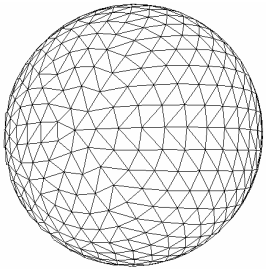

(a) Triangular-patch Model.

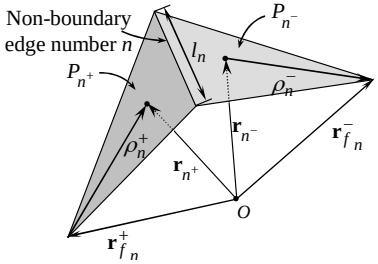

(b) Two triangular patches sharing an edge.

Fig. 1. Triangular-patch model for surfaces of arbitrarily-shaped scatterers and antennas.

Let the number of the triangular patches constituting the surface model be Q and the number of the non-boundary edges be N. Let P_q denote the triangular patch whose index (number) is q; q = 0,1,2,……Q-1. Two adjacent triangular patches P_{n^+} and P_{n^-} sharing the edge number n are shown in Fig. 1-b, where n^+ and n^- are, respectively, the patch indices. It should be noted that both the values of n^+ and n^- have no relation to the value of n. This notation is used only to indicate that the triangular patches whose indices are $q=n^+$ and $q=n^-$ are adjacent patches and share the edge number n, with a plus or minus designation determined by the choice of a positive current reference direction for the shared edge number n. This direction is assumed to be from P_{n^+} to P_{n^-}. That is, n^+ is the number of the patch of which the current component associating the edge number n is assumed to be flowing out, whereas n^- is the number of the patch into which this current is flowing. This means that n^+=1,2,3,…..,Q and n^-=1,2,3,…,Q whereas n=1,2,3,…..,N. A point in P_{n^+} can be specified by the position vector $\mathbf{r}_{n^+}$ defined with respect to the origin O, or by the position vector $\boldsymbol{\rho}_n^+$ defined with respect to the free vertex, $\mathbf{r}_{f\,n}^+$, of the triangular facet P_{n^+} (*i.e.* the vertex of P_{n^+} which does not belong to P_{n^-}). Similarly,

a point in P_{n^-} can be specified by $\mathbf{r}_{n^-}$ or $\boldsymbol{\rho}_n^-$. It should be noticed that the position vector $\boldsymbol{\rho}_n^+$ is directed from the free vertex, $\mathbf{r}_{f\,n}^+$, of P_{n^+} toward the point in the patch whereas the position vector $\boldsymbol{\rho}_n^-$ is directed from the point to the free vertex, $\mathbf{r}_{f\,n}^-$, of P_{n^-}. Thus one can write,

$$\boldsymbol{\rho}_n^{\pm} = \pm\,(\mathbf{r}_{n^{\pm}} - \mathbf{r}_{f\,n}^{\pm})\,. \tag{1}$$

B. Representation of the Current on the Scatterer

The current flowing on the conducting surface is expressed as a summation of vector basis functions with unknown amplitudes. The most suitable basis function for describing the current flowing on the triangular patches used for modeling the conducting surface is the Rao-Wilton-Glisson basis function given in [8]. For each non-boundary edge, a vector basis function is defined as follows,

$$\mathbf{f}_n(\mathbf{r}) = \begin{cases} \dfrac{l_n}{2S_{n^+}}\boldsymbol{\rho}_n^+, & \mathbf{r}\in P_{n^+} \\ \dfrac{l_n}{2S_{n^-}}\boldsymbol{\rho}_n^-, & \mathbf{r}\in P_{n^-} \\ 0, & \text{otherwise} \end{cases} \tag{2}$$

where l_n is the length of the non-boundary edge number n, S_{n^+} and S_{n^-} are the areas of the triangular patches P_{n^+} and P_{n^-}, respectively. It can be shown that the normal component of $f_n(r)$ at the n^{th} edge is unity [8]. Using the basis function $f_n(r)$, the linear current density on the conducting surface can be expressed as,

$$\mathbf{J} = \sum_{n=1}^{N} I_n \mathbf{f}_n(\mathbf{r}) \tag{3}$$

where I_n; n = 1,2,3…N are unknown amplitudes of the basis functions and to be determined by the following procedure.

C. Application of the Galerkin's Testing Procedure

The electric field radiated by a surface charge density σ and linear current density **J** flowing on a conducting surface, S, can be obtained by the following expression,

$$\mathbf{E}^s(\mathbf{r}) = -\,j\omega\mathbf{A}(\mathbf{r}) - \nabla\Phi(\mathbf{r}) \tag{4}$$

where $\mathbf{A}(\mathbf{r})$ is the vector magnetic potential defined as,

$$\mathbf{A}(\mathbf{r}) = \frac{\mu}{4\pi}\int_{S'} \mathbf{J}\,\frac{e^{-jk|\mathbf{r}-\mathbf{r}'|}}{|\mathbf{r}-\mathbf{r}'|}\,dS'\,, \tag{5}$$

and $\Phi(\mathbf{r})$ is the scalar electric potential defined as,

$$\Phi(\mathbf{r}) = \frac{1}{4\pi\varepsilon}\int_{S'} \sigma\,\frac{e^{-jk|\mathbf{r}-\mathbf{r}'|}}{|\mathbf{r}-\mathbf{r}'|}\,dS' \tag{6}$$

where $\mathbf{r}'$ is a point on S and $\mathbf{r}$ is a point in the near or far zone of free space. The surface charge density σ is related to the surface divergence of the current **J** flowing on S through the equation of continuity,

$$\nabla_s \cdot \mathbf{J} = -\,j\omega\sigma\,. \tag{7}$$

On the conducting surface, the tangential electric field must vanish yielding the following equation,

$$-\,\mathbf{E}_{tan}^i(\mathbf{r}) = -\,j\omega\mathbf{A}_{tan}(\mathbf{r}) - \nabla_s\Phi(\mathbf{r})\,. \tag{8}$$

Define the product

$$\langle \mathbf{a},\mathbf{b}\rangle = \int_S \mathbf{a}\cdot\mathbf{b}\;dS\,. \tag{9}$$

This product can be applied to (8) to get

$$\left\langle \mathbf{E}^i(\mathbf{r}),\mathbf{f}_m(\mathbf{r})\right\rangle = j\omega\left\langle \mathbf{A}(\mathbf{r}),\mathbf{f}_m(\mathbf{r})\right\rangle + \left\langle \nabla\Phi(\mathbf{r}),\mathbf{f}_m(\mathbf{r})\right\rangle \tag{10}$$

where the surface S in equation (9) is the combined area of the two patches sharing the non-boundary edge m. The product in the first term on the right-hand side of equation (10) can be expressed as,

$$\left\langle \mathbf{A}(\mathbf{r}),\mathbf{f}_m(\mathbf{r})\right\rangle = \int_{P_{m^+}} \mathbf{A}(\mathbf{r})\cdot\mathbf{f}_m(\mathbf{r})\,dS + \int_{P_{m^-}} \mathbf{A}(\mathbf{r})\cdot\mathbf{f}_m(\mathbf{r})\,dS\,. \tag{11}$$

The vector magnetic potential **A** can be expressed as the summation of its components which are attributed to the currents associating the non-boundary edges as follows,

$$\mathbf{A}(\mathbf{r}) = \sum_{n=1}^{N}\left[\mathbf{A}_{n^+}^n(\mathbf{r}) + \mathbf{A}_{n^-}^n(\mathbf{r})\right] \tag{12}$$

where $\mathbf{A}_{n^{\pm}}^n$ is the vector magnetic potential due to the current flowing through the patch $P_{n^{\pm}}$ and associated with the non-boundary edge n. Substituting equation (12) in equation (11), one gets

$$\left\langle \mathbf{A}(\mathbf{r}),\mathbf{f}_m(\mathbf{r})\right\rangle = \sum_{n=1}^{N}\left(A_{m^+n^+}^{mn} + A_{m^+n^-}^{mn} + A_{m^-n^+}^{mn} + A_{m^-n^-}^{mn}\right) \tag{13}$$

where

$$A_{m^{\pm}n^{\pm}}^{mn} = \int_{P_{m^{\pm}}} \mathbf{A}_{n^{\pm}}^n\cdot\mathbf{f}_m(\mathbf{r})\,dS\,. \tag{14}$$

According to equation (5), $\mathbf{A}^{n}_{n^{\pm}}$ can be expressed as

$$\mathbf{A}^{n}_{n^{\pm}}(\mathbf{r}) = \frac{\mu\, I_n}{4\pi} \int_{P_{n^{\pm}}} \mathbf{f}_n(\mathbf{r}')\ F_R\ \ dS' \tag{15}$$

where

$$F_R = \frac{e^{-jkR}}{R}. \tag{16}$$

Substituting equation (15) into equation (14), one gets

$$A^{mn}_{m^{\pm}n^{\pm}} = \frac{\mu\, I_n}{4\pi} \int_{P_{m^{\pm}}} \int_{P_{n^{\pm}}} \mathbf{f}_n(\mathbf{r}')\, F_R\ dS' \cdot \mathbf{f}_m(\mathbf{r})\ dS\,. \tag{17}$$

Substituting $\mathbf{f}_n(\mathbf{r}')$ and $\mathbf{f}_m(\mathbf{r})$ into equation (17), one gets

$$A^{mn}_{m^{+}n^{+}} = \frac{\mu\, I_n l_m l_n}{16\pi\, S_{m^{+}} S_{n^{+}}} \int_{P_{m^{+}}} \int_{P_{n^{+}}} F_R \boldsymbol{\rho}^{+}_n \cdot \boldsymbol{\rho}^{+}_m dS' dS\,, \tag{18-a}$$

$$A^{mn}_{m^{+}n^{-}} = \frac{\mu\, I_n l_m l_n}{16\pi\, S_{m^{+}} S_{n^{-}}} \int_{P_{m^{+}}} \int_{P_{n^{-}}} F_R \boldsymbol{\rho}^{-}_n \cdot \boldsymbol{\rho}^{+}_m\ dS' dS\,, \tag{18-b}$$

$$A^{mn}_{m^{-}n^{+}} = \frac{\mu\, I_n l_m l_n}{16\pi\, S_{m^{-}} S_{n^{+}}} \int_{P_{m^{-}}} \int_{P_{n^{+}}} F_R \boldsymbol{\rho}^{+}_n \cdot \boldsymbol{\rho}^{-}_m dS' dS\,, \tag{18-c}$$

$$A^{mn}_{m^{-}n^{-}} = \frac{\mu\, I_n l_m l_n}{16\pi\, S_{m^{-}} S_{n^{-}}} \int_{P_{m^{-}}} \int_{P_{n^{-}}} F_R \boldsymbol{\rho}^{-}_n \cdot \boldsymbol{\rho}^{-}_m\ dS' dS\,. \tag{18-d}$$

The product in the second term on the right-hand side of equation (10) can be expressed as follows [8],

$$\left\langle \nabla\Phi(\mathbf{r}), \mathbf{f}_m(\mathbf{r}) \right\rangle = \int_S \nabla\Phi(\mathbf{r}) \cdot \mathbf{f}_m(\mathbf{r})\ dS = -\int_S \Phi(\mathbf{r})\, \nabla_s \cdot \mathbf{f}_m(\mathbf{r})\ dS\,. \tag{19}$$

Taking S in equation (19) as the combined area of the triangular patches $P_{m^{+}}$ and $P_{m^{-}}$, equation (19) can be written as

$$\left\langle \nabla\Phi(\mathbf{r}), \mathbf{f}_m(\mathbf{r}) \right\rangle = -\int_{P_{m^{+}}} \Phi(\mathbf{r})\, \nabla_s \cdot \mathbf{f}_m(\mathbf{r})\ dS - \int_{P_{m^{-}}} \Phi(\mathbf{r})\, \nabla_s \cdot \mathbf{f}_m(\mathbf{r})\ dS\,. \tag{20}$$

The scalar potential Φ can be expressed as the summation of its components which are attributed to the currents associating the non-boundary edges as follows,

$$\Phi(\mathbf{r}) = \sum_{n=1}^{N} \left[\Phi_{n^{+}}(\mathbf{r}) + \Phi_{n^{-}}(\mathbf{r}) \right] \tag{21}$$

where $\Phi^{n}_{n^{\pm}}$ is the scalar potential due to the current flowing through the patch $P_{n^{\pm}}$ and associated with the non-boundary edge number n. Substituting equation (21) into equation (20), one gets,

$$\left\langle \nabla\Phi(\mathbf{r}), \mathbf{f}_m(\mathbf{r}) \right\rangle = \sum_{n=1}^{N} \left(\Phi^{mn}_{m^{+}n^{+}} + \Phi^{mn}_{m^{+}n^{-}} + \Phi^{mn}_{m^{-}n^{+}} + \Phi^{mn}_{m^{-}n^{-}} \right) \tag{22}$$

where

$$\Phi^{mn}_{m^{\pm}n^{\pm}} = \int_{P_{m^{\pm}}} \Phi^{n}_{n^{\pm}} \nabla_s \cdot \mathbf{f}_m(\mathbf{r})\ dS\,, \tag{23}$$

$$\Phi^{n}_{n^{\pm}}(\mathbf{r}) = -\frac{I_n}{4\pi\, j\, \omega\varepsilon} \int_{P_{n^{\pm}}} \nabla_s \cdot \mathbf{f}_n(\mathbf{r}')\ \frac{e^{-jkR}}{R}\ dS'\,, \tag{24}$$

$$\Phi^{mn}_{m^{\pm}n^{\pm}} = -\frac{I_n}{4\pi\, j\omega\varepsilon} \int_{P_{m^{\pm}}} \int_{P_{n^{\pm}}} \nabla_s \cdot \mathrm{f}_n(\mathrm{r}')\ \ \nabla_s \cdot\ \mathrm{f}_m(\mathrm{r}) F_R dS' dS. \tag{25}$$

Substituting $\mathbf{f}_n(\mathbf{r}')$ in equation (25), one gets the expressions,

$$\Phi^{mn}_{m^{+}n^{+}} = \frac{-I_n l_m l_n}{4\pi\ j\ \omega\varepsilon\ S_{m^{+}} S_{n^{+}}} \int_{P_{m^{+}}} \int_{P_{n^{+}}} F_R\ dS'\ \ dS\,, \tag{26-a}$$

$$\Phi^{mn}_{m^{+}n^{-}} = \frac{I_n l_m l_n}{4\pi\ j\ \omega\varepsilon\ S_{m^{+}} S_{n^{-}}} \int_{P_{m^{+}}} \int_{P_{n^{-}}} F_R\ dS'\ \ dS\,, \tag{26-b}$$

$$\Phi^{mn}_{m^{-}n^{+}} = \frac{I_n l_m l_n}{4\pi\ j\ \omega\varepsilon\ S_{m^{-}} S_{n^{+}}} \int_{P_{m^{-}}} \int_{P_{n^{+}}} F_R\ dS'\ \ dS\,, \tag{26-c}$$

$$\Phi^{mn}_{m^{-}n^{-}} = \frac{-I_n l_m l_n}{4\pi\ j\ \omega\varepsilon\ S_{m^{-}} S_{n^{-}}} \int_{P_{m^{-}}} \int_{P_{n^{-}}} F_R\ dS'\ \ dS\,. \tag{26-d}$$

Equation (13) can be rewritten as,

$$\left\langle \mathbf{A}(\mathbf{r}), \mathbf{f}_m(\mathbf{r}) \right\rangle = \sum_{n=1}^{N} \frac{\mu\, I_n}{4\pi} l_m l_n\ \alpha_{mn} \tag{27}$$

where

$$\alpha^{mn} = \alpha^{mn}_{m^{+}n^{+}} + \alpha^{mn}_{m^{+}n^{-}} + \alpha^{mn}_{m^{-}n^{+}} + \alpha^{mn}_{m^{-}n^{-}}\ , \tag{28}$$

$$\alpha^{mn}_{m^{+}n^{+}} = \frac{1}{4\, S_{m^{+}} S_{n^{+}}} \int_{P_{m^{+}}} \int_{P_{n^{+}}} \boldsymbol{\rho}^{+}_n\ F_R\ dS' \cdot \boldsymbol{\rho}^{+}_m\ dS\,, \tag{29-a}$$

$$\alpha^{mn}_{m^{+}n^{-}} = \frac{1}{4\, S_{m^{+}} S_{n^{-}}} \int_{P_{m^{+}}} \int_{P_{n^{-}}} \boldsymbol{\rho}^{-}_n\ F_R\ dS' \cdot \boldsymbol{\rho}^{+}_m\ dS\,, \tag{29-b}$$

$$\alpha^{mn}_{m^{-}n^{+}} = \frac{1}{4\, S_{m^{-}} S_{n^{+}}} \int_{P_{m^{-}}} \int_{P_{n^{+}}} \boldsymbol{\rho}^{+}_n\ F_R\ dS' \cdot \boldsymbol{\rho}^{-}_m\ dS\,, \tag{29-c}$$

$$\alpha^{mn}_{m^{-}n^{-}} = \frac{1}{4\, S_{m^{-}} S_{n^{-}}} \int_{P_{m^{-}}} \int_{P_{n^{-}}} \boldsymbol{\rho}^{-}_n\ F_R\ dS' \cdot \boldsymbol{\rho}^{-}_m\ dS\,. \tag{29-d}$$

Equation (20) can be written as,

$$\left\langle \nabla\Phi(\mathbf{r}), \mathbf{f}_m(\mathbf{r}) \right\rangle = \sum_{n=1}^{N} \frac{I_n}{\pi\ j\ \omega\varepsilon} l_m l_n\ \beta_{mn} \tag{30}$$

where,

$$\beta^{mn} = \beta^{mn}_{m^+n^+} + \beta^{mn}_{m^+n^-} + \beta^{mn}_{m^-n^+} + \beta^{mn}_{m^-n^-}, \quad (31)$$

$$\beta^{mn}_{m^+n^+} = \frac{1}{4\,S_{m^+}S_{n^+}} \int_{P_{m^+}} \int_{P_{n^+}} F_R \, dS' \, dS, \quad (32\text{-a})$$

$$\beta^{mn}_{m^+n^-} = \frac{1}{4\,S_{m^+}S_{n^-}} \int_{P_{m^+}} \int_{P_{n^-}} F_R \, dS' \, dS, \quad (32\text{-b})$$

$$\beta^{mn}_{m^-n^+} = \frac{1}{4\,S_{m^-}S_{n^+}} \int_{P_{m^-}} \int_{P_{n^+}} F_R \, dS' \, dS, \quad (32\text{-c})$$

$$\beta^{mn}_{m^-n^-} = \frac{1}{4\,S_{m^-}S_{n^-}} \int_{P_{m^-}} \int_{P_{n^-}} F_R \, dS' \, dS. \quad (32\text{-d})$$

The product in the left-hand side of equation (10) can be expressed as,

$$\left\langle \mathbf{E}^i(\mathbf{r}), \mathbf{f}_m(\mathbf{r}) \right\rangle = \frac{l_m}{2\,S_{m^+}} \int_{P_{m^+}} \mathbf{E}^i(\mathbf{r}) \cdot \boldsymbol{\rho}^+_m \, dS + \frac{l_m}{2\,S_{m^-}} \int_{P_{m^-}} \mathbf{E}^i(\mathbf{r}) \cdot \boldsymbol{\rho}^-_m \, dS. \quad (33)$$

Equation (33) can be written as,

$$\left\langle \mathbf{E}^i(\mathbf{r}), \mathbf{f}_m(\mathbf{r}) \right\rangle = V_m \quad (34)$$

where

$$V_m = l_m \, (v^m_{m^+} + v^m_{m^-}), \quad (35)$$

$$v^m_{m^\pm} = \frac{1}{2\,S_{m^\pm}} \int_{P_{m^\pm}} \mathbf{E}^i(\mathbf{r}) \cdot \boldsymbol{\rho}^\pm_m \, dS. \quad (36)$$

Making use of equations (27), (30) and (34), equation (10) yield,

$$\sum_{n=0}^{N-1} Z_{mn} \, I_n = V_m \quad (37)$$

where

$$Z_{mn} = l_m l_n \left(\frac{j\omega\mu}{4\pi} \alpha^{mn} + \frac{1}{\pi \, j\omega\varepsilon} \beta^{mn} \right). \quad (38)$$

Equation (37) can be written in a matrix form as,

$$[Z][I] = [V]. \quad (39)$$

The last matrix equation constitutes a linear system of *N* equations in *N* unknowns which are the amplitudes of the basis functions in the current expansion series of equation (3). It should be noticed that due to the Galerkin's formulation, the matrix [*Z*] is symmetric. The evaluation of the elements of [Z] requires the calculation of the integrals in equations (29) and (32), which are singular when the observation point coincides with the source point. The evaluation of such integrals requires, first, their transformation from the Cartesian coordinates to the so-called simplex coordinates.

III. TRANSFORMATION OF INTEGRALS TO SIMPLEX COORDINATES

The integrals in equations (29) and (32) are carried out on planar triangular patches, and hence, they can be evaluated by, first, transforming from ordinary 3-D Cartesian coordinates to the so-called simplex coordinate system, which is a 2-D coordinate system. Referring to Fig. 2, a point $\mathbf{r}_q$ that lies in the triangle whose vertices are described in the Cartesian coordinates as $\mathbf{r}_{1q}$, $\mathbf{r}_{2q}$, $\mathbf{r}_{3q}$ can be mapped to the simplex coordinate system to lie inside a standard triangle, shown in Fig. 3, defined by

$$(\eta, \xi): \quad 0 < \eta < 1, \quad 0 < \xi < (1 - \eta) \quad (40)$$

where the new coordinates are determined by,

$$\eta = \frac{S_1}{S_q}, \quad \xi = \frac{S_2}{S_q}. \quad (41)$$

Define a third coordinate ζ as,

$$\zeta = \frac{S_3}{S_q}. \quad (42)$$

Since $\frac{S_1}{S_q} + \frac{S_2}{S_q} + \frac{S_3}{S_q} = 1$, one gets,

$$\eta + \xi + \zeta = 1. \quad (43)$$

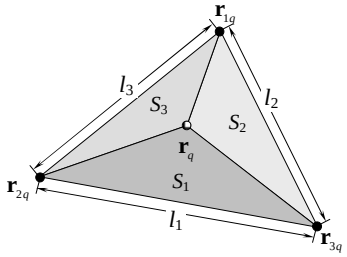

(a) Triangle in Cartesian coordinate system.

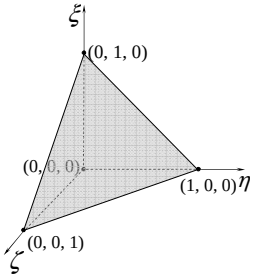

(b) The same triangle in simplex coordinate system.

Fig. 2. Transformation from Cartesian to simplex or normalized-area coordinates.

For this reason, the triplet (η, ξ ,ζ) describes the so-called normalized-area coordinate system shown in Fig. 2-b, which is equivalent to the simplex coordinate system (η, ζ) described by equations (40) and (41). Thus, a point r_q that lies in the triangular patch P_q and described in the simplex coordinate or normalized-area coordinate system as (η, ζ) or (η, ξ ,ζ) respectively, can be mapped to the 3D Cartesian coordinate system with the vertices $\mathbf{r_{1q}}$, $\mathbf{r_{2q}}$, $\mathbf{r_{3q}}$ of P_q using the transformation.

$$\mathbf{r}_q = \xi\ \mathbf{r}_{1q} + \eta\ \mathbf{r}_{2q} + (1 - \eta - \xi)\ \mathbf{r}_{3q} \tag{44}$$

or

$$\mathbf{r}_q = \eta\, \mathbf{r}_{1q} + \xi \mathbf{r}_{2q} + \zeta\, \mathbf{r}_{3q}\,. \tag{45}$$

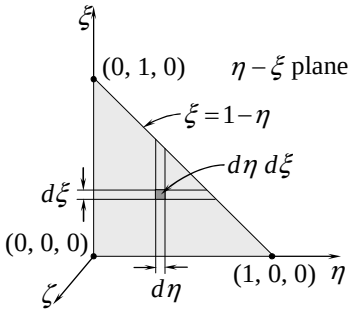

Fig. 3. Triangle transformed to simplex η-ξ plane.

It is required to express an infinitesimal element of area dS in terms of $d\eta$ and $d\xi$. Using η, ξ as 2D Cartesian-like coordinate as shown in Fig. 3, the triangular patch (of area S) is mapped to the right-angle triangle shown in the figure. If we express the area element in the η-ξ plane as $d\eta d\xi$, then integrating this element over the entire range of η, ξ results in the area of this triangle. To get the surface integrals in the η-ξ plane equivalent to the surface integrals in the ordinary 3D-Cartesian coordinates, the element $d\eta d\xi$ should be scaled; thus, we must have,

$$\int_0^1 \int_0^{1-\eta} S_f \ \ d\xi\, d\eta = S \tag{46}$$

where S_f is unknown scale factor that can be determined by carrying out the integration in equation(46). This leads,

$$S_f = 2S\,. \tag{47}$$

Thus, the surface integrals over P_q can be evaluated in the simplex coordinates by replacing dS by $2Sd\eta d\xi$, as follows,

$$\int_{P_q} g(\mathbf{r})\, dS\ =$$

$$2\,S_q \int_0^1 \int_0^{1-\eta} g[\xi\, \mathbf{r}_{1q} + \eta\, \mathbf{r}_{2q} + (1-\xi-\eta)\, \mathbf{r}_{3q}]\, d\xi d\eta\,. \tag{48}$$

Making use of equation (48), equations (29) and (32) can be written as,

$$\begin{aligned}
\alpha_{m^{\pm}n^{\pm}}^{mn} = \pm \Big[& \mathbf{r}_{1m^{\pm}} \cdot \mathbf{r}_{1n^{\pm}}\ I_{\eta\eta'}^{m^{\pm}n^{\pm}} + \mathbf{r}_{2m^{\pm}} \cdot \mathbf{r}_{1n^{\pm}}\ I_{\xi\eta'}^{m^{\pm}n^{\pm}} \\
& + \mathbf{r}_{3m^{\pm}} \cdot \mathbf{r}_{1n^{\pm}}\ I_{\zeta\eta'}^{m^{\pm}n^{\pm}} - \mathbf{r}_{f\,m}^{\pm} \cdot \mathbf{r}_{1n^{\pm}}\ I_{\eta'}^{m^{\pm}n^{\pm}} \\
& + \mathbf{r}_{1m^{\pm}} \cdot \mathbf{r}_{2n^{\pm}}\ I_{\eta\xi'}^{m^{\pm}n^{\pm}} + \mathbf{r}_{2m^{\pm}} \cdot \mathbf{r}_{2n^{\pm}}\ I_{\xi\xi'}^{m^{\pm}n^{\pm}} \\
& + \mathbf{r}_{3m^{\pm}} \cdot \mathbf{r}_{2n^{\pm}}\ I_{\zeta\xi'}^{m^{\pm}n^{\pm}} - \mathbf{r}_{f\,m}^{\pm} \cdot \mathbf{r}_{2n^{\pm}}\ I_{\xi'}^{m^{\pm}n^{\pm}} \\
& + \mathbf{r}_{1m^{\pm}} \cdot \mathbf{r}_{3n^{\pm}}\ I_{\eta\zeta'}^{m^{\pm}n^{\pm}} + \mathbf{r}_{2m^{\pm}} \cdot \mathbf{r}_{3n^{\pm}}\ I_{\xi\zeta'}^{m^{\pm}n^{\pm}} \\
& + \mathbf{r}_{3m^{\pm}} \cdot \mathbf{r}_{3n^{\pm}}\ I_{\zeta\zeta'}^{m^{\pm}n^{\pm}} - \mathbf{r}_{f\,m}^{\pm} \cdot \mathbf{r}_{3n^{\pm}}\ I_{\zeta'}^{m^{\pm}n^{\pm}} \\
& - \mathbf{r}_{1m^{\pm}} \cdot \mathbf{r}_{f\,n}^{\pm}\ I_{\eta}^{m^{\pm}n^{\pm}} - \mathbf{r}_{2m^{\pm}} \cdot \mathbf{r}_{f\,n}^{\pm}\ I_{\xi}^{m^{\pm}n^{\pm}} \\
& - \mathbf{r}_{3m^{\pm}} \cdot \mathbf{r}_{f\,n}^{\pm}\ I_{\zeta}^{m^{\pm}n^{\pm}} + \mathbf{r}_{f\,m}^{\pm} \cdot \mathbf{r}_{f\,n}^{\pm}\ I^{m^{\pm}n^{\pm}} \Big],
\end{aligned} \tag{49}$$

$$\beta_{m^{\pm}n^{\pm}}^{mn} = I^{m^{\pm}n^{\pm}}, \tag{50}$$

where

$$I_{\eta\eta'}^{pq} = \int_0^1 \int_0^{1-\eta} \int_0^1 \int_0^{1-\eta'} \eta\eta'\, F_R\ d\xi'\, d\eta'\, d\xi\, d\eta\,, \tag{51}$$

$$I_{\eta\xi'}^{pq} = \int_0^1 \int_0^{1-\eta} \int_0^1 \int_0^{1-\eta'} \eta\xi'\, F_R\ d\xi'\, d\eta'\, d\xi\, d\eta\,, \tag{52}$$

$$I_{\xi\eta'}^{pq} = \int_0^1 \int_0^{1-\eta} \int_0^1 \int_0^{1-\eta'} \xi\eta'\, F_R\ d\xi'\, d\eta'\, d\xi\, d\eta\,, \tag{53}$$

$$I_{\xi\xi'}^{pq} = \int_0^1 \int_0^{1-\eta} \xi \int_0^1 \int_0^{1-\eta'} \xi'\, F_R\ d\xi'\, d\eta'\, d\xi\, d\eta\,, \tag{54}$$

$$I_{\eta'}^{pq} = \int_0^1 \int_0^{1-\eta} \int_0^1 \int_0^{1-\eta'} \eta'\, F_R\ d\xi'\, d\eta'\, d\xi\, d\eta\,, \tag{55}$$

$$I_{\xi'}^{pq} = \int_0^1 \int_0^{1-\eta} \left(\int_0^1 \int_0^{1-\eta'} \xi'\, F_R\ d\xi'\, d\eta' \right) d\xi\, d\eta\,, \tag{56}$$

$$I_{\eta}^{pq} = \int_0^1 \int_0^{1-\eta} \eta \left(\int_0^1 \int_0^{1-\eta} F_R\ d\xi'\, d\eta' \right) d\xi\, d\eta\,, \tag{57}$$

$$I_{\xi}^{pq} = \int_0^1 \int_0^{1-\eta} \xi \left(\int_0^1 \int_0^{1-\eta} F_R\ d\xi'\, d\eta' \right) d\xi\, d\eta\,, \tag{58}$$

$$I^{pq} = \int_0^1 \int_0^{1-\eta} \left(\int_0^1 \int_0^{1-\eta'} F_R\ d\xi'\, d\eta' \right) d\xi\, d\eta \tag{59}$$

where $P = m^+, m^-$; $q = n^+, n^-$. The remaining integrals can be calculated from the above integrals as follows.

$$I_{\eta\zeta'}^{pq} = I_{\eta}^{pq} - I_{\eta\eta'}^{pq} - I_{\eta\xi'}^{pq}, \tag{60}$$

$$I_{\xi\zeta'}^{pq} = I_{\xi}^{pq} - I_{\xi\eta'}^{pq} - I_{\xi\xi'}^{pq}, \tag{61}$$

$$I^{pq}_{\zeta\eta'} = I^{pq}_{\eta'} - I^{pq}_{\eta\eta'} - I^{pq}_{\xi\eta'}, \quad (62)$$

$$I^{pq}_{\zeta\xi'} = I^{pq}_{\xi'} - I^{pq}_{\eta\xi'} - I^{pq}_{\xi\xi'}, \quad (63)$$

$$I^{pq}_{\zeta\zeta'} = I^{pq}_{\zeta'} - I^{pq}_{\eta\zeta'} - I^{pq}_{\xi\zeta'}, \quad (64)$$

$$I^{pq}_{\zeta'} = I^{pq} - I^{pq}_{\eta'} - I^{pq}_{\xi'}, \quad (65)$$

$$I^{pq}_{\zeta} = I^{pq} - I^{pq}_{\eta} - I^{pq}_{\xi}. \quad (66)$$

Thus, only nine independent integrals from equation (51) to equation (59) must be numerically evaluated for each combination of pairs; *p* and *q*. The nine integrals, in turn, contribute to up to nine elements of [*Z*] in equation (39). For a closed surface with *N* edges, the number of independent integrals computed is $4N^2$. By contrast, the edge-by-edge approach would require the evaluation of $36N^2$ integrals or nine times as many.

Due to the Galerkin's EFIE procedure applied as described above, and since the basis and testing functions chosen are identical, the *Z* matrix would then satisfy the symmetry property $Z_{mn}=Z_{nm}$. Also, the integrals in equation (51) to equation (66) are symmetric; i.e. $I^{pq}=I^{qp}$ and the same is true for the other integrals. Thus the number of the independent integrals that must be computed are reduced to $N(2N+3)$ instead of $4N^2$. Using the same coordinate transformation, equation (36) can be expressed as

$$v^m_{m^\pm} = \pm \int_0^1 \int_0^{1-\eta} \mathbf{E}^i(\mathbf{r}) \cdot \left| \xi \mathbf{r}_{1m^\pm} + \eta \mathbf{r}_{2m^\pm} + (1-\eta-\xi)\mathbf{r}_{3m^\pm} - \mathbf{r}^\pm_{f\,m} \right| d\xi\, d\eta\,. \quad (67)$$

Equation (67) can be written as,

$$v^m_{m^\pm} = \pm \left| \mathbf{r}_{1m^\pm} \cdot \mathbf{I}^{m^\pm}_\eta + \mathbf{r}_{2m^\pm} \cdot \mathbf{I}^{m^\pm}_\xi + \mathbf{r}_{3m^\pm} \cdot \mathbf{I}^{m^\pm}_\zeta - \mathbf{r}^\pm_{f\,m} \cdot \mathbf{I}^{m^\pm} \right| \quad (68)$$

where,

$$\mathbf{I}^p_\eta = \int_0^1 \int_0^{1-\eta} \eta\, \mathbf{E}^i[\xi \mathbf{r}_{1p} + \eta \mathbf{r}_{2p} + (1-\xi-\eta)\mathbf{r}_{3p}]\, d\xi\, d\eta\,, \quad (69)$$

$$\mathbf{I}^p_\xi = \int_0^1 \int_0^{1-\eta} \xi\, \mathbf{E}^i[\xi \mathbf{r}_{1p} + \eta \mathbf{r}_{2p} + (1-\xi-\eta)\mathbf{r}_{3p}]\, d\xi\, d\eta\,, \quad (70)$$

$$\mathbf{I}^p = \int_0^1 \int_0^{1-\eta} \mathbf{E}^i[\xi \mathbf{r}_{1p} + \eta \mathbf{r}_{2p} + (1-\xi-\eta)\mathbf{r}_{3p}]\, d\xi\, d\eta\,, \quad (71)$$

$$\mathbf{I}^p_\zeta = \mathbf{I}^p - \mathbf{I}^p_\eta - \mathbf{I}^p_\xi. \quad (72)$$

IV. EVALUATION OF SINGULAR INTEGRALS

Integrals of equation (51) to equation (59) are singular for *p=q i.e.*, when the source and observation patches are the same. In this case, each of these integrals can be divided into two parts one of which is non-singular and can be evaluated numerically whereas the other is weakly singular and can be evaluated analytically. The integral in equation (51) can be rewritten as,

$$I^{qq}_{\eta\eta'} = \int_0^1 \int_0^{1-\eta} \int_0^1 \int_0^{1-\eta'} \eta\eta' G_R \; d\xi'\, d\eta'\, d\xi\, d\eta + \Gamma^{qq}_{\eta\eta'} \quad (73)$$

where

$$G_R = \frac{e^{-jkR}-1}{R}, \quad (74)$$

$$\Gamma^{qq}_{\eta\eta'} = \int_0^1 \int_0^{1-\eta} \int_0^1 \int_0^{1-\eta'} \eta\eta' \frac{1}{R} \; d\xi'\, d\eta'\, d\xi\, d\eta \quad . \quad (75)$$

It should be noted that the first term on the right hand side of equation (73) is a non-singular integral and can be evaluated numerically whereas $\Gamma^{qq}_{\eta\eta'}$ is weakly singular and should be evaluated analytically. The same can be repeated for equations (52) to (59), where these singular integrals appear,

$$\Gamma^{qq}_{\eta\eta'} = \int_0^1 \int_0^{1-\eta} \int_0^1 \int_0^{1-\eta'} \eta\eta' \frac{1}{R} \; d\xi'\, d\eta'\, d\xi\, d\eta \quad , \quad (76)$$

$$\Gamma^{qq}_{\eta\xi'} = \int_0^1 \int_0^{1-\eta} \int_0^1 \int_0^{1-\eta'} \eta\xi' \frac{1}{R} \; d\xi'\, d\eta'\, d\xi\, d\eta \quad , \quad (77)$$

$$\Gamma^{qq}_{\xi\eta'} = \int_0^1 \int_0^{1-\eta} \int_0^1 \int_0^{1-\eta'} \xi\eta' \frac{1}{R} \; d\xi'\, d\eta'\, d\xi\, d\eta \quad , \quad (78)$$

$$\Gamma^{qq}_{\xi\xi'} = \int_0^1 \int_0^{1-\eta} \int_0^1 \int_0^{1-\eta'} \xi\xi' \frac{1}{R} \; d\xi'\, d\eta'\, d\xi\, d\eta \quad , \quad (79)$$

$$\Gamma^{qq}_{\eta'} = \int_0^1 \int_0^{1-\eta} \int_0^1 \int_0^{1-\eta'} \eta' \frac{1}{R} \; d\xi'\, d\eta'\, d\xi\, d\eta \quad , \quad (80)$$

$$\Gamma^{qq}_{\xi'} = \int_0^1 \int_0^{1-\eta} \int_0^1 \int_0^{1-\eta'} \xi' \frac{1}{R} \; d\xi'\, d\eta'\, d\xi\, d\eta \quad , \quad (81)$$

$$\Gamma^{qq}_{\eta} = \int_0^1 \int_0^{1-\eta} \int_0^1 \int_0^{1-\eta'} \eta \frac{1}{R} \; d\xi'\, d\eta'\, d\xi\, d\eta \quad , \quad (82)$$

$$\Gamma^{qq}_{\xi} = \int_0^1 \int_0^{1-\eta} \int_0^1 \int_0^{1-\eta'} \xi \frac{1}{R} \; d\xi'\, d\eta'\, d\xi\, d\eta \quad , \quad (83)$$

$$\Gamma^{qq} = \int_0^1 \int_0^{1-\eta} \int_0^1 \int_0^{1-\eta'} \frac{1}{R} \; d\xi'\, d\eta'\, d\xi\, d\eta \quad . \quad (84)$$

Closed form expressions for the singular integrals in equations (76) to (84) are given in Appendix A.

V. ANTENNA EXCITATION AND INPUT IMPEDANCE

In this section, a method is described for accurate computation of the input impedance of antennas composed of conducting surfaces using the EFIE technique.

For antennas composed of complex or curved conducting surfaces, the EFIE technique is preferable to the FDTD method [2]. The accuracy of the latter is often limited by the computer memory requirement and the "staircase" approximation of the antenna geometry. In antenna problems, the staircase approximation could become a major drawback for accurate impedance calculation since in this case very fine discretization of the antenna region near the feed point is required, which may be difficult for curved or complex surfaces. The EFIE technique employing triangular-patch model does not suffer from the staircase approximation and, moreover, the density of the triangular patches can be simply increased near the feeding point, as shown in Fig. 4, to get accurate evaluation of the impedance [13].

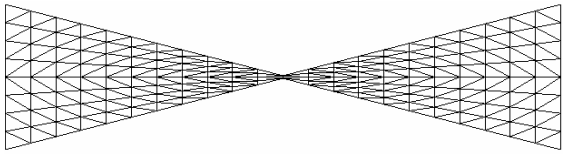

Fig. 4. Increasing the density of triangular patches near the feeding point of the antenna.

In scattering problems treated by the EFIE technique applied on a triangular-patch model of the scatterer, all the facets (triangular patches) are illuminated by the incident field. To excite an antenna by a delta-gap voltage generator, the delta gap is made as a cut along one or more of the non-boundary edges of the surface model. A voltage generator is then applied across the excitation edge(s). In this case, only the facets on the sides of each of the excitation edges have voltage difference applied on them. However, the method of evaluating the input impedance in the case of a conducting surface antenna excited by infinitesimal-gap voltage generator can be obtained from the model of scattering problem as detailed in the following analysis. Let m_x be the edge at which a delta-gap voltage source is applied and let m_x^+ and m_x^- be the numbers of triangular patches sharing this edge (the current is assumed to flow from m_x^+ to m_x^-). Consider the element number m_x in the excitation vector [V], which is expressed as,

$$\frac{V_{m_x}}{l_{m_x}} = \frac{1}{2S_{m_x^+}} \int_{P_{m_x^+}} \mathbf{E}^i \cdot \boldsymbol{\rho}_{m_x}^+ \, dS + \frac{1}{2S_{m_x^-}} \int_{P_{m_x^-}} \mathbf{E}^i \cdot \boldsymbol{\rho}_{m_x}^- \, dS \,. \quad (85)$$

For the purpose of physical interpretation of equation (85), this expression can be approximated as,

$$V_{m_x} / l_{m_x} \approx \mathbf{E}^i_{c\,m_x^+} \cdot \frac{\boldsymbol{\rho}_{c\,m_x}^+}{2} + \mathbf{E}^i_{c\,m_x^-} \cdot \frac{\boldsymbol{\rho}_{c\,m_x}^-}{2} \quad (86)$$

where, $E^i_{c\,m_x^+}$ and $E^i_{c\,m_x^-}$ are the values of the incident electric field at the centroids of the patches $P_{m_x^+}$ and $P_{m_x^-}$, respectively, and $\rho_{c\,m_x}^+$ and $\rho_{c\,m_x}^-$ are the position vectors of the centroids of the triangles $P_{m_x^+}$ and $P_{m_x^-}$ relative to the vertices $r_{f\,m_x}^+$ and $r_{f\,m_x}^-$, respectively. Thus, by the aid of Fig. 5, the quantity between square brackets in equation (86) can be interpreted as, approximately, the voltage difference between the centroids of the patches $P_{m_x^+}$ and $P_{m_x^-}$ or, in other words, the voltage drop across the excitation edge (*i.e.*, the voltage applied at the input port of the antenna). It should be noted that the value of V_{m_x} used in the present analysis is the exact one that is given by equation (85) and not equation (86). The purpose of obtaining the approximate expression is, only, to get a clear physical meaning of equation (85). According to equation (86), the voltage applied at the antenna input (*i.e.*, the voltage across the excitation edge) is expressed as,

$$V_{in} = V_{m_x} / l_{m_x} \,. \quad (87)$$

As discussed before, the coefficient I_{m_x} in the current expansion series is the normal component of the linear current density flowing past the edge m_x. Since this current density component is constant along the edge number m_x, the input current can be expressed as,

$$I_{in} = l_{m_x} I_{m_x} \,. \quad (88)$$

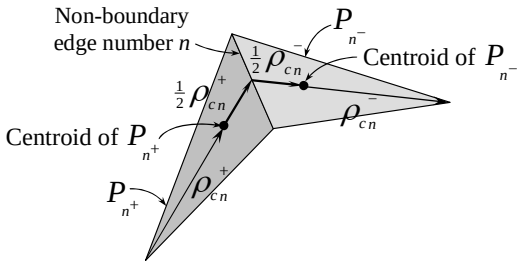

Fig. 5. The voltage drop across a non-boundary edge.

Using a triangular-patch model for the antenna, the input impedance can be defined as the voltage drop across the excitation edge, divided by the current flowing past this edge. Employing equations (87) and (88), one gets the following expression for the input impedance of the antenna,

$$Z_{in} = \frac{V_{in}}{I_{in}} = \frac{1}{l_{m_x}^2} \frac{V_{m_x}}{I_{m_x}}. \quad (89)$$

It has been found that for an accurate calculation of input impedance, it is essential to use very fine discretization in the antenna region near the feed point. To reduce the number of unknowns, the region that is further away from the feed point can be descritized by less fine patches without essentially affecting accuracy. The mesh of a bow-tie antenna descritized with higher resolution in the region near the feeding point to get accurate value of the input impedance is shown in Fig. 4 [13].

VI. RESULTS AND DISCUSSION

The input impedance is one of the antenna parameters whose accuracy is strongly dependent on the efficiency of the computational technique through which it is evaluated. Hence, the evaluation of the antenna input impedance is one of the most stringent tests of the efficiency of a computational technique. Therefore the Galerkin's EFIE algorithm described in the present work is examined by its application to compute the input impedance of well-known conducting surface antennas such as the planar strip-dipole, bow-tie dipole and planar equiangular spiral antennas and comparing the obtained results with other published results concerning the same antennas.

A. Strip Dipole Antenna

The triangular-patch model for a straight strip-dipole antenna of length L and width W is shown in Fig. 6. A delta-gap generator of unity voltage is applied at the cut A-A'. The applied voltage is maintained constant along the feeding edge, which is the non-boundary edge at the center of the dipole. In this case, the input impedance can be obtained by calculating the current crossing the non-boundary edge A-A', and then employing equation (89).

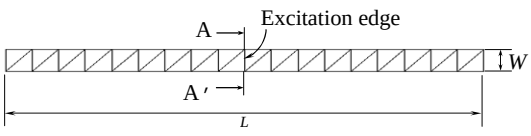

Fig. 6. Triangular patch model of a strip dipole antenna.

Figure 7 presents plots of the resistive and reactive components of the input impedance of a strip-dipole antenna against the operating frequency. The dipole length is 27 cm and its width is 0.001 of its length. The triangular-patch model of this antenna has 36 patches and 35 non-boundary edges. The results show agreement with those of [14]. Figure 8 shows a plot of the VSWR of the strip dipole with respect to 75 Ω source impedance against the frequency. It is clear in the Figure that the bandwidth of this antenna can be considered as 10%, a feature which is well-known for a half-wavelength straight dipole.

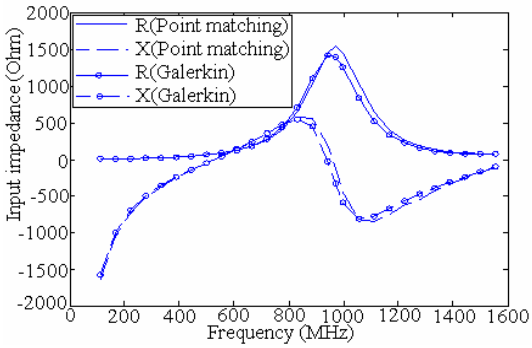

Fig. 7. Input Impedance of a planar strip dipole, L=27 cm and W= 2.7 mm.

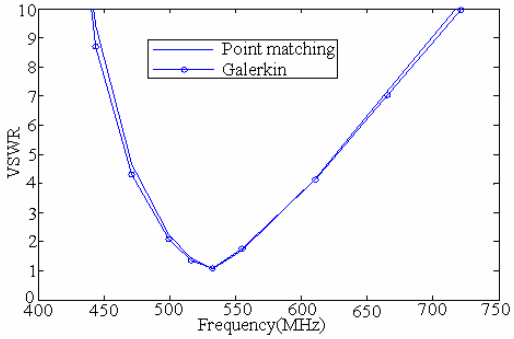

Fig. 8. VSWR of a planar strip dipole, L=27 cm, and W= 2.7 mm.

B. Bow-Tie Antenna

The main advantages of the bow-tie antenna are simple design and broad-band impedance. For this reason, a planar bow-tie antenna is used in many challenging recent applications such as ground penetrating radar (GPR) and global position system (GPS) applications and cellular-based mobile communication services [13], [14 - 20]. Figure 9 shows a triangular-patch model for a bow-tie antenna. The length of the antenna is 27 cm and the flare angle is 90º. The neck width of the antenna (length of the excitation edge) is 1.35 cm. The triangular-patch model of this antenna has 96 patches and 125 non-boundary edges. A delta-gap generator of unity voltage

is applied across the cut A-A', i.e. across the non-boundary edge at the center of the antenna. The current crossing this edge is calculated to get the input impedance via equation (89).

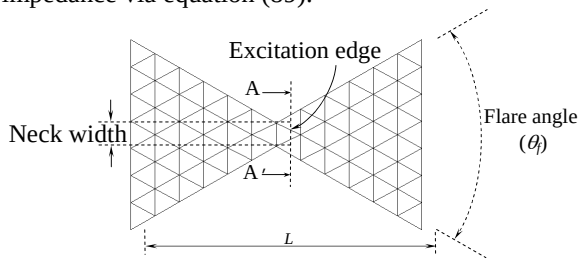

Fig. 9. Triangular patch model of a bow-tie antenna.

The dependence of the input impedance of a bow-tie antenna with the frequency is shown in Fig. 10. The results show good agreement with those of [16]. It should be noted that the antenna of the given dimensions is resonant at about 800 MHz where the input impedance is pure resistive. The VSWR of this antenna is plotted against the frequency as shown in Fig. 11, where the source impedance is assumed 300 Ω. It is clear in the figure that the bandwidth of the bow-tie antenna can be considered as about 400 MHz around its resonant frequency, *i.e.*, about 50%. Thus, the bow-tie antenna exhibits a much wider bandwidth than the dipole antenna, a feature which is well-established and is attributed to the fact that the width dimension of the bow-tie is described as an "angle" rather than a "length" but, however the bow-tie length is the dimensional parameter that limits the bandwidth of such an antenna.

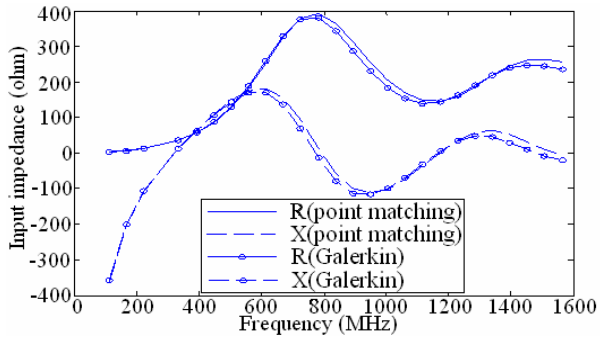

Fig. 10. Input Impedance of a bow-tie antenna, L=27 cm, and W= 1.35 cm, θ_f = 90°.

C. Planar Equiangular Spiral Antenna

One of the ultra wideband (UWB) antennas used in recent applications that require a well-suited transient antenna response is the planar equiangular spiral antenna. Due to its circular polarization, this antenna finds important applications such as short-pulse GPR systems that detect the objects buried in anisotropic ground. It also finds application in stepped-frequency GPR (SF-GPR) to detect buried non-metallic anti-personnel mines in humanitarian mine detection system [22]. Due to their characteristics of quite broad bandwidth and circular polarization, the spiral antennas are widely used in mobile-communication, early-warning and direction-finding systems [23]. The spiral antenna is also suitable as a wideband illuminator for a parabolic reflector working in ultra wideband of frequencies [24].

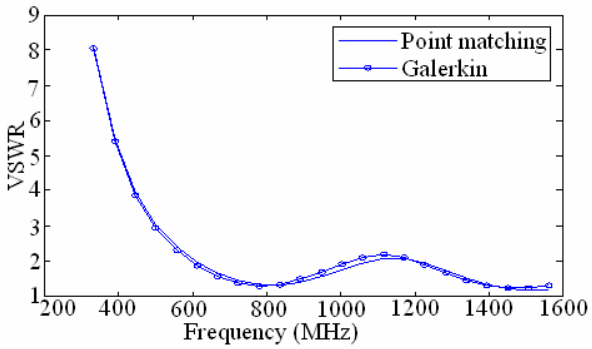

Fig. 11. VSWR for a bow-tie antenna, L=27 cm, and W=1.35cm, θ_f = 90°.

The radiation of spiral elements at the selected operating frequency comes from the active region where spiral circumference is approximately one wavelength. This means that the active region moves from the outermost circle to the innermost one as the frequency increases. Low frequency cutoff f_L is equal to $c/\pi D$ (c is the speed of light and D is the outermost diameter), but the upper frequency is determined by the feed point separation [20], [23] and [25].A triangular patch model for the equiangular spiral antenna surface model and the EFIE technique constitute the most efficient electromagnetic modeling of such an antenna. The triangular-patch model for this antenna is shown in Fig. 12.

Let us consider an equiangular spiral antenna of the following dimensions: the innermost diameter of the spiral (d) is 3 mm, the outermost diameter (D) is 29 cm, the wrapping angle (α) is 70° and the angular width of the spiral arm (δ) is 90°. The spiral arms are wound to make 4 complete revolutions. Figure 12-b shows the detailed triangular patch arrangement at the location of the antenna excitation. The triangular-patch model of this antenna has 138 patches and 177 non-boundary edges. A delta-gap generator of unity voltage slot generator is applied across the non-boundary edge at the cut A-A', where the voltage is maintained constant along this edge.

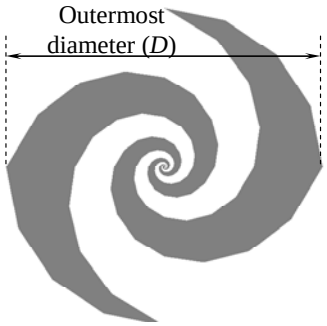

(a) Complete antenna.

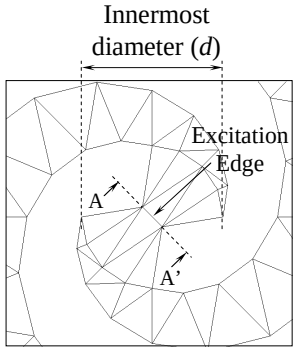

(b) Part of the antenna at the excitation.

Fig. 12. Triangular-patch model of an equiangular spiral antenna.

The input impedance is evaluated using equation (89). The variations of the resistive and reactive parts of the input impedance of the antenna described above with the frequency are presented in Fig. 13. It is clear that the input impedance is stable along a very wide range of the frequency; a fact that is well-known for such an antenna. The VSWR with respect to a source impedance of 150 Ω is plotted against the frequency as shown in Fig. 14. It is evident that this antenna is ultra-wideband; a feature which is attributed to the fact that the dimensions of such a spiral are mainly described as "angles" rather than "lengths".

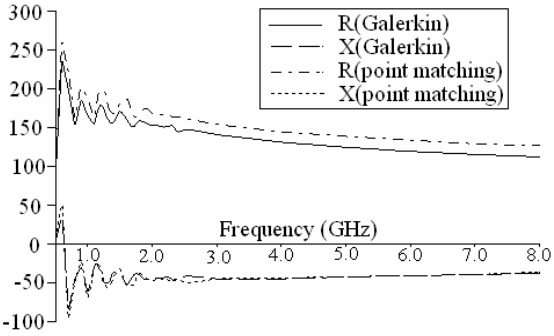

Fig. 13. Input Impedance of an equiangular spiral antenna, d = 3 mm, D = 29 cm, α = 70º and δ = 90º.

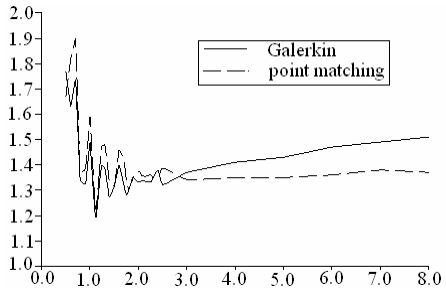

Fig. 14. VSWR of an equiangular spiral antenna, d = 3 mm, D = 29 cm, α = 70º and δ = 90º.

VII. CONCLUSION

A robust and efficient Galerkin's EFIE algorithm is developed to get the current distribution on arbitrarily-shaped conducting surface that act as scatterers or antennas. A new method is applied for accurate evaluation of the input impedance of antennas composed of conducting surfaces which are modeled by triangular patches when the antenna is excited by delta-gap voltage generator. The singular integrals arising when the source and observation points coincide are accurately evaluated. The efficiency of the algorithm is examined by calculating the input impedance and the VSWR of well-known types of antennas, where the results show good agreement with the already well-known characteristics of these antennas and are also in good agreement with some published results concerning the same antennas. The antennas examined in the present work are the strip-dipole, bow-tie and planar equiangular spiral antennas.

Appendix A: Analytic Evaluation of Singular Integrals

The following expressions for the singular integrals are given in [11] after making the corrections in [26],

$$\Gamma^{qq} = \frac{1}{6\sqrt{a}}(\gamma_2+\gamma_6)+\frac{1}{6\sqrt{c}}(\gamma_1+\gamma_5)+\frac{1}{6\sqrt{d}}(\gamma_3+\gamma_4), \tag{A-1}$$

$$\Gamma^{qq}_{\eta\eta'} = \frac{2a+b}{120\,a^{3/2}}(\gamma_2+\gamma_6)+\frac{1}{40\sqrt{c}}(\gamma_1+\gamma_5) + \frac{2a-5b+3c}{120\,d^{3/2}}(\gamma_3+\gamma_4)+\frac{e-f}{60\,a^{3/2}}+\frac{e-g}{60\,d^{3/2}}, \tag{A-2}$$

$$\Gamma^{qq}_{\eta\xi} = \frac{1}{120\sqrt{c}}\gamma_1+\frac{1}{120\sqrt{a}}\gamma_2+\frac{2a-3b+c}{120\,d^{3/2}}\gamma_3 + \frac{a-3b+2c}{120\,d^{3/2}}\gamma_4+\frac{3b+2c}{120\,c^{3/2}}\gamma_5+\frac{2a+3b}{120\,a^{3/2}}\gamma_6 + \frac{e-f}{40\,a^{3/2}}+\frac{g-f}{40\,c^{3/2}}, \tag{A-3}$$

$$\Gamma_{\eta'}^{qq} = \frac{1}{24\sqrt{c}}\gamma_1 + \frac{1}{24\sqrt{a}}\gamma_2 + \frac{1}{24\sqrt{d}}\gamma_3 + \frac{a-3b+2c}{24d^{3/2}}\gamma_4 + \frac{1}{12\sqrt{c}}\gamma_5 + \frac{a+b}{24a^{3/2}}\gamma_6 + \frac{e-f}{24a^{3/2}} + \frac{e-g}{24d^{3/2}} \quad \text{(A-4)}$$

where

$$\gamma_1 = \ln(f+b) - \ln(g+i), \quad \text{(A-5)}$$

$$\gamma_2 = \ln(e+h) - \ln(f-b), \quad \text{(A-6)}$$

$$\gamma_3 = \ln(e+h) - \ln(g+i), \quad \text{(A-7)}$$

$$\gamma_4 = \ln(g-i) - \ln(e-h), \quad \text{(A-8)}$$

$$\gamma_5 = \ln(g-i) - \ln(f-b), \quad \text{(A-9)}$$

$$\gamma_6 = \ln(f+b) - \ln(e-h), \quad \text{(A-10)}$$

$$a = (\mathbf{r}_3 - \mathbf{r}_1)\cdot(\mathbf{r}_3 - \mathbf{r}_1), \quad \text{(A-11)}$$

$$b = (\mathbf{r}_3 - \mathbf{r}_1)\cdot(\mathbf{r}_3 - \mathbf{r}_2), \quad \text{(A-12)}$$

$$c = (\mathbf{r}_3 - \mathbf{r}_2)\cdot(\mathbf{r}_3 - \mathbf{r}_2), \quad \text{(A-13)}$$

$$d = a - 2b + c, \quad \text{(A-14)}$$

$$e = \sqrt{a\,d}, \quad \text{(A-15)}$$

$$f = \sqrt{a\,c}, \quad \text{(A-16)}$$

$$g = \sqrt{c\,d}, \quad \text{(A-17)}$$

$$h = a - b, \quad \text{(A-18)}$$

$$i = b - c. \quad \text{(A-19)}$$

It can be shown that

$$\Gamma_{\xi\xi'}^{qq} = \Gamma_{\eta\eta'}^{qq}, \quad \text{(A-20)}$$

$$\Gamma_{\eta\xi'}^{qq} = \Gamma_{\xi\eta'}^{qq}, \quad \text{(A-21)}$$

$$\Gamma_{\xi'}^{qq} = \Gamma_{\eta'}^{qq} = \Gamma_{\xi}^{qq} = \Gamma_{\eta}^{qq}. \quad \text{(A-22)}$$

REFERENCES

[1] G. Miano and F. Villone, "A surface integral formulation of Maxwell equations for topologically complex conducting domains," *IEEE Trans. Antennas Propagat.*, vol. 53, no. 12, pp. 4001 - 4014, Dec. 2005.

[2] D. B. Davidson, "Computational Electromagnetics for RF and Microwave Engineering," Cambridge University, 2005.

[3] V. I. Okhmatovski, J. D. Morsey and A. C. Cangellaris, "Loop-tree implementation of adaptive integral method (AIM) for numerically-stable, broadband, fast electromagnetic modeling," *IEEE Trans. Antennas Propagat.*, vol. 52, pp. 2130 - 2140, 2004.

[4] Y. Wang, D. Gope, V. Jandhyala, and C. J. R. Shi, "Generalized Kirchoff's current and voltage law formulation for coupled circuit-electromagnetic simulation with surface integral equations," *IEEE Trans. Microwave Theory Tech.*, vol. 52, pp. 1673 - 1682, 2004.

[5] Z. Wang, J. Volakis, K. Saitou, and K. Kurabayashi, "Comparison of semi-analytic formulations and Gaussian-quadrature rules for quasi-static double-surafce potential integrals," *IEEE Antennas Propagat. Magazine*, vol. 45, no. 6, pp. 96 – 102, Dec. 2003.

[6] J. S. Zhao and W. C. Chew, "Integral equation solution of Maxwell's equations from zero frequency to microwave frequency," *IEEE Trans. Antennas Propagat.*, vol. 48, pp. 1635 - 1645, 2000.

[7] J. Lee, R. Lee, and R. J. Burkholder, "Loop star basis functions and a robust preconditioner for EFIE scattering problems," *IEEE Trans. Microwave Theory Tech.*, vol. 51, pp. 1855 – 1863, Aug. 2003.

[8] S. M. Rao, D. R. Wilton, and A. W. Glisson, "Electromagnetic scattering by surfaces of arbitrary shape," *IEEE Trans. Antennas Propagat.*, vol. 30, no. 3, pp. 409 - 418, May 1982.

[9] D. J. Taylor, "Accurate and efficient numerical integration of weakly singular integrals in Galerkin EFIE solutions," *IEEE Trans. Antennas Propagat.*, vol. 51, no. 7, pp. 1630 - 1637, July 2003.

[10] P. Acrioni, M. Bressan, and L. Perregrini, "On the evaluation of the double surface integrals arising in the application of the boundary integral method to 3-D problems," *IEEE Trans. Microwave Theory Tech.*, vol. 45, no 3, pp. 436 - 439, March 1997.

[11] T. F. Eibert and V. Hansen, "On the calculation of potential integrals for linear source distributions on triangular domains," *IEEE Trans. Antennas Propagat.*, vol. 43, no. 12, pp. 1499 - 1502, Dec. 1995.

[12] K. F. A. Hussein, "Analysis of conical equiangular spiral antenna using EFIE technique," *National Radio Science NRCS'2004*, B21, Cairo, Egypt, pp. 1-11, March 2004.

[13] A. A. Lestari, A. G. Yarovoky, and L. P. Ligthart, "Numerical analysis of transient antennas," http://www.tudelft.nl/live/binaries/33dc3ad6-3e8a-4bdd-8456-1f3d10b39c8c/doc/Lestari_turin.PDF.

[14] S. Watanabe and M. Taki, "An improved FDTD model for the feeding gap of a thin-wire antenna," *IEEE Microwave Guided Wave Lett.*, vol. 8, no. 4, pp. 152 – 154, April 1998.

[15] Y. Cho, D. Choi, and S. Park, "FDTD analysis of bow-tie antenna by incorporating approximated static field solutions," *IEEE Antennas Wireless Propagat. Lett.*, vol. 3, pp. 176 - 179, 2004.

[16] A. J. Kerkhoff, R. L. Rogers, and H.Ling, "Design and analysis of planar monopole antennas using a genetic algorithm approach," *IEEE Trans. Antennas Propagat.*, vol. 52, no. 10, pp. 2709 - 2718, Oct. 2004.

[17] K. Lee, C. Chen, F. L. Teixeira, and R. Lee, "Modeling and investigation of a geometrically complex UWB GPR antenna using FDTD," *IEEE Trans. Antennas Propagat.*, vol. 52, no. 8, pp. 1983 - 1991, Aug. 2004.

[18] A. A. Lestari, A. G. Yarovoky, and L. P. Ligthart, "An efficient ultra wideband bow-tie antenna," http://www.tudelft.nl/live/binaries/33dc3ad6-3e8a-4bdd-8456-1f3d10b39c8c/doc/Lestari_london.PDF.

[19] A. A. Lestari, A. G. Yarovoky, and L. P. Ligthart, "Ground influence on the input impedance of transient dipole and bow-tie antennas," *IEEE Trans. Antennas Propagat.*, vol. 52, no. 8, pp. 1970 - 1975, Aug. 2004.

[20] F. J. Gonzalez and G. D. Boreman, "Comparison of dipole, bowtie, spiral and log-periodic IR antennas," *Elsevier Infrared Physics Technology*, vol. 46, pp. 418 – 428, 2005.

[21] D. Uduwawala, M. Norgren, and P. Fuks, "A complete FDTD simulation of a real GPR antenna system operating above lossy and dispersive grounds," PIER, vol. 50, pp. 209 – 229, 2005.

[22] J. Thaysen, K. B. Jakobsen, and J. Apple-Hansen, "A logarithmic spiral antenna for 0.4 to 3.8 GHz," *Applied Microwave and Wireless*, http://www.ctsystemes.com/zeland/public /pg32. pdf.

[23] L. Sevgi and G. Cakir, "A broadband array of Archimedean spiral antennas for wireless applications," *Microwave Optical Tech. Lett.*, vol. 48, no. 1, pp. 195 - 200, Jan. 2006.

[24] P. Piska, "Log-spiral antenna from 2 to 40 GHz with impedance matching," http://www. ctsystemes.com/zeland/publi/j2004_266.pdf, Jan. 2004.

[25] R. Sivan-Sussman, "Various modes of the equiangular spiral antenna," *IEEE Trans. Antennas Propagat.*, vol. 11, pp. 533 – 539, 1963.

[26] D. Sievers, T. F. Eibert, and V. Hansen, "Correction to on the calculation of potential integrals for linear source distributions on triangular domains," *IEEE Trans. Antennas Propagat.*, vol. 53, pp. 3113, 2005.

Khalid F. A. Hussein was born in Hawamdiah, Giza, Egypt in 1968. He received the BSc., MSc., and PhD. from Cairo University, Faculty of Engineering, Electronics and Electrical Communications Department in 1990, 1995, and 2001, respectively. He is interested in the research fields of antennas, electromagnetic scattering, GPR, and biological effects of electromagnetic radiation.

Electric and Magnetic Dual Meshes to Improve Moment Method Formulations

M. Felipe Cátedra, Oscar Gutiérrez, Iván González, and Francisco Saez de Adana

Computer Sciences Department, Universidad de Alcalá,
28806 Alcalá de Henares, Spain
felipe.catedra@uah.es

Abstract – A new Moment Method (MM) scheme to solve the Electric Field Integral Equation (EFIE) for some ill-conditioned problems is presented. The approach is an alternative to the Combined-Field Integral Equation (CFIE). The proposed formulation employs the Impedance Boundary Condition (IBC) to compute the scattering from conducting bodies uncoated or coated by dielectric materials. The scheme uses dual meshes to represent the currents: one mesh for the electric current and another mesh for the magnetic current. Each mesh is defined by a grid of quadrangles that can be conformed to arbitrarily curved surfaces. The quadrangle grids are interlocked; the corners of the quadrangles of one mesh are the centers of the quadrangles of the other mesh and vice versa. Several examples showing the potential of the approach to solve ill-conditioned problems are included.

I. INTRODUCTION

It is well known that many electromagnetic radiation or scattering problems can be too ill-conditioned to be solved using MM. This happens, particularly, when we analyze electrically large bodies using formulations based on either the EFIE or the Magnetic-Field Integral Equation (MFIE). In these cases, the MM equation systems are ill-conditioned at the resonance frequencies of the internal cavity defined by the volume of the body under analysis [1]. In these situations it is difficult to find reliable solutions, and thus these problems suffer from poor convergence and present spurious solutions.

To reduce the difficulty of these ill-conditioned problems, several formulations have been proposed to improve the condition number of the corresponding MM matrix that may help solve these problems. One of the most powerful formulations to avoid in these ill-conditioned problems is the CFIE, which is based on a linear combination of the EFIE and the MFIE, [1], [2]. Like the MFIE, the CFIE is only applicable to closed bodies. The practice has shown that the CFIE is able to treat most problems, however there are still cases where difficulties remain because the accuracy of CFIE results depend on a correct choice in the weights of the EFIE and MFIE linear combination, and on the sampling density (number of MM subdomains per wavelength) [3]. In these cases, convergence studies on the relative weights of the CFIE and on the sampling density are performed in order to obtain "stable" solutions. These difficulties can be due to the MFIE component of the CFIE which gives poor results for sharp wedges and tips, [4].

More recently formulations based on Dual-Surface Field Integral Equations (DSFIE), [5], [6] have been investigated because they appear to be free of spurious problems and offer better solutions for bodies with sharp wedges or tips. The DSFIE forces boundary conditions on the body surface and also in a dual surface located inside the body. The separation between the surfaces is usually less than half a wavelength, and on the dual surface the boundary conditions are multiplied by a constant with an imaginary part. The DSFIE reduces spurious resonances and can treat geometries with sharp parts like cone-spheres with narrow vertices where the CFIE does not yield reliable results. However, a suitable definition of the dual surface in the DSFIE application for a particular problem needs to be adjusted in order to obtain accurate results [6]. For electrically small objects, the approach in [7], [8], which uses an accurate computation of the MM matrix terms of the MFIE and monopolar basis functions, gives reliable computations for problems with sharp wedges and tips.

Here, a numerical scheme based on a combination of the EFIE and the IBC approach, [9-11] is presented as an alternative formulation to solve these difficult problems.

The scheme, outlined in [12], uses dual quadrangular meshes. One mesh is used to represent the discretized electric current and the other to represent the discretized magnetic current. The corners of the quadrangles of one mesh are in the centers of the quadrangles of the other mesh and vice versa. The scheme combines the operator which generates the electric field due to an electric current with the operator which generates an electric field due to a magnetic current. Both currents are expanded in terms of rooftop basis functions [13]. The testing functions are blade functions, [13], defined in the mesh used to represent the electric current. With this

choice of testing and basis functions we have found a simple and accurate way to descritize the electric field due to electric and magnetic currents. The meshes are defined over the iso-parametric lines of a NURBS´s (Non Uniform Rational Bi-Spline Surface) [14]. Using the discretization procedure shown in [15-17] we can work with curved quadrangles and we do not need any re-meshing in terms of flat patches.

One objective of our approach is to analyze real conducting bodies. It can be noticed that at microwave frequencies the surface impedance of a good conductor is a hundredth or a thousandth of the free space wave impedance and the solution for a good conductor at such frequencies is very similar to the case of a perfect electric conducting (PEC) body. Therefore, the proposed approach can give good results for PEC if we model PEC with a surface impedance of about a thousandth of the free space wave impedance. One of the advantages of the present approach is that it permits the analysis of open or closed surfaces or a combination of them. The proposed approach can be considered as a regularization method, [18-19], because it diminishes the Q factor of the internal cavities of closed bodies and in this way the formulation reduces the problems of spurious responses at resonances frequencies. In addition, the approach is able to treat accurately problems with sharp wedges and tips using a reduced number of samples per wavelength. It is also useful in analyzing the scattering from lossy dielectric or conducting bodies that can be totally or partially coated by thin materials using the IBC approach.

Dual meshes of quadrangles over curved surfaces are also considered in [20] to solve a CFIE in problems with dielectric bodies. In this reference, divergence-conforming basis functions are defined over one mesh and curl-conforming basis functions over the other mesh. Either current (electric or magnetic) is represented by both types of basis functions: divergence-conforming functions when the electric(magnetic) field of an electric(magnetic) current is computed, and curl-conforming basis functions when the magnetic(electric) field of an electric(magnetic) current is evaluated. Our approach is different from that of [20] because we solve the EFIE for metallic or body governed by the IBC and therefore, we can consider open and closed surfaces. Furthermore, we only use divergence-conforming functions in such a way that each mesh is reserved to only one kind of current, one mesh for the electric current and the other one for the magnetic current.

The paper is organized as follows; section 2 presents the theoretical formulation of the EFIE considered. The dual meshes and the numerical details of the method are shown in section 3. Some results that probe the capability of the approach to solve coated bodies, and ill-conditioned problems are presented in section 4, finally, the conclusion section.

II. FORMULATION

We formulated the integral equation to be solved based on the equivalence principle, [21]. Figure 1 shows the application of the equivalence principe to obtain the fields in the region external to volume V. On the surface S that encloses volume V the equivalent currents are given by

$$\vec{J}_S(\vec{r}) = \hat{n}(\vec{r}) \times \vec{H}_T(\vec{r}), \tag{1.a}$$

$$\vec{M}_S(\vec{r}) = -\hat{n}(\vec{r}) \times \vec{E}_T(\vec{r}) \tag{1.b}$$

where $\vec{r} = r_x\hat{x} + r_y\hat{y} + r_z\hat{z}$ is the observation point on S and ($\vec{E}_T$, $\vec{H}_T$) are the total fields that are in the region external to V and can be expressed as,

$$\vec{E}_T(\vec{r}) = \vec{E}^{imp}(\vec{r}) + \vec{E}^S(\vec{r}), \tag{2.a}$$

$$\vec{H}_T(\vec{r}) = \vec{H}^{imp}(\vec{r}) + \vec{H}^S(\vec{r}) \tag{2.b}$$

where ($\vec{E}^{imp}$, $\vec{H}^{imp}$) are the fields due to the impressed currents ($\vec{J}^{imp}$, $\vec{M}^{imp}$) located outside V and ($\vec{E}^S$, $\vec{H}^S$) are the scattered fields due to the equivalent currents ($\vec{J}_S$, $\vec{M}_S$)

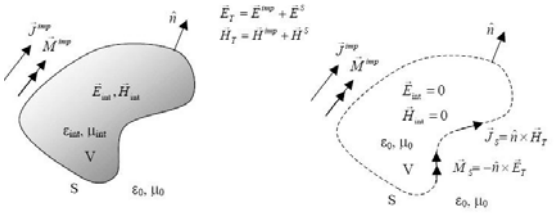

Fig. 1. The equivalence principle states that the field external to volume V in the problem shown in the left part of the figure can be computed considering the equivalent problem shown to the right.

Writing the scattered fields as a function of the electric and magnetic equivalent density currents for the external region, we get,

$$\vec{E}^S(\vec{r}) = -j\omega\frac{\mu}{4\pi}\iint_S \vec{J}_S(\vec{r}\,')G(\vec{r},\vec{r}\,')ds' - j\frac{1}{4\pi\omega\varepsilon}\nabla\left(\iint_S \nabla'\vec{J}_S(\vec{r}\,')G(\vec{r},\vec{r}\,')ds'\right) - \nabla\times\left(\frac{1}{4\pi}\iint_S \vec{M}_S(\vec{r}\,')G(\vec{r},\vec{r}\,')ds'\right), \tag{3.a}$$

$$\vec{H}^S(\vec{r}) = \nabla\times\left(\frac{1}{4\pi}\iint_S \vec{J}_S(\vec{r}\,')G(\vec{r},\vec{r}\,')ds'\right) - j\omega\frac{\varepsilon}{4\pi}\iint_S \vec{M}_S(\vec{r}\,')G(\vec{r},\vec{r}\,')ds' - j\frac{1}{4\pi\omega\mu}\nabla\left(\iint_S \nabla'\vec{M}_S(\vec{r}\,')G(\vec{r},\vec{r}\,')ds'\right). \quad (3.b)$$

These expressions can be written in a more compact form using the following linear operator notation,

$$\vec{E}^S(\vec{r}) = L_{EJ}\left[\vec{J}_S\right] + L_{EM}\left[\vec{M}_S\right], \quad (4.a)$$

$$\vec{H}^S(\vec{r}) = L_{HJ}\left[\vec{J}_S\right] + L_{HM}\left[\vec{M}_S\right]. \quad (4.b)$$

We can combine equations (2) and (4) to obtain the EFIE and MFIE formulations,

$$\vec{E}_T(\vec{r}) = \vec{E}^{imp}(\vec{r}) + \vec{E}^S(\vec{r}) = \vec{E}^{imp}(\vec{r}) + L_{EJ}\left[\vec{J}_S\right] + L_{EM}\left[\vec{M}_S\right], \quad (5.a)$$

$$\vec{H}_T(\vec{r}) = \vec{H}^{imp}(\vec{r}) + \vec{H}^S(\vec{r}) = \vec{H}^{imp}(\vec{r}) + L_{HJ}\left[\vec{J}_S\right] + L_{HM}\left[\vec{M}_S\right]. \quad (5.b)$$

For the case of a non-PEC body, like a real conducting body, a lossy dielectric body or a conducting body coated by a dielectric, the EFIE can be written as,

$$\vec{M}_S(\vec{r}) = -\hat{n}(\vec{r})\times\vec{E}^{imp}(\vec{r}) - \hat{n}(\vec{r})\times L_{EJ}\left[\vec{J}_S\right] - \hat{n}(\vec{r})\times L_{EM}\left[\vec{M}_S\right]. \quad (6)$$

By reordering the EFIE we have

$$\vec{E}^{imp}(\vec{r}) = -\hat{n}\times\vec{M}_S(\vec{r}) - L_{EJ}\left[\vec{J}_S\right] - L_{EM}\left[\vec{M}_S\right]. \quad (7)$$

Taking advantage of the duality between operators, we can write

$$L_{EM}\left[\vec{M}_S\right] = \frac{1}{\varepsilon}\nabla\times\left(\frac{\varepsilon}{4\pi}\iint_S -\vec{M}_S(\vec{r}\,')G(\vec{r},\vec{r}\,')ds'\right) = L_{HJ}^{dual}\left[-\vec{M}_S\right] \quad (8)$$

where L_{HJ}^{dual} is obtained from L_{HJ} substituting the permeability μ by the permittivity ε.

Using the IBC relation between the electric and magnetic currents,

$$\vec{J}_S(\vec{r}) = \hat{n}\times\frac{\vec{M}_S(\vec{r})}{Z_{\sup}}, \quad (9.a)$$

$$\vec{M}_S(\vec{r}) = -\left(\hat{n}\times\vec{J}_S(\vec{r})\right)Z_{\sup}, \quad (9.b)$$

we obtain the following expression of the EFIE, where we only have the current $\vec{J}_S$ as the unknown function

$$\vec{E}^{imp}(\vec{r}) = -L_{EJ}\left[\vec{J}_S\right] - \frac{\hat{n}\times\left(\hat{n}\times\vec{J}_S(\vec{r})\right)Z_{\sup}}{2} + L_{EM}^{c}\left[\left(\hat{n}\times\vec{J}_S(\vec{r})\right)Z_{\sup}\right] \quad (10)$$

where Z_{sup} stands for the surface impedance of the body and L_{EM}^{c} is the resulting operator after extracting the singular value of L_{EM}.

III. COMPUTATIONAL METHOD

The continuous operators in equation (10) can be discretized using the Moment Method. The scheme described in [15-17] has been followed to descritize the operator $L_{EJ}\left[\vec{J}_S\right]$. Using this scheme the body surface is modelled by means of NURBS´s [14]. Considering u- and v-isoparameter lines, [17], each NURBS can be split into a mesh of small curved quadrangles. The solid lines of Fig. 2 are an example of a rectangular mesh over a NURBS, which has been represented to be flat to simplify the drawing. The same figure shows a second mesh that is dual of the first one. The electric current is expanded in terms of rooftops defined over pairs of contiguous rectangles in the mesh defined by the solid lines. This expansion can be written as,

$$\vec{J}_S(\vec{r}) = \sum_{j=1}^{Nju} I_{Ju}(j)\,\vec{f}_{Ej}^{\,u}(\vec{r}) + \sum_{j=1}^{Njv} I_{Jv}(j)\,\vec{f}_{Ej}^{\,v}(\vec{r}) \quad (11.a)$$

where $\vec{f}_{Ej}^{\,u}(\vec{r})$ and $\vec{f}_{Ej}^{\,v}(\vec{r})$ are rooftop functions for the u and v-components, respectively, of the electric current (see Fig. 3). In a similar way, the magnetic current can be expressed in terms of the rooftop functions $\vec{f}_{Mj}^{\,u}(\vec{r})$ and $\vec{f}_{Mj}^{\,v}(\vec{r})$, defined over the magnetic mesh (see Fig. 3). For the magnetic current we have,

$$\vec{M}_S(\vec{r}) = \sum_{j=1}^{Nmu} I_{Mu}(j)\,\vec{f}_{Mj}^{\,u}(\vec{r}) + \sum_{j=1}^{Nmv} I_{Mv}(j)\,\vec{f}_{Mj}^{\,v}(\vec{r}). \quad (11.b)$$

We can notice that for each u-rooftop/v-rooftop of the electric current a v-rooftop/u-rooftop of the magnetic current can be found such that the two rooftops have the same centre, they are perpendicular and they have a "dual" shape (the length of one is the width of the other and vice versa). Using this duality between couples of rooftops and the IBC of equations (9) the following relations between the weights of the current expansion of equation (11) can be found,

$$I_{Mu}(j) = \frac{\Delta^j_{Mu}}{\Delta^j_{Jv}} \left\|(\hat{u}\times\hat{v})\right\| Z_{\sup} I_{Jv}(j), \qquad (12.a)$$

$$I_{Mv}(j) = -\frac{\Delta^j_{Mv}}{\Delta^j_{Ju}} Z_{\sup} \left\|(\hat{u}\times\hat{v})\right\| I_{Ju}(j), \qquad (12.b)$$

where it is assumed that the parameter coordinates have been chosen so that $(\hat{u}\times\hat{v})\bullet\hat{n}\geq 0$, Δ^j_{Mu}, Δ^j_{Jv}, Δ^j_{Mv} and Δ^j_{Ju} are the widths of rooftops $\vec{f}^{\,u}_{Mj}(\vec{r})$, $\vec{f}^{\,v}_{Ej}(\vec{r})$, $\vec{f}^{\,v}_{Mj}(\vec{r})$ and $\vec{f}^{\,u}_{Ej}(\vec{r})$, respectively, and $\left\|(\hat{u}\times\hat{v})\right\|$ is the amplitude of the vector product $(\hat{u}\times\hat{v})$. It is noticed that eventually $\hat{u}$ and $\hat{v}$ can not be orthogonal in real 3D space. However, following the IBC in equation (9) $I_{Mu}(j)$ will never depend on $I_{Ju}(j)$ because both currents are parallel (neither $I_{Mv}(j)$ will depend on $I_{Jv}(j)$). Moreover, the following relations between the total numbers of rooftops are satisfied,

$$Nmv = Nju, \qquad (13.a)$$

$$Nmu = Njv. \qquad (13.b)$$

The descritized operators can be expressed as,

$$L^D_{EJ}\left[\vec{J}_s\right] = V_{EJ}(i) = \sum_{j=1}^{Nju} Z^J_{ij} I_{Ju}(j) + \sum_{j=1}^{Njv} Z^J_{ij} I_{Jv}(j), \qquad (14.a)$$

$$L^D_{EM}\left[\vec{M}_S\right] = V_{EM}(i) = \sum_{j=1}^{Nmu} Z^M_{ij} I_{Mu}(j) + \sum_{j=1}^{Nmv} Z^M_{ij} I_{Mv}(j), \qquad (14.b)$$

where the total number of rooftops used to represent the electric or the magnetic currents is given by

$$N = Nju + Njv \qquad (15)$$

Z^J_{ij} and Z^M_{ij} represent the coupling between subdomains i and j of the electric and magnetic meshes, respectively. The terms $V_{EJ}(i)$ and $V_{EM}(i)$ stand for the impressed voltage due to the electric and magnetic current, respectively, computed in the electrical subdomain i, using as testing function a razor-blade function [15-17]. Other testing procedures can be used such as a Galerkin testing function. However, we have chosen a test by the razor-blade function because it is very simple and it needs fewer computations than other approaches, [13].

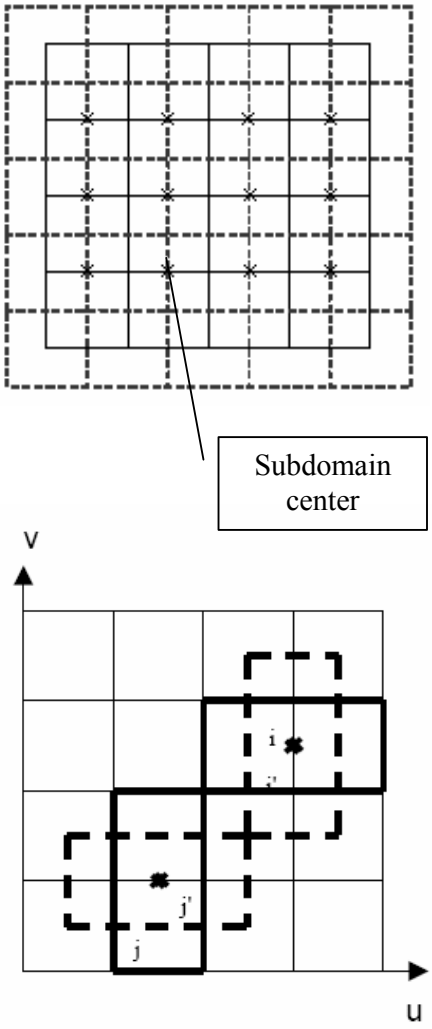

Fig. 2. A mesh of solid lines covers completely a NURBS. A second mesh is drawn using dashed lines. Both meshes are dual in the sense that the nodes of one mesh are the centres of the rectangles of the other mesh and vice versa.

The descritized operator L^D_{EJ} of equation (14.a) can be obtained from the continuous operator L_{EJ} of equation (7) following the numerical scheme shown in [13], [15-17]. The term L^D_{EM} of equation (14.b) is obtained by descritizing the operator,

$$L_{EM}^{T} = -\frac{\hat{n}\times\vec{M}_S(\vec{r})}{2} - L_{EM}^{c}\left[\vec{M}_S(\vec{r})\right]. \qquad (16)$$

Considering the testing-function corresponding to an electric rooftop completely cuts its dual rooftop of magnetic current by a transversal line (see Fig. 4).

$$Z_{ij}^{M} = \begin{Bmatrix} sign(i)(\Delta i/2) + Z_{ij}^{c} & for\ i = j \\ Z_{ij}^{c} & elsewhere \end{Bmatrix} \qquad (17)$$

where

$$sign(i) = \begin{Bmatrix} -1 & if\ subdomain\ i\ is\ a\ u-rooftop \\ 1 & if\ subdomain\ i\ is\ a\ v-rooftop \end{Bmatrix} \qquad (18)$$

and Δi is the length of the razor-blade function of subdomain i of the electrical mesh. The term Z_{ij}^{c} accounts for the coupling between the magnetic rooftop j and the electrical subdomain i considering the operator L_{EM}^{c} that gives the electric field of a magnetic current but excluding the singular value of the integral operator. The computation of the term Z_{ij}^{c} does not have serious numerical difficulties and it can be calculated following a numerical approach similar to that indicated in [15-17] for the computation of Z_{ij}^{J} .

Defining the total induced voltage $V(i)$ as,

$$V(i) = V_{EJ}(i) + V_{EM}(i) \qquad (19)$$

the following systems of linear equations can be obtained considering equations (12), (14) and (17)

$$V(i) = \sum_{j=1}^{Nju}\left(Z_{ij}^{J} - \frac{\Delta_{Mv}^{j}}{\Delta_{Ju}^{j}} Z_{\sup}\left\|(\hat{u}\times\hat{v})\right\| Z_{ij}^{M}\right) I_{Ju}(j) + \sum_{j=1}^{Njv}\left(Z_{ij}^{J} + \frac{\Delta_{Mu}^{j}}{\Delta_{Jv}^{j}}\left\|(\hat{u}\times\hat{v})\right\| Z_{\sup} Z_{ij}^{M}\right) I_{Jv}(j);$$
$$for\ \ i = 1, 2, \ldots N\ . \qquad (20)$$

Solving this system of linear equations the electric current is obtained. The magnetic current is obtained from the electric current using equation (12).

The approach is valid for problems defined by closed or open surfaces. When dealing with open surfaces the meshes near the aperture edges of the surfaces need to be defined in such a way so as to preserve the duality. Figures 5 and 6 show a way to define the meshes for a squared flat plate saving the duality between the electric and magnetic meshes. In both cases the rooftops of the two meshes cover completely the plate surface (the same domain), or in other words, the boundary of the meshes is the actual plate boundary. It can be noticed that the rooftops for representing the electric and magnetic currents are spatially shifted but additionally they are defined near the edges of the plate in different ways: we have parallel and perpendicular rooftops for representing the electric current and these rooftops are defined over couple of patches of the same size, however we have not rooftops for representing the magnetic current parallel to the edges and the rooftops for representing the magnetic current perpendicular to the edges are defined over pairs of patches of different sizes (the patches bounded by the edges have a size that is the half of the size of the other patches).

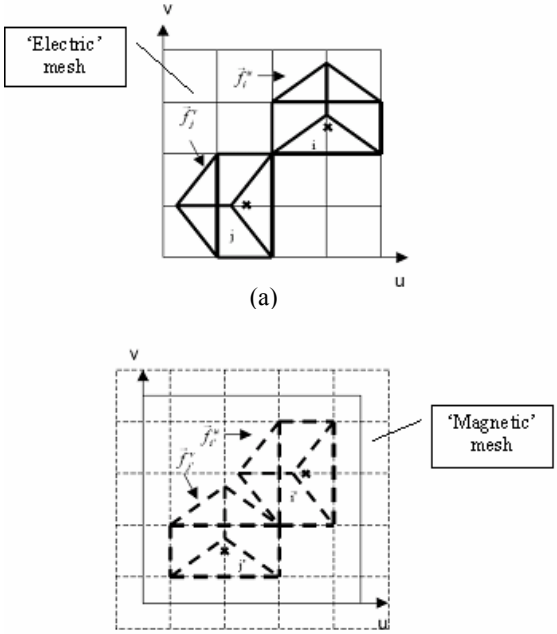

Fig. 3. (a) shows an example of rooftops for the u-component, $\vec{f}_{Ei}^{u}(\vec{r})$, and for the v-component of the electric current, $\vec{f}_{Ej}^{v}(\vec{r})$. (b) shows an example of the dual rooftops $\vec{f}_{Mj'}^{u}(\vec{r})$ and $\vec{f}_{Mi'}^{v}(\vec{r})$ used to represent the u and v-components, respectively, of the magnetic current. It can be noticed that the rooftops for the electric and magnetic components are defined in dual meshes and that the rooftop for the u-component/v-component of the electric current and the rooftop for the v-component/u-component of the magnetic current have the same centre.

IV. RESULTS

Figure 7 shows the condition number, [18], versus frequency for a sphere with a radius of 1.m for the single and the dual mesh schemes. Ten subdomains per wavelength were considered in both approaches. The meshes for the electric current were the same in both approaches. The results for the single and the dual mesh schemes were obtained considering PEC and a surface impedance of 1 Ohm, respectively.

A step of 10 MHz was used in the frequency sweep. In the frequency range considered we have two interior resonances at frequencies very close to the two large peaks. It can be appreciated that the dual mesh approach has a better behavior because the condition number for this approach is quite less than for the simple EFIE. As shown in [18] a reduction in the condition number means better convergence and more accurate results. Figure 8 presents the Bi-static RCS results for the co-polar plane cut obtained using the dual approach for the sphere at a frequency of 200 MHz, which is very close to the first internal resonance. A number of 20 divisions per wavelength and a surface impedance of 1 Ohms were considered. The results were obtained with a residual error of 10^{-3}, which was reached after 965 iterations of the BICGSTAB (L) method, [22], with L=5**,** which has been used to solve all the MM system of equations in this work. The total number of unknowns was 4836. The numerical results obtained using the dual mesh approach are compared with analytical results derived from the Mie series. A very good accuracy of the numerical results for a frequency very close to an internal resonance was obtained.

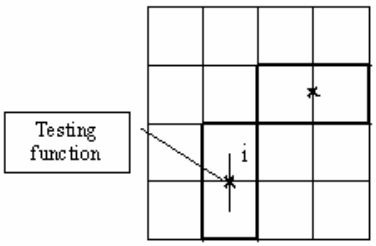

(a)

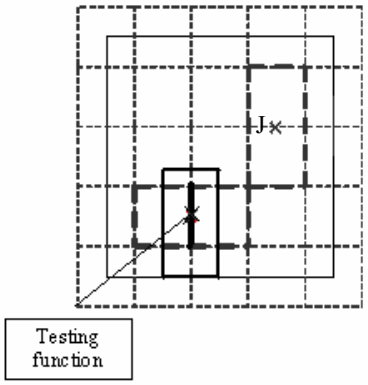

(b)

Fig. 4. a) The areas covered by the electric rooftops *i* and *j* are indicated by solid lines. The MM impedance term Z_{ij}^{J} that gives the coupling between rooftop *j* (active) and i (passive) is computed considering a blade-function as a testing function that extends along the segment indicated in the center of rooftop *i*. B) The dual magnetic rooftops are represented by dashed lines. The testing function of the electric rooftop i is a segment that cuts transversally the dual magnetic rooftop.

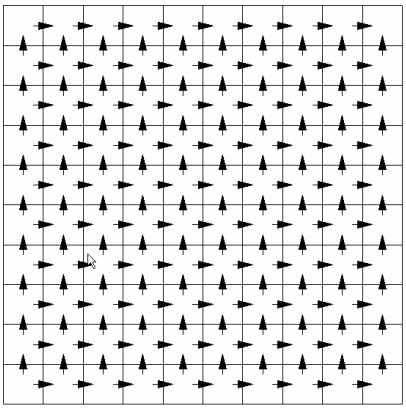

Fig. 5. Mesh used to represent the electric current in a plate. Each arrow corresponds to an electric rooftop.

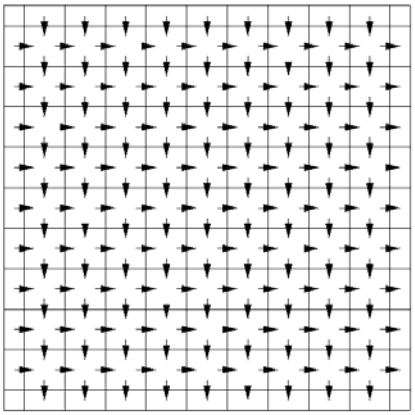

Fig. 6. Mesh used to represent the magnetic current in a plate. Each arrow corresponds to a magnetic rooftop.

In order to show the capacity of the proposed approach to treat coated conducting bodies the case indicated in Fig. 9 was chosen. Numerical and analytical values of the Bi-static RCS are compared in Fig. 9 for the E-plane cut. The surface impedance of the coat is Zs=j72.75 and the current is represented by 20 subdomains per wavelength. The numerical results for the coated sphere are obtained after 780 iterations with an error of 10^{-3}.

The second structure considered is a very sharp metallic wedge. This geometry gives a very ill-conditioned problem when a plane wave is incident in a direction perpendicular to the edge of the wedge, with the E-field normal to that edge, as indicated in the sketch of Figure 10. The geometry of the problem is defined by two plates of size 1 m × 1 m. In the back part of the wedge the plates are separated by 1.0 cm. The working frequency is 300 MHz. The Bi-static RCS results obtained using the EFIE with a single mesh and with the proposed dual mesh are shown in Figs. 11and 12, respectively. The plates were treated as PEC with the simple mesh approach and with a 1 Ω

surface impedance with the dual mesh approach. A slow convergence of the results is apparent when the number of subdomains per wavelength is changed for the single mesh case in contrast with the fast convergence of the dual mesh case. The results of both formulations converge to nearly the same values for the higher values of divisions per wavelength as shown in Fig. 12. However, the efficiency of the formulations is quite different. As shown in Table 1, the single mesh formulation needs a number of iterations greater than the dual approach for obtaining a residual error of 10^{-3}.

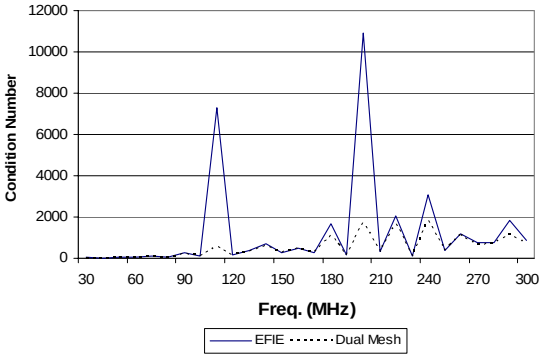

Fig. 7. Condition number versus frequency for a conducting sphere of radius 1 m.

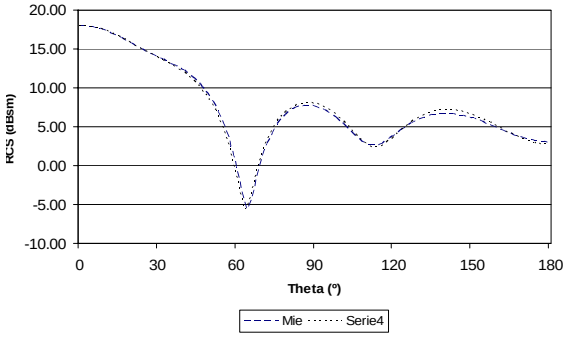

Fig. 8. Bi-static RCS results for a conducting sphere of radius 1 m, frequency 200 MHz.

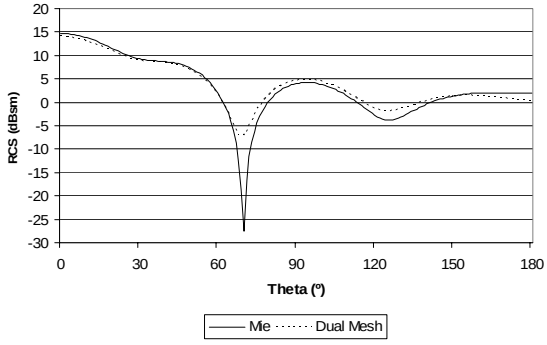

Fig. 9. Bi-static RCS results at a frequency of 300 MHz for a coated PEC sphere with an external radius 0.6 m. The coat is 0.03 m thick and has a relative permittivity of 2.0.

Fig. 10. Wedge geometry considered to compute the Bi-static RCS for a phi-cut = 0º, theta varying from 0º to 180º for an incident plane wave in the direction shown and perpendicularly polarized to the edge of the wedge.

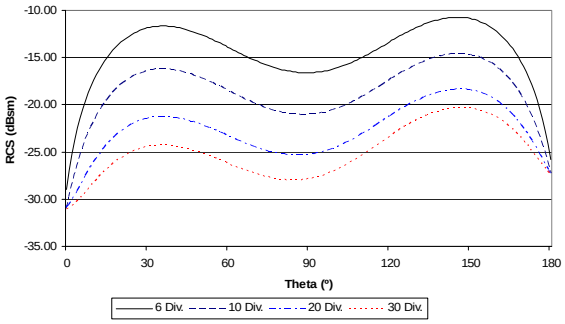

Fig. 11. Bi-static RCS results of the wedge shown in Fig. 10 obtained using the EFIE with a simple mesh for different number of subdomains per wavelength.

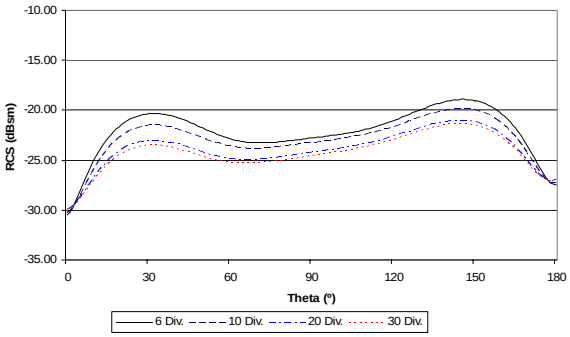

Fig. 12. Bi-static RCS results of the wedge shown in Fig. 10 obtained using the dual mesh approach for different number of subdomains per wavelength.

Table 1. Comparison between the numbers of iterations required for the single and dual mesh approaches for obtaining a residual error of 10^{-3} for different sampling densities for the wedge case.

Subdomains per wavelength	Single Mesh	Dual Mesh
6	2.061	1.310
10	19.189	2.495
20	19.304	3.388
30	20.684	4.460

The following case considered is of a rotor structure shown in Fig. 13. This structure is the bottom part of the CHANNEL cavity from ONERA. The height of the structure is 13.7 cm and the external cylinder has a diameter of 18.8 cm. This cylinder has

been modelled as a volumetric structure with a 2 mm of thickness. The blades have a thickness of about 4 mm. The coordinates system has been fixed considering the z axis in the rotor axis. As can be noticed the rotor is a structure with lots of electrically thin plates oriented in many directions, and is quite a difficult problem for the EFIE because it presents lots of thin wedges and therefore it is an interesting problem for testing the efficiency of the dual mesh approach. Figures 14 and 15 show results of the Bi-static RCS of the rotor structure for a frequency of 3.0 GHz and for a θ=0º incidence. Again, the plates were treated as PEC with the simple mesh approach and with 1.Ω of surface impedance with the dual mesh approach. Results were obtained from different values of the sampling density. Table 2 shows the convergence rate for both approaches. It is evident that the dual approach convergence rate always is better than the simple mesh approach.

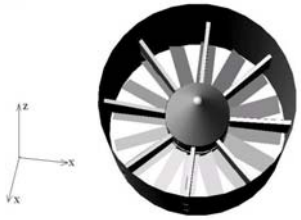

Isometric view

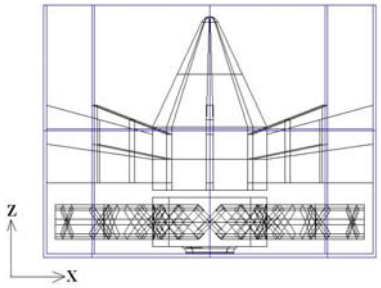

Profile view

Fig. 13. Isometric and profile views of the rotor located at the end of the engine cavity "CHANEL" from ONERA.

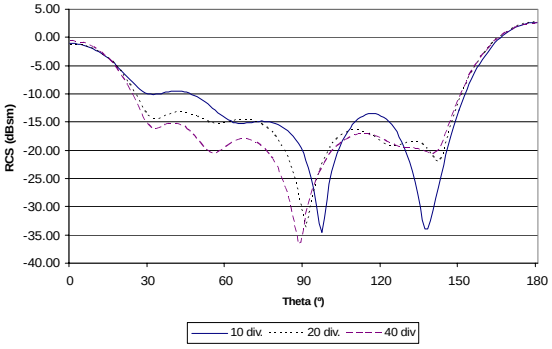

Fig. 14. Bi-static RCS results of the CHANEL rotor obtained using the EFIE approach for different subdomain densities.

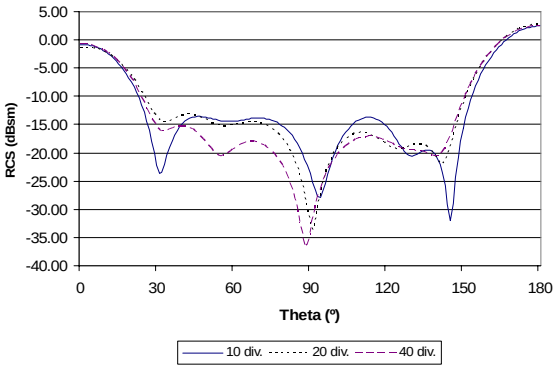

Fig. 15. Bi-static RCS results of the CHANEL rotor obtained using the dual mesh approach for different subdomain densities.

Table 2. Comparison between the numbers of iterations required for the single and dual mesh approach for obtaining a residual error of 10^{-3} for different sampling densities for the CHANEL rotor case.

Subdomains per wavelength	Single Mesh	Dual Mesh
10	465	399
20	4.233	3.950
30	9.325	8.127

V. CONCLUSIONS

A new approach to solve the EFIE using a MM formulation based on dual meshes and on the IBC has been presented. Each mesh is defined by a grid of quadrangles. The meshes are dual because the quadrangle corners of one mesh are the centers of the quadrangles of the other mesh and vice versa**.** One of the meshes is used to represent the electric current and the other the magnetic current. In both meshes rooftop and razor-blade functions are used as basis and testing functions, respectively. This choice of the basis and testing functions enforces the duality of the formulation: the segment on which the testing function of one mesh extends is perpendicular and completely crosses the basis function of the other mesh. This fact is important because it makes the computation of the electric field due to a magnetic current more easy and accurate.

Any body over which the IBC applies can be treated with the dual mesh formulation including realistic conducting bodies and lossy dielectric bodies. PEC bodies can be analyzed with a very small error by assuming they present small surface impedances, for example a thousandth of the free space wave impedance. All these bodies can be analyzed very efficiently using this method because it requires a lower number of subdomains per wavelength and it

presents better convergence when the MM system of equations is solved by an iterative method. Using the IBC approach we only shall consider the electric current unknowns. The approach is useful to solve structures with open or closed surfaces and it does not suffer a loss of convergence at the frequencies of the internal resonances or other classes of problems, for instance ill-conditioning due to very narrow wedges. In the future the potentiality of the dual mesh approach will be extended to solve the CFIE.

ACKNOWLEDGEMENTS

This work has been supported in part by the Spanish Department of Education and Science, Project TEC 2004-03187, and by the Madrid Community Project S-0505/TIC/0255.

The authors would like to thank ONERA for the geometry data of the rotor of the CHANNEL cavity.

REFERENCES

[1] W. C. Chew, J. Jin, E. Michielssen, and J. Song, *Fast and Efficient Algorithms in Computational Electromagnetics*, Artech House Inc. 2001.

[2] J. R. Mautz and R. F. Harrington, "H-field, E-field, and Combined-Field Solutions for Conducting Bodies of Revolution," AEU, vol 32, pp. 157-164, 1978.

[3] W. D. Wood Jr *et al*, "Convergence Properties of the CFIE for several Conducting Scatterers," *Proceedings of Applied Computational Electromagnetics*, Monterey, CA, pp 677-682, March 2000.

[4] R. A. Shore and A. D. Yaghjian, "Dual-Surface electric Integral Equation," Air *Force Research Laboratory* Rep. AFRL-SN-HS-TR-2001-013, 2001.

[5] V. V. S. Prakash and R. Mittra, "Dual Surface Combined Field Integral Equation for Three-Dimensional Scattering," *Microwave and Opt. Tech. letts.,* vol. 29, pp. 293-296, June 2001.

[6] R. A. Shore and A. D. Yaghjian, "Dual-Surface Integral Equation in Electromagnetic Scattering," *IEEE Trans. Antennas and Propag.*, vol. 53, pp. 1706-1709, May 2005.

[7] J. M. Rius, E. Úbeda, and J. Parrón, "On The Testing of the Magnetic Field Integral Equation With RWG Basis Functions in Method of Moments," *IEEE Trans. Antennas and Propag.*, vol. 49, pp. 1550-1553, November 2001.

[8] E. Ubeda and J. M. Rius, "Novel monopolar MFIE MoM-discretization for the scattering analysis of small objects," *IEEE Trans. Antennas and Propag.*, vol. 54, pp. 50-57, January 2005.

[9] S. Lee and W. Gee, "How good is the impedance boundary condition?," *IEEE Trans. Antennas and Propag.,* vol. 35, pp. 1313- 1315, November 1987.

[10] T. B. A. Senior and J. L. Volakis, "Approximate boundary conditions in electromagnetics," *The Institution of Electrical Engineers*, 1995.

[11] Y. Rahmat-Samii and D. J. Hoppe, "Impedance Boundary Conditions in Electromagnetics," *Hemisphere Pub.*, 1995.

[12] O. Gutierrez, J. Bueno, I. Gonzalez, and F. Catedra, "An Improvement of the Method of Moments Combining EFIE and MFIE Formulations for Coated Conducting Bodies," *2005AP/S-URSI International Symposium, Washington*, July 2005.

[13] A. W. Glisson and D. R. Wilton, "Simple and Efficient Numerical Methods for Problems of Electromagnetic Radiation and Scattering from Surfaces," *IEEE Trans. Antennas and Propag.*, vol. 28, pp. 593-603, October 1997.

[14] G. Farin, *Curves and Surfaces for Computer Aided Geometric Design: A practical Guide*, Academic Press.

[15] L. Valle, F. Rivas, and M. F. Cátedra, "Combining the Moment Method with Geometrical Modelling by NURBS Surfaces and Bezier Patches," *IEEE Trans. Antennas and Propag.*, pp. 373-381, March 1994.

[16] F. Rivas, L. Valle, and M. F. Cátedra, "A moment method formulation for the analysis of wire antennas attached to arbitrary conducting bodies defined by parametric surfaces," *Journal of Applied Computational Electromagnetics Society Journal*. pp. 32-39, July 1996.

[17] M. F. Cátedra, F. Rivas, and L. Valle, "A Moment Method Approach Using Frequency Independent Parametric Meshes," *IEEE Trans. Antennas and Propag.*, pp. 1567-1568, October 1997.

[18] C. A. Klein and R. Mittra, "An Application of the 'Condition Number' Concept to the Solution of Scattering Problems in the Presence of the Interior Resonances Frequencies," *IEEE Trans. Antennas and Propag.*, vol. 23, pp. 431-435, May 1975.

[19] G. A. Deschamps and H. S. Cebayan, "Antenna Synthesis and Solution of Inverse Problems by Regularization Methods," *IEEE Trans. Antennas and Propag.*, vol. 20, pp. 268-274, May 1972.

[20] M. H. Smith and A. F. Peterson, "Numerical Solution of the CFIE Using Vector Bases and Dual Interlocking Meshes," *IEEE Trans. Antennas and Propag.*, vol. 53, pp. 3334-3339, October 2005.

[21] C. Balanis, *Advanced Engineering Electromagnetics*, John Wiley&Sons, 1989, New York.

[22] G. L. G. Sleijpen and D. R. Fokkema, "BICGSTAB(L) For Linear Equations

Involving Unsymmetric Matrices With Complex Spectrum," *Electronic Transactions On Numerical Analysis,* vol. 1, pp. 11-32, September 1993.

Manuel F. Catedra received his M.S. and Ph. D. degrees in Telecommunications Engineering from the Polytechnic University of Madrid (UPM) in 1977 and 1982 respectively. From 1976 to 1989 he was with the Radiocommunication and Signal Processing Department of the UPM. He has been Professor at the University of Cantabria from 1989 to 1998. He is currently Professor at the University of Alcalá, in Madrid, Spain.

He has worked on about 60 research projects solving problems of Electromagnetic Compatibility in Radio and Telecommunication Equipment, Antennas, Microwave Components and Radar Cross Section and Mobile Communications. He has developed and applied CAD tools for radio-equipment systems such as Navy-ships, aircraft, helicopters, satellites, the main contractors being Spanish or European Institutions such as EADS, ALCATEL, CNES, ALENIA, ESA, DASA, SAAB, INTA, BAZAN, INDRA, the Spanish Defence Department.

He has directed about 15 Ph. D. dissertations, has published about 45 papers (IEEE, Electronic Letters, etc), two books, about 10 chapters in different books, has given short courses and has given around a hundred and thirty presentations in International Symposia.

Oscar Gutiérrez Blanco was born in Torrelavega, Spain, in 1970. He received the BS and MS degrees in Telecommunications Engineering from the University of Cantabria, Spain, in 1993 and 1996, respectively. From 1995 to 1998, he was with the Communications Engineering Department of the Cantabria as Research assistant. He received the Ph. D. degree in Telecommunication from the Alcala university, Spain, in 2002. From 1998 to 2000, he was with the Signal Theory and communications Deparment of the Alcala University, Madrid. In 2001, he is currently an assistant professor in the Computational Science Department in the Alcalá University, Madrid.

He has participated in more than 40 research projects, with Spanish and European companies, related with analysis of on board antennas, radio propagation in mobile communication, RCS computation, etc. His research interests are in high-frequency methods in electromagnetic radiation and scattering, and ray-tracing acceleration techniques.

Iván González Diego was born in Torrelavega, Spain in 1971. He received the B.S. and M.S. degrees in telecommunications engineering from the University of Cantabria, Spain, in 1994 and 1997 respectively, and the Ph. D. degree in telecommunications engineering from the Univeristy of Alcalá , Madrid, Spain in 2004. He worked in the Detectability Laboratory of the National Institute of Technical Aerospace (INTA), Madrid, Spain and as an Assistant Researcher at the University of Alcalá. He currently works as Assistant Professor in this university. He has participated in several research projects with Spanish and European companies, related with analysis of on board antennas, radio propagation in mobile communications, RCS computation, etc. His research interests are in numerical methods applied to the electromagnetic problems, like genetic algorithms and numerical methods to represent complex bodies for the electromagnetic techniques.

Francisco Saez de Adana was born in Santander, Spain, in 1972. He received the BS, MS and Ph. D. degrees in Telecommunications Engineering from the University of Cantabria, Spain, in 1994, 1996 and 2000, respectively. Since 1998 he works at the University of Alcalá, first as assistant professor and since 2002 as professor. He has worked as faculty research at Arizona State University from March 2003 to August 2003.

He has participated in more than forty research projects with Spanish, European, American and Japanese companies and universities, related with analysis of on board antennas, radio propagation in mobile communication, RCS computation, etc. He has directed two Ph. D. Dissertations, has published sixteen papers in referred journals and more than 40 conference contributions at international symposia. His research interests are in areas of high-frequency methods in electromagnetic radiation and scattering, on-board antennas analysis, radio propagation on mobile communications and ray-tracing acceleration techniques.

Optimum Plannar Antenna Design Based on an Integration of IE3D Commercial Code and Optimization Algorithms

Hsi-Tseng Chou, Yuan-Chang Hou, and Wen-Jiao Liao

The Department of Communication Engineering, Yuan Ze University
135 Yuan-Tung Rd., Chung-Li 320, Taiwan
Email: hchou@saturn.yzu.edu.tw

Abstract – The optimum planar antenna design utilizing a simulation tool based an integration of IE3D commercial code as an electromagnetic computational engine and an add-on optimization algorithm is proposed in this paper. The work is motivated by the popularity of planar antennas and the need of customized designs in industrial applications, which can be effectively achieved by using simulation tools. Currently available commercial codes are reliable and relatively accurate in the analysis with more efforts tending to enhance the efficiency. The quality of the antenna design will mainly rely on an effective optimization algorithm that can be and should be developed independently according to engineers' own need since the variables and cost functions for optimization can be flexibly selected. The integration of existing analysis codes, as mentioned above, and self-developed algorithms will be most effective for an engineer in the customized antenna design. The concepts and strategies are addressed with numerical examples to validate.

I. INTRODUCTION

The fast growing of wireless communications has spurred an increasing need for customized antenna designs. Microstrip (or planar) antennas, which are conformal and can be integrated within devices' profiles, provide a very flexible design. In realistic applications, it however appears more constraints on the antenna design since portable devices usually have limited PCB space in irregular shapes. Thus a reliable computer-aided tool is very essential to less experienced engineers and capable of designing antennas in an effective fashion without ending up with tuning antenna parameters in an ad hoc manner, which is time consuming and inefficient.

Considering the development of design tools, currently available commercial codes such as IE3D and HFSS are very reliable and relatively accurate in the analysis with currently more efforts tending to enhance the efficiency. The quality of the antenna design will mainly rely on an effective optimization algorithm that can be and should be developed independently according to engineers' own need since the variables and cost functions for optimization can be flexibly selected. Thus it can be foreseen that more efforts of the engineers will be spent on developing a design procedure and algorithms to optimize their antenna designs. This work demonstrates the idea that an external design optimizer can work with a commercial EAD tool. An algorithm developer can choose either genetic algorithm or other optimizers for design optimization. The integration of existing analysis codes, as mentioned above, and self-developed algorithms will be most effective for an engineer in the customized antenna design.

This code integration concept is demonstrated in this work by using IE3D as the electromagnetic (EM) computation engine. A program is designed to automate the optimization process. The program monitors the optimization process and interacts with the computation engine. The process begins with an initial design. The computation engine returns prescribed performance parameters. The program next adjusts the stepping size of the adjustable parameters according to its built-in optimization algorithm. Above process is performed iteratively until the desired performance or the specified iteration number is met. Several optimization schemes have been implemented including classical Euler method, predictor correlator method and other nonlinear optimization methods. In this paper, generic algorithm (GA) [1-4] is employed to demonstrate the concept because it can be effectively employed to optimize discrete variables.

As to the application potential, such an add-on optimization program could be made more capable than the optimization functions provided by commercial simulation packages. Comparing to the existing GeneticEM optimizer of IE3D, which can tune multiple geometric parameters that is already defined in the initial design, an external add-on optimizer provides more degree of freedom in modifying the problem geometry. Though not demonstrated in the following design example, it is possible to have the optimizer choosing from a variety of antenna structures to meet specified performance needs. For example, the optimizer may be allowed to choose from either corner truncated patch or diagonally-fed square patch to produce circular polarization. Furthermore, an external add-on optimizer enables the developer to directly access the optimizing

algorithm. GA related parameters such as the population size and gene number can be adjusted to achieve an efficient optimization according to the application characteristics. Design packages from different venders could also be coordinated using this intermediate program, and thus create most values in the antenna design.

This paper is formatted in the following order. Section 2 addresses the implementation strategies of this code integration as well as the interface to interact with the IE3D. Section 3 demonstrates the concepts by considering a dual-band antenna design for the applications of Wi-Fi [5] and dedicated short range communication systems (DSRC) [6]. Finally a short discussion is presented in section 4 for a conclusion.

II. IMPLEMENTATION STRATEGIES

A. General Concepts and the Program Structure

The general concept of this work is composed by a general procedure of an antenna design optimization as illustrated in Fig. 1(a). It starts with an initial guess of the antenna structure and parameter inputs to classify the antenna performance expectations through an EM analysis, where the analysis is performed by IE3D. The antenna performance is justified by a comparison with the expectation through an evaluation of a cost function or fitness function. If the expectation is reached, then the design procedure stops. Otherwise, a new design with improved performances is created based on the values of the fitness function, where the new antenna structure is produced by a genetic algorithm procedure. This new antenna structure is used in the next iteration (or next generation) for EM analysis to justify the performance with respect to the expectation. This procedure continues until the expectation is reached. To realize the concepts with respect to the utilization of IE3D as an EM analysis engine with an add-on procedure of generic algorithm to adjust the antenna's parameters, the implementation of the program structure is illustrated in Fig. 1(b). It begins with the establishment of an automation control program that first sets up the program control parameters such as the desired antenna performance and the maximum number of iteration, and then establishes the procedure of code control and optimization algorithm. The initial antenna design is performed by IE3D program to yield the analysis of antenna performance parameters, which is used to generate the fitness value. Thus the parameters with respect to the antenna operation such as the operational frequency bands are input through IE3D GUI. The main body of the automation program is composed by four blocks as illustrated in Fig. 1(b). The "geometry controller" specifies the parameters and variables of the antenna structure to be optimize such as the dimensions and coordinates of particular geometries in the structure, which are used in the "GA operator block" to produce new values for creating new antenna structure with superior performances. The "GA operator" implements the GA algorithm. Also the antenna performance with respect to the design anticipation is evaluated in the "fitness function" block to justify whether the expectation has been reached based on the analysis of "simulation" block which uses the IE3D as the EM analysis tool. If the fitness value meets the prescribed conditions of requirement, we can declare that a satisfying design is found. Otherwise, the GA operator will sort designs according to the fitness values, then generate new designs as well as new values of the parameters for the next generation from superior designs.

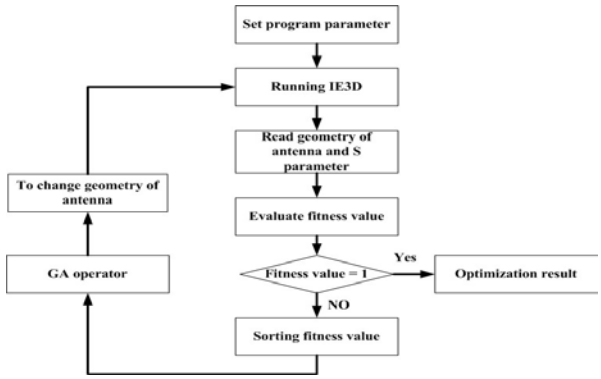

(a) Optimization Procedure.

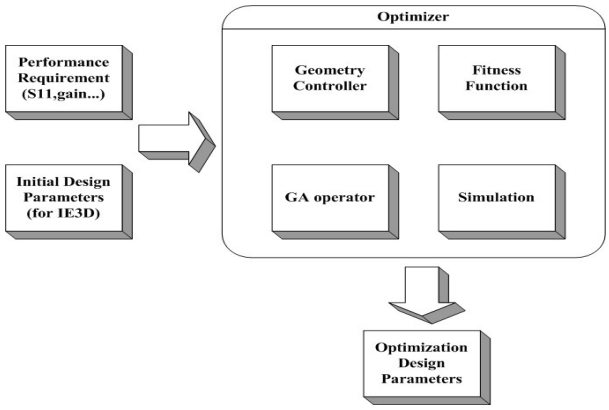

(b) Automation Control Program Structure.

Fig. 1. The demonstration of the antenna design optimization procedure as well as the program structure of the proposed strategies to integrate IE3D commercial analysis code with an optimization algorithm based on genetic algorithm.

B. Generic Algorithm for Antenna Design Optimization ("GA operator" block)

GA is employed to optimize the antenna structure to meet the prior requirement of the antenna operation. It sorts the design according to computed values of the fitness function, and creates a better design according to the superior designs in the previous generations as illustrated in Fig. 2 (a), where eight genes (n = 8, each gene corresponds to a set of parameter's values for an individual antenna structure) were assumed to generate superior new antenna designs. The fitness function is computed for each gene, and compared to justify the superiority of the antenna performance. In Fig. 2 (a) a larger fitness value indicates a superior performance of the antenna associated with this gene. The superior genes are retained while the rest is abandoned in the next generation, where new offspring genes are produced from the superior parent genes (i.e., the superior genes retained in the previous generation) to form the same number of genes in the competition based on a roulette wheel parent selection. The creation of the new offspring genes uses either crossover or mutation methods as illustrated in Fig. 2 (b). The crossover method means that design parameters are swapped between two parent designs, while the mutation method implies that a parameter of the parent design is replaced with a randomly generated number. The decision of using either crossover or mutation method is also random. The selection of parent designs is done via the roulette wheel method, that is, a superior design is assigned to a larger piece in the wheel, which is equivalent to a larger probability density value. Therefore, stronger parents are more likely to produce more children.

In this work, the following formulations are found to work well for the crossover method [7] to produce an offspring gene X_o,

$$X_o = 0.5X_{p,1} + 0.5X_{p,2} \tag{1}$$

$$X_o = 1.5X_{p,1} - 0.5X_{p,2}, \tag{2}$$

and

$$X_o = -0.5X_{p,1} + 1.5X_{p,2} \tag{3}$$

where $X_{p,1}$ and $X_{p,2}$ are the superior parent genes. Also mutation can use the following formulation,

$$X_o = X_p + \Delta X \tag{4}$$

where X_p is the superior gene and ΔX is an random number.

After the number of the iteration has been reached, the gene with largest fitness value (or best performance) is employed to determine the optimized antenna structure.

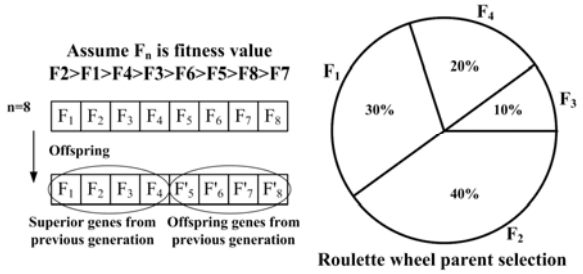

(a) The general concept of GA.

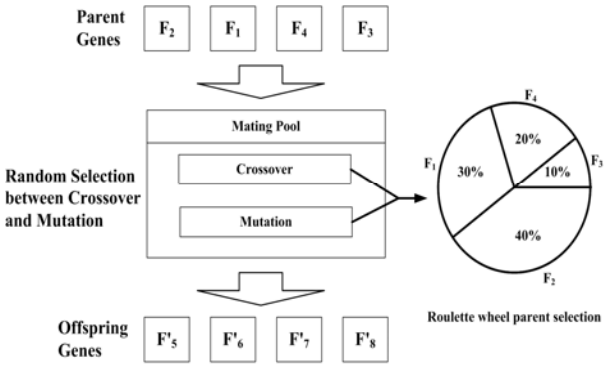

(b) Methods to produce superior offspring genes.

Fig. 2. Illustrations of genetic algorithm to generate new antenna structures with superior performance.

C. Interface to Interact with IE3D Code

(1) *Initial parameter setup*

An initial antenna design is first performed within the framework of IE3D. The fundamental parameters such as the sampled frequencies, radiation patterns and geometry of antenna structure should be assigned tentatively. Figure 3 shows the input for a demonstration example of a simple microstrip antenna design for WLAN applications, where the antenna geometry is shown in Fig. 3 (a) with the return loss of antenna obtained in Fig. 3 (b). The parameter setup page of IE3D is shown in Fig. 3 (c), where the parameters designated will be used throughout the procedure of the antenna design within the proposed work of this paper. Three important parameters on this setup pages are the sampled frequencies, cell sizes and the "After setup" operation selection. In this case, 31 sampled frequencies between 2.3 GHz and 2.6 GHz are selected for IE3D analysis, which will be used in the later optimization of return loss. The cell size should be properly selected to assure accurate analysis at the sampled frequencies. The "After Setup" should select "Invoke IE3D" so that the required data files of antenna geometry (filename.geo file) and return loss data (filename.sp file) will be created, which

can be used later as an interface to interact with IE3D and the GA algorithm for antenna design optimization. Note that if "Create .sim file only" is selected, then only the file to record the simulation procedure (filename.sim file) is created.

The selection of the initial antenna design plays a significant role for the success of the optimization procedure. It should provide the essential possibility to achieve the design goal since the optimization procedure tends to minor tune of the antenna structure. For example, if a dual band antenna design is of interest, the initial antenna design should provide a dual band operation, and the GA will tune the antenna structure to adjust the operational bands to the designated bands of interest.

(2) *Interaction via the IE3D's input and output files*

Once the initial antenna geometry as well as the run parameters are designated, they are recorded in data files as the inputs to control the IE3D analysis in each iteration without any changes throughout the entire antenna design procedure except the antenna geometry file (i.e., filename.geo) that records the coordinates of the initial antenna geometry as shown in Figure 4 and will be changed at each iteration by the GA procedure to obtain new antenna design with superior performance. Note that a new design will be created if any of the coordinates is changed, and re-running IE3D will result in the performance analysis of the new antenna. The antenna performance such as the return loss of the example demonstrated in this paper will be recorded in a data file (i.e., filename.sp) as shown in Figure 5, which will be used to compute the fitness functions for the use in the GA to create the coordinates of a new antenna structure.

(3) *Execution of IE3D program based on DOS command*

The execution of the entire antenna design procedure is performed within the controls of the automation program. The program shall know when to call the IE3D for the EM analysis, when the IE3D has completed the analysis, and where to pass the parameters of IE3D to the GA operator. The access of the IE3D is performed through the DOS command by setting the common paths in "C:\autoexec.bat" so that the paths can be linked as the computer starts. The commands are shown in Figure 6 where the first line shows the path to find the IE3D program and the second line shows the path of the automation program. The IE3D execution is performed through a run-time function. In Virtual Fortran, the command is "AA=RUNQQ ("IE3D","filename.sim")", where the "filename.sim" passes the IE3D parameters to the IE3D for execution. The **RUNQQ** function

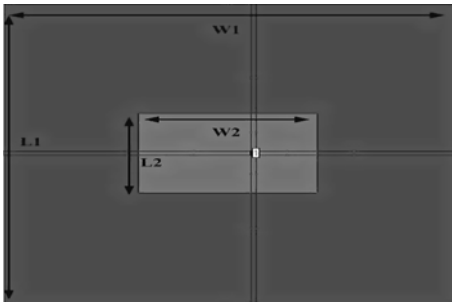

(a) Antenna geometry.

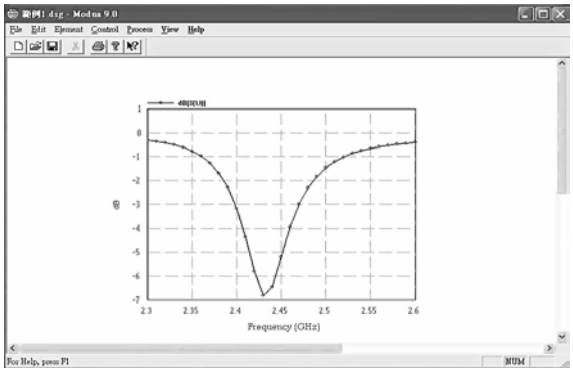

(b) IE3D parameter setup page.

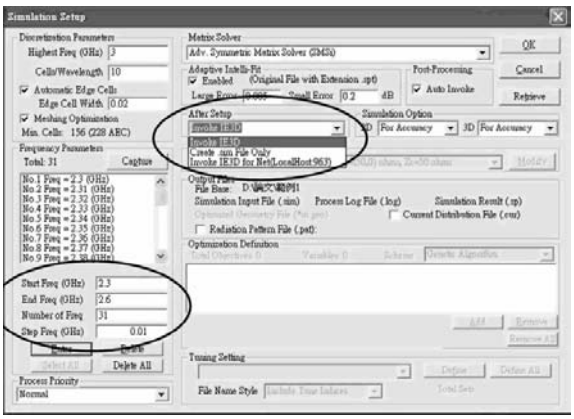

(c) Return loss of the antenna.

Fig. 3. An example of an initial antenna design using IE3D for WLAN applications. In (a) the dimensions of the geometry are W1 = 75 mm, W2 = 30 mm, L1 = 75 mm and L2 = 20 mm with a thickness 1.6 mm for an Fr4 substrate ($\varepsilon_r = 4.4$).

executes a new process for the operating system using the same path, environment, and resources as the process that launched it. The launching process is suspended until execution of the launched process is complete. "AA" is dummy variable to record the status of the function execution. If the program executed with **RUNQQ** terminates normally, the exit code of that

program is returned to "AA". If the program fails, -1 is returned to "AA".

This usually involves identification of numerical accuracy or other limitations, solution convergence, numerical and physical modeling error, and parameter tradeoffs. However, it is also permissible to address issues such as ease-of-use, set-up time, run time, special outputs, or other special features.

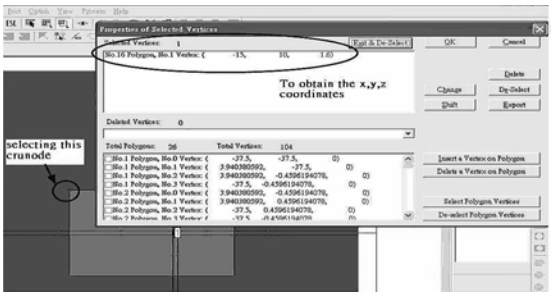

(a) IE3D GUI window for the coordinates of the polygon's vertex.

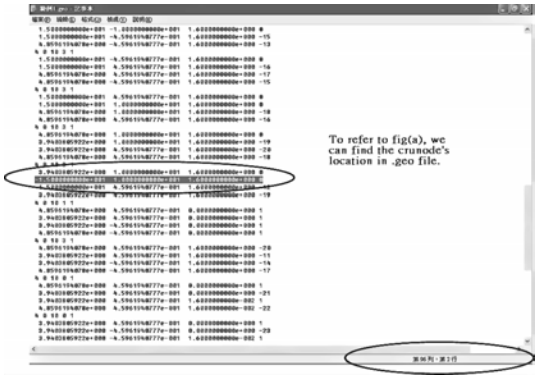

(b) Geometry file records the coordinates of the polygon's vertex.

Fig. 4. The IE3D GUI and *.geo file to record the coordinates of the antenna structures.

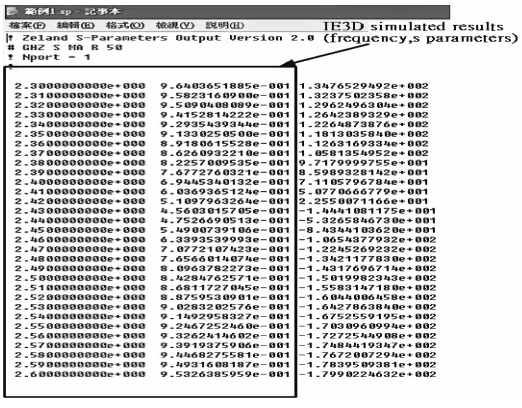

Fig. 5. The IE3D *.sp file to record the return loss at sampled frequencies.

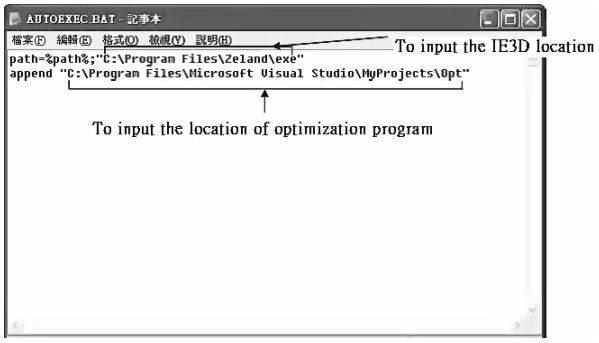

Fig. 6. The setting of the "C:\autoexec.bat" for the common paths setup.

III. DEMONSTRATION EXAMPLES: DUAL BAND PATCH DESIGNS

The proposed strategies are demonstrated by considering a dual band microstrip patch antenna design for the applications of Wi-Fi [5] and dedicated short range communications (DSRC) [6] where the operational frequency bands of 2.45 GHz and 5.8 GHz are pursued. Thus the GA operator uses a fitness function based on the return loss spectra to evaluate the performance of a design. The fitness function for n^{th} gene is defined by

$$F_n = \frac{1}{\left(\sum_{m=1}^{m} C_{nm}\right)+1} \tag{5}$$

where

$$C_{nm} = \begin{cases} S_{11}(f_m) - S_{11}^*(f_m) & \text{if} \quad S_{11}(f_m) > S_{11}^*(f_m), \\ 0 & \text{if} \quad S_{11}(f_m) \le S_{11}^*(f_m) \end{cases} \tag{6}$$

and M sampled frequency points are selected in the designated frequency bands with f_m being the sampled frequency so that we can handle dual band or multiple band designs. For each frequency point, if the simulated S_{11} (in dB) is lower than the prescribed S^*_{11}, C_{nm} is assigned as 0. Otherwise, the difference in simulated and desired values in dB is assigned to C_{nm}. The summation of C_{nm} contributes to the denominator of F_n. A proper design, which meets the S_{11} specifications in all bands, will yield a fitness value of one (F_n =1) that is the largest value to occur in the optimization procedure. Also the larger value of F_n implies a superior performance as required in the GA procedure.

Figure 7 shows the geometry of the proposed dual band antenna design, which is basically a patch printed on a substrate which is placed by Z_1 beyond a ground plane. The patch is fed slightly off center. There are several slots cut into the patch, which perturb the fields to yield multiple resonant modes. Those geometric parameters

such as the slot position, slot length, slot width and patch dimensions can be altered to yield different designs, and thus can be used as parameters in the GA operator to create new design by changing their values according to the algorithm. The initial design with the dimensions shown in Table 1 is capable of creating two resonance frequencies as shown in the return loss of Fig. 8. The GA procedure tends to adjust the resonant frequencies to the designated frequencies of interest. In the procedure, each subsequently created design by GA is fed to the IE3D program for performance analysis, where the return losses at sampled frequencies are simulated and used to compute the fitness function as defined in equation (5). If the fitness value has not met the prior designated requirement, it is fed back to the GA operator to produce a new design of the next generation.

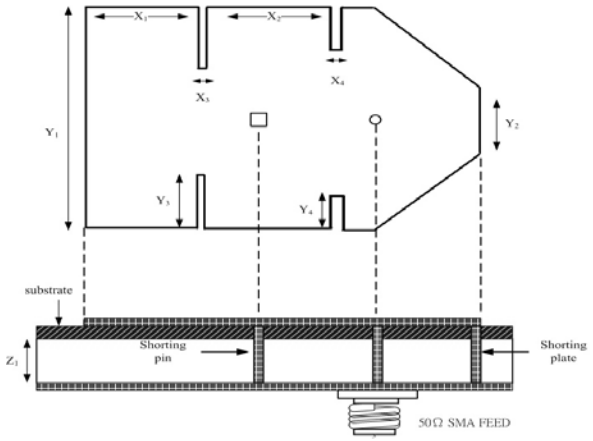

Fig. 7. Geometry of the initial patch antenna design.

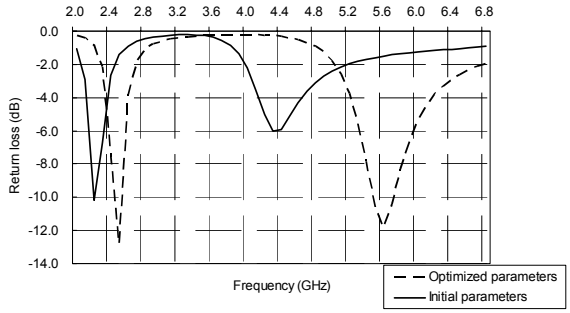

Fig. 8. Comparison of simulated reflection spectra of the patch before and after optimization.

In this case, the optimization goal is to obtain the first resonance at 2.45 GHz with a return loss smaller than -7 dB, which is equivalent to a VSWR of 2.5, and the second resonance should be broad enough to cover the 5.2 GHz to 6 GHz band. An optimized design was derived by altering eight geometric parameters sequentially as shown in Table 1. For each parameter, four iterations were executed. The optimization process took on a Pentium IV machine of 2.4 GHz with 512 GB RAM, approximately 36 hours to complete. In each IE3D simulation, antenna performance was examined from 2 GHz to 6.8 GHz with a 0.1 GHz frequency step. The cell size is one fifteenth of a wavelength. Most of the time was spent on the IE3D program, which is proportional to the complexity of the simulated structure, and the time spent on the GA operator is negligible. Figure 8 shows the comparison of return loss spectra of the initial and optimized designs. According to this figure, both resonant bands are shifted up and the higher band fits the 5.2 GHz to 5.8 GHz range. The optimized values of the antenna dimensions are also shown in Table 1.

Table 1. The initial and optimized values of the antenna dimensions as illustrated in Fig. 7.

Parameter	Initial Values(mm)	Optimized Values(mm)
X1	4	8
X2	2	8.5
X3	2	0.5
X4	2	1
Y1	16	18
Y2	18	5.2
Y3	4	4.5
Y4	4	2.9
Z1	4	3.2

To validate the optimization scheme, we manufactured the initial and optimized patch designs and measured their reflection coefficients. Figure 9 shows the two return loss spectra. The null levels are slightly different from simulation results. However, the curves exhibit a similar trend in the movement of resonant ban locations. The difference can be attributed to the error in selecting material parameters. Nevertheless, the result indicates the proposed approach can effectively predict the performance changes due to geometric variation, which in turn validate the optimization scheme.

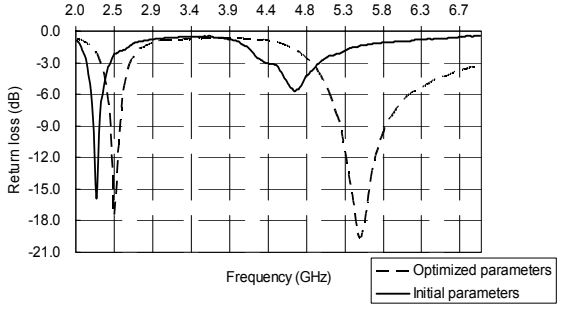

Fig. 9. Comparison of measured reflection spectral of initial and optimized designs.

The radiation patterns of the antenna were measured and shown in Fig. 10 at 2.47 GHz and 5.6 GHz, where the patterns as well as the beamwidths meet the general behaviors of a general planar microstrip antenna. Also gains of these two bands are 0.23 dBi and 2.5 dBi, respectively.

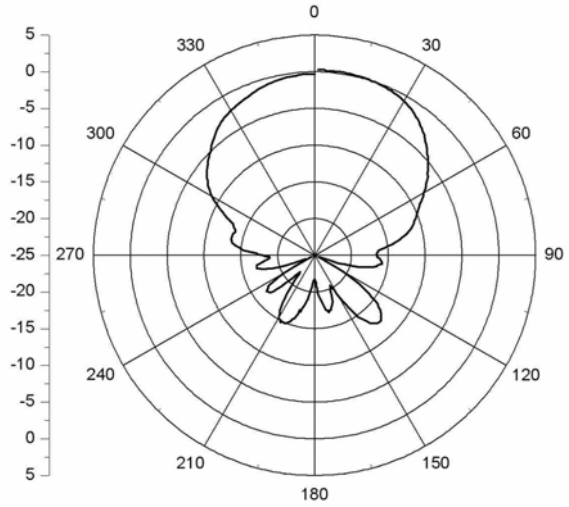

(a) 2.47 GHz

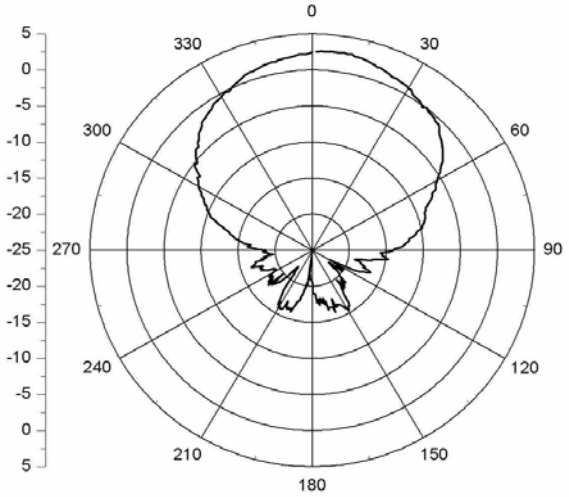

(b) 5.6 GHz

Fig. 10. The radiation patterns of the dual band patch antenna at 2.47 GHz and 5.6 GHz.

IV. CONCLUSION

In this work, we integrated the GA-based design optimizer and IE3D simulation tools within the automation control program. The validness of this optimizer is verified via the optimization of the dual band patch design for the applications of Wi-Fi and DSRC applications. Both the simulation and measurement results confirm improvement in antenna bandwidth performance and demonstrate that the optimizer developed can contribute to design automation.

REFERENCES

[1] F. Hsu, P.-R. Chang, and K.-K. Chan, "Optimization of two-dimensional radome boresight error performance using simulated annealing technique," *IEEE Trans. on Antennas Propagat.*, vol. 41, pp. 1195-1203, Sept. 1993.

[2] J. H. Holland, "Genetic algorithm," *Scientific American*, pp. 44-51, Jul. 1992.

[3] J. M. Johnson and Y. Rahmat-Samii, "Genetic algorithms in engineering electromagnetics," *IEEE Antennas and Propagat. Magazine*, vol. 39, no. 4, pp. 7-21, Aug. 1997.

[4] Y. Kim, *Development of Automobile Antenna Design and Optimization for FM/GPS/SDARS Applications*, Ph. D Dissertation, Ohio State University, 2003.

[5] A. Khaleghi, A. Azoulay, and J. C. Bolomey, "A dual band coupled meanderline antenna for wireless LAN application," *Proceeding of Vehicular Technology Conference, 2005 IEEE 61st*, vol. 1, pp. 226-229, Jun. 2005.

[6] G. Villino, C. Passmann, D. Mansen, C. Brenzel, and T. Wixforth, "Integrated 5.8 GHz phase array antenna for electronic toll collection," *Microwave Symposium Digest, 1998 IEEE MTT-S International*, vol. 3, pp. 1215-1218, Jun. 1998.

[7] A. Wright, "Genetic algorithms for real parameter optimization," *Foundations of Genetic Algorithms*, San Mateo, CA, Morgan Kaufmann, pp. 205-218, 1991.

Hsi-Tseng Chou was born in Taiwan, R.O.C., in 1966. He received the B.S. degree from National Taiwan University, Taiwan, in 1988 and the M.S. and Ph.D. degrees from The Ohio State University (OSU), Columbus, in 1993 and 1996, respectively, all in electrical engineering. He joined Yuan-Ze University (YZU), Taiwan, in 1998, where he is currently a Professor in the Department of Communications Engineering. After completing his military obligation, he was with China Raydon Corp. as an R&D Engineer for a year. He was with the ElectroScience Laboratory (ESL), OSU, as a Graduate Research Associate during 1991–1996 and as a Postdoctoral Researcher during 1996–1998. He was a Visiting Scholar to Far Eastone Telecomm between 1999 and 2004. His research interests include wireless communication network, antenna design, antenna measurement, electromagnetic scattering, asymptotic high frequency techniques such as uniform geometrical theory of diffraction (UTD), novel Gaussian beam techniques, and UTD-type solution for periodic structures. In 2006, he became a Chair Professor with YZU and the Y. Z. Hsu Science and Technology Memory Foundation, the youngest in YZU's history. He has published more than 170 journal and conference papers. Dr. Chou is a Senior Member of IEEE AP-S and a member of URSI US Commission B. He received a Young Scientist Award from URSI and a Best Paper Award from OSU-ESL in 1999. In 2002, he received a Young Scientist Research Award from Academia Sinica of Taiwan and a distinguished research award from YZU. In 2003, he received an award from the Education Ministry for his distinguished contribution to promoting interacademic and industrial cooperation and a Young Electrical Engineer Award from the Chinese Institute of Electrical Engineering. Commercial products resulting from his cooperation with industries have been recognized in 1998 and 2003, respectively, by the Economic Ministry as "Taiwan Symbols of Excellence" and elected as one of the 11 distinguished commercial products in Hsin-Chu Science Part of Taiwan in 2003. As a result, the cooperating industry had been awarded "Fast Growth of the Export and Import in the International Trade" in 2002 by the Economic Ministry due to the successful commercialization, and YZU received a Distinguished Inter-Academic and Industrial Cooperation Award from the Chinese Institute of Engineers in 2004. Also in 2004, he received a Distinguished Engineering Professor Award from the Chinese Institute of Engineers and a Distinguished Service Award from YZU. He was elected one of the nation's ten outstanding young persons by Junior Chamber International. In 2005, he received a National Young Person Medal from China Youth Corps of Taiwan and a Distinguished Professor Award from the Y. Z. Hsu Science and Technology Memory Foundation. In 2006, he was elected as one of the top ten rising stars in Taiwan by Central News Agency of Taiwan. He has received several research awards from the National Science Council.

Yuan-Chang Hou was born in Taipei, Taiwan, on December 23, 1981. He received the B.S. degree in electrical engineering from the National Taipei University of Technology, Taipei, Taiwan in 2004. He received the M.S. degrees in communications engineering from Yuan-Ze University , Chung-Li , Taiwan in 2006. He is currently employed Lite-On Technology Corporation as an antenna engineer for IMG-PID department. His research area includes miniaturized microstrip antennas and high directive patch array designs.

Wen-Jiao Liao was born in Taipei, Taiwan. He received the B.S. degree in electrical engineering from the National Taiwan University, Taipei, Taiwan in 1995. He received the M.S. and Ph.D. degrees in electrical engineering from The Ohio State University, Columbus, in 1999 and 2003, respectively. After receiving his Ph.D. degree in 2003, He was employed by Syntonics, LLC as a project scientist. In 2004, he continued his research work in the Electroscience laboratory of the Ohio State University as a post-doctoral researcher. Since 2004, he has been an Assistant Professor at Yuan-Ze University in the Department of Communications Engineering. His main interests are antenna design and measurement, wave propagation, EMC/EMI issues, electro-optical sensor signatures, and image processing.

Analysis and Design of Quad-Band Four-Section Transmission Line Impedance Transformer

Hussam Jwaied, Firas Muwanes, and Nihad Dib

Electrical Eng. Dept., Jordan Univ. of Science and Technology,
P. O. Box 3030, Irbid 22110, Jordan, E-mail: nihad@just.edu.jo

Abstract **–** The design of four-section transmission line matching transformer, operating at four arbitrary frequencies, is presented. Standard transmission line theory is used to obtain a closed form expression that is solved using particle swarm optimization technique to find the required transformer parameters (lengths, and characteristic impedances). Different examples are presented which validate the design approach. To further validate the analysis and design approach, a microstrip line four-section quad-band transmission line transformer is designed, analyzed, fabricated and measured.

I. INTRODUCTION

With the advent of multi-band operation in wireless communication systems, it becomes essential to have matching transformers that operate at several frequencies. Recently, several papers have been published in which different techniques were proposed to design dual-frequency matching transformers [1-4]. In [1], a λ/4 - shorted stub was added to a conventional single-shunt-stub matching network that enabled impedance matching at two separate frequencies simultaneously. In [2], a novel dual-band two-section transmission line transformer (TLT) was proposed and simple design equations for the impedances and lengths of the two sections were derived in [3]. In [4], an extension of this dual-band TLT to match complex impedances was presented and applied to wideband high-frequency amplifiers. Very recently, a triple-band three-section TLT, extended from the two-section TLT concept, was designed and analyzed in [5]. Using simple transmission line theory, design expressions for the three-section TLT for three arbitrary operating frequencies were derived. Two non-linear equations were solved simultaneously via an optimization process to obtain the parameters of the transformer. As an application of these TLTs, dual-band two-section TLT and triple-band three-section TLT have been successfully used to design dual-band and triple-band Wilkinson power dividers, respectively, [6-8].

In this paper, the quad-band four-section TLT, which is matched at four arbitrary frequencies (f_1, f_2, f_3 and f_4) for any transforming ratio (Z_L/Z_0) is designed and analyzed. Four non-linear equations are derived using standard transmission line theory, which are then solved simultaneously using the particle swarm optimization (PSO) technique. The PSO technique is used to find the characteristic impedances and lengths of the first two sections, from which the impedances and lengths of the other sections are obtained using the antimetry conditions [9]. The PSO algorithm is a multiple-agents optimization algorithm that was introduced by Kennedy and Eberhart [10] in 1995 while studying the social behavior of groups of animals and insects such as flocks of birds, schools of fish, and swarms of bees. Recently, this technique found many successful applications in Electromagnetics [11-13]. PSO is similar in some ways to genetic algorithms, but requires less computational bookkeeping and generally fewer lines of code, including the fact that the basic algorithm is very easy to understand and implement. It should be mentioned that other optimization techniques could be used too, but recently, we have been interested in the application of PSO method in the design of different microwave passive elements [14, 15], and antennas [16]. The interested reader can refer to [10-16], and the references therein, for details of the PSO algorithm.

II. ANALYSIS AND DESIGN

Figure 1 shows a four-section transmission line transformer (TLT) that will be used to match a purely resistive load Z_L to a lossless transmission line with characteristic impedance Z_0. The characteristic impedances of the transmission-line sections are denoted as Z_1, Z_2, Z_3, and Z_4, with physical lengths l_1, l_2, l_3, and l_4, respectively. The problem is to find the lengths and impedances of the four sections such that a perfect match is obtained at four arbitrary frequencies f_1, f_2, f_3, and f_4.

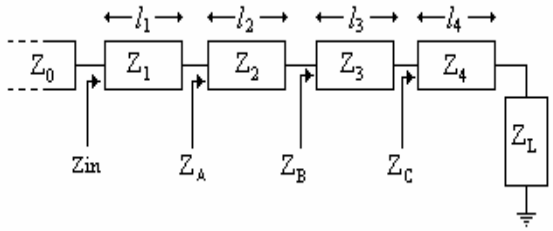

Fig. 1. Four-section quad-band TLT.

Using standard transmission line theory, the input impedance of the four-section TLT is given by,

$$Z_{in} = Z_1 \frac{Z_A + jZ_1 \tan(\beta\ell_1)}{Z_1 + jZ_A \tan(\beta\ell_1)} \quad (1)$$

where

$$Z_A = Z_2 \frac{Z_B + jZ_2 \tan(\beta\ell_2)}{Z_2 + jZ_B \tan(\beta\ell_2)}, \quad (2)$$

$$Z_B = Z_3 \frac{Z_C + jZ_3 \tan(\beta\ell_3)}{Z_3 + jZ_C \tan(\beta\ell_3)}, \quad (3)$$

$$Z_C = Z_4 \frac{Z_L + jZ_4 \tan(\beta\ell_4)}{Z_4 + jZ_L \tan(\beta\ell_4)}. \quad (4)$$

For perfect matching at specific frequencies, the lengths and impedances should be chosen such that $Z_{in} = Z_0$ at those frequencies. Imposing this condition on equation (1) and solving for Z_A gives,

$$Z_A = Z_1 \frac{Z_0 - jZ_1 \tan(\beta\ell_1)}{Z_1 - jZ_0 \tan(\beta\ell_1)}. \quad (5)$$

Solving equation (2) for Z_B gives,

$$Z_B = Z_2 \frac{Z_A - jZ_2 \tan(\beta\ell_2)}{Z_2 - jZ_A \tan(\beta\ell_2)}. \quad (6)$$

Substituting equation (5) in equation (6), gives,

$$Z_B = Z_2 \frac{Z_1 \dfrac{Z_0 - jZ_1 \tan(\beta\ell_1)}{Z_1 - jZ_0 \tan(\beta\ell_1)} - jZ_2 \tan(\beta\ell_2)}{Z_2 - jZ_1 \dfrac{Z_0 - jZ_1 \tan(\beta\ell_1)}{Z_1 - jZ_0 \tan(\beta\ell_1)} \tan(\beta\ell_2)}. \quad (7)$$

Another equation for Z_B can be obtained by substituting equation (4) in equation (3), which gives,

$$Z_B = Z_3 \frac{Z_4 \dfrac{Z_L + jZ_4 \tan(\beta\ell_4)}{Z_4 + jZ_L \tan(\beta\ell_4)} + jZ_3 \tan(\beta\ell_3)}{Z_3 + jZ_4 \dfrac{Z_L + jZ_4 \tan(\beta\ell_4)}{Z_4 + jZ_L \tan(\beta\ell_4)} \tan(\beta\ell_3)}. \quad (8)$$

Equating the complex equations (7) and (8), we get the following two expressions,

$$\begin{aligned}
&\left(\frac{Z_2}{Z_1} - \frac{Z_1}{Z_2}k\right)\tan(\beta\ell_1)\tan(\beta\ell_2) \\
&+\left(\frac{Z_3}{Z_1} - \frac{Z_1}{Z_3}k\right)\tan(\beta\ell_1)\tan(\beta\ell_3) \\
&+\left(\frac{Z_4}{Z_1} - \frac{Z_1}{Z_4}k\right)\tan(\beta\ell_1)\tan(\beta\ell_4) \\
&+\left(\frac{Z_3}{Z_2} - \frac{Z_2}{Z_3}k\right)\tan(\beta\ell_2)\tan(\beta\ell_3) \\
&+\left(\frac{Z_4}{Z_2} - \frac{Z_2}{Z_4}k\right)\tan(\beta\ell_2)\tan(\beta\ell_4) \\
&+\left(\frac{Z_4}{Z_3} - \frac{Z_3}{Z_4}k\right)\tan(\beta\ell_3)\tan(\beta\ell_4) \\
&+\left(\frac{Z_1Z_3}{Z_2Z_4}k - \frac{Z_2Z_4}{Z_1Z_3}\right)\times\left\{\begin{matrix}\tan(\beta\ell_1)\tan(\beta\ell_2)\\ \times\tan(\beta\ell_3)\tan(\beta\ell_4)\end{matrix}\right\} = (1-k),
\end{aligned} \quad (9)$$

$$\begin{aligned}
&\left(\frac{Z_L}{Z_1} - \frac{Z_1}{Z_0}\right)\tan(\beta\ell_1) + \left(\frac{Z_L}{Z_2} - \frac{Z_2}{Z_0}\right)\tan(\beta\ell_2) \\
&+\left(\frac{Z_L}{Z_3} - \frac{Z_3}{Z_0}\right)\tan(\beta\ell_3) + \left(\frac{Z_L}{Z_4} - \frac{Z_4}{Z_0}\right)\tan(\beta\ell_4) \\
&+\left(\frac{Z_1Z_3}{Z_0Z_2} - \frac{Z_2Z_L}{Z_1Z_3}\right)\tan(\beta\ell_1)\tan(\beta\ell_2)\tan(\beta\ell_3) \\
&+\left(\frac{Z_1Z_4}{Z_0Z_2} - \frac{Z_2Z_L}{Z_1Z_4}\right)\tan(\beta\ell_1)\tan(\beta\ell_2)\tan(\beta_4) \\
&+\left(\frac{Z_1Z_4}{Z_0Z_3} - \frac{Z_3Z_L}{Z_1Z_4}\right)\tan(\beta\ell_1)\tan(\beta\ell_3)\tan(\beta\ell_4) \\
&+\left(\frac{Z_2Z_4}{Z_0Z_3} - \frac{Z_3Z_L}{Z_2Z_4}\right)\tan(\beta\ell_1)\tan(\beta\ell_2)\tan(\beta\ell_3) = 0
\end{aligned} \quad (10)$$

where k is the impedance transforming ratio (or the normalized load impedance) defined as $k=Z_L/Z_0$.

For a compact size, the characteristics impedances must be monotonically increasing or monotonically decreasing, i.e., they should satisfy one of the following conditions [5],

For k<1: $Z_L < Z_4 < Z_3 < Z_2 < Z_1 < Z_0$
For k>1: $Z_0 < Z_1 < Z_2 < Z_3 < Z_4 < Z_L$

Moreover, since an optimized transformer, in the sense of achieving global minima of the reflection coefficient at the design frequencies, is being designed, it should satisfy the antimetry conditions given as, [9],

$$l_1 = l_4 \text{ and } l_2 = l_3\,, \tag{11a}$$

$$Z_1Z_4 = Z_2Z_3 = Z_0Z_L. \tag{11b}$$

It is worth mentioning that the dual-band TLT [3] and the tri-band TLT [5] were found to satisfy these conditions too. Enforcing the above antimetry conditions on the left side of equation (10) gives a zero; that is equation (10) is satisfied if the lengths and the impedances satisfy the antimetry conditions. This validates, to some extent, that indeed the antimetry conditions have to be satisfied. On the other hand, enforcing the antimetry conditions in equation (9), and after some simplification, the following expression is obtained,

$$2a + b\frac{\tan(\beta\ell_1)}{\tan(\beta\ell_2)} + c\frac{\tan(\beta\ell_2)}{\tan(\beta\ell_1)} + d\tan(\beta\ell_1)\tan(\beta\ell_2) + \frac{(k-1)}{\tan(\beta\ell_1)\tan(\beta\ell_2)} = 0 \tag{12}$$

where

$$a = \left(\frac{z_2}{z_1} - \frac{z_1}{z_2}k\right) + \left(\frac{k}{z_1 z_2} - z_1 z_2\right), \tag{13a}$$

$$b = \frac{k}{z_1^2} - z_1^2\,, \tag{13b}$$

$$c = \frac{k}{z_2^2} - z_2^2\,, \tag{13c}$$

$$d = \frac{z_1^2}{z_2^2}k - \frac{z_2^2}{z_1^2}\,. \tag{13d}$$

In equation (13), normalized impedances are used where $z_1=Z_1/Z_0$, and $z_2=Z_2/Z_0$. It is clear that there are four unknowns in equation (12); namely: z_1, z_2, l_1, and l_2. Now, equation (12) should be satisfied at the four design frequencies f_1, f_2, f_3, and f_4 which can be written as follows: $f_2=u_1 f_1$, $f_3=u_2 f_1$, and $f_4=u_3 f_1$, where u_1, u_2, and u_3 are any positive real numbers.

At f_1, we get,

$$2a + b\frac{\tan(\beta_1\ell_1)}{\tan(\beta_1\ell_2)} + c\frac{\tan(\beta_1\ell_2)}{\tan(\beta_1\ell_1)} + d\tan(\beta_1\ell_1)\tan(\beta_1\ell_2) + \frac{(k-1)}{\tan(\beta_1\ell_1)\tan(\beta_1\ell_2)} = 0. \tag{14}$$

At f_2, we get,

$$2a + b\frac{\tan(u_1\beta_1\ell_1)}{\tan(u_1\beta_1\ell_2)} + c\frac{\tan(u_1\beta_1\ell_2)}{\tan(u_1\beta_1\ell_1)} + d\tan(u_1\beta_1\ell_1)\tan(u_1\beta_1\ell_2) + \frac{(k-1)}{\tan(u_1\beta_1\ell_1)\tan(u_1\beta_1\ell_2)} = 0. \tag{15}$$

At f_3, we get,

$$2a + b\frac{\tan(u_2\beta_1\ell_1)}{\tan(u_2\beta_1\ell_2)} + c\frac{\tan(u_2\beta_1\ell_2)}{\tan(u_2\beta_1\ell_1)} + d\tan(u_2\beta_1\ell_1)\tan(u_2\beta_1\ell_2) + \frac{(k-1)}{\tan(u_2\beta_1\ell_1)\tan(u_2\beta_1\ell_2)} = 0. \tag{16}$$

At f_4, we get,

$$2a + b\frac{\tan(u_3\beta_1\ell_1)}{\tan(u_3\beta_1\ell_2)} + c\frac{\tan(u_3\beta_1\ell_2)}{\tan(u_3\beta_1\ell_1)} + d\tan(u_3\beta_1\ell_1)\tan(u_3\beta_1\ell_2) + \frac{(k-1)}{\tan(u_3\beta_1\ell_1)\tan(u_3\beta_1\ell_2)} = 0. \tag{17}$$

Finally, given k, u_1, u_2 and u_3, the previous four non-linear equations (14) to (17), need to be solved simultaneously for the four unknowns z_1, z_2, l_1/λ_1 and l_2/λ_1 via an optimization process, where λ_1 is the wavelength at f_1.

As mentioned in the introduction, the particle swarm optimization (PSO) technique is used here to solve these four equations. The fitness function is chosen to be the sum of the absolute values of the left sides of equations (14) to (17). Once the four unknowns (z_1, z_2, l_1, and l_2) are obtained, the other four unknowns z_3, z_4, l_3, and l_4 can be calculated using the antimetry conditions. In all the results presented in the next section, 20 particles are used in the PSO code, and the search is stopped once the value of the fitness function becomes less than 10^{-10}. Depending on the initial swarm positions, 1500-2000 iterations were usually needed to reach an acceptable solution. Typically, this took around 15-30 seconds using Pentium-3 PC. The algorithm was run more than once to make sure that it converges to the same solution each time.

III. RESULTS

Using the approach described in the previous section, several designs have been performed to achieve matching at four arbitrary frequencies. Table 1 shows the obtained results for the case with $u_1 = 2$, $u_2 = 3$, and $u_3 = 4$, while the impedance ratio k is changed from 0.5 to 10. Figure 2 shows the return loss versus frequency for different values of k. It can be noticed that there is a perfect match at the four design frequencies. From the figure, as expected, one can observe that the response for k and its inverse $1/k$ are the same. Moreover, from the results in Table 1, we notice that changing the impedance ratio k changes the characteristic impedances, while the lengths of the sections are not affected.

Another case that has been considered is to fix u_2, u_3 and k, while changing u_1. Table 2 includes some results in which u_1 is changed between 1.4 and 2.6, with $u_2 = 3$, $u_3 = 4$, $k = 2$. It can be noticed that as u_1 increases, the impedance and length of the first section decrease, while

the impedance and length of the second section increase. Figure 3 shows the frequency response for some of these cases.

Table 1. Impedances and normalized lengths of a quad-band four-section TLT with $Z_0 = 50\ \Omega$, $u_1 = 2$, $u_2 = 3$, and $u_3 = 4$.

k	Z_1	Z_2	Z_3	Z_4	l_1/λ_1	l_2/λ_1
0.5	43.47	37.87	33.01	28.76	0.1	0.1
2	57.51	66.02	75.74	86.94	0.1	0.1
4	66.68	87.51	114.27	149.95	0.1	0.1
6	73.22	103.54	144.86	204.87	0.1	0.1
8	78.56	116.89	171.09	254.56	0.1	0.1
10	83.21	128.58	194.42	300.44	0.1	0.1

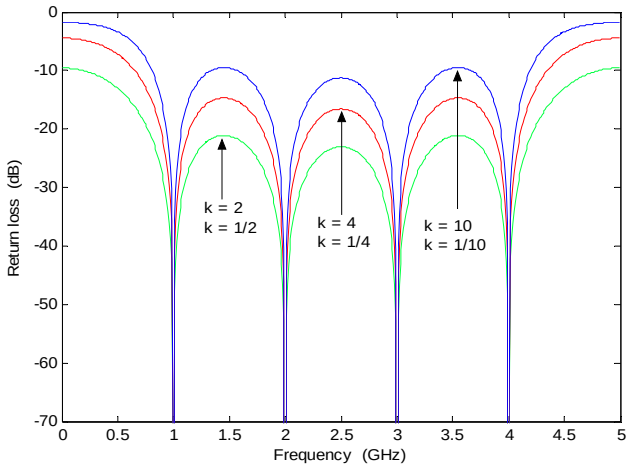

Fig. 2. Return loss of the four-section transformer presented in Table 1 with f_1=1 GHz.

Table 2. Impedances and normalized lengths of a four-section TLT with $u_2 = 3$, $u_3 = 4$, $k = 2$, $Z_0 = 50\ \Omega$.

u_1	Z_1	Z_2	Z_3	Z_4
1.4	59.09	63.78	78.39	84.60
1.8	57.98	65.2	76.68	86.24
2.2	57.17	66.69	74.97	87.45
2.6	56.81	67.71	73.85	88.02

u_1	l_1/λ_1	l_2/λ_1
1.4	0.1493	0.0660
1.8	0.1079	0.0964
2.2	0.0943	0.1019
2.6	0.0858	0.1035

Similarly, one can fix u_1, u_3, and k, while changing u_2. Table 3 includes some results in which u_2 is changed between 2.4 and 3.6, with $u_1 = 2$, $u_3 = 4$, and $k = 2$. In this case, as u_2 increases, Z_1 and l_2 increase, while Z_2 and l_1 decrease. Figure 4 shows the frequency response for some of these cases.

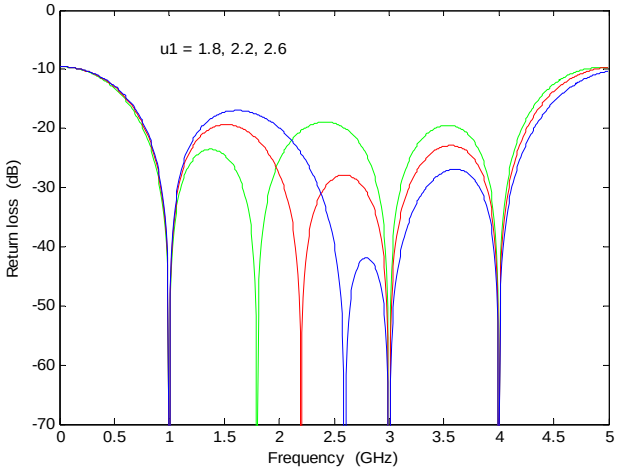

Fig. 3. Return loss of the four-section transformer presented in Table 2 with f_1=1 GHz.

Table 3. Impedances and normalized lengths of a four-section TLT with $u_1 = 2$, $u_3 = 4$, $k = 2$, $Z_0 = 50\ \Omega$.

u_2	Z_1	Z_2	Z_3	Z_4
2.4	56.77	67.84	73.70	88.07
2.8	57.25	66.55	75.13	87.33
3.2	57.78	65.56	76.53	86.53
3.6	58.36	64.81	77.14	85.67

u_2	l_1/λ_1	l_2/λ_1
2.4	0.1221	0.0921
2.8	0.1068	0.0974
3.2	0.0937	0.1025
3.6	0.0822	0.1074

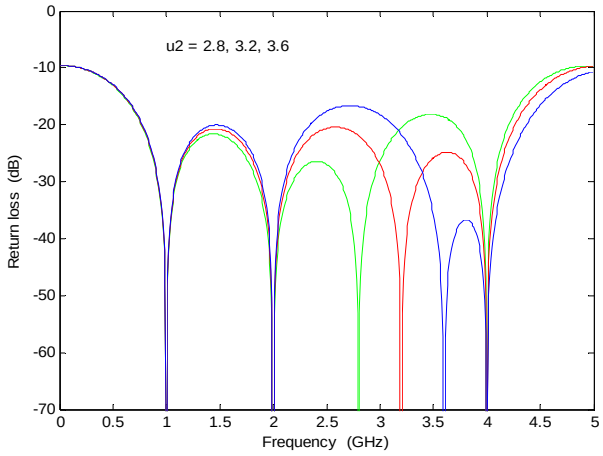

Fig. 4. Return loss of the four-section transformer presented in Table 3 with f_1=1 GHz.

Finally, k, u_1 and u_2 are fixed, and u_3 is changed to different arbitrary values. Table 4 shows some cases in which u_3 is changed between 3.4 and 4.6, with $u_1 = 2$, $u_2 = 3$, and $k = 2$. Figure 5 shows the frequency response for these cases.

Table 4. Impedances and normalized lengths of a four-section TLT with $u_1 = 2$, $u_2 = 3$, $k = 2$, $Z_0 = 50\ \Omega$.

u_3	Z_1	Z_2	Z_3	Z_4
3.4	56.01	65.29	76.58	89.24
3.8	56.95	65.69	76.11	87.77
4.2	58.06	66.49	75.19	86.11
4.6	59.00	68.13	73.38	84.74

u_3	l_1/λ_1	l_2/λ_1
3.4	0.0987	0.1145
3.8	0.0982	0.1059
4.2	0.1033	0.0928
4.6	0.1140	0.0765

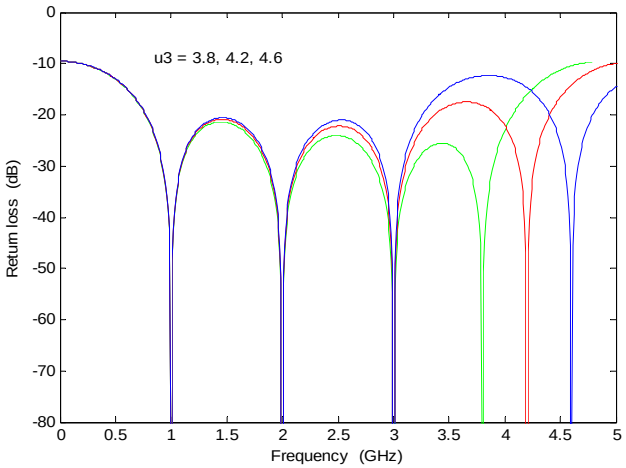

Fig. 5. Return loss of the four-section transformer presented in Table 4 with f_1=1 GHz.

To further validate our analysis, a quad-band four-section microstrip line transformer is designed, fabricated and measured. This transformer is designed to match a load impedance Z_L = 100 Ω to a 50 Ω microstrip transmission line at f_1 = 0.3 GHz, f_2 = 0.6 GHz, f_3 = 0.95 GHz, and f_4 = 1.25 GHz. The ideal transmission line sections impedances and lengths are found to be as follows: Z_1 = 56.8519 Ω, Z_2 = 66.8843 Ω, Z_3 = 74.7559 Ω, Z_4 = 87.9478 Ω, $l_1 = l_4$ = 69.677 degrees, $l_2 = l_3$ = 34.839 degrees, where the electrical lengths refer to f_1.

Using the software *Ansoft Designer SV* [17], and assuming a 1.6 mm thick FR-4 substrate, the physical lengths and microstrip widths are found to be as follows: ℓ_1 =107.225 mm, ℓ_2 = 54.2794 mm, ℓ_3 = 54.7366 mm, ℓ_4 = 110.761 mm. W_1 = 2.312 mm, W_2 = 1.697 mm, W_3 = 1.343 mm, and W_4 = 0.9157 mm. It should be noted that although the electrical lengths of opposite sections are equal, their physical lengths differ slightly due to the difference in the effective dielectric constant of each section, which depends on the microstrip line width. Figure 6 presents the simulation results obtained using *Designer SV*, which shows a very good match at the four design frequencies. Using the available PCB facility, this quad-band microstrip line TLT was fabricated, in which a surface mount resistor was used as the load. The overall size of the practical circuit seen in Fig. 7 is 25×7 cm. Figure 8 presents the measured return loss, which clearly shows the quad-band impedance matching. Some of the design frequencies are slightly shifted which could be due to losses of the connectors, and the inaccuracies in the widths and lengths of the microstrip line sections.

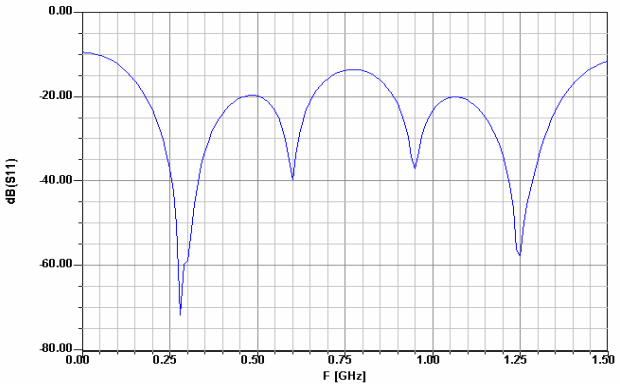

Fig. 6. Simulation results for a quad-band microstrip TLT with a 1.6 mm thick FR-4 substrate (ε_r = 4.6).

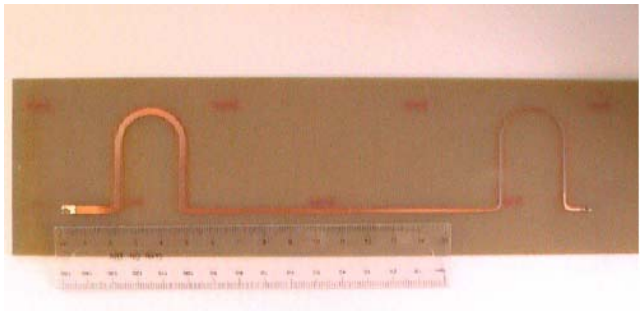

Fig. 7. Photograph of the fabricated quad-band microstrip line TLT. The first and last sections are bent to reduce the total length of the TLT.

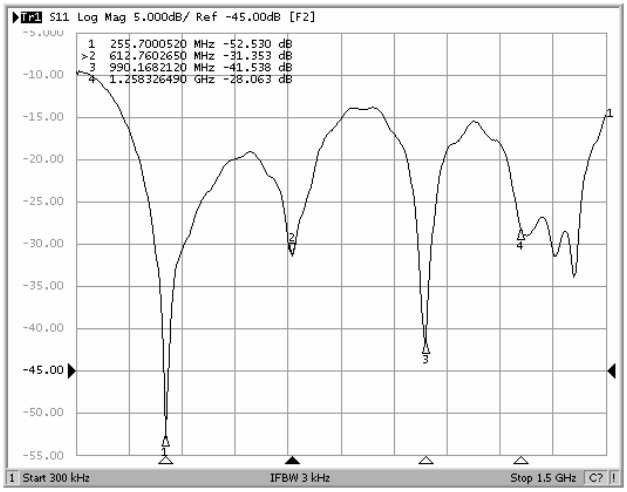

Fig. 8. Measured return loss for the fabricated quad-band microstrip line TLT.

IV. CONCLUSIONS

The contributions presented in this paper can be summarized as follows:

(a) A simple configuration for a quad-band transmission line transformer (TLT) has been proposed which uses four transmission line sections. Using ideal transmission line theory, a single equation, that needs to be satisfied simultaneously at the four design frequencies, has been derived. This equation involved only four unknowns (z_1, z_2, l_1/λ_1, and l_2/λ_1) to be solved for.

(b) The particle swarm optimization (PSO) technique, which is drawing much attention at the present time, has been used to design the quad-band TLT by searching for the four parameters z_1, z_2, l_1/λ_1, and l_2/λ_1. The other four variables z_3, z_4, l_3/λ_1, and l_4/λ_1 were obtained using the antimetry conditions. In effect, the obtained impedances and lengths minimize the reflection coefficient at the four design frequencies.

(c) Finally, to validate the analysis, several quad-band four-section TLTs have been designed. The results were as expected; perfect match at the four frequencies. It has been found that the lengths of the sections do not depend on the transforming ratio k for fixed design frequencies. Moreover, a microstrip line quad-band TLT has been designed, simulated using *Ansoft Designer SV*, fabricated and measured. At the present time, we are investigating the possibility of building a quad-band Wilkinson divider based on the quad-band TLT studied here. Moreover, the design a quad-band transformer that is able to match complex impedances, similar to that presented in [4], will be investigated.

REFERENCES

[1] H. Nakajima, and M. Muraguchi, "Dual-Frequency matching technique and its application to an octave-band (30-60 GHz) MMIC amplifier," *IEICE Trans. Electron.*, vol. E80-C, no. 12, pp. 1614-1621, Dec. 1997.

[2] Y. Chow, and K. Wan, "A transformer of one-third wavelength in two sections – for a frequency and its first harmonic," *IEEE Microwave and Wireless Components Letters*, vol. 12, no. 1, pp. 22-23, Jan. 2002.

[3] C. Monzon, "A small dual-frequency transformer in two sections," *IEEE Trans. on Microwave Theory and Techniques*, vol. 51, no. 4, pp. 1157-1161, April 2003.

[4] P. Colantonio, F. Giannini, and L. Scucchia, "Matching network design criteria for wideband high-frequency amplifiers," *Int. J. RF and Microwave CAE*, vol. 15, pp. 423-433, 2005.

[5] M. Chongcheawchamnan, S. Patisang, S. Srisathit, R. Phromloungsri, and S. Bunnjaweht, "Analysis and design of a three-section transmission-line transformer," *IEEE Trans. on Microwave Theory and Techniques*, vol. 53, no. 7, pp. 2458-2462, July 2005.

[6] S. Srisathit, S. Virunphun, K. Bandudej, M. Chongcheawchamnan, and A. Worapishet, "A dual-band 3-dB three-port power divider based on a two-section transmission line transformer," *2003 IEEE MTT-S Int. Microwave Symp. Digest*, pp. 35-38, 2003.

[7] L. Wu, Z. Sun, H. Yilmaz, and M. Berroth, "A dual-frequency wilkinson power divider," *IEEE Transactions on Microwave Theory and Techniques,* vol. 45, no. 1, pp. 278-284, Jan. 2006.

[8] M. Chongcheawchamnan, S. Partisang, M. Krairiksh, and I. Robertson, "Tri-band wilkinson power divider using a three-section transmission-line transformer," *IEEE Microwave and Wireless Components Letters,* vol. 16, no. 8, pp. 452-454, Aug. 2006.

[9] V. Meschanov, I. Rasukova, and V. Tupikin, "Stepped transformers on TEM-transmission lines," *IEEE Trans. Microw. Theory Tech.,* vol. 44, no. 6, pp. 793-798, June 1996.

[10] J. Kennedy and R. C. Eberhart, "Particle swarm optimization," in *Proc. IEEE Int. Conf. Neural Networks*, vol. IV, Perth, Australia, Nov./Dec. 1995, pp. 1942–1948.

[11] D. Gies and Y. Rahmat-Samii, "Particle swarm optimization for reconfigurable phase-differentiated array design," *Microwave Opt. Technol. Lett.*, vol. 38, pp. 168–175, Aug. 2003.

[12] J. Robinson and Y. Rahmat-Samii, "Particle swarm optimization in electromagnetics," *IEEE Trans. Antennas Propag.*, vol. 52, no. 2, pp. 397–407, Feb. 2004.

[13] M. Khodier and C. Christodoulou, "Linear array geometry synthesis with minimum sidelobe level and null control using particle swarm optimization," *IEEE Trans. Antennas Propagat.*, vol. 53, no. 8, pp. 2674-2679, August 2005.
[14] J. Ababneh, M. Khodier, and N. Dib, "Synthesis of interdigital capacitors based on particle swarm optimization and artificial neural networks," *International Journal of RF and Microwave Computer-Aided Engineering*, vol. 16, pp. 322-330, July 2006.
[15] N. Dib and J. Ababneh, "Physical modeling and particle swarm design of coplanar waveguide square spiral inductor," accepted for publication in *Int. J. of Modeling and Simulation*, to appear beginning of 2008.
[16] Y. Najjar, M. Moneer, and N. Dib, "Design of optimum gain pyramidal horn with improved formulas using particle swarm optimization," accepted for publication in *International Journal of RF and Microwave Computer-Aided Engineering*, to appear in July 2007 issue.
[17] Available at www.ansoft.com.

Hussam Jwaied was born in Ajloun, Jordan, on July 9, 1984. He received his B. Sc. degree in telecommunication and electronics engineering from Jordan University of Science and Technology, Irbid, Jordan, in 2007. His research interests include RF and microwave integrated circuits.

Firas Muwanes was born in Zarqa, Jordan on June 5, 1984. He received the B. Sc. degree in telecommunication and electronics engineering from Jordan University of Science and Technology, Irbid, Jordan, in 2007. His current research interests include RF and microwave integrated circuits.

Nihad Dib obtained his B. Sc. and M. Sc. in EE from Kuwait University in 1985 and 1987, respectively. He obtained his Ph. D. in EE (major in Electromagnetics and Microwaves) in 1992 from University of Michigan, Ann Arbor. Then, he worked as an assistant research scientist in the radiation laboratory at the same school. In Sep. 1995, he joined the EE department at Jordan University of Science and Technology (JUST) as an assistant professor, and became a full professor in Aug. 2006. In 2002-2003, he was a senior research engineer with Ansoft Corporation, USA. His research interests are in computational electromagnetics and modeling of passive microwave components and circuits.

Analysis of Dielectric Loaded Scalar Horn Radiators

Bahattin TÜRETKEN

The Scientific and Technical Research Council of Turkey (TUBITAK)
National Research Institute Electronics and Cryptology (UEKAE)-EMC & TEMPEST
Test Center 41470 Gebze Kocaeli, TURKEY

Abstract **–** The dielectric loaded horn radiators are commonly used in various applications due to their distinguished features, such as low cross-polarization, pattern symmetry and simple production. The analysis of this kind of horn, mode matching (MM) and integral equation methods have been preferred in the literature. In the present study, the radiation of plane harmonic scalar waves from a dielectric loaded circular horn radiator is treated by using the mode matching method in conjunction with theWiener-Hopf technique. The solution is exact but formal since infinite series of unknowns and some branch-cut integrals with unknown integrands are involved. Approximation procedures based on rigorous asymptotic are used and the approximate solution to the Wiener-Hopf equations are derived in terms of infinite series of unknowns, which are determined from infinite systems of linear algebraic equations. Numerical solution of these systems is obtained for various values of the parameters, of the problem. Their effect is presented on the directivity of the circular feed horn.

Key words **–** Dielectric loaded wide angle scalar horn radiator, Wiener-Hopf Technique, integral equations, circular waveguide, step discontinuity.

I. INTRODUCTION

In the recent years, scalar feed horns are commonly used widespread applications such as feeds in reflector radiator systems used in microwave and acoustics, because of their well-known properties of pattern symmetry and zero or low cross-polarization. To analyze the performance of such feeds, one needs to know accurately their near- and far-field patterns. The aperture fields of a pure-mode horn are generated by a single mode, which is the dominant mode in the waveguide. These horns use "hybrid" modes where there is a single mode, which is composed of hybrid combination of two other modes. The scalar feed is circular horn antenna with grooves, perpendicular to the wall of the horn. The grooves change the fields so as to provide desirable properties of axial beam symmetry, low side lobes and cross-polarization. This means that the horn produces an aperture field in which the field's distributions are approximately linear. The very low cross-polarization means that the field in the aperture are essentially scalar and for this reason, the corrugated horn is sometimes referred as scalar horn [1]. The radiation characteristics of circular waveguides and horns have been the subject to several previous investigations [2 - 5]. Some of the approximate and computational methods such as surface integral methods; hybird MM/ finite element (FE)/ method of moment (MoM)/ finite difference (FD) methods have been presented for the analysis of horns [6]. The analysis reported in [7] is recently generalized [8] to the case where the aperture's inner surface and the intersection area with the flange of the waveguide horn are treated as different impedance materials. The aim of the present work is to produce an analysis of the case where the aperture of the waveguide horn is loaded as different dielectric materials, as shown in Fig. 1.

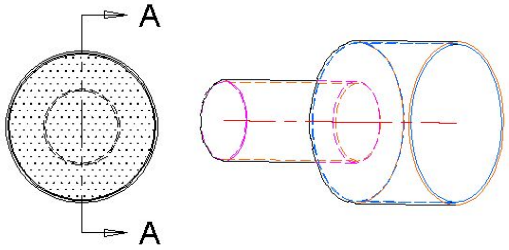

a. Dielectric loaded circular horn radiator.

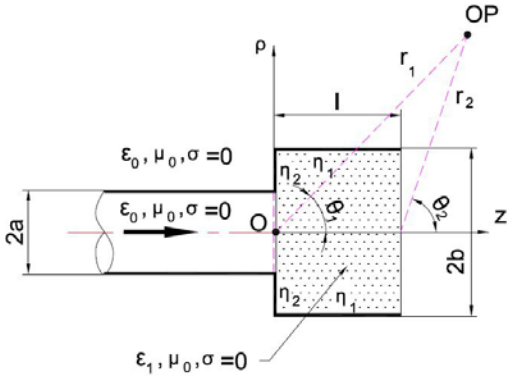

b. Geometry of the problem.

Fig. 1. a. Dielectric loaded circular horn radiator, b. geometry of the problem.

The aperture region of the scalar horn is loaded by a simple dielectric material (non-magnetic and non-conducting-dielectric rod) having the permitivity

ε_1. The variables η_1 and η_2 are the complex admittance of the aperture's inner surface of the horn and the intersection area with the flange of the waveguide, respectively. To this end we consider the problem of dominant modes in the circular waveguides propagating out of semi-infinite duct, via another coaxial cylindrical duct of finite length and bigger radius, and the issuing into free space.

In the progress of the radiation pattern analysis of dielectric loaded scalar feed horn, attention has been given to consider the propagation of plane waves by circular structures, because the complexity of these structures is not always possible to obtain rigorous analytical solutions to radiation problems. The Wiener-Hopf Technique is applicable to open and closed structures.

The method adopted here is similar to the one employed in [8] and consists of expressing the total field in the waveguide region in terms of normal waveguide modes and using the Fourier transform elsewhere. To this end, by introducing the Fourier transform for the scattered field and applying the boundary conditions in the transform domain, the problem is reduced into a modified Wiener-Hopf equation. Using the mode matching method in conjunction with the Wiener-Hopf technique the radiation of plane harmonic scalar waves from a scalar feed horn were treated. The solution is exact but formal since infinite series of unknowns and some branch-cut integrals with unknown integrands are involved. Approximated procedures based on rigorous asymptotic are used, and the approximate solution to the Wiener-Hopf equations are derived in terms of infinite series of unknowns, which are determined from infinite systems of linear algebraic equations. Numerical solution of these systems is obtained for various values of the parameters of the problem and their effect on the directivity of the scalar feed horn is presented. The time dependence is assumed to be $\exp(-i\omega t)$, with ω being the angular frequency, and is suppressed throughout the paper.

II. ANALYSIS

Consider the radiation of a time harmonic plane wave propagating along the positive z direction from a rigid cylindrical horn is defined by, $\{\rho = a, z \in (-\infty, 0)\} \cup \{\rho \in (a,b), z = 0\} \cup \{\rho = b, z \in (0,l)\}$ where (ρ, ϕ, z) denotes the usual cylindrical polar coordinates (Fig. 1). From the symmetry of the geometry of the problem, and of the incident field, the scalar field everywhere will be independent of ϕ.

Assuming the incident field is given by

$$u^i = \exp(ikz) \tag{1}$$

where $k = \omega/c$ denotes the wave number. For the sake of analytical convenience we will assume that the surrounding medium is slightly lossy and k has a small positive imaginary part. The lossless case can be obtained by letting $Imk \to 0$ at the end of the analysis.

The total field $u^T(\rho, z)$ can be written as,

$$u^T(\rho,z) = \begin{cases} u_1(\rho,z) & ;\ \rho > b, \quad z \in (-\infty,\infty) \\ u_2(\rho,z) & ;\ \rho \in (a,b),\ z < 0 \\ u_3(\rho,z) + u^i(\rho,z) & ;\ \rho \in (0,a),\ z < 0 \\ u_4(\rho,z) & ;\ \rho \in (0,b),\ z \in (0,l) \\ u_5(\rho,z) & ;\ \rho \in (0,b),\ z > l \end{cases} . \tag{2}$$

By considering k_1 as the wave number of dielectric region, $u_j(\rho,z)$, $j = 1-5$ denote the scattered fields $u_j(\rho,z)$, $j = 1-5$, which satisfy the Helmholtz equation,

$$\left[\frac{1}{\rho}\frac{\partial}{\partial\rho}\left(\rho\frac{\partial}{\partial\rho}\right) + \frac{\partial^2}{\partial z^2} + k^2\right] u_j(\rho,z) = 0, \quad j = 1,2,3,5, \tag{3a}$$

$$\left[\frac{1}{\rho}\frac{\partial}{\partial\rho}\left(\rho\frac{\partial}{\partial\rho}\right) + \frac{\partial^2}{\partial z^2} + k_1^2\right] u_j(\rho,z) = 0, \quad j = 4 \tag{3b}$$

is the expression to be determined with the help of well known boundary, edge, and radiation conditions for the perfectly conducting structures. The boundary condition on the internal surfaces of the horn yield $\frac{\partial u}{\partial n} + ik\eta u = 0$, where n is the normal pointing outward the lining, and η is the complex specific admittance of the surfaces,

$$u_1(b,z) = u_2(b,z),\ z < 0, \tag{4a}$$

$$\frac{\partial u_1}{\partial\rho}(b,z) = \frac{\partial u_2}{\partial\rho}(b,z),\ z < 0, \tag{4b}$$

$$\frac{\partial}{\partial\rho}u_2(a,z) = 0,\ z < 0, \tag{4c}$$

$$\frac{\partial}{\partial\rho}u_3(a,z) = 0,\ z < 0, \tag{4d}$$

$$u_1(b,z) = u_5(b,z),\ z > l, \tag{4e}$$

$$\frac{\partial u_1}{\partial\rho}(b,z) = \frac{\partial u_5}{\partial\rho}(b,z)\ \ z > l, \tag{4f}$$

$$\frac{\partial}{\partial\rho}u_1(b,z) = 0,\ z \in (0,l), \tag{4g}$$

$$(ik_1 n_1 - \frac{\partial}{\partial\rho})u_4(b,z) = 0 \quad z \in (0,l), \tag{4h}$$

$$u_3(\rho,0) + u^i,\ \rho \in (0,a), \tag{4i}$$

$$\frac{\partial}{\partial z}u_3(\rho,0) + \frac{\partial}{\partial z}u^i, \rho \in (0,a), \tag{4j}$$

$$u_4(\rho,l) = u_5(\rho,l), \rho \in (0,b), \tag{4k}$$

$$\frac{\partial u_4}{\partial z}(\rho,l) = \frac{\partial u_5}{\partial z}(\rho,l), \rho \in (0,b), \tag{4l}$$

$$\frac{\partial u_2}{\partial z}(\rho,0)=0\,,\ \rho\in(a,b)\,, \tag{4m}$$

$$(ik_1n_2+\frac{\partial u_4}{\partial z})(\rho,0)=0\,,\ \rho\in(a,b)\,. \tag{4n}$$

To ensure the uniqueness of the mixed boundary-value problem, one has to take into account the following radiation and edge conditions,

$$u\approx\frac{e^{ikr}}{r},\ r=\sqrt{\rho^2+z^2}\,, \tag{4o}$$

$$u^T(b+0,z)=O\,,\ z\to-0\,, \tag{4p}$$

$$\frac{\partial}{\partial\rho}u^T(b+0,z)=O(z^{-1/3})\,,\ z\to-0\,, \tag{4q}$$

$$u^T(b,z)=O\,,\ z\to l+0\,, \tag{4r}$$

$$\frac{\partial}{\partial\rho}u^T(b,z)=O((z-l)^{-1/2})\,,\ z\to l+0\,. \tag{4s}$$

By taking the Fourier transform of $u(\rho,z)$ with respect to the variable z and considering also above mentioned boundary and continuity conditions in the transform domain α, the problem is reduced into the following modified Wiener-Hopf equation of the third kind, which is valid in the strip $Im(-k)<Im(\alpha)<Im(k)$,

$$\begin{aligned}&-\frac{b}{2}F_1(b,\alpha)+\frac{\dot{H}_-(b,\alpha)}{K^2(\alpha)}Q(\alpha)+\frac{e^{i\alpha l}\dot{H}_+(b,\alpha)}{K^2(\alpha)R(\alpha)}\\&=\frac{i\alpha}{\pi}\sum_{m=0}^{\infty}\frac{J_1(Z_ma)}{J_1(Z_mb)}\frac{f_m}{Z_m}\frac{1}{\delta_m^2-\alpha^2}\\&\quad+e^{i\alpha l}\frac{b}{2}\sum_{m=0}^{\infty}\frac{J_0(\xi_m)}{\alpha_m^2-\alpha^2}[g_m-i\alpha h_m]\end{aligned} \tag{5a}$$

where

$$H_-(\rho,\alpha)=\int_{-\infty}^{0}u_1(\rho,z)e^{i\alpha z}dz\,, \tag{5b}$$

$$H_+(\rho,\alpha)=\int_{l}^{\infty}u_1(\rho,z)e^{i\alpha(z-l)}dz\,, \tag{5c}$$

$$H_1(\rho,\alpha)=\int_{0}^{l}u_1(\rho,z)e^{i\alpha z}dz\,, \tag{5d}$$

$$K(\alpha)=\sqrt{k^2-\alpha^2}\,, \tag{5e}$$

$$R(\alpha)=i\pi J_1(Kb)H_1^{(Kb)}\,, \tag{5f}$$

$$Q(\alpha)=\frac{H_1^{(1)}(Ka)}{\pi H_1^{(1)}(Kb)\left[J_1(Ka)Y_1(Kb)-J_1(Kb)Y_1(Ka)\right]}\,, \tag{5g}$$

$$Z_m=K(\delta_m),\quad m=0,1,2,..\,, \tag{5h}$$

$$J_1(j_m)=0,\ m=0,1,2,...\,, \tag{5i}$$

$$\alpha_m=\sqrt{k^2-\left(\dot{J}_m/b\right)^2},\quad m=0,1,2,...\,, \tag{5j}$$

$$f_m=\frac{\pi^2}{2}\frac{J_1^2(Z_mb)Z_m^2}{J_1^2(Z_ma)-J_1^2(Z_mb)}\int_a^b f(t)\left[J_1(Z_ma)Y_0(Z_mt)-Y_1(Z_ma)J_0(Z_mt)\right]tdt\,, \tag{5k}$$

$$g_m=\frac{2}{b^2J_0^2(j_m)}\int_0^b g(t)J_0(\frac{j_m}{b}t)tdtm\neq0\,, \tag{5l}$$

and

$$h_m=\frac{2}{b^2J_0^2(j_m)}\int_0^b h(t)J_0(\frac{j_m}{b}t)tdt,m\neq0\,. \tag{5m}$$

Using the factorization and the decomposition procedures together with the Liouville theorem, the modified Wiener-Hopf equation in (5a) can be reduced to the following system of Fredholm integral equations of the second kind,

$$\begin{aligned}&\frac{\dot{H}_+(b,\alpha)}{(k+\alpha)R_+(\alpha)}=\\&-\frac{1}{2\pi i}\int_{L^+}\frac{\dot{H}_-(b,\tau)R_-(\tau)Q(\tau)e^{-i\tau l}}{(k+\tau)(\tau-\alpha)}d\tau\\&+\frac{b}{2}\sum_{m=0}^{\infty}\frac{J_0(\xi_m)\left[g_m+i\alpha_mh_m\right](k+\alpha_m)R_+(\alpha_m)}{2\alpha_m(\alpha+\alpha_m)}\\&-\frac{i}{2\pi}\sum_{m=0}^{\infty}\frac{J_1(Z_ma)}{J_1(Z_mb)}\frac{f_m}{Z_m}\frac{k+\delta_m}{\delta_m+\alpha}R_+(\delta_m)e^{i\delta_ml}\end{aligned} \tag{6a}$$

$$\begin{aligned}&\frac{\dot{H}_-(b,\alpha)Q_-(\alpha)}{(k-\alpha)}=\\&\frac{1}{2\pi i}\int_{L^-}\frac{\dot{H}_+(b,\tau)e^{i\tau l}}{(k-\tau)R(\tau)Q_+(\tau)(\tau-\alpha)}d\tau\\&-\frac{b}{2}\sum_{m=0}^{\infty}\frac{J_0(\xi_m)\left[g_m-i\alpha_mh_m\right](k+\alpha_m)e^{i\alpha_ml}}{2\alpha_m(\alpha-\alpha_m)Q_+(\alpha_m)}\\&+\frac{i}{2\pi}\sum_{m=0}^{\infty}\frac{J_1(Z_ma)}{J_1(Z_mb)}\frac{f_m}{Z_m}\frac{k+\delta_m}{\delta_m-\alpha}\frac{1}{Q_+(\delta_m)}\end{aligned} \tag{6b}$$

where the paths of integration L^+ and L^- are depicted in [7]. Here, $R_+(\alpha),Q_+(\alpha)$ and $R_-(\alpha)=R_+(-\alpha)$, $Q_-(\alpha)=Q_+(-\alpha)$ are the split functions [8] regular and free of zeros in the upper $\left(Im\alpha>Im(-k)\right)$ and lower $\left(Im\alpha<Imk\right)$ halves of the complex $\alpha-$ plane, respectively, resulting from the Wiener-Hopf factorization of $R(\alpha)$ and $Q(\alpha)$, which are given by (5f) and (5g), in the following form,

$$R(\alpha)=R_+(\alpha)R_-(\alpha)\,, \tag{7a}$$

$$Q(\alpha)=Q_+(\alpha)Q_-(\alpha)\,. \tag{7b}$$

The explicit expressions for $R_+(\alpha)$ and $Q_+(\alpha)$ can be obtained by using the results of [9], [10]. For $kl>>1$, the coupled system of Fredholm integral equations of the second kind in (6a) and (6b), are susceptible to a treatment by iterations

$$\dot{H}_+(b,\alpha)_-=\dot{H}_+^{(1)}(b,\alpha)+\dot{H}_+^{(2)}(b,\alpha)+\cdots\,, \tag{8a}$$

$$\dot{H}_-(b,\alpha)_-=\dot{H}_-^{(1)}(b,\alpha)+\dot{H}_-^{(2)}(b,\alpha)+\cdots. \tag{8b}$$

III. MODAL MATCHING TECHNIQUE: DETERMINATION OF THE EXPANSION COEFFICIENTS

Modal matching technique (MMT) is a powerful numeric method of analyzing horn radiators in which the actual profile of the horn is replaced by a series of uniform waveguide sections. The MMT can be

considered as a method of obtaining the overall transmission and reflection properties of a horn. The horn is represented as a box as shown in Fig. 2, where [A] and [B] are column matrices containing the forward and reflection coefficients of all the modes looking into the horn from source side. Similarly, [C] and [D] represent column matrices containing the forward and reflection coefficients of all the modes looking into the aperture of the horn from outside [11 - 13].

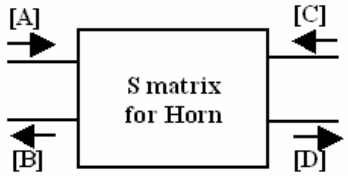

$$\begin{bmatrix}[B]\\[D]\end{bmatrix}=[S]\begin{bmatrix}[A]\\[C]\end{bmatrix}\quad [S]=\begin{bmatrix}[s_{11}]\,[s_{12}]\\[s_{21}]\,[s_{22}]\end{bmatrix}$$

Fig. 2. Horn represented as a scattering matrix [S].

The field in the cavity can be expressed in terms of the waveguide normal modes as follow,

$$u_3(\rho,z)=\sum_{n=0}^{\infty}c_n e^{-i\beta_n z}J_0(j_n\frac{\rho}{a}) \tag{9a}$$

with

$$\beta_n=\sqrt{k^2-\frac{j_n^2}{a^2}},\qquad n=0,1,2\ldots. \tag{9b}$$

Here ξ_n 's are the roots of the characteristic equation

$$J_1(j_n)=0,\qquad n=0,1,2\ldots. \tag{9c}$$

Similarly, in the region $0<\rho<b,\quad 0<z<l$, $u_4(\rho,z)$ can be expressed in terms of the following normal waveguide modes,

$$u_4(\rho,z)=\sum_{n=0}^{\infty}\left(p_n e^{i\nu_n z}+q_n e^{-i\nu_n z}\right)J_0(\xi_n\frac{\rho}{b}), \tag{10a}$$

$$ik_1 b\eta_1 J_0(\xi_n)+\xi_n J_1(\xi_n)=0,\qquad n=0,1,2\ldots, \tag{10b}$$

$$\nu_n=\sqrt{k_1^2-\frac{\xi_n^2}{b^2}},\qquad n=0,1,2\ldots. \tag{10c}$$

Now, from the continuity relations we get

$$\frac{\partial}{\partial z}u_4(\rho,0)=\begin{cases}\dfrac{\partial}{\partial z}u_3(\rho,0)+ik, & \rho\in(0,a)\\ -ik_1\eta_2 u_4(\rho,0), & \rho\in(a,b)\end{cases} \tag{11a}$$

$$u_4(\rho,0)=u_3(\rho,0)+1;\qquad \rho\in(0,a), \tag{11b}$$

$$\frac{\partial u_4}{\partial z}(\rho,l)=g(\rho)=\sum_{m=0}^{\infty}g_m J_0(\xi_m\frac{\rho}{b});\ \rho\in(0,b), \tag{11c}$$

and

$$u_4(\rho,l)=h(\rho)=\sum_{m=0}^{\infty}h_m J_0(\xi_m\frac{\rho}{b});\ \rho\in(0,b). \tag{11d}$$

Inserting the series expansions of $g(\rho)$ and $h(\rho)$ [14] given in equations (5l) and (5m) into equations (11c) and (11d), respectively, and using equations (9a) and (10a) we get,

$$-\sum_{n=0}^{\infty}i\nu_n\left[p_n-q_n\right]J_0(\xi_n\frac{\rho}{b})=$$

$$\begin{cases}\sum_{m=0}^{\infty}i\beta_m c_m J_0(j_m\dfrac{\rho}{a})-ik,\ \rho\in(0,a)\\ ik_1 n_2 u_4(\rho,0),\quad \rho\in(a,b),\end{cases} \tag{12a}$$

$$\sum_{n=0}^{\infty}\left[p_n+q_n\right]J_0(\xi_n\frac{\rho}{b})=$$

$$\sum_{m=0}^{\infty}c_m J_0(j_m\frac{\rho}{a})+1,\quad \rho\in(0,a), \tag{12b}$$

$$\sum_{n=0}^{\infty}i\nu_n\left[p_n e^{i\nu_n l}-q_n e^{-i\nu_n l}\right]J_0(\xi_n\frac{\rho}{b})=$$

$$\sum_{m=0}^{\infty}g_m J_0(\xi_m\frac{\rho}{b}), \tag{12c}$$

and

$$\sum_{n=0}^{\infty}\left[p_n e^{i\nu_n l}+q_n e^{-i\nu_n l}\right]J_0(\xi_n\frac{\rho}{b})=$$

$$\sum_{m=0}^{\infty}h_m J_0(\xi_m\frac{\rho}{b}). \tag{12d}$$

Multiplying both sides of equations (12a) and (12b) by $\rho J_0(\xi_l\frac{\rho}{b})$ and by $J_0(\xi_l\frac{\rho}{a})$, respectively, and integrating from 0 to b and from 0 to a, respectively, we obtain the following system of linear algebraic equations (13a)-(13f),

$$\left.\begin{aligned}&\frac{a}{b}\sum_{m=0}^{\infty}\beta_m c_m\frac{J_0(j_m)}{(j_m/a)^2-(\xi_l/b)^2}\times\\ &\quad\xi_l J_1(\xi_l\frac{a}{b})-\frac{kab}{\xi_l}J_1(\xi_l\frac{a}{b})=0\\ &k_1\eta_2\sum_{m=0}^{\infty}(p_n+q_n)\frac{ab}{\xi_m^2-\xi_l^2}\times\\ &\quad\left[\xi_l J_0(\xi_n\frac{a}{b})J_1(\xi_l\frac{a}{b})-\xi_n J_1(\xi_n\frac{a}{b})J_0(\xi_l\frac{a}{b})\right]=0\end{aligned}\right\}n\neq l, \tag{13a}$$

$$\nu_n(p_n-q_n)\frac{b^2}{2}\frac{J_0^2(\xi_n)}{\xi_n^2}\left[\xi_n^2-(k_1 b\eta_1)^2\right]$$

$$=\begin{cases}\dfrac{a}{b}\sum_{m=0}^{\infty}\beta_m c_m\dfrac{J_0(j_m)}{(j_m/a)^2-(\xi_l/b)^2}\times\\ \qquad\xi_l J_1(\xi_l\dfrac{a}{b})+\dfrac{kab}{\xi_l}J_1(\xi_l\dfrac{a}{b})\\ -k_1\eta_2(p_n+q_n)\left\{\begin{aligned}&\frac{b^2}{2}\frac{J_0^2(\xi_n)}{\xi_n^2}\times\\ &\left[\xi_n^2-(k_1 b\eta_1)^2\right]-\\ &\frac{a^2}{2}\left[J_0^2(\xi_n\frac{a}{b})+J_1^2(\xi_n\frac{a}{b})\right]\end{aligned}\right.\end{cases},n=l, \tag{13b}$$

$$c_0=\sum_{n=0}^{\infty}(p_n+q_n)\frac{2b}{a\xi_n}J_1(\xi_n\frac{a}{b})-1,m=0, \tag{13c}$$

$$c_m = \frac{2}{abJ_0(j_m)}\times \sum_{n=0}^{\infty}\left[\begin{array}{l}(p_n+q_n)\dfrac{\xi_n}{(\xi_n/b)^2-(j_m/a)^2}\\ \times J_1(\xi_n\dfrac{a}{b})\end{array}\right],\ m=1,2,...,$$

(13d)

$$g_m = i\alpha_m\left[p_m e^{i\alpha_m l}-q_m e^{-i\alpha_m l}\right],\ m=0,1,2,....,\quad (13e)$$

$$h_m = p_m e^{i\alpha_m l}+q_m e^{-i\alpha_m l},\ m=0,1,2,.....\quad (13f)$$

This system of equations can be rearranged as,

$$g_m - i\alpha_m h_m = -2i\alpha_m q_m e^{-i\alpha_m l},\ m=0,1,2,....,\quad (13g)$$

$$g_m + i\alpha_m h_m = 2i\alpha_m p_m e^{i\alpha_m l}\quad m=0,1,2,....,\quad (13h)$$

$$\nu_r(p_r-q_r)\frac{b^2}{2}\frac{J_0^2(\xi_r)}{\xi_r^2}\left[\xi_r^2-(k_1 b\eta_1)^2\right]=$$
$$\frac{2}{b^2}\sum_{m=0}^{\infty}\beta_m\left[\sum_{n=0}^{\infty}(p_n+q_n)\frac{\xi_n J_1(\xi_n\frac{a}{b})}{(\xi_n/b)^2-(j_m/a)^2}\right]$$
$$\times\frac{\xi_r J_1(\xi_r\frac{a}{b})}{(j_m/a)^2-(\xi_r/b)^2}+2\frac{kab}{\xi_r}J_1(\xi_r\frac{a}{b})$$
$$-k_1\eta_2(p_r+q_r)\left\{\begin{array}{l}\dfrac{b^2}{2}\dfrac{J_0^2(\xi_r)}{\xi_r^2}\left[\xi_r^2-(k_1 b\eta_1)^2\right]\\ -\dfrac{a^2}{2}\left[J_0^2(\xi_r\frac{a}{b})+J_1^2(\xi_r\frac{a}{b})\right]\end{array}\right\}.$$

(13i)

To obtain an approximate value for $\dot{H}_{+}(a,\alpha)$ and $\dot{H}_{-}(a,\alpha)$, we substitute $\alpha = k,\alpha_1,\alpha_2,...,\alpha_N$ in equation (6a) and $\alpha = -\delta_1,-\delta_2,...,-\delta_N$ in equation (6b). These equations together with equations (13g) to (13i) result in $3(N+1)$ equations for $3(N+1)$ unknowns. The solution of these simultaneous equations yields approximate solutions for $\dot{H}_{+}(b,k)$, $\dot{H}_{+}(b,\alpha_1)$, $\dot{H}_{+}(b,\alpha_2),...$ and $\dot{H}_{-}(b,-\delta_1)$, $\dot{H}_{-}(b,-\delta_2),..$. Using equations (5k) to (5m) we obtain equations (14a) and (14b) together with equations (14c) to (14h),

$$-\frac{b}{2}\frac{J_0(j_r)(g_r-i\alpha_r h_r)}{2(k+\alpha_r)R_+(\alpha_r)}=$$
$$\frac{b}{2}\sum_{m=0}^{\infty}\frac{J_0(j_m)(k+\alpha_m)}{2\alpha_m}\left\{\begin{array}{l}\dfrac{(g_m+i\alpha_m h_m)R_+(\alpha_m)}{\alpha_r+\alpha_m}\\ -\dfrac{(g_m-i\alpha_m h_m)e^{i\alpha_m l}}{Q_+(\alpha_m)}T_{rm}^1\end{array}\right\}\quad (14a)$$
$$-\frac{i}{2\pi}\sum_{m=0}^{\infty}S_m(k+\delta_m)\times\left\{\frac{R_+(\delta_m)}{\delta_m+\alpha_r}e^{i\delta_m l}-\frac{T_{rm}^2}{Q_+(\delta_m)}\right\}$$

$$\frac{i\delta_r}{\pi Z_r}\frac{J_1^2(Z_r b)-J_1^2(Z_r a)}{J_1(Z_r a)J_1(Z_r b)}\frac{Q_+(\delta_r)f_r}{(k+\delta_r)}=$$
$$\frac{b}{2}\sum_{m=0}^{\infty}\frac{J_0(j_m)(k+\alpha_m)}{2\alpha_m}\times\left\{\begin{array}{l}(g_m+i\alpha_m h_m)R_+(\alpha_m)T_{rm}^3\\ +\dfrac{(g_m-i\alpha_m h_m)e^{i\alpha_m l}}{(\alpha_m+\delta_r)Q_+(\alpha_m)}\end{array}\right\}$$
$$-\frac{i}{2\pi}\sum_{m=0}^{\infty}S_m(k+\delta_m)\times\left\{\begin{array}{l}R_+(\delta_m)e^{i\delta_m l}T_{rm}^4-\\ \dfrac{1}{Q_+(\delta_m)(\delta_m+\delta_r)}\end{array}\right\},$$

(14b)

$$S_m = \frac{J_1(Z_m a)}{J_1(Z_m b)}\frac{f_m}{Z_m},\quad (14c)$$

$$T_{rm}^1 = \left\{\begin{array}{l}-(kb)^2\dfrac{R_+(k)}{Q_+(k)}\dfrac{e^{ikl}}{(k+\alpha_m)}W_{-1/2}(-il(\alpha_r+k))\\ +\dfrac{2k\pi b^2}{(a^2-b^2)}\dfrac{R_+(k)e^{ikl}}{Q_+(k)(k+\alpha_r)(k+\alpha_m)}\times\\ \sum_{n=0}^{\infty}\dfrac{(k+\delta_n)R_+(\delta_n)}{(k-\delta_n)H_1^{(1)}(Z_n b)Q_+(\delta_n)}\times\\ \dfrac{H_1^{(1)}(Z_n a)e^{i\delta_n l}}{(\delta_n+\alpha_m)(\delta_n+\alpha_r)\dot{M}(-\delta_n)}\end{array}\right\},$$

(14d)

$$T_{rm}^2 = (kb)^2\frac{R_+(k)}{Q_+(k)}\frac{e^{ikl}}{(k+\delta_m)}W_{-1/2}(-il(\alpha_r+k))$$
$$-\frac{2k\pi b^2}{(a^2-b^2)}\frac{R_+(k)e^{ikl}}{Q_+(k)(k+\alpha_r)(k+\delta_m)}\times$$
$$\frac{(k+\delta_n)R_+(\delta_n)H_1^{(1)}(Z_n a)e^{i\delta_n l}}{(\delta_m+\delta_n)(k-\delta_n)H_1^{(1)}(Z_n b)Q_+(\delta_n)(\delta_n+\alpha_r)\dot{M}(-\delta_n)},$$

(14e)

$$T_{rm}^3 = (kb)^2\frac{R_+(k)}{Q_+(k)(\alpha_m+k)}e^{ikl}W_{-1/2}(-il(\delta_r+k))$$
$$+\frac{1}{2}\sum_{n=0}^{\infty}\frac{R_+(\alpha_n)(k+\alpha_n)^2e^{i\alpha_n l}}{\alpha_n(\delta_r+\alpha_n)(\alpha_n+\alpha_m)Q_+(\alpha_n)},\quad (14f)$$

$$T_{rm}^4 = (kb)^2\frac{R_+(k)}{Q_+(k)(\delta_m+k)}e^{ikl}W_{-1/2}(-il(\delta_r+k))$$
$$+\frac{1}{2}\sum_{n=0}^{\infty}\frac{R_+(\alpha_n)(k+\alpha_n)^2e^{i\alpha_n l}}{\alpha_n(\delta_r+\alpha_n)(\alpha_n+\delta_m)Q_+(\alpha_n)}\quad .\quad (14g)$$

The function $W_{-1/2}(\xi)$ is related to the Whittaker function $W_{-1/2,0}(\xi)$ [15] by the relation (14h),

$$W_{-1/2}(\xi) = \exp(\xi/2)\xi^{-1/2}W_{-1/2,0}(\xi)\ .\quad (14h)$$

By substituting equations (13g) and (13h) into equations (14a) and (14b) and also considering equation (13i), one can easily obtain the three infinite systems of linear algebraic equations with coefficients p_n , q_n and f_n .

IV. THE RADIATED FAR-FIELD AND COMPUTATIONAL RESULTS

The radiated field in the region $\rho > b$ can be obtained using,

$$u_1(\rho,z) = -\frac{1}{2\pi}\int_L \frac{H_0^{(1)}(K\rho)}{K(\alpha)H_1^{(1)}(Kb)}\times [\dot{H}_-(b,\alpha)+e^{i\alpha l}\dot{H}_+(b,\alpha)]e^{-i\alpha z}d\alpha \quad (15a)$$

where L is a straight line parallel to the real α -axis, lying in the strip $Im(-k) < Im(\alpha) < Im(k)$. Utilizing the asymptotic expansion of $H_0^{(1)}(k\rho)$ as $k\rho \to \infty$

$$H_0^{(1)}(K\rho) = \sqrt{\frac{2}{\pi K\rho}}e^{i(K\rho-\pi/4)}. \quad (15b)$$

The asymptotic evaluation of the integral in equation (15a) using the saddle point technique yields for the diffracted field for $k\sqrt{\rho^2+z^2} >> kl$,

$$u_1(\rho,z) \approx \frac{i}{\pi}\left\{\begin{array}{l} \dfrac{e^{ikr_1}}{kr_1}\dfrac{\dot{H}_+(b,-k\cos\theta_1)}{\sin\theta_1 H_1^{(1)}(kb\sin\theta_1)} \\ +\dfrac{e^{ikr_2}}{kr_2}\dfrac{\dot{H}_-(b,-k\cos\theta_2)}{\sin\theta_2 H_1^{(1)}(kb\sin\theta_2)} \end{array}\right\} \quad (16)$$

where $\dot{H}_+(b,\alpha)$ and $\dot{H}_-(b,\alpha)$ are given by equations (6a) and (6b), respectively. r_1,θ_1, and r_2,θ_2 are the spherical coordinates defined by

$$\rho = r_1\sin\theta_1 , z = r_1\cos\theta_1 \quad (17a)$$

and

$$\rho = r_2\sin\theta_2 , \; z-l = r_2\cos\theta_2 . \quad (17b)$$

In the far field region equation (16) reduces to

$$u_1(\rho,z) \approx \frac{i}{\pi}\left\{\frac{\dot{H}_+(b,-k\cos\theta_1)+e^{-ikl\cos\theta_1}\dot{H}_-(b,-k\cos\theta_1)}{\sin\theta_1 H_1^{(1)}(kb\sin\theta_1)}\right\}\frac{e^{ikr_1}}{kr_1}. \quad (18)$$

We can see that f_m and q_m decay exponentially with m so that the infinite algebraic systems converge very rapidly. Thus, they can be solved by truncating the infinite matrix and numerically inverting the resulting finite system. The value of the truncation number N is increased until the final physical quantities such as the amplitude of the radiated field or the reflection coefficients become insensitive up to desired digit after the decimal point.

The reflection coefficient is calculated by using hybrid mode-matching (hMM)/ method-of-moment (MoM) technique presented in the waveguide synthesis program for waveguide networks WASP-Net [16]. The reflection coefficient calculating by WH is very close to hMM-MoM. The discrepancy between WH and hMM-MoM is %0.23 at the dominant mode propagation of the waveguide. The amplitude of the reflection coefficient is reduced by increasing the radius of the waveguide (*ka*) and the length of the aperture (*kl*) while *kb* is fixed. It is observed that the relative errors are reduced for higher frequencies by increasing number truncation number N.

Showing numerically can make another effective check of the analysis that the continuity relation in equation (12b) is satisfied. The absolute error is less than %1.02 for $N \geq 14$.

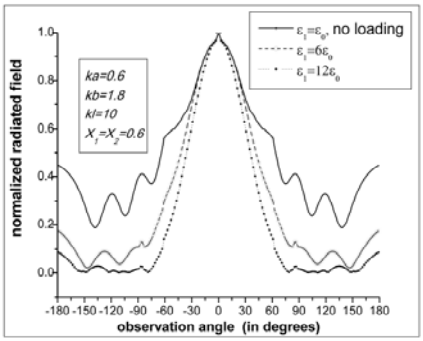

Fig. 3. Normalized radiated field versus the observation angle for different values of the k_1 $(\eta_1 = iX_1, \eta_2 = iX_2, X_1, X_2 > 0)$.

Figure 3 shows the variation of the normalized diffracted field amplitude $|u_1(r_1,\theta_1)/u_1(r_1,0)|$ versus the observation angle θ_1 , for different values of k_1 when ka, kb and kl is fixed. Note that the directivity of the horn increases with increasing values of the dielectric material. Also it has been noted side lobe level is decrease explicitly with increasing values of the dielectric material.

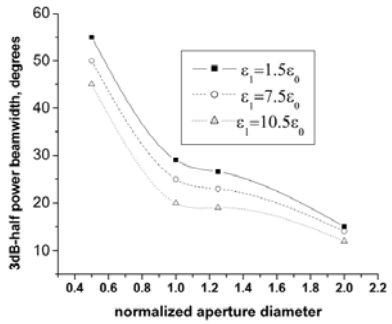

Fig. 4. 3dB beam-width to aperture diameter ($2b/\lambda$) ($X_1 = X_2 = 0.1, a/\lambda = 0.6, l = 1.5\lambda$).

Figure 4 shows the variation of the -3dB beamwidth versus the observation angle for different values of normalized aperture diameter. The 3-dB

beamwidth decrease with the increasing values of $2b/\lambda$. Also note that the 3-dB beamwidth of the horn decreases with increasing values of the dielectric material.

Finally, Fig. 5 display the amplitude of the relative power level obtained in the present work for $a/\lambda = 0.0875$, $b/\lambda = 0.5$, $l/\lambda = 1.6$, the numerical results calculated by using MoM programmed by [17]. We can see that the results obtained in this work approach the numerical solution for $\eta_1 = \eta_2$ and fit quite well along the observation angle.

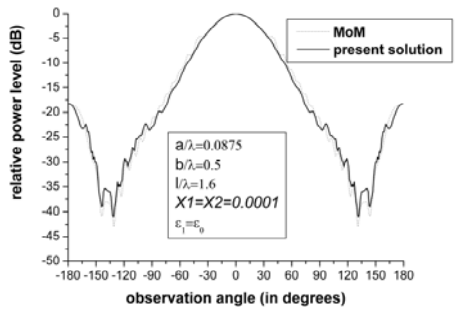

Fig. 5. Relative power level versus the observation angle (comparison with the MoM solution).

V. CONCLUSION

The radiation of plane harmonic scalar waves from a dielectric loaded using the mode matching method in conjunction with the Wiener-Hopf technique treats scalar feed horn. The solution is exact but formal since infinite series of unknowns and some branch-cut integrals with unknown integrands are involved. Approximation procedures based on rigorous asymptotic are used and the approximate solution to the Wiener-Hopf equations are derived in terms of infinite series of unknowns, which are determined from infinite systems of linear algebraic equations. The advantage of the WH Technique over other methods is that it is rigorous in the sense that the edge condition is explicitly incorporated in the analysis and that it has the potential of providing accurate and reliable results over broad frequency ranges. Furthermore, contrary to some numerical techniques, which are efficient only when the problem involves finite boundaries of limited length, the WH method does not suffer from restrictions. Numerical solution of these systems is obtained for various values of the dielectric materials of the problem and their effect on the directivity of the circular feed horn is presented in the scope of this work. By dielectric loading, it is possible to narrowing of the beamwidth and can provide low levels of the side lobes.

ACKNOWLEDGEMENT

The author is indebted to the referees for their constructive critics, which led to improving this work.

REFERENCES

[1] A. D. Olver, "Corrugated Horns," *Electronics & Communication Engineering Journal*, pp. 4-10, February, 1992.

[2] H. Levine and J. Schwinger, "On the sound radiation of sound from an unflanged circular pipe," *Journal of Physics*, vol. 73, pp. 383, 1948.

[3] Y. Ando, "On the sound radiation from semi-infinite circular pipe of certain wall thickness," *Acustica*, vol. 22, pp. 219-225, 1969/70.

[4] A. D. Rawlins, "A bifurcated circular waveguide problem," *IMA J. Appl. Math*., vol. 54, pp. 59-81, 1995.

[5] A. Büyükaksoy and B. Polat, "Diffraction of acoustic waves by semi-infinite cylindrical impedance pipe of certain wall thickness," *J. Eng. Math*., vol. 33, no. 4, pp. 333-352, 1998.

[6] F. Arndt, et al., "Fast CAD and optimization of waveguide components and aperture antennas by hybird MM/FE/MoM/FD methods-State-of-the-art and recent advances," *IEEE Trans. Microwave Theory and Tech*. vol. 52, pp. 292-305, Jan. 2004.

[7] B. Turetken, A. Buyukaksoy, and A. Demir, "Radiation of sound waves from a rigid stepped cylindrical waveguide," *J. Eng.. Math.*, vol. 46, pp. 33–54, 2003.

[8] B. Turetken, "Rigorous analysis of scalar feed horn with different impedance internal surfaces," *Journal of Electromagnetics Waves and Applic.*, vol. 26, no. 5, pp. 359-385, July 2006.

[9] S-W. Lee, V. Jamnejad, and R. Mittra, "Near field of scattering by a hollow semi-infinite cylinder and its application to sensor booms," *IEEE Trans. Antennas and Propagat.*, vol. 21, no. 2, pp. 182-188, 1973.

[10] B. Turetken, "Analysis of the radiation of scalar waves by circular horn radiator," *Ph.D. Thesis, Istanbul Technical University*, TURKEY, 2002.

[11] A. Wexler, "Solution of waveguide discontinuities by modal analysis" *IEEE Trans. Microwave Theory and Tech*., vol. 15, pp. 508-517, 1967.

[12] P. H. Masterman and P. J. B. Clarricoats, "Computer field matching solution of waveguide transverse discontinuties," *IEE Proceedings*, vol. 118, pp 51-63, 1971.

[13] W. J. English, "The circular waveguide step discontinuity mode transducer," *IEEE Trans. Microwave Theory and Tech*., vol. 21, pp. 633-636, 1973.

[14] I. H. Sneddon, *The Use of Integral Transforms*, Mc Graw Hill, NewYork, 1972.

[15] E. T. Whittaker and G. N. Watson, "Modern analysis," *Cambridge* 1902.

[16] Tutorial Manual and WASP-Net Waveguide Component Design and Optimization Handbook. WASP-Net 6.2 Program, MiG GmbH & Co. KG, HR A 22515, Bremen, Germany.

[17] T. H. Lee and R. C. Rudduck, *OSU Reflector Antenna Code*, NecRef V. 3, *Technical Report 318021-1*, Electroscience Laboratory, Ohio State University, Feburuary 1994.

Electromagnetic Scattering Problems Utilizing a Direct, Parallel Solver

William R. Dearholt[1] and Steven P. Castillo[2]

[1] Box 1663, MS F644
Los Alamos National Laboratory
Los Alamos, New Mexico 87544
[2] College of Engineering
New Mexico State University
Box 30001, MSC 3449
Las Cruces, New Mexico 88003

Abstract - Finite-element discretization of the vector wave equation is a common method of analyzing the electromagnetic field scattered by an object. One of the most challenging aspects of this research concerns the solution of the system of equations resulting from the finite-element analysis. Advanced solution algorithms have enabled researchers to generate more realistic computational models for scattering problems. The work presented here represents what is believed to be a unique parallel algorithm offering researchers a method of solving large, sparse systems of equations with advantages that are not found in previously published works.

This research uses a parallel sparse matrix decomposition algorithm to solve very large algebraic systems arising from the finite-element solution of electromagnetic scattering problems. This article provides an overview of the scattering problem and how the direct, parallel algorithm offers an efficient method of solution.

I. INTRODUCTION

The solution of large, sparse, irregular systems of equations is an important part of many computational tasks in science and engineering. In general, such a system can be solved iteratively or directly. The former path typically utilizes a Krylov-based method with preconditioning while the latter is some variation of Gaussian elimination. The convergence of the iteration procedure depends not only on the spectral content of the coefficient matrix but also on the right-hand-side excitation as well. Convergence difficulties have been reported in electromagnetics scattering problems similar to those discussed in this research [16]. In the case of problems with many excitation vectors, Krylov methods lose their advantage over Gaussian elimination methods since the iterative procedure typically has to be repeated for each right-hand side. The majority of the parallel, sparse matrix solvers are implemented with an iterative algorithm. They have been easier to code and they work well for many applications. A number of public domain codes using iterative techniques are available for download. For more information on iterative solvers that are available for public use, see references [2-5] or see the URL `http://www.netlib.org/utk/papers/iterative-survey`.

There are a number of parallel, direct solver algorithms available for sparse irregular systems. One that is currently being distributed is the PSPASES code from the University of Minnesota [7]. PSPASES uses a Cholesky algorithm for factorization of the coefficient matrix. A similar code is also available from the IBM Watson Research Center [8]. The discussion of their algorithm and a list of results were published in [9].

SUPERLU is a sparse matrix code that is available via the Gnu Public License. SUPERLU was initially a sequential code but was recently released to run on distributed-memory computers. While results are not available for problems with multiple excitation vectors, runtimes have been published in a number of papers and conference proceedings including [10, 11]. More information can be found at the URL `http://www.nersc.gov/ xiaoye/SuperLU/`.

References [13, 14] discuss the algorithm used as a basis for the numerical linear algebra in this paper. In [13, 14] , timing results are shown for solution of electrostatic problems. These papers summarize how the original parallel Cholesky factorization algorithm was modified to allow for indefinite and numerically nonsymmetric coefficient matrices. The solution domains for these problems were quite simple. The one-way dissection graph partitioning and the parallel LU factorization algorithm used at the time were sufficient to solve these problems. When more complex geometries were discretized with tetrahedral elements however, it was apparent that these methods of solution were not adequate. One fundamental problem was the one-way dissection algorithm used to subdivide the solution domain. The algorithm was not sophisticated enough for the finite-element problem of interest and resulted in poor load balancing. In addition, the early versions of the present algorithm were only able to solve a system with a single excitation vector which defeated the purpose for using the direct solution method.

II. COMPUTATIONAL METHODOLOGY

A parallel, computational algorithm for the direct solution of large, sparse, irregular systems of equations generated by the finite-element method as applied to partial differential equations has been developed. The resulting linear systems may be definite or indefinite but are structurally symmetric and may contain many excitation vectors. The computer code is called *mp_solve*. The *mp_solve* code is currently used as a tool by researchers in science and engineering to solve these algebraic systems resulting from finite-element discretizations of field equations in areas including bioelectromagnetics, semiconductor device modeling, fluid flow, remote sensing, electromagnetic radiation, microwave circuit simulation and scattering problems. The current implementation of the *mp_solve* algorithm has the capability to solve a linear system for many excitation vectors as is commonly done for electromagnetic scattering problems. The focus of the research presented here is the utilization of the *mp_solve* software as a tool for solving large systems resulting from the finite-element discretization of the vector wave equation. In the following section, the computational techniques used in the *mp_solve* application are described in detail.

A. Block LU Factorization of the System of Equations

The goal of the *mp_solve* software is to solve the linear system of equations,

$$\mathbf{Ax} = \mathbf{b} \tag{1}$$

where $\mathbf{A}$ is the coefficient matrix, $\mathbf{b}$ is the excitation vector and $\mathbf{x}$ is the solution vector.

A reordering scheme can be applied to matrix $\mathbf{A}$ to obtain the border-block diagonal matrix shown in Fig. 2. The border-block diagonal system is represented by four submatrices,

$$\mathbf{A} = \begin{bmatrix} \mathbf{B} & \mathbf{V} \\ \mathbf{Z^T} & \bar{\mathbf{C}} \end{bmatrix} \tag{2}$$

where $\mathbf{B}$ represents the diagonal blocks, $\mathbf{V}$ represents the upper-right border block, $\mathbf{Z^T}$ represents the lower-left border block and $\bar{\mathbf{C}}$ is the lower-right block.

The coefficient matrix $\mathbf{A}$ can be factored into upper and lower triangular matrices,

$$\mathbf{A} = \mathbf{LU} \tag{3}$$

where,

$$\mathbf{L} = \begin{bmatrix} \mathbf{L_B} & \mathbf{0} \\ \mathbf{W^T} & \mathbf{L_C} \end{bmatrix} \tag{4}$$

and,

$$\mathbf{U} = \begin{bmatrix} \mathbf{U_B} & \mathbf{G} \\ \mathbf{0} & \mathbf{U_C} \end{bmatrix}. \tag{5}$$

The submatrices $\mathbf{L_B}$ and $\mathbf{U_B}$ and $\mathbf{L_C}$ and $\mathbf{U_C}$ are the factors of the submatrices $\mathbf{B}$ and $\mathbf{C}$, respectively. The upper and lower factors of the diagonal blocks are computed,

$$u_{i,j} = b_{i,j} - \sum_{k=1}^{i-1} l_{i,j} u_{k,j} \tag{6}$$

and,

$$l_{i,j} = \frac{b_{i,j} - \sum_{k=1}^{j-1} l_{i,j} u_{k,j}}{U_{j,j}}. \tag{7}$$

The submatrix $\mathbf{C}$ is found by computing,

$$\mathbf{C} = \bar{\mathbf{C}} - \mathbf{Z^T U_B^{-1} L_B^{-1} V}. \tag{8}$$

With a few algebraic manipulations, the modification to submatrix $\bar{\mathbf{C}}$ becomes,

$$\mathbf{Z^T U_B^{-1} L_B^{-1} V} = \mathbf{Z^T U_B^{-1} L_B^{-1} L_B G} = \mathbf{Z^T G}. \tag{9}$$

To find the columns in the matrix $\mathbf{G}$, solve the system $\mathbf{U_B G} = \mathbf{G}$ for each column $\tilde{\mathbf{g}}_\mathbf{i}$ of the matrix $\mathbf{G}$ and finally write the modifications to submatrix $\bar{\mathbf{C}}$ as,

$$\mathbf{C} = \bar{\mathbf{C}} - \mathbf{Z^T \tilde{G}}. \tag{10}$$

Each column of $\mathbf{Z^T}$ and $\tilde{\mathbf{G}}$ can be computed as they are needed and no two-dimensional arrays need to be stored thus cutting down significantly on memory requirements. When the modifications are complete, the subdomain-boundary block is factored using a block-column wrapped, dense LU factorization algorithm.

B. Partitioning the Solution Domain

Prior to solving the system of equations on the parallel computer, the computational domain must be partitioned. The mesh connectivity data produced by the mesh generator is used to produce a graph. Graph partitioning software is then employed to subdivide the graph of the elements into a specified number of subdomains. The cuts (or subdomain boundaries) are made through the graph so that approximately the same number of elements are assigned to each subdomain while trying to minimize the number of elements which fall on the subdomain boundaries. The process of cutting the graph is repeated until the desired number of subdomains is obtained.

The graph formed by the elemental graph however is not a representation of the nonzero structure of the coefficient matrix. The unknowns in the problem are associated with the edges (and faces) of the mesh. Further work is needed to determine which edges (and faces) from each element reside on each subdomain.

Once this is known, another graph is produced representing the edge (and face) connectivity for each subdomain. The adjacency data in these new graphs indicate the locations of the nonzero entries in the coefficient matrix. This process results in a nested dissection of the coefficient matrix.

Figure 1 illustrates a mesh of rectangular elements partitioned into four subdomains. The edges which fall on the subdomain boundaries are shown with thick lines. The algorithm described in this research depends on the coefficient matrix being stored in the border-block diagonal form illustrated in Fig. 2. To obtain this matrix ordering, the edges that reside on the interior of each subdomain are numbered first and those residing on the subdomain boundaries are numbered last. The interactions between edges on the interior of each subdomain form the four diagonal blocks shown in Fig. 2. The interactions between interior edges and subdomain-boundary edges form the border-blocks on the upper-right and lower-left and the interactions between subdomain-boundary edges form the darkest block on the lower-right of Fig. 2. Note that this ordering results in a matrix of the form shown in equation (2) of the previous section. Details regarding this border-block diagonal matrix ordering can be found in George and Liu [2].

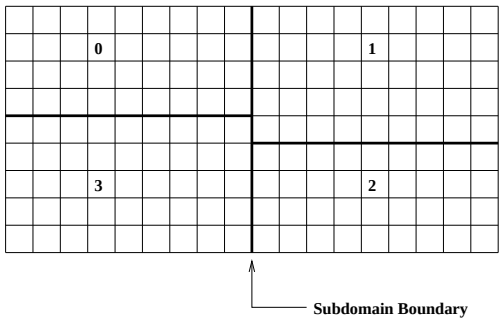

Fig. 1. Graph of solution domain partitioned into four subdomains.

C. Implementation of the Solution Domain Partitioner

The pre-processing phase of this application consists of subdividing the finite-element mesh into the number of subdomains desired by the user. The *Chaco* (http://www.cs.sandia.gov/CRF/chac.html) graph partitioner obtained from Sandia National Laboratory is used to perform a partitioning into a specified number of subdomains. Because of the recursive partitioning of the graph that is performed by *Chaco*, the number of processors required will be 2^p where p is the number of bisections performed by *Chaco*.

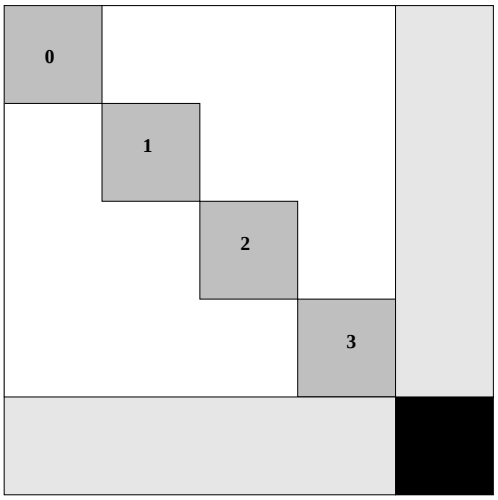

Fig. 2. Border-block diagonal system.

Alternative graph partitionings could be considered to remove the power-of-two restriction although that has not been explored in this research. Figure 1 shows the graph of a matrix partitioned into four subdomains.

The order in which the unknowns are numbered is of crucial interest for our application. One goal of the nested dissection is to obtain a border-block diagonal system (see Fig. 2) which can be distributed to the processors with the number of processors used equal to the number of diagonal blocks. Each diagonal block is mapped to a different processor. The data on the off-diagonal borders is mapped to the same set of processors depending on which processor the interior unknowns reside on. The subdomain boundary block is distributed among the same processors in a block-column wrapped format. Figure 3 illustrates the distribution of the block-columns of the subdomain boundary block to all of the processors.

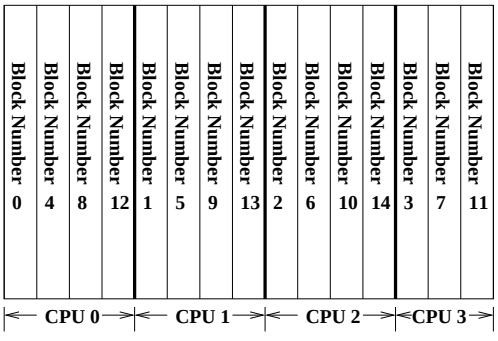

Fig. 3. Block-column distribution for the subdomain-boundary block.

D. Implementation of the Parallel, Direct Solver Application

The primary goal of this research was to develop and implement a parallel, sparse solver for linear algebraic systems. Figure 4 shows the program flow for *mp_solve*. The grey-shaded boxes indicate operations requiring interprocessor communications. The boxes without shading indicate computations done in parallel with no interprocessor communications necessary.

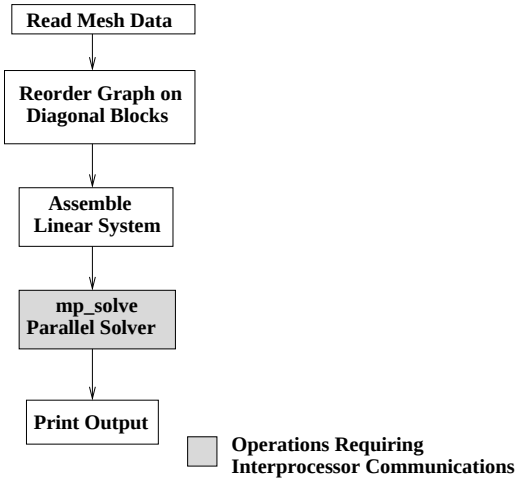

Fig. 4. Flowchart of the parallel application including *mp_solve*.

One-Way Dissection Reordering The first operation in this parallel application is a one-way dissection reordering of the graph representing the nonzero structure of the diagonal blocks [2]. This is the second reordering performed in the solution process; the first being a global reordering for the purpose of obtaining a border-block diagonal system. The reason for this second, local reordering on the diagonal blocks is to minimize the number of nonzeros that have to be stored in the global system. An example of the border-block diagonal system produced by the graph partitioning software prior to reordering the diagonal blocks is shown in Fig. 5. This mesh was subdivided into four subdomains hence the four diagonal blocks. Using a one-way dissection reordering, the rows in each diagonal block are permuted in such a way to move the first nonzero closer to the diagonal. This reordering minimizes the memory usage and computation time. Figure 6 illustrates the results of reordering the rows of the matrix shown in Fig. 5. The differing shades of grey shown in both figures indicate nonzero matrix entries assigned to different processors.

The graph of each diagonal block is cut into several subgraphs as determined by the reordering algorithm. The edges within each subgraph are numbered first and

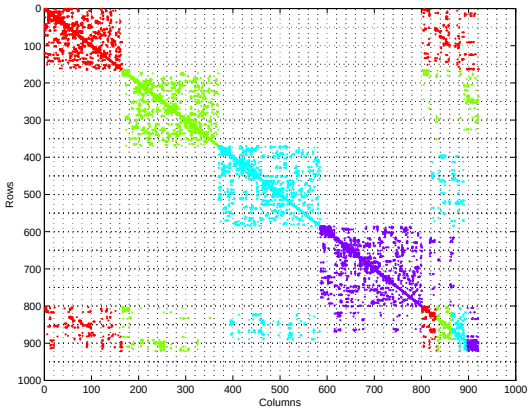

Fig. 5. Nonzero pattern of a four-subdomain border-block diagonal system.

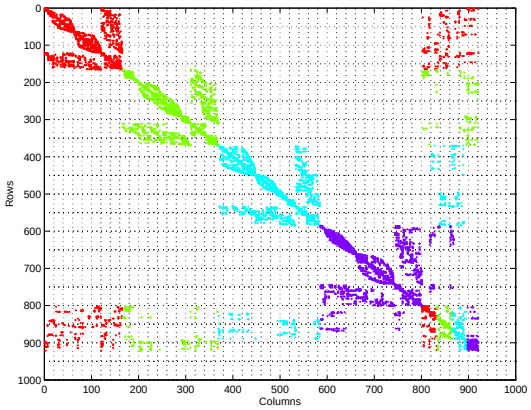

Fig. 6. Nonzero pattern of matrix shown in Fig. 5 after one-way dissection reordering for each subdomain block.

those edges forming the cuts are numbered last. This numbering scheme is analogous to the global reordering by the code which uses the *Chaco* graph partitioning software. This results in a border-block diagonal pattern on each diagonal block. In the small example matrix shown in Figs. 5 and 6, the total memory needed to store all of entries in the global system was reduced from $1,878,912$ bytes to $710,720$ bytes due to the one-way dissection reordering.

System Assembly The next function in the parallel application is the global system assembly. The matrix assembly process inserts the coefficient matrix and excitation vector(s) values in the locations specified by the one-way dissection reordering performed in the previous step. Each processor fills only the part of the global system assigned to it and no interprocessor communication is necessary.

Different parts of the global coefficient matrix are

stored differently depending on the density of a particular portion of the system. First, consider the nonzero entries in each reordered diagonal block. The edges which fell on the interior of the subgraph during the one-way dissection are numbered first so they form the "diagonal" portion of each diagonal block. For each row along this diagonal, all numbers are stored starting with the first nonzero through up to the diagonal including any intervening zeros. An accompanying array of indices is used to access specific entries in the envelope. The same index array is used to locate entries in the coefficient matrix above the main diagonal since it is assumed that the matrix is structurally symmetric. More information on this storage scheme can be found in George and Liu [2].

The off-diagonal nonzeros in both the upper and lower borders of each diagonal block are stored in a compressed row-column format. These values represent interactions between edges on the interior of the subgraph and on the boundaries between adjacent subgraphs. An index array is used to keep track of the number of nonzeros in a row of the off-diagonal block and an accompanying array indicates which columns of the off-diagonal block contains the nonzero values. No zeros are stored in the border block portions of the coefficient matrix since this part of the system is very sparse. This method of storage closely follows that found in [2].

The subdomain-boundary block is shown in black in Fig. 2. This portion of the coefficient matrix is stored in a dense, block-column wrapped format. The number of the columns comprising a block is specified by the code accompanying the graph partitioning software. Since this part of the coefficient matrix is assumed to be dense, no special indexing arrays are needed to keep track of nonzeros. The only information needed for retrieving a particular block of the matrix is a global-to-local mapping to determine which processor is storing a particular block of columns. This mapping can be computed easily on each processor since it is known how many processors are in the job, the number of columns per block and the number of subdomain-boundary unknowns in the problem. Each block of columns of the subdomain-boundary matrix are distributed among all of the processors in the job in a "round-robin" ordering as shown in Fig. 3.

mp_solve **Software** When the linear system is assembled, the parallel solver *mp_solve* is called. The solver software is passed the coefficient matrix and the excitation vector(s) from the calling program. The *mp_solve* function returns a matrix of solutions; one column for each excitation vector. A flowchart showing the sequence of steps is shown in Fig. 7 and a detailed description of *mp_solve* is presented in the following section.

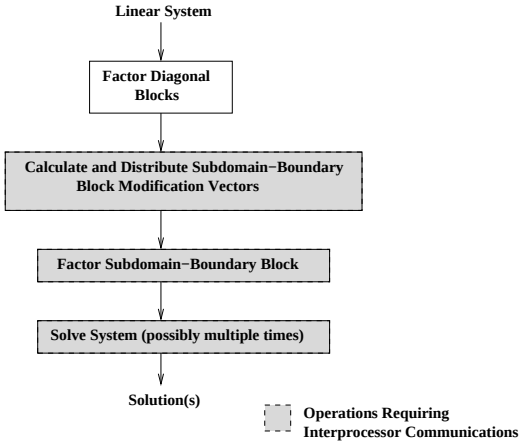

Fig. 7. Flowchart of the *mp_solve* algorithm.

The *mp_solve* function called after the global system has been filled. It accepts the linear system as input and returns the solution vector(s). The first computation executed by *mp_solve* is the diagonal block factorization. This factorization is shown mathematically in equations (6) and (7). This step is performed in parallel with no interprocessor communications necessary.

The next operation in the *mp_solve* code is determined by the number of processors used to solve the problem. If a serial job was specified, i.e., one processor is used, then the forward and backward solves are performed and the solution is returned to the calling program. While the solution phase of the serial job takes advantage of the sparsity of the system, the operations are relatively simple and can be found in most linear algebra texts.

If multiple processors are used to solve the problem, then the solution process is more complicated. First, modifications have to be performed on the subdomain-boundary block prior to its factorization. The modification computations are outlined in equations (8) through (10). To increase the efficiency of the modification communications, a mapping of the modification vectors to their destination processors is made prior to beginning the computations. Once the communication pattern is known for each modification vector, the computations take place and the data can be sent to other processors as needed.

The next step in a multiple-processor job is to factor the subdomain-boundary block into upper and lower factors. The first part of the factorization function performs some "bookkeeping" operations so that a mapping is made of which processor stores each column and each block of columns The subdomain-boundary

block factorization algorithm utilizes the BLAS-3 functions to enhance the computational performance. The blocks typically contained 32 columns apiece which was shown to run most efficiently on a Hewlett-Packard parallel server in earlier timing tests. During the factorization computations, local pivoting is performed to ensure numerical stability.

When the factorization is complete, a parallel solution function is called to perform a forward and backward solve for each excitation vector. One advantage of the direct solver is the ability to solve for many excitation vectors efficiently. The parts of the solution computations involving the diagonal blocks are performed completely in parallel but the portion of the solution involving the subdomain-boundary block requires a number of communication function calls. This is due to the fact that the dense block is stored on all of the processors in the job. Each processor performs solution operations on the diagonal blocks for one excitation vector, repeating the steps for each excitation vector. The solution operations which take place on the subdomain-boundary block handle as many excitation vectors simultaneously as there are processors in the job. Figure 8 illustrates the sequence of steps taken to perform the solve on the subdomain-boundary block for four excitation vectors.

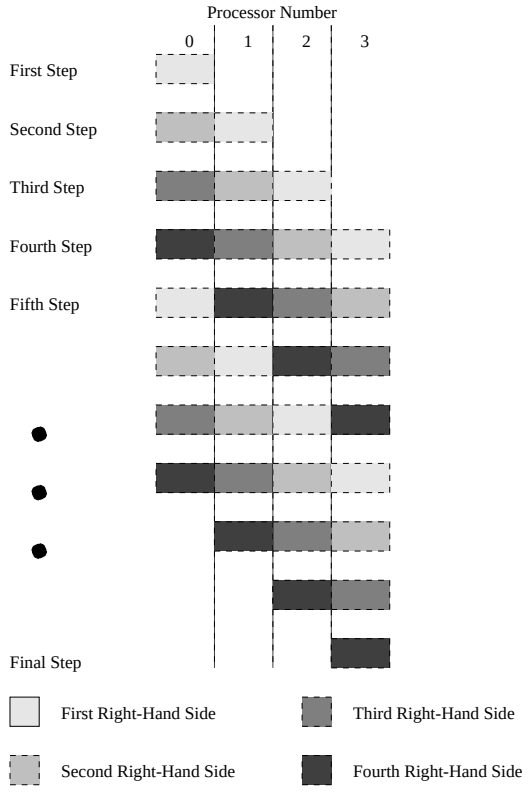

Fig. 8. Subdomain-boundary block solve.

The first step in the parallel solution on the subdomain-boundary matrix is that processor 0 starts with the solve on the portion of the matrix in its memory. When CPU 0 has done all of the computations it can on one row of the matrix, the data is passed to CPU 1 and CPU 0 starts working with the next excitation vector. When CPU 1 is done with its computations on the first right-hand side, that data is passed to processor 2, processor 1 receives the data concerning the second right-hand side and processor 0 begins working on data associated with the third right-hand side. These operations continue on the subdomain-boundary block for all four excitation vectors until this phase of the solve is complete. If there are more excitation vectors than there are processors in the job, the solution functions are called until all solutions have been computed.

III. MATHEMATICAL DEVELOPMENT OF THE ELECTROMAGNETIC SCATTERING PROBLEM

The primary reason for the development of the *mp_solve* algorithm is for solving large systems of equations resulting from the finite-element analysis of the vector wave equation. Electromagnetic scattering problems arise when analyzing radar signature of aircraft or missiles as well as when searching for buried objects such as land mines or industrial waste. The following sections give an overview of the mathematical derivations behind the scattering problem of interest in this research.

A. Overview of the Finite-Element Derivation

Finite-element discretization of the vector wave equation has been covered in a number of publications, therefore only a brief derivation will be shown here [3, 17]. Begin with the vector wave equation,

$$\nabla \times \bar{\bar{\mu}}_r^{-1} \times \bar{E} - \beta_o^2 \bar{\bar{\epsilon}}_r \bar{E} = 0 \tag{11}$$

and substitute $\bar{E}^s + \bar{E}^i$ for $\bar{E}$ in equation (11) to obtain the scattered field formulation,

$$\nabla \times \bar{\bar{\mu}}_r^{-1} \nabla \times (\bar{E}^i + \bar{E}^s) - \beta_o^2 \bar{\bar{\epsilon}}_r (\bar{E}^i + \bar{E}^s) = 0. \tag{12}$$

Collect the unknown scattered field on the left and the known incident field on the right, equation (12) becomes,

$$\nabla \times \bar{\bar{\mu}}_r^{-1} \nabla \times \bar{E}^s - \beta_o^2 \bar{\bar{\epsilon}}_r \bar{E}^s = \beta_o^2 \bar{\bar{\epsilon}}_r \bar{E}^i - \nabla \times \bar{\bar{\mu}}_r^{-1} \nabla \times \bar{E}^i. \tag{13}$$

Now apply the Method of Weighted Residuals using a vector weighting function $\bar{T}$ to equation (13),

$$\int_V \bar{T} \cdot (\nabla \times \bar{\bar{\mu}}_r^{-1} \nabla \times \bar{E}^s - \beta_o^2 \bar{\bar{\epsilon}}_r \bar{E}^s) dV = \int_V \bar{T} \cdot (\beta_o^2 \bar{\bar{\epsilon}}_r \bar{E}^i - \nabla \times \bar{\bar{\mu}}_r^{-1} \nabla \times \bar{E}^i) dV. \quad (14)$$

The final governing equation is,

$$-\oint_S \bar{T} \times (\bar{\bar{\mu}}_r^{-1} \nabla \times \bar{E}^s) \cdot d\bar{s} + \int_V (\bar{\bar{\mu}}_r^{-1} \nabla \times \bar{E}^s) \cdot (\nabla \times \bar{T}) dV - \beta_o^2 \int_V \bar{T} \cdot \bar{\bar{\epsilon}}_r \bar{E}^s dV = \beta_o^2 \int_V \bar{T} \cdot \bar{\bar{\epsilon}}_r \bar{E}^i dV - \int_V \bar{T} \cdot (\nabla \times (\bar{\bar{\mu}}_r^{-1} \nabla \times \bar{E}^i)) dV. \quad (15)$$

A mesh generator is used to discretize the solution domain into finite elements,

$$V = \sum_{N_e} V_e \quad (16)$$

where N_e is the number of elements. On each element, the FEM approximation for the scattered field is,

$$\bar{E}^s = \sum_{j=1}^{N_u^e} \bar{N}_j^e (E_j^s)^e \quad (17)$$

where N_u^e is the number of unknowns on this particular element and $\bar{N}_j^e$ is the shape function. The Galerkin Method stipulates that the weighting functions are equal to the shape functions,

$$\bar{T}_i = \bar{N}_i. \quad (18)$$

Substitute these summations into the volume integral terms on the left side of equation (15) to obtain,

$$\sum_{N_e} \sum_{j=1}^{N_u^e} (E_j^s)^e \left(\int_{V_e} (\bar{\bar{\mu}}_r^{-1} \nabla \times \bar{N}_i^e) \cdot (\nabla \times \bar{N}_j^e) dV^e - \beta_o^2 \int_{V_e} \bar{N}_i^e \cdot \bar{\bar{\epsilon}}_r \bar{N}_j^e dV^e \right), \quad i = 1, ..., N_u^e. \quad (19)$$

The excitation vectors are computed by summing the contribution of each element in the solution domain. Using the right-hand side of equation (15),

$$\sum_{N_e} \left(\beta_o^2 \int_{V_e} \bar{N}_i^e \cdot (\bar{\bar{\epsilon}}_r \bar{E}^i) dV_e - \int_{V_e} \bar{N}_i^e \cdot (\nabla \times \bar{\bar{\mu}}_r^{-1} \nabla \times \bar{E}^i) dV_e \right), i = 1, ..., N_u^e. \quad (20)$$

Substituting equations (19) and (20) into equation (15) yields a linear system of equations of the form,

$$\mathbf{Ax} = \mathbf{b}. \quad (21)$$

where $\mathbf{A}$ is the coefficient or stiffness matrix, $\mathbf{b}$ is the vector representing the discretization of the forcing function and $\mathbf{x}$ is the vector of unknowns.

The software developed for this research utilizes first- and second-order tetrahedral finite elements. The first-order tetrahedrons have one vector basis function (and hence one unknown) lying along each edge. The second-order tetrahedrons have two vector basis functions along each edge and two vector basis functions on each face for a total of twenty unknowns per element. Detailed development of the elemental matrix entries can be found in the computational electromagnetics text by Peterson [17].

B. Mesh Termination

There are a number of methods available for terminating computational domains for electromagnetic scattering problems. Commonly-used techniques include radiation boundary conditions and integral equations terminations. In the past several years, attention has been given to ficticious materials surrounding the scatterer that causes the scattered wave to be attenuated. These are often referred to as "Perfectly Matched Layers" or PML for short. A PML layer is simple to implement and when the material parameters are chosen correctly, the PML is an effective mesh termination technique. The material parameters for each element in the PML are stored as diagonal tensors of the form,

$$\bar{\bar{\mu}}_r = \bar{\bar{\epsilon}}_r = \begin{pmatrix} a & 0 & 0 \\ 0 & b & 0 \\ 0 & 0 & c \end{pmatrix} \quad (22)$$

where a, b, and c are complex. The outer surface of the PML is terminated by a perfect electric conductor. Further information and derivations can be found in a number of publications including [16, 18, 19].

***mp_fem* Software** The *mp_fem* application is a parallel electromagnetic scattering code which utilizes the *mp_solve* software. The sequence of steps in the *mp_fem* code is shown in Fig. 4 with the only difference being in how the entries in the linear system are filled.

The system assembly for *mp_fem* is done on an element-by-element basis with the boundary conditions and material properties accounted for as each elemental matrix is filled. When the elemental matrix entries have been computed, the elemental matrix data is assembled into the global system. Since *mp_fem* uses the *mp_solve* software, the system storage scheme is the same as described earlier with the diagonal blocks

stored in an envelope format, the off-diagonal blocks stored in a compressed row-column format and the subdomain-boundary block stored as a dense matrix. No interprocessor communication is needed during matrix assembly because the preprocessing software provides all of the elemental data needed for each processor to completely build it's portion of the global system.

Currently, the *mp_fem* software contains code for 1st- and 2nd-order, vector-based tetrahedral elements though other element types could be added. The finite-element computations for the elemental matrix entries closely follow those found in [17].

IV. RESULTS

This section outlines the results gathered from a variety of electromagnetics problems using the *mp_fem* software. The results serve two purposes: (1) to test the efficiency of the parallel solver as a tool for solving this class of problems and (2) to verify that this software models the electromagnetic scattering problems accurately. The efficiency of the parallel algorithm is checked by running scaled and unscaled speedups. The accuracy of the electromagnetics modeling is verified by comparing the solution that *mp_fem* returns to the solution of a problem with a known result.

A. Parallel Computer Architecture

A 256-CPU linux cluster housed at the University of Michigan was used to obtain the results shown in this section. Each node on the computer has two AMD processors with a clock speed of 2 gigahertz. Each CPU has access to one gigabyte of memory. The nodes are interconnected with 2 gigabit/second Myrinet used for interprocessor communication. The CPUs are allocated to each user during a run so that only one job runs on each CPU at a time. This eliminates the problems associated with swapping jobs among users while attempting to get reliable parallel speedup results.

B. Parallel-Plate Waveguide

Three geometries were used to verify correct electromagnetic solutions. The first geometry of interest is a parallel-plate waveguide with one end containing PML. While this is not an electromagnetic scattering problem, this simple geometry is convenient for verifying the that the finite element operations are being done correctly and for testing the parallel performance of the code. Figure 9 illustrates the geometry for this problem.

The top and bottom plates of the waveguide, at $z = 0$ and $z = .2\ m$, are perfect electric conductor (PEC). The right end of the waveguide ($x \geq 1.2\ m$) is filled with PML material which is backed by PEC at the

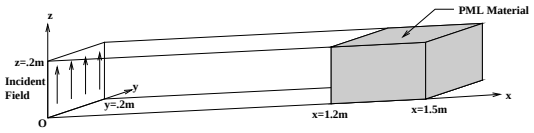

Fig. 9. Parallel-plate waveguide.

$x = 1.5\ m$ plane. The diagonal terms for the material tensor of the PML was chosen to be $1.5 - j1.5$. The natural boundary condition

$$\bar{H}^{tan} = 0 \tag{23}$$

is employed on the sides of the waveguide in the planes $y = 0$ and $y = .2\ m$. For all of the results shown in this section, the waveguide was excited at the plane $x = 0$ by an incident field,

$$\bar{E}^i = \hat{z} E_o e^{-j\beta_x x} \tag{24}$$

with a frequency of 300 MHz.

Several meshes of different densities were run to verify the results for first- and second-order tetrahedrons. Figure 10 shows the magnitude and phase for the wave propagating down the parallel plate waveguide. This particular mesh has 360 first-order tetrahedrons and 682 edges. The edge length is specified in the mesh generator to be 0.083333333 m or approximately 12 edges per wavelength.

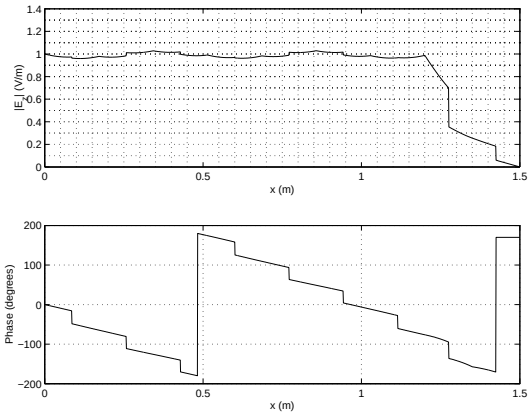

Fig. 10. Magnitude and phase plots for the first-order mesh, parallel-plate waveguide.

Figure 11 illustrates the magnitude and phase results using second-order tetrahedrons in the parallel-plate waveguide. The edge length was again specified to be 0.083333333 m and, like the first-order mesh, there are 360 elements. However, due to the fact that there are two basis functions for each edge and face in the mesh, this problem has 3108 unknowns.

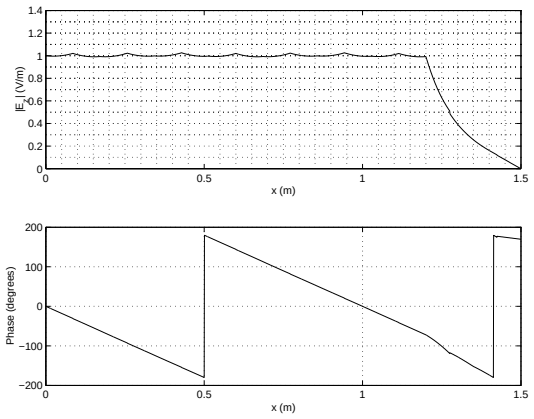

Fig. 11. Magnitude and phase plots for the second-order mesh, parallel-plate waveguide.

Several mesh densities were tested for both first- and second-order meshes on the parallel-plate waveguide in order to draw conclusions on accuracy. For both element orders, mesh densities from six through twenty edges per wavelength were run. The average magnitude and phase error was computed from each of a 1000 points longitudinally along the center of the waveguide. For first-order elements at a mesh density of six edges per wavelength, the magnitude error was approximately 1.5% and the phase error was approximately 40%. These numbers decreased, respectively, to .28% and 2% at a mesh density of twenty edges per wavelength. The second-order elements performed considerably better as expected. At a mesh density of six edges per wavelength, the error in both the magnitude and phase was approximately 1%. At a mesh density of twenty edges per wavelength, the error decreases to about 0.05% for the magnitude and to 0.1% for the phase.

Unscaled Speedup The first test of the scalability of the *mp_fem* algorithm is the unscaled speedup. In this test, a problem of a fixed size is run on an increasing number of processors. However, as the number of subdomains is increased, the amount of time spent on operations involving the subdomain-boundary block increases so dramatically that there is no longer a benefit to using more CPUs.

The first-order mesh using the parallel-plate waveguide geometry was run using a fixed problem size of 72,330 tetrahedral elements containing 81,249 edges. The first test was run with one processor and increased by a power-of-two until 32 CPUs were used to solve the problem. The runtimes for the 32-CPU job indicate that partitioning this mesh into more subdomains did not decrease the runtime so no further tests were conducted. Figure 12 illustrates the runtimes in seconds for all of the jobs in this test.

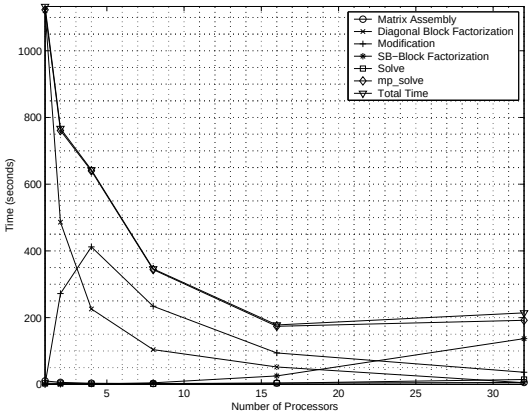

Fig. 12. Wall-clock times for fixed problem size, 1st-order mesh, parallel-plate waveguide.

A similar unscaled timing test was run on the waveguide geometry using second-order tetrahedrons. This mesh is constructed of 10,422 elements which are composed of 74,322 edges and faces. Similar to the first-order unscaled test, this problem was run on one CPU and then the problem was decomposed by a power of two until 32 processors were used. Because the total runtime was increasing when 32 processors were used, no further unscaled tests were done. Figure 13 illustrates the runtimes in seconds for all of the jobs in the test.

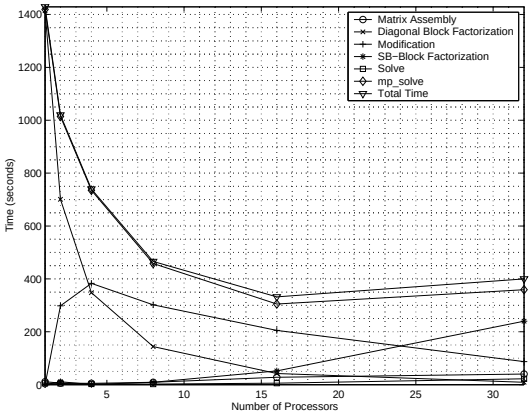

Fig. 13. Wall-clock times for fixed problem size, 2nd-order mesh, parallel-plate waveguide.

The scaling problems appear when modifying and factoring the subdomain-boundary block on multiprocessor runs. Both of these operations require extensive interprocessor communications. The modification portion of the solver executes as many forward and backward solves as there are subdomain-boundary unknowns. In addition, interprocessor communications

are necessary to send the modification vector to the appropriate processor to execute the subtraction in equation (10). For both orders of finite elements, the modifications performed worst on four processors and then proceeded to have a shorter runtime as more processors were added. As the size of the diagonal blocks decreased, the execution time for the forward and backward solves decreased substantially. While the number of interprocessor communications increased, the time required to perform the communications did not offset the gains made by the faster solve times. This results in a net improvement in the modification time as the number of processors in the job increases.

The subdomain-boundary block factorization time increases for both first- and second-order elements. This is a result of having a larger subdomain-boundary block as the solution domain is subdivided more times. In addition, increasing the number of CPUs increases the interprocessor communication needed to carry out the factorization. For jobs running on 16 or fewer processors, the subdomain-boundary block factorization time remains under 15% of the total runtime. However, on jobs distributed over 32 CPUs, the factorization time increase to over 50% of the total runtime.

Additional unscaled speedups were performed on larger waveguide problems to confirm performance data. Tests were done so that there were approximately the same number of unknowns for both 1st- and 2nd-order tetrahedral meshes. The 1st-order mesh had 477,274 edges requiring a minimum of 16 processors. Tests were also run on this mesh for 32 and 64 subdomains. Because the runtime increased on 64 processors, no further tests were run. The results are shown in Fig. 14.

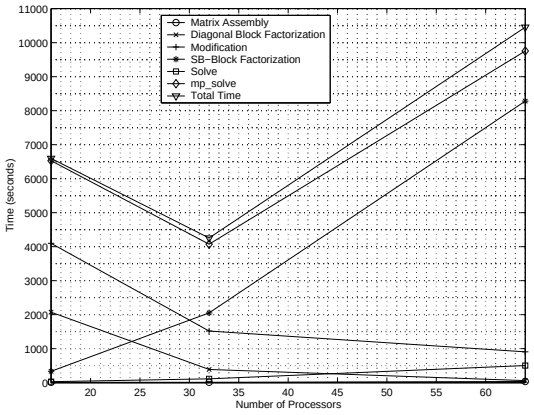

Fig. 14. Wall-clock times for fixed problem size, 1st-order mesh, parallel-plate waveguide (477,274 unknowns).

A similar test was done on a large parallel-plate waveguide geometry using 2nd-order elements. This mesh resulted in 469,192 edges and faces. Due to memory limitations, the problem could not be run on fewer than eight processors. This mesh was not successfully run on 64 processors because the subdomain-boundary block became too large and the computers operating system started to swap memory with disk space. Figure 15 illustrates the timings for the 2nd-order waveguide runs.

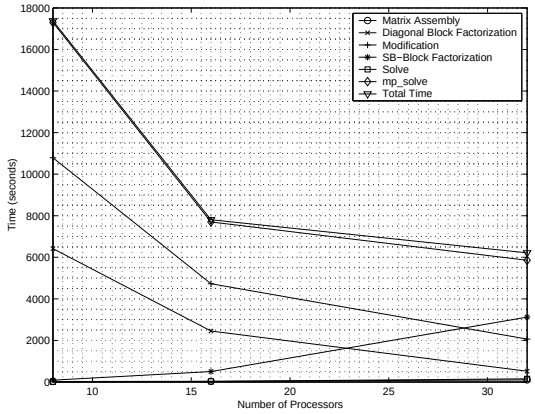

Fig. 15. Wall-clock times for fixed problem size, 2nd-order mesh, parallel-plate waveguide (469,192 unknowns).

Another way to examine the unscaled speedup is to consider the decrease in the runtime as the number of processors increase. Ideally, using two processors on a job should result in a runtime of half of that needed for solving the same problem on one processor. Likewise, running a problem on four processors should result in a runtime of one quarter of that required if the same problem was assigned to only one CPU. Figure 16 illustrates the unscaled speedup for the small first- and second-order parallel-plate waveguide results shown in Fig. 12 and 13.

Note that the plots in Fig. 16 for both 1st- and 2nd-order elements, the speedup obtained from the *mp_fem* software differs greatly from the optimal unscaled speedup. For instance, in the 1st-order mesh, as the number of processors is increased from 1 CPU to 2 CPUs, ideally, the CPU time should divide in half. The speedup obtained through from the parallel software is only 0.66. The gain for 2nd-order problems is even worse with a speedup of only about 0.71 when spreading the problem over two processors.

There are a couple of likely causes in this lack of efficiency. The first problem is load imbalance (discussed below). The other problem is a lack of scalability in the portions of the code dealing with the subdomain-boundary block. In both unscaled speedup tests of the waveguide problem, the factorization of the subdomain-boundary block increases as the num-

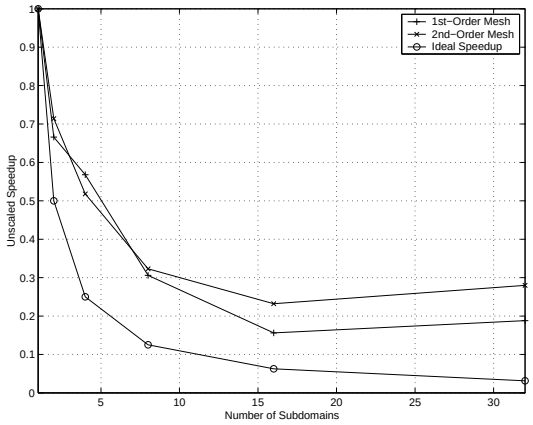

Fig. 16. Unscaled speedup for the 1st- and 2nd-order meshes, parallel-plate waveguide.

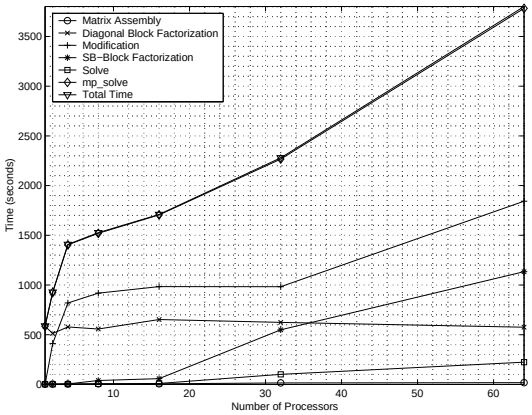

Fig. 17. Wall-clock times for scaled problem size, 1st-order mesh, parallel-plate waveguide.

ber of subdomains increase. While the other operations such as the diagonal-block factorization and the modification of the subdomain-boundary block do not scale optimally, their decreasing runtimes do not have the impact on the overall runtime that the factorization of the subdomain-boundary block has. A torus-wrapped ordering for the subdomain-boundary block shows promise for improving scalability in this part of the code [20].

Scaled Speedup Another measure of parallel efficiency is the scaled speedup. In this series of runs, the problem size is increased proportionally to the number of processors in a job; i.e. if the problem size is doubled, then the number of processors is also doubled. Ideally, the execution time for each problem in the series of runs should remain constant no matter how large the problem. Due to increased communication costs as more CPUs are added to each run, the execution time is rarely ever constant.

The first scaled tests that were run involved the parallel-plate waveguide geometry meshed with first-order tetrahedrons. Figure 17 shows the scaled speedup for the first-order tetrahedrons. Each processor in each step in the test sequence was loaded with approximately 20,000 edges. Table 1 shows the problem sizes for each of the runs used for the first-order scaled speedup tests.

The second scaled speedup tests involved the same geometry but used the second-order elements. Figure 18 shows the scaling that was achieved in this sequence of runs. Table 2 shows the size of the problem for each run.

The diagonal-block factorization is a parallel operation that requires no inter-processor communication. For the scaled speedups, there were approximately the same number of edges on each CPU so the factorization time was kept relatively constant as shown in both Figs. 17 and 18.

The modification of the subdomain-boundary block requires considerable communication as well as many

Table 1. Problem sizes for the first-order scaled speedup tests.

Number of Processors	*Number of Elements*	*Number of Unknowns*
1	15,000	21,500
2	30,000	39,980
4	60,000	79,640
8	120,000	158,960
16	240,000	317,600
32	480,000	634,880
64	960,000	1,269,440

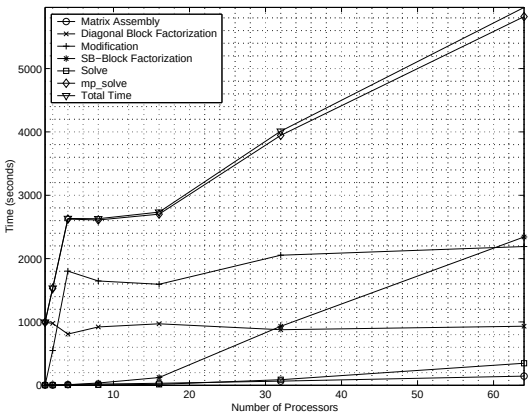

Fig. 18. Wall-clock times for scaled problem size, 2nd-order mesh, parallel-plate waveguide.

Table 2. Problem sizes for the second-order scaled speedup tests.

Number of Processors	*Number of Elements*	*Number of Unknowns*
1	2,880	20,768
2	5,940	42,426
4	11,880	84,468
8	23,760	168,552
16	47,520	336,720
32	95,040	673,056
64	190,080	1,345,728

forward and backward solves. The size of the diagonal blocks are kept nearly constant so the forward and backward solve times increase only slightly. This increase is due to that fact that with more processors in the job, more interprocessor communication is necessary to perform the forward and backward solves in the subdomain-boundary block.

The subdomain-boundary block factorization time increases as the number of unknowns in that part of the matrix increases. As the number of CPUs and the size of the subdomain-boundary block increases, the computation time and the communication time increase. This results in the rising curve shown in the subdomain-boundary block factorization time in both Figs. 17 and 18.

Another way of analyzing the scaled speedup data is to consider parallel efficiency. Hennigan defines the scaled speedup as,

$$S_s = p \times \frac{T(1,N)}{T(p,pN)} \tag{25}$$

where N is the number of unknowns in the system and p is the number of processors in the job [3]. Hennigan then goes on to define the parallel efficiency as,

$$\eta_p = \frac{S_s}{p}. \tag{26}$$

Figure 19 illustrates the parallel efficiency of the *mp_fem* algorithm for both 1st- and 2nd-order elements in the parallel-plate waveguide geometry. The runtimes shown in Figs. 17 and 18 were used to calculate the efficiency.

For a perfect scaled speedup, the efficiency is 1.0 for any number of processors and the corresponding problem size. Due to load imbalances and interprocessor communications however, the efficiency is rarely ever optimal. These problems along with the poor scalability of the subdomain-boundary block modification and factorization result in efficiencies that are less than one and continue to get worse as more processors are added to the job.

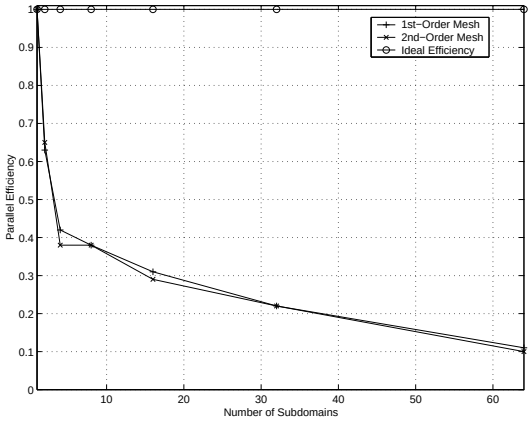

Fig. 19. Parallel efficiency for the 1st- and 2nd-order tetrahedral meshes.

Load Balance Obtaining a good load balance across all of the processors in a job is a primary concern of the graph partitioning software. Good load balancing means that each CPU will have the same number of computations so that no processor is sitting idle while other processors continue to work. Poor load balancing has a direct effect on parallel performance and can cause the parallel efficiency of an algorithm to be reduced considerably. While it is not possible to show here the load balance for every problem, a few decompositions are given.

The four-subdomain decomposition used in the unscaled speedup for the first-order element waveguide simulations is a matter of interest. Table 3 shows the load balancing results and diagonal-block factorization times for this decomposition.

Table 3. Load balance for four-subdomain decomposition of parallel-plate waveguide.

Processor Number	*Number of Equations*	*Envelope Size*	*Memory Usage (MB)*
1	19,764	2,978,154	93.3
2	20,030	2,868,948	95.5
3	20,292	3,675,486	121.3
4	20,489	3,026,150	100.5

It is evident from the table that while the number of equations on each processor vary by less than 3%, the envelope size varies by almost 22%. Since the speed of the factorization of the diagonal blocks depend on the size of the envelope, the processor with the largest envelope size in this problem requires 1.6 times the execution time to factor the matrix on its memory than the processor with the smallest envelope. For this problem, processor 2 sat idle for 135 seconds while processor 3 finished factoring its portion of the matrix.

This idle time accounts for approximately 18% of the total runtime for this problem. While only the discrepancies in the diagonal-block factorization times are shown here, modification of the subdomain-boundary block is also negatively effected by poor load balancing. The modification to the subdomain-boundary block requires many calls to a linear solve function that is dependent on the envelope size (see equations (9) and (10)). When the size of the envelope differs greatly among the processors, the time to perform these solves differs resulting in some processors sitting idle. The factorization of the subdomain-boundary block is not affected by load imbalance since the columns are distributed in a block-column wrapped manner to all of the processors in the job. Any differences in the number of columns assigned a processor has a negligible impact on the factorization time.

The load imbalance illustrated here points to the need for more thorough investigation into graph partitioning software issues as well as the need to explore alternatives to using the one-way dissection reordering on the diagonal blocks.

C. Perfectly Conducting Cylinder

The first electromagnetic scattering problem of interest is an infinite perfectly conducting cylinder. This is a standard "textbook" problem with a well-known series solution composed of Bessel and Hankel functions.

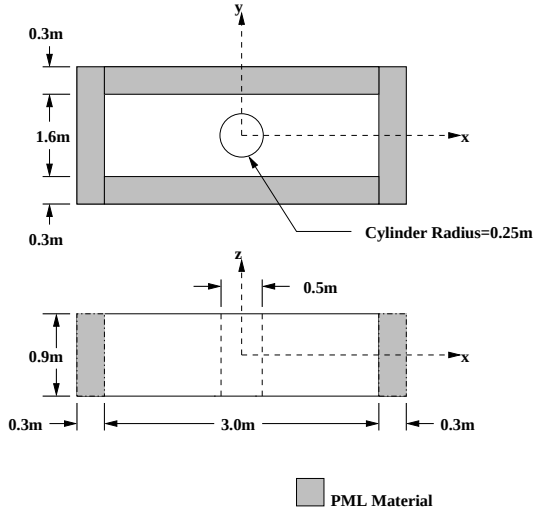

Fig. 20. Perfectly conducting cylinder.

The geometry consists of a box containing a cylinder with a diameter of 0.5 m. The center of the cylinder lies at the origin (see Fig. 20). The interior of the box is 3.0 m long so as to capture the standing wave in the incident ($-x$ direction) and the shadow ($+x$ direction) regions of the solution domain. A layer of artificial absorber (PML) 0.3 m thick is placed at the edges of the box surrounding the cylinder. The PML regions are shown in grey. The top and bottom planes of the box, at $z = -0.45$ m and $z = +0.45$ m, are covered in PEC.

For the tests run in this section, the cylinder was illuminated by an incident plane wave of the form,

$$\bar{E}^i = \hat{z} E_o e^{-j\beta_x x} \tag{27}$$

at a frequency of 300 MHz.

Two initial tests were done with first- and second-order tetrahedral elements to ascertain that the physics is being modeled accurately. The first-order test was run with 66,213 first-order elements and 86,824 edges. The electric field was sampled in two directions shown by the heavy dashed lines in Fig. 21. The scale in Fig. 21 is the same as that shown in Fig. 20.

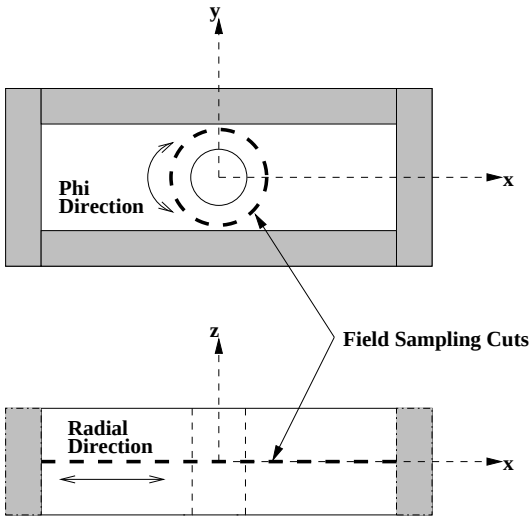

Fig. 21. Field sampling lines on the PEC cylinder.

The field in the radial direction is computed at 1000 places along the x-axis of the box containing the cylinder. The magnitude and phase components of the total field are shown in Fig. 22. The solid line is the solution computed using the *mp_fem* software while the dashed line represents the series solution.

The field in the ϕ direction is computed at 360 angles (one-degree increments) in a constant radius centered about the cylinders axis. The field points are computed at constant distance of 0.4 m from the center of the cylinder. The magnitude and phase components of the total field are shown in Fig. 23. The solid line is the solution computed using the *mp_fem* software while the dashed line represents the series solution.

There are a couple of important considerations when determining how dense to make a mesh. The first issue is that the electric field has to be modeled correctly.

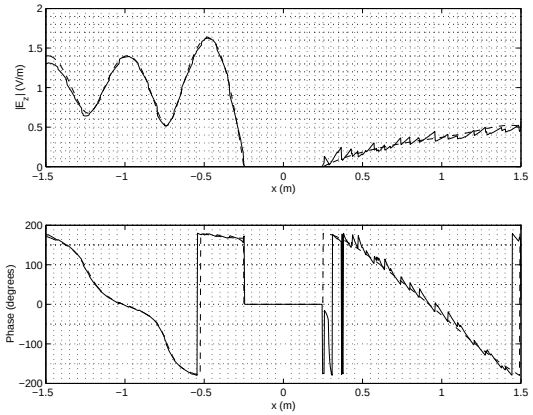

Fig. 22. Magnitude and phase plots for the first-order mesh, cylindrical scatterer (radial direction).

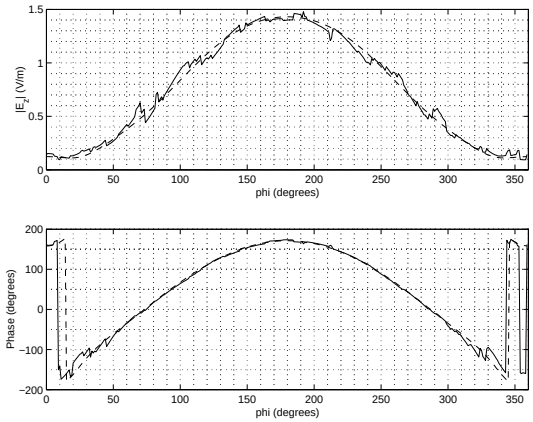

Fig. 23. Magnitude and phase plots for the first-order mesh, cylindrical scatterer (phi direction).

This issue was addressed with the parallel-plate waveguide and it was found that reasonably accurate answers were obtained using 12-14 edges per wavelength. Unfortunately, while a mesh with this density produces good answers on a rectangular geometry, it does not accurately model the curvature of the cylinder. The mesh generator used in this research allows a person to choose a different mesh densities in different places in the computational domain. For results shown in Figs. 23 through 25, a mesh density of 16 edges per wavelength was used near the surface of the cylinder while along the edges of the PML box, a mesh density of about 12 edges per wavelength was used.

Figure 24 shows the total field along the x-axis for the second-order mesh. The solid line is the field computed by the *mp_fem* software and the dashed line is the field computed using the series solution. In many places on the plot, they are indistinguishable.

Figure 25 shows the total field in a circle around the cylinder at a distance of 0.4 m away from the center. Again, the solid line is the field computed by the *mp_fem* software and the dashed line is the field computed using the series solution. On both plots, these lines are generally superimposed.

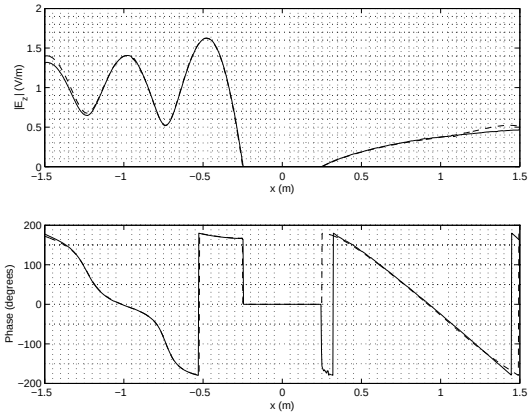

Fig. 24. Magnitude and phase plots for the second-order mesh, cylindrical scatterer (radial direction).

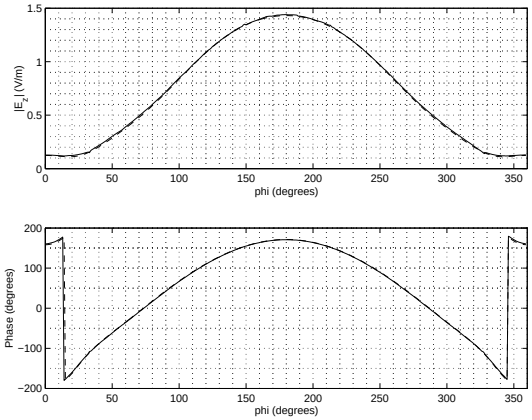

Fig. 25. Magnitude and phase plots for the second-order mesh, cylindrical scatterer (phi direction).

Multiple Excitation Vectors One of the strengths of a direct solver is the ability to amortize the high matrix factorization costs over the time required to perform a large number of solves for multiple excitation vectors. In this finite-element application, each new excitation vector represents a new angle from which the incident field illuminates the scatterer.

Two meshes were run for the purpose of obtaining the runtime statistics for multiple right-hand sides. The first-order mesh consisted of 125,000 tetrahedral elements containing 175,877 edges surrounding a cylindrical scatterer. The incident waves illuminated the

cylinder from 360 angles at 1° increments. The time needed to solve for each excitation vector is shown in Fig. 26. In each of the three decompositions shown for first-order elements, the total solution time for 360 excitation vectors remained less than 40% of the overall wall-clock runtime for the *mp_fem* code.

The second-order mesh had approximately 28,000 elements containing 201,890 unknowns. The cylinder was illuminated at 1° increments from 360 angles. The time for each solve is shown by the upper line in Fig. 26. The percentage of the total runtime spent on solving for each excitation vector increased from approximately 26% on the 8-subdomain decomposition to 41% on the 32-subdomain decomposition. This increase in the percentage of runtime spent on the solve is primarily a reflection of the decrease in the overall runtime since the time required to solve for each right-hand side increases only slightly between 16− and 32−subdomain decompositions.

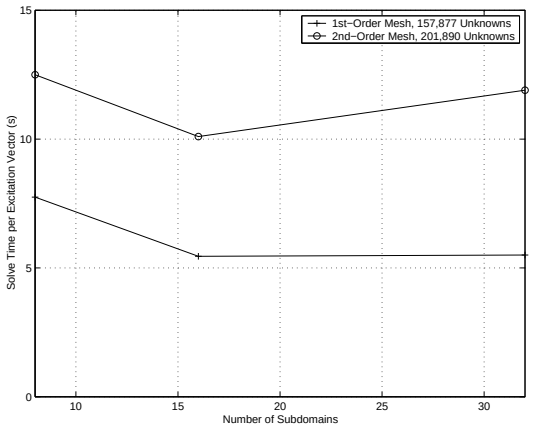

Fig. 26. Wall-clock times for each solve for multiple excitation vectors, 1st- and 2nd-order meshes, cylindrical scatterer.

D. PEC Sphere

The second electromagetic scatterer of interest is the perfectly conducting sphere. Similar to the last problem, electromagnetic scattering from a sphere has a known series solution. The geometry for this problem is shown in Fig. 27. The PEC sphere is placed in a box with the center of the sphere at the origin. Unlike the cylindrical scatterer which can be modeled in two dimensions, the sphere is a true three-dimensional scattering problem and therefore the scatterer must be surrounded on all sides by absorbing material. The shaded areas in Fig. 27 around the sphere represent the PML absorber.

The interior of the box is 3.0 m long so as to capture the standing wave in the incident region ($-x$ direction)

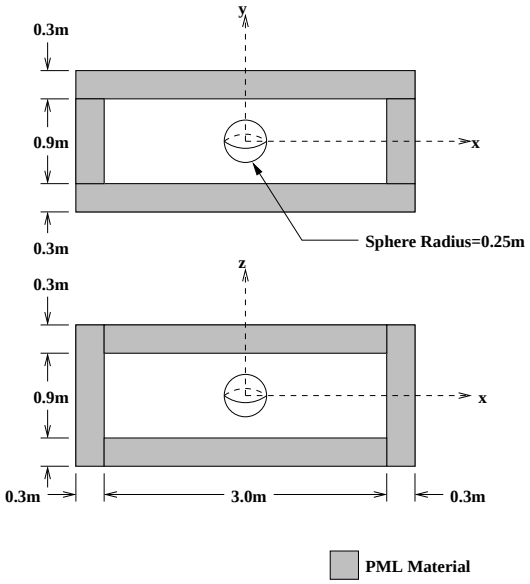

Fig. 27. Perfectly conducting sphere.

and the shadow ($+x$ direction) region of the solution domain. The sphere has a diameter of 0.5 m. A layer of artificial absorber (PML) 0.3 m thick is placed at the edges of the box surrounding the sphere. The PML regions are shown in grey in Fig. 27. For this set of results, the sphere was illuminated by the incident field,

$$\bar{E}^i = \hat{z} E_o e^{-j\beta_x x} \tag{28}$$

at a frequency of 300 MHz.

After the runs were completed, the magnitude and phase computations for the total field were performed at 1000 points along the bold, dashed line in the radial direction shown in Fig. 28. In addition, another set of field computations were taken in the ϕ direction at 360 angles.

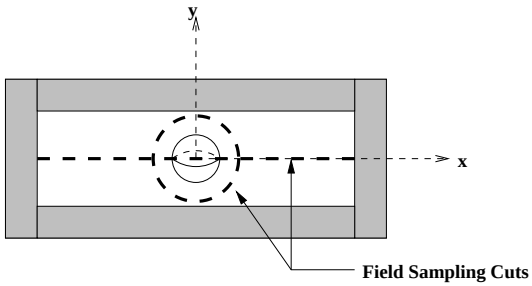

Fig. 28. Field sampling line on PEC sphere geometry.

Two meshes were run to verify that the code was correctly modeling the electromagnetic scattering problem. The first problem was a first-order mesh with

284,092 elements and 350,109 edges. The average edge length was approximately 32 edges per wavelength.

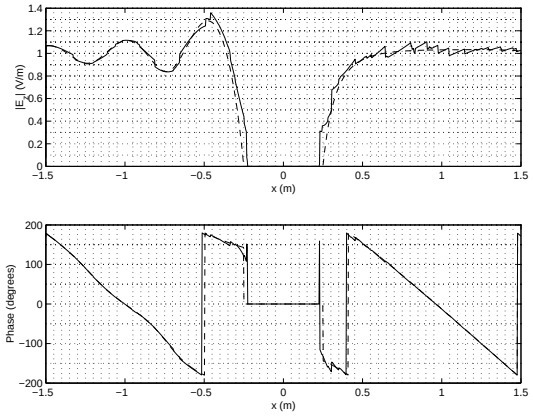

Fig. 29. Magnitude and phase plots for the 1st-order mesh, spherical scatterer (radial direction).

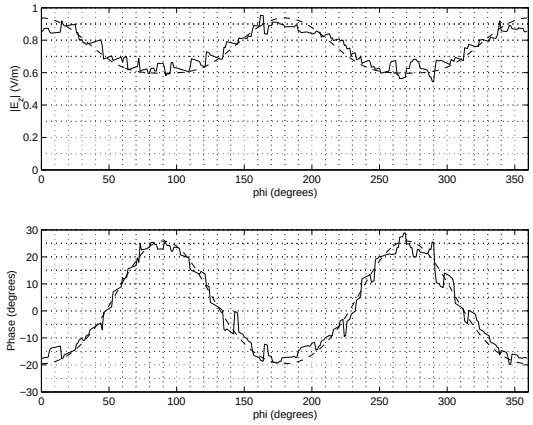

Fig. 30. Magnitude and phase plots for the 1st-order mesh, spherical scatterer (phi direction).

The solid lines in Figs. 29 and 30 are the fields in the radial and phi directions computed using the results of the *mp_fem* software. The dashed line in both plots are the field values computed using the Legendre solution. It is evident from the figures that the results obtained from the *mp_fem* software are very close to the series solution.

The second verification mesh for this geometry involved 2nd-order elements. The mesh density was set to 8 edges per wavelength resulting in 37,161 elements and 244,452 unknowns. The results for this run are shown in Fig. 31.

Similar to previous plots, the solid line is the field pattern computed using the *mp_fem* software and the dashed line is the field pattern computed using the series solution. Clearly, using a mesh with only eight

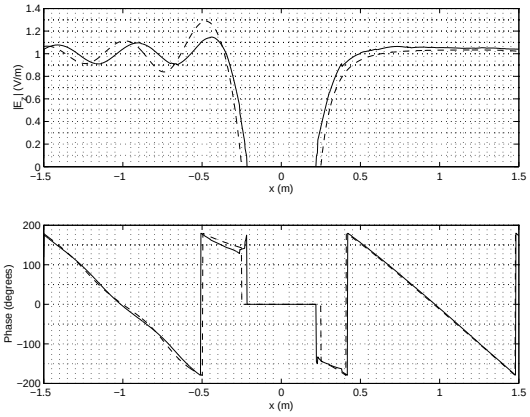

Fig. 31. Magnitude and phase plots for the 2nd-order mesh, spherical scatterer (radial direction).

edges per wavelength is not sufficient to model the spherical geometry. While the phase plot is very accurate, this coarse mesh does not resolve the field well in the incident side of the sphere. A considerable amount of computational resources were required to obtain this solution. The problem was run on 16 CPUs and required approximately 12 GB of memory. For comparison purposes, a 1st-order mesh with a density of 8 edges per wavelength requires about 750 MB of memory. Due to memory limitations, no other 2nd-order meshes were run with the spherical scatterer.

V. CONCLUSIONS

The purpose of this research was to develop a parallel, direct solver and use it as a tool for use for electromagnetic scattering simulations. While the use of the finite-element method (FEM) is well known and has been documented extensively, the simulations of interest to researchers are often limited by the lack of memory and processing power. One goal of this research was to develop a parallel software application which would alleviate some of the constraints imposed by other available software and to include some capabilities not found elsewhere. While it is recognized that the scaling properties of the *mp_solve* software are not optimal, it has shown to be a useful tool in solving common problems of interest to the electromagnetics research community.

A. The Parallel Solver

This research revolves around the parallel solver which was specifically developed for use with the scattering problems of interest. Several features were built into this code which are not found in other software packages including the ability to handle numerically unsymmetric matrices, complex numbers and multiple

excitation vectors. Local pivoting is also included in the subdomain-boundary block factorization function to help improve numerical stability.

As was illustrated in the results section of this dissertation, the parallel algorithm scaling is less than ideal as the problem size or the number of processors are increased. A more sophisticated approach to the partitioning problem might produce better load balances with certain geometries. In addition, the simple block-column LU factorization used here had a severe impact on the runtime and on the parallel scaling.

While poor scaling is a serious drawback to any parallel algorithm, the *mp_solve* software remains a useful tool. The *mp_solve* software has been used to solve linear systems containing up to 1.35 million unknowns in just over an hour on 64 processors. An engineer or scientist can expect to use this software to solve large problems in a reasonable time.

B. The Electromagnetic Scattering Simulation Software

Software has been developed to find solutions to the vector wave equation using the finite-element method. While this is a well-documented area of research in the electromagnetics community, a few words are in order here concerning the results.

The two orders of vector tetrahedral elements used offered both advantages and disadvantages. Code development for the first-order elements was relatively easy and the answers were found to be reasonably accurate; often within 10% of the accepted solutions. In addition, the memory requirements were considerably less than those required by the second-order elements.

If more accuracy is necessary, the second-order elements offer a substantial improvement for a given mesh density. Several of the scattering problems discussed in the previous section had accuracies within 1% of the accepted solutions. This increase in accuracy does not come without cost however. One problem with second-order elements is the memory required for a given mesh density. Experience in this research has shown that the second-order elements require seven to ten times more memory for a particular mesh density than the first-order elements. The memory consumption associated with the second-order elements limited the tests that could be run with this code. This problem was particularly evident when using second-order elements to mesh curved surfaces.

Another aspect of this research which warrants comment is the use of the Perfectly Matched Layer (PML) absorbing boundary condition. The PML was proven to be quite effective as shown by the accuracy of the results. While this research did not focus on finding optimal values for the PML material parameters, those used by Hennigan worked well in the scattering problems shown in the results section [3]. The PML domain termination conditions are easy to implenent and avoid the need for the dense matrix computations associated with the boundary-element method of solution domain termination. They also did not require the spherical terminating surface necessitated by the radiation boundary conditions.

VI. ACKNOWLEDGEMENTS

Several government agencies and private companies contributed financial support and provided access to the computers necessary to see this project through. The National Aeronautical and Space Administration (NASA) sponsored this research through a Graduate Research Fellowship, Grant #5-50117 and through NASA/JPL FAR Grant #959913. CPU time was provided for this work by the Maui High Performance Computing Center (MHPCC), Start-up Grant #UNIVY-0279-U00 and by the National Partnership for Advanced Computing Infrastructure at the University of Michigan. Dr. Abijit Bose of The University of Michigan was instrumental in helping me obtain access to their parallel computer. The Hewlett-Packard Corporation provided a parallel server at no cost to our department. Much of the code used in this research was developed on this machine.

References

[1] D. B. Davidson, "Large, parallel processing revisited: a second tutorial," *IEEE Antennas and Propagation Magazine*, vol 34, pp. 9-21, 1992.

[2] A. George and J. Liu, *Computer Solution of Large, Sparse Positive Definite Systems*, Englewood Cliffs, N.J.: Prentice-Hall, 1981.

[3] G. L. Hennigan, *Open-Region Electromagnetic Finite-Element Scattering Calculations in Anisotropic Media on Parallel Computers*, Doctoral Dissertation, New Mexico State University, 1999.

[4] Y. Saad, A. Malevsky, G. C. Lo, S. Kusnetsov, M. Sosonkina, and I. Moulitsa, *A Portable Library of Parallel Sparse Iterative Solvers*, University of Minnesota, 1999.

[5] S. Balay, W. Gropp, L. C. McInnes, and B. Smith, *The Portable, Extensible Toolkit for Scientific Computation*, Argonne National Laboratory, 1999. URL:http://www-fp.mcs.anl.gov/petsc

[6] R. Tuminaro, J. Shadid, S. Hutchinson, L. Prevost, and C. Tong, *A Massively Parallel Iterative*

Solver Library for Solving Sparse Linear Systems, Sandia National Laboratory, 1999. URL: http://www.cs.sandia.gov/CRF/aztec1.html

[7] A. Gupta, M. Joshi, G. Karypis, V. Kumar, and F. Gustavson, *Scalable Parallel Direct Solver Library for Sparse Symmetric Positive Definite Systems*, University of Minnesota, 1999. URL: http://www-users.cs.umn.edu/mjoshi/pspases/index.html #people

[8] A. Gupta, M. Joshi, and V. Kumar, *Watson Symmetric Sparse Matrix Package*, IBM Watson Research Center, 1999. URL: http://www.research.ibm.com/mathsci/ams /ams_WSSMP.htm

[9] A. Gupta, M. Joshi, and V. Kumar, "A Highly Scalable, Parallel Algorithm for Sparse Matrix Factorization," *IEEE Transactions on Parallel and Distributed Systems*, vol. 8, no. 5, pp. 502-520, May 1997.

[10] J. Demmel and X. Li, "Making Sparse Gaussian Elimination Scalable by Static Pivoting," *Proceedings of Supercomputing '98*, Orlando, Florida, November 1998.

[11] X. Li and J. Demmel, "A Scalable Sparse Direct Solver Using Static Pivoting," *Proceedings of the Ninth SIAM Conference on Parallel Processing for Scientific Computing*, 1999.

[12] J. Demmel, S. Eisenstat, J. Gilbert, X. Li, and J. Liu, "A Supernodal Approach for Sparse Gaussian Elimination," *Technical Report UCB//CSD-97-943*, Computer Science Division, U.C. Berkeley, 1997.

[13] W. Dearholt, S. Castillo and G. L. Hennigan, "Solution of Large, Sparse, Irregular Systems on a Massively Parallel Computer," Third International Workshop, IRREGULAR '96, Santa Barbara, CA, August 1996, *Lecture Notes in Computer Science*, Springer-Verlag, Berlin, 1996.

[14] W. Dearholt, S. Castillo and V. Bokil, "Solution of Large, Sparse Systems on a Parallel Computer," Conference Proceedings, *IEEE Antennas and Propagation Conference*, Baltimore, MD. July 1996.

[15] M. Hagger and L. Stals, *Domain Decomposition on Unstructured Grids*, Department of Mathematics, University of Bath, Claverton Down, Bath, BA2 7AY, England, URL: http://www.maths.bath.ac.uk/parsoft/doug

[16] J. Tang, K. Paulsen, and S. Haider, "Perfectly Matched Layer Mesh Terminations for Nodal-Based Finite-Element Methods in Electromagnetic Scattering," *IEEE Transactions on Antennas and Propagation*, vol. 46, pp. 507-517, April 1998.

[17] A. Peterson, S. Ray, and R. Mittra, *Computational Methods for Electromagnetics*, IEEE Press. New York, NY 1997.

[18] J. Y. Wu, D. M. Kingsland, J. F. Lee and R. Lee, "A Comparison of Anisotropic PML to Berenger's PML and Its Application to the Finite-Element Method for EM Scattering," *IEEE Transactions on Antennas and Propagation*, vol 45, pp. 40-50, January 1997.

[19] Z. Sacks, D. Kingsland, R. Lee, and J. F. Lee, "A Perfectly Matched Anisotropic Absorber for Use as an Absorbing Boundary Condition," *IEEE Transactions on Antennas and Propagation*, vol 43, pp. 1460-1464, December 1995.

[20] B. A. Hendrickson and D. E. Womble, "The torus-wrap mapping for dense matrix calculations on massively parallel computers," *Tech. Rep. SAND92-0792*, Sandia National Laboratories, 1992.

Will Dearholt received the B.S.E.E., M.S. and Ph.D. degrees from New Mexico State University in 1992, 1996 and 2003, respectively. He has been employed by NASA, IBM and Los Alamos National Laboratory as both a summer intern and a cooperative education student. He was an instructor at NMSU from 1997 to 2002. Dr. Dearholt received the NASA Graduate Research Fellowship in 1998 which funded the majority of the work described in this paper. Since graduating from New Mexico State University in 2003, he

has been a Technical Staff Member at Los Alamos National Laboratory in Los Alamos, New Mexico working on mesh generation and geometric modeling for problems of interest to the computational physics community. Dr. Dearholt is a member of IEEE, ACES and Eta Kappa Nu.

Steven Castillo received the B.S.E.E. degree from New Mexico State University, Las Cruces, in 1982, and the M.S. and Ph.D. degrees in Electrical Engineering from the University of Illinois, Urbana, in 1984 and 1987, respectively, where he conducted research in electromagnetic analysis of high speed digital circuits. He has been employed at White Sands Missile Range, NASA Johnson Space Center, and Bell Telephone Laboratories. Since 1987, he has been on the faculty at New Mexico State University and is now an NMSU Regents Professor in the Klipsch School of Electrical and Computer Engineering where he served as Department Head from 1998 until 2004. He began his duties as Dean of Engineering July 1st, 2004. He has conducted research in computational methods in electromagnetics, electromagnetic theory and the solution of partial differential equations on parallel computers. Dr. Castillo is a member of the IEEE Antennas and Propagation, Electromagnetic Compatibility, and the Microwave Theory and Techniques societies. He currently serves on several boards and external committees including the Advisory Committee on Cyber Infrastructure for the National Science Foundation, the board of directors for the Center of Excellence for Hazardous Materials, the Computational Sciences review panel at Sandia National Laboratories, and the Advanced Simulation and Computing Program review at Sandia National Laboratories. He is a past Associate Editor of the IEEE Antennas and Propagation Transactions. He is a member of Eta Kappa Nu, Tau Beta Pi, Phi Kappa Phi and Sigma Xi and received the National Science Foundation Presidential Young Investigator Award in 1991.

Scattering from a Semi-Elliptic Channel in a Ground Plane Loaded by a Lossy or Lossless Dielectric Elliptic Shell

A-K. Hamid

Department of Electrical and Computer Engineering
University of Sharjah
P.O. Box 27272, Sharjah, U.A.E
email: akhamid@Sharjah.ac.ae

Abstract **–** An analytic solution to the problem of scattering of a plane electromagnetic wave by a lossy or lossless dielectric confocal elliptic shell loading a semi-elliptic channel is derived. The incident, scattered and transmitted fields in every region are expressed in terms of complex Mathieu functions. Applying the boundary conditions at various faces and interfaces along with the partial orthogonality properties of angular Mathieu functions, the unknown scattered and transmitted field coefficients are obtained. The presented numerical results show a good agreement with the published data especially for the case of a lossless dielectric shell loading a semi-circular channel.

I. INTRODUCTION

The electromagnetic scattering from grooves, channels and cracks have been investigated by many researchers. The investigations have shown that when these structures are loaded with dielectric materials, the overall scattering patterns significantly change and thus it is important to obtain an analytic solution to predict the new scattering behavior of the target.

Lately, there have been many analytic studies available in the literature on the scattering by hollow and lossless dielectric loaded semi-circular or elliptic channels [1-9]. Most of these studies were based on the exact series eigen-function solution. On the other hand, numerical solutions based on the coupled integral equations for the induced currents were obtained by Senior et. al. [10-11].

To the best of our knowledge, there has been no analytical or numerical solution to the problem of scattering from a lossy or lossless dielectric elliptic shell loading a semi-elliptic channel in a ground plane.

In this paper, we present the solution to the scattering by a semi-elliptic channel loaded by two lossy dielectric layers. The presented solution will be the most general one available in the literature and the special lossless circular case may be deduced by making the axial ratios almost equal to unity [5], while the lossless dielectric coated conducting elliptic cylinder may be deduced by making the relative permittivity of the inside dielectric layer very high [9].

II. THEORY

Consider the case of a linearly polarized electromagnetic TM plane wave assumed to be incident on a lossy or lossless dielectric elliptic shell loading a semi-elliptic channel in a ground plane at an angle ϕ_i with respect to the x axis, as shown in Fig. 1. The major axis of the outer dielectric coating is denoted by a_2 and the minor axis is denoted by b_2. Furthermore, the major axis of inner dielectric elliptic cylinder is denoted by a_1 and the minor axis is denoted by b_1. The ground plane is assumed to be perfectly conducting.

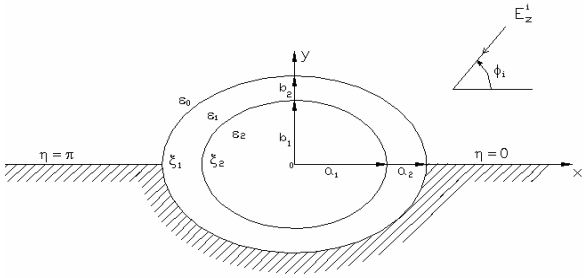

Fig. 1. Scattering geometry of a semi-elliptic channel in a ground plane loaded by a lossy or losslessconfocal dielectric elliptic shell.

The time dependence $e^{j\omega t}$ is assumed and omitted throughout. The elliptical coordinate system (u,v,z) is defined in terms of the Cartesian coordinate system (x,y,z) by $x = F\cosh(u)\cos(v)$ and $y = F\sinh(u)\sin(v)$, where F is the semi focal length of the elliptical cross section [12]. The electric field component of the TM polarized plane wave of amplitude E_0 is given in terms of polar coordinates ρ, ϕ by,

$$E_z^i = E_o e^{jk\rho\cos(\phi-\phi_i)} \tag{1}$$

where $k=2\pi/\lambda$ and λ is the wavelength. The incident electric field may be expressed in terms of Mathieu functions in elliptic cylindrical coordinates ξ, η as follows [12],

$$E_z^i = \sum_{m=0}^{\infty} A_{em}\,\mathrm{Re}_m^{(1)}(c_0,\xi)Se_m(c_0,\eta) + \sum_{m=1}^{\infty} A_{om}\,Ro_m^{(1)}(c_0,\xi)So_m(c_0,\eta) \quad (2)$$

$A_{\substack{em\\om}}$ and $N_{\substack{em\\om}}(c_o)$ are defined in [9], $c_o = kF$, Se_m and So_m are the even and odd angular Mathieu functions of order *m*, respectively, $\mathrm{Re}_m^{(1)}$ and $Ro_m^{(1)}$ are the even and odd radial Mathieu functions of the first kind of order *m*, while N_{em} and N_{om} are the even and odd normalized constants of order m. It should be noted that $\xi=\cosh u$ and $\eta=\cos\nu$ [12]. The reflected field ($\xi > \xi_1$ and $0\le\eta\le\pi$) due to the presence of the ground plane can bewritten as,

$$E_z^{ref} = -\sum_{m=0}^{\infty} A_{em}\,\mathrm{Re}_m^{(1)}(c_0,\xi)Se_m(c_0,\eta) + \sum_{m=1}^{\infty} A_{om}\,Ro_m^{(1)}(c_0,\xi)So_m(c_0,\eta)\,. \quad (3)$$

The scattered field ($\xi > \xi_1$ and $0\le\eta\le\pi$) due to the presence of the channel can be written as,

$$E_z^{diff} = \sum_{m=1}^{\infty} B_{om}\,Ro_m^{(4)}(c_0,\xi)So_m(c_0,\eta) \quad (4)$$

where B_{om} are the unknown odd scattered field expansion coefficients and $Ro_m^{(4)}$ is the odd radial Mathieu function of the fourth kind. The transmitted electric field inside the outer dielectric layer ($\xi_1 \le \xi \le \xi_2$) can also be written also in terms of Mathieu functions as,

$$E_z^I = \sum_{m=0}^{\infty}\begin{bmatrix} C_{em}\,\mathrm{Re}_m^{(1)}(c_1,\xi) \\ +D_{em}\,\mathrm{Re}_m^{(2)}(c_1,\xi)\end{bmatrix}Se_m(c_1,\eta) + \sum_{m=1}^{\infty}\begin{bmatrix} C_{om}Ro_m^{(1)}(c_1,\xi) \\ +D_{om}Ro_m^{(2)}(c_1,\xi)\end{bmatrix}So_m(c_1,\eta) \quad (5)$$

where $c_1 = k_1F$, $k_1=k\sqrt{\varepsilon_{r1}}$, $\varepsilon_{r1}=\varepsilon_{r1}^{'}-j\varepsilon_{r1}^{''}$, C_{em}, D_{em} and C_{om}, D_{om} are the even and odd unknown tansmitted field expansion coefficients, and $\mathrm{Re}_m^{(2)}$ and $Ro_m^{(2)}$ are the even and odd radial Mathieu functions of the second kind [12]. Furthermore, the transmitted electric field inside the inner dielectric layer ($0\le\xi\le\xi_2$) can also be expressed in terms of Mathieu functions as,

$$E_z^{II} = \sum_{m=0}^{\infty} G_{em}\,\mathrm{Re}_m^{(1)}(c_2,\xi)Se_m(c_2,\eta) + \sum_{m=1}^{\infty} G_{om}\,Ro_m^{(1)}(c_2,\xi)So_m(c_2,\eta) \quad (6)$$

where $c_2 = k_2F$, $k_2=k\sqrt{\varepsilon_{r2}}$, $\varepsilon_{r2}=\varepsilon_{r2}^{'}-j\varepsilon_{r2}^{''}$ while G_{em} and G_{om} are the even and odd unknown transmitted field expansion coefficients. The magnetic field in every region can be obtained using Maxwell's equations. The unknown field expansion coefficients given in equations (4) to (6) are yet to be determined using the boundary conditions. The boundary conditions at $\xi=\xi_2$ require the tangential electric and magnetic field components in the inner and outer dielectric layers to be continuous. Enforcing this boundary condition along with orthogonality property of the angular Mathieu functions, we obtain

$$\sum_{m=0}^{\infty}\begin{bmatrix} C_{em}\,\mathrm{Re}_m^{(1)}(c_1,\xi_2) \\ +D_{em}\,\mathrm{Re}_m^{(2)}(c_1,\xi_2)\end{bmatrix}M_{emn}(c_1,c_2) = N_{en}(c_2)G_{en}\,\mathrm{Re}_n^{(1)}(c_2,\xi_2)\,, \quad (7)$$

$$\sum_{m=0}^{\infty}\begin{bmatrix} C_{em}\,\mathrm{Re}_m^{(1)'}(c_1,\xi_2) \\ +D_{em}\,\mathrm{Re}_m^{(2)'}(c_1,\xi_2)\end{bmatrix}M_{emn}(c_1,c_2) = N_{en}(c_2)G_{en}\,\mathrm{Re}_n^{(1)'}(c_2,\xi_2) \quad (8)$$

where

$$M_{\substack{emn\\omn}}(c_1,c_2) = \int_0^{2\pi} S_{om}^{en}(c_1,\eta)S_{on}^{en}(c_2,\eta)dv\,. \quad (9)$$

The prime in equation (8) denotes derivative with respect to u. Similar equations can be written corresponding to the odd solution. To eliminate $G_{en,}$ we solve for G_{en} from equation (8) and substitute into equation (7). This leads to

$$\sum_{m=0}^{\infty} C_{em}\left\{\begin{matrix}\mathrm{Re}_m^{(1)}(c_1,\xi_2)- \\ \mathrm{Re}_m^{(1)'}(c_1,\xi_2)u_{en}\end{matrix}\right\}M_{emn}(c_1,c_2) + \sum_{m=0}^{\infty} D_{em}\left\{\begin{matrix}\mathrm{Re}_m^{(2)}(c_1,\xi_2)- \\ \mathrm{Re}_m^{(2)'}(c_1,\xi_2)u_{en}\end{matrix}\right\}M_{emn}(c_1,c_2) = 0\,. \quad (10)$$

We can write a similar equation for the odd solution, i.e,

$$\sum_{m=0}^{\infty} C_{om} \left\{ \begin{matrix} Ro_m^{(1)}(c_1,\xi_2) - \\ Ro_m^{(1)'}(c_1,\xi_2)u_{on} \end{matrix} \right\} M_{omn}(c_1,c_2) + \sum_{m=0}^{\infty} D_{om} \left\{ \begin{matrix} Ro_m^{(2)}(c_1,\xi_2) - \\ Ro_m^{(2)'}(c_1,\xi_2)u_{on} \end{matrix} \right\} M_{omn}(c_1,c_2) = 0 \quad (11)$$

where

$$u_{\substack{en \\ on}} = \frac{R_{on}^{en(1)}(c_2,\xi_2)}{R_{om}^{en\,(1)'}(c_2,\xi_2)} \quad (12)$$

The boundary condition at $\xi = \xi_1 (\pi < \eta < 2\pi)$ requires the tangential electric field component to vanish at surface, and the total tangential electric and magnetic field components to be continuous across the interface at $\xi = \xi_1$ $(0 < \eta < \pi)$. Enforcing these boundary conditions along with the partial orthogonality property of the angular Mathieu functions, we get [7, 9]

$$\sum_{m=0}^{\infty} \left[\begin{matrix} C_{em}\,\mathrm{Re}_m^{(1)}(c_1,\xi_1) + \\ D_{em}\,\mathrm{Re}_m^{(2)}(c_1,\xi_1) \end{matrix} \right] L_{mn} + \left[\begin{matrix} C_{on} Ro_n^{(1)}(c_1,\xi_1) + \\ D_{on} Ro_n^{(2)}(c_1,\xi_1) \end{matrix} \right] (\pi/2.0) = 0.0, \quad (13)$$

$$\sum_{m=1}^{\infty} 2A_{om} Ro_m^{(1)}(c_0,\xi_1) W_{mn} + \sum_{m=1}^{\infty} B_{om} Ro_m^{(4)}(c_0,\xi_1) W_{mn} = \sum_{m=0}^{\infty} \left[\begin{matrix} C_{em}\,\mathrm{Re}_m^{(1)}(c_1,\xi_1) + \\ D_{em}\,\mathrm{Re}_m^{(2)}(c_1,\xi_1) \end{matrix} \right] F_{mn} + \left[\begin{matrix} C_{on} Ro_n^{(1)}(c_1,\xi_1) + \\ D_{on} Ro_n^{(2)}(c_1,\xi_1) \end{matrix} \right] (\pi/2.0), \quad (14)$$

$$\sum_{m=1}^{\infty} 2A_{om} Ro_m^{(1)'}(c_0,\xi_1) W_{mn} + \sum_{m=1}^{\infty} B_{om} Ro_m^{(4)'}(c_0,\xi_1) W_{mn} = \sum_{m=0}^{\infty} \left[\begin{matrix} C_{em}\,\mathrm{Re}_m^{(1)'}(c_1,\xi_1) + \\ D_{em}\,\mathrm{Re}_m^{(2)'}(c_1,\xi_1) \end{matrix} \right] F_{mn} + \left[\begin{matrix} C_{on} Ro_n^{(1)'}(c_1,\xi_1) + \\ D_{on} Ro_n^{(2)'}(c_1,\xi_1) \end{matrix} \right] (\pi/2.0) \quad (15)$$

where

$$W_{mn} = \int_0^{\pi} So_m(c_0,\eta) So_n(c_1,\eta) dv, \quad (16)$$

$$F_{mn} = \int_0^{\pi} Se_m(c_1,\eta) So_n(c_1,\eta) dv, \quad (17)$$

$$L_{mn} = \int_{\pi}^{2\pi} Se_m(c_1,\eta) So_n(c_1,\eta) dv = -F_{mn}. \quad (18)$$

Equations (13) to (15) are evaluated for m=0,1,2… and n=0,1,2,.... In case of c_o=c_1, equation (16) reduces to Wmn=$(\pi/2.0)\,\delta_{mn}$, where δ_{mn} is the Kronecker delta. Equations (10), (11), and (13) to (15) may be written in matrix form to solve for the unknown scattered and transmitted field expansion coefficients [9].

The lossy case requires the computation of Mathieu functions with complex argument and more details on the computation of Mathieu function can be found in [13-14].

III. NUMERICAL RESULTS

The scattered near and far fields can be calculated once the scattered field expansion coefficients are computed. The scattered far field expression may be written as follows,

$$E_z^s = \sqrt{\frac{j}{k\rho}} e^{-jk\rho} P(c_o,\eta) \quad (19)$$

where

$$P(c_o,\eta) = \sum_{m=1}^{\infty} j^m \left[B_{om} So_m(c_o,\eta) \right]. \quad (20)$$

In order to solve for the unknown scattered field coefficients, the infinite series are first truncated to include only the first *N* terms, where *N* in general is a suitable truncation number proportional to the channel electrical size. In the computation, the value of *N* has been chosen to impose a convergence condition that provides solution accuracy with at least four significant figures, The accuracy of the numerical results is checked against the special case of a semi-circular channel loaded with a lossless dielectric shell [4].

Figure 2 shows the normalized backscattered field $|P(c_o,\cos\phi_i)|$ for a lossy or lossless dielectric shell loading a semicircular channel versus ka_2 with ka_1=1.0, a_1/b_1=1.0, ε_{r1} = 1.5, ε_{r2} = 12 and ϕ_i = 90°. The solid line represents the calculated numerical results while the circled curve represents the solution in [4]. For example, the convergence for this is achieved for *N*=9. It can be seen that the calculated results agree very well with [4] for ka_2 < 3.2, the range given by [4]. Further, high peak resonances occur at different values of ka_2 and the

amplitude of these peaks becomes even larger with the channel size. The strong resonant behavior may be due to the multiple scattering between the circular shell and channel. Finally, the dotted line represents the lossy dielectric case with ε_{r1} = 1.5- j0.5 and ε_{r2} = 12-j0.5. For example, the convergence for this is achieved for N = 7. The presence of lossy material seems to have little effect on the normalized backscattered field especially for ka_2 < 2.0, and attenuates the amplitude of the high peak resonances for ka_2 > 2.0. Figure 3 shows the normalized backscattered field for a lossy or lossless confocal dielectric elliptic shell loading a semi-elliptic channel versus the major axis of electrical size ka_2 . The major axis electrical size of the inner elliptic dielectric shell is kept constant at ka_1=1.0 with axial ratio a_1/b_1=1.43 and ϕ_i = 90°. The solid line represents the lossless dielectric case, ε_{r1} = 3.0 and ε_{r2} = 5.0. The circled line represents the weakly lossy case, ε_{r1} = 3.0-j0.1 and ε_{r2} = 5.0-j0.1, while the dotted curve represents the strongly lossy case of ε_{r1} = 3.0-j0.5 and ε_{r2} = 5.0-j0.5.

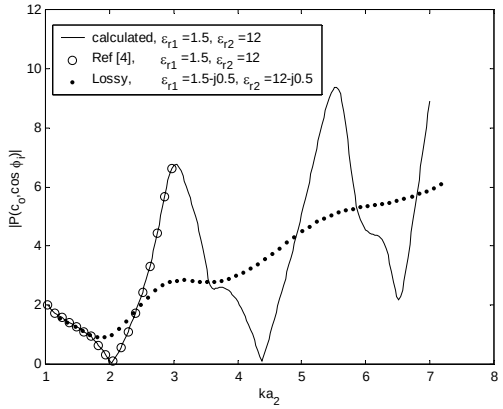

Fig. 2. Normalized backscattered field versus electrical size ka_2 for a lossy or lossless dielectric circular shell loading a semi-circular channel with ka_1=1.0, a_1/b_1=1.0 and ϕ_i = 90°.

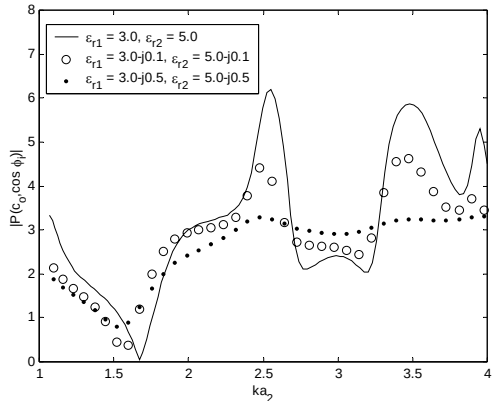

Fig. 3. Normalized backscattered field versus electrical size ka_2 for a lossy or lossless confocal dielectric elliptic shell loading a semi-elliptic channel with ka_1=1.0, a_1/b_1=1.43 and ϕ_i = 90°.

In Fig. 4 we have plotted the normalized echo pattern width $|P(c_o,\cos\phi)|$ against the scattering angle ϕ for a lossy or lossless dielectric circular shell loading a semi-circular channel with ka_1=2.0, a_1/b_1=1.0, $ka_2=2\pi$, a_2/b_2=1.0 and ϕ_i =60°. The solid line represents the lossless case with ε_{r1} = 4.0, ε_{r2} = 2.0. A strong resonance with high amplitude is located at ϕ =120°, as expected, in addition to other resonances located at ϕ =40° and 90°. It seems that the presence of lossy dielectric material has little effect on the amplitude of the resonance at ϕ =120° while strong effect may be observed on the amplitude of the resonances located at ϕ = 40° and 90°. Figure 5 shows normalized echo pattern width for a lossy or lossless dielectric elliptic shell loading a semi-elliptic channel with ka_1=5.73, a_1/b_1=5.73, $ka_2=2\pi$, a_2/b_2=2.3 and ϕ_i = 60°. The solid line represents the lossless case, ε_{r1} = 4.0, ε_{r2} = 2.0, which seems to have strong resonances at different scattering angles and the strongest resonance peak is located at ϕ = 120°. It can also be observed that the presence of the lossy dielectric material has a significant effect on the amplitude of the high peaks resonances, but has no effect on the location of resonances.

Figure 6 shows the normalized backscattered far field versus the incident angle ϕ_i for a lossy or lossless dielectric elliptic shell loading a semi-elliptic channel with ka_1=2.0, a_1/b_1=2.0, ka_2=4.36 and a_2/b_2=1.1. It seems that the normalized backscattered field of the elliptical channels is highest at the incident angle ϕ_i = 90°. It can also be observed that the presence of lossy dielectric material has shifted the resonance peaks at ϕ_i = 30° and 55°.

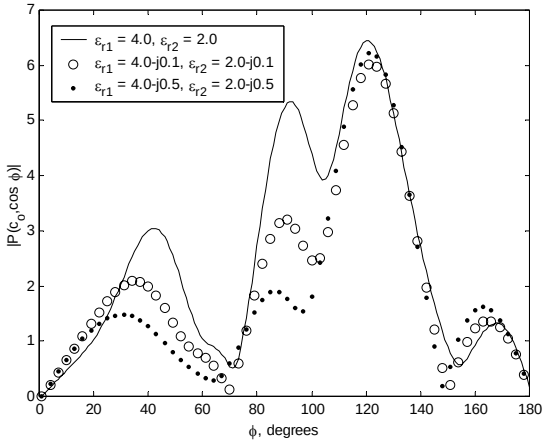

Fig. 4. Normalized scattered field versus the scattering angle ϕ for a lossy or lossless dielectric circular shell loading a semi-circular channel with ka_1=2.0, a_1/b_1=1.0, $ka_2 = 2\pi$, a_2/b_2 = 1.0 and ϕ_i = 60°.

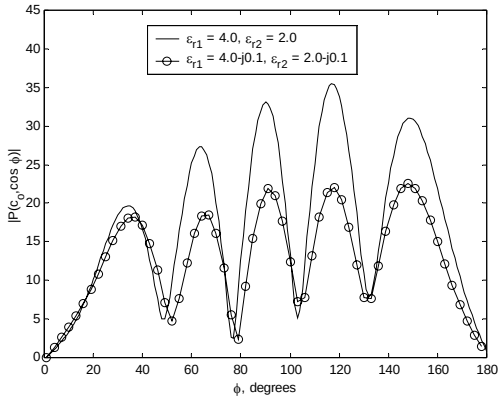

Fig. 5. Normalized scattered field versus the scattering angle ϕ for a lossy or lossless dielectric elliptic shell loading a semi-elliptic channel with $ka_1 = 5.73$, $a_1/b_1 = 5.73$, $ka_2 = 2\pi$, $a_2/b_2 = 2.3$ and $\phi_i = 60^o$.

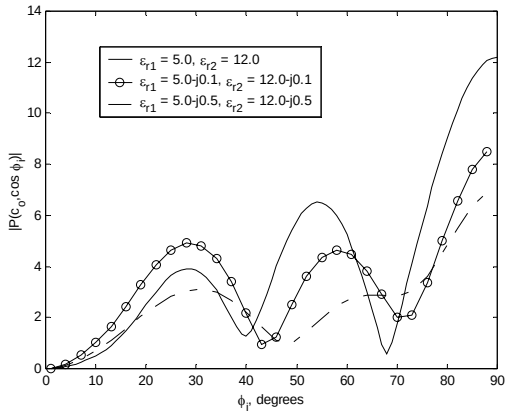

Fig. 6. Normalized backscattered field versus the incident angle ϕ_i for a lossy or lossless dielectric elliptic shell loading a semi-elliptic channel with $ka_1 = 2.0$, $a_1/b_1 = 2.0$, $ka_2 = 4.36$, $a_2/b_2 = 1.1$.

IV. CONCLUSIONS

An analytical solution and numerical results for the electromagnetic scattering by a lossy or lossless dielectric circular or elliptic shell loading a semi-circular or semi-elliptical channel in a ground plane is obtained. The presence of lossy or lossless dielectric shell has significantly affected the appearance and attenuation of the channel resonances. Finally, the presented solution is the most general one available in the literature and special cases can be deduced by choosing the appropriate axial ratio and dielectric constant.

ACKNOWLEDGEMENT

The author wishes to acknowledge the support provided by the University of Sharjah, U.A.E.

REFERENCES

[1] B. K. Sachdeva and R. A. Hurd, "Scattering by a dielectric-loaded trough in a conducting plane," *J. Appl. Phys.*, vol. 48, no. 4, pp. 1473-1476, 1977.

[2] M. K. Hinders and A. D. Yaghjian, "Dual-series solution to scattering from a semicircular channel in a ground plane," *IEEE Microwave Guided Wave Lett.*, vol. 1, no. 9, pp. 239-242, 1991.

[3] T. J. Park, H. J. Eom, W.-M. Boerner, and Y. Yamaguchi, "TM scattering from a dielectric-loaded semi-circular trough in a conducting plane," *IEICE Trans. Commun.*, vol. E75-B, no. 2, pp. 87-91, 1992.

[4] T. J. Park, H. J. Eom, Y. Yamaguchi, W.-M. Boerner, and S. Kozaki, "TE-plane wave scattering from a dielectric-loaded semi-circular trough in a conducting plane," *J. Electromagnetic Waves Applicat.*, vol. 7, pp. 235-245, 1993.

[5] H. A. Ragheb, "Electromagnetic scattering from a coaxial dielectric circular cylinder loading a semicircular gap in a ground plane," *IEEE Trans. Microwave Theory Tech.*, vol. 43, no. 6, pp. 1303-1309, 1995.

[6] T. Shen, W. Dou, and Z. Sun, "Gaussian beam scattering from a semicircular channel in a conducting plane," *Progress In Electromagnetics Research (PIER)*, vol. 16, pp. 67-85, 1997.

[7] W. J. Byun, J. W. Yu, and N. H. Myung, "TM scattering from hollow and dielectric –filled semielliptic channels with arbitrary eccentricity in a perfectly conducting plane," *IEEE Trans. Microwave Theory Tech.*, vol. 46, no. 9, pp. 1336-1339, 1998.

[8] D. Erricolo and P. L. E. Uslenghi, "Exact radiation and scattering for an elliptic metal cylinder at the interface between isorefractive half-spaces" *IEEE Trans. on Antennas and Propag.*, vol. 52, no. 9, pp. 2214-2225, 2004.

[9] A-K. Hamid, "Electromagnetic scattering from a dielectric coated conducting elliptic cylinder loading a semi-elliptic channel in a ground plane," *J. Electromagnetic Waves Applicat.*, vol. 19, no. 2, pp. 257-269, 2005.

[10] T. B. Senior and J. L. Volakis, "Scattering by gaps and cracks," *IEEE Trans. Antennas Propag.*, vol. 37, pp. 744-750, 1989.
[11] T. B. Senior, K. Sarabandi, and J. Natzke, "Scattering by a narrow gap," *IEEE Trans. Antennas Propag.*, vol. 38, pp. 1102-1110, 1990.
[12] P. M. Morse and H. Feshbach, *Methods of TtheoreticalPphysics*, vols. I and II. New York: McGraw-Hill, 1953.
[13] A-K. Hamid, M. I. Hussein, H. Ragheb, and M. Hamid, "Mathieu functions of complex arguments and their applications to the scattering by lossy elliptic cylinders," *Applied Computational Electromagnetics Society*, vol. 17, no. 3, pp. 209-217, 2002.
[14] A-K. Hamid and M. I. Hussein, "Electromagnetic scattering by a lossy dielectric coated elliptic cylinder," *Canadian Journal of Physics*, vol. 81, no. 5, pp. 771-778, 2003.

A.-K. Hamid was born in Tulkarm, West Bank, on Sept. 9, 1963. He received the B.Sc. degree in Electrical Engineering from West Virginia Tech, West Virginia, U.S.A. in 1985. He received the M.Sc. and Ph.D. degrees from the University of Manitoba, Winnipeg, Manitoba, Canada in 1988 and 1991, respectively, all in Electrical Engineering. From 1991-1993, he was with Quantic Laboratories Inc., Winnipeg, Manitoba, Canada, developing two and three dimensional electromagnetic field solvers using boundary integral method. From 1994-2000 he was with the faculty of electrical engineering at King Fahd University of Petroleum and Minerals, Dhahran, Saudi Arabia. Since Sept. 2000 he has been an associate Prof. in the electrical/electronics and computer engineering department at the University of Sharjah, Sharjah, United Arab Emirates. His research interest includes EM wave scattering from two and three dimensional bodies, propagation along waveguides with discontinuities, FDTD simulation of cellular phones, and inverse scattering using neural networks.

Investigation of Wire Grid Modeling in NEC Applied to Determine Resonant Cavity Quality Factors

Franz A. Pertl, Andrew D. Lowery, and James E. Smith

Department of Mechanical and Aerospace Engineering
West Virginia University, Morgantown, WV 26506, USA
franz.pertl@mail.wvu.edu, dlowery@gmail.com, james.smith@mail.wvu.edu

Abstract **–** Numerical computer simulations using the NEC Method of Moments (MoM) code were performed on wire grid models of resonant cavities in order to study how well conductive structures and their surface impedances can be modeled by wire meshes. The resonant cavity quality factor, or *Q,* was examined due to its high sensitivity to surface impedance. Several half-wave coaxial cavities were simulated using various mesh element sizes. The cavities' outer conductor radius was varied to obtain different geometries. The quality factor *Q* was determined from the simulated input impedance spectra. The wire grid model results were compared to well known theoretical and experiment results. Qualitative agreement between simulation, theoretical, and experimental results was achieved for fixed mesh parameters, giving confidence in comparative simulation using the same wire grid meshing parameters. Quantitative agreement of simulation results was achieved through repeated simulation with varying mesh element lengths and extrapolating the simulation results to a conceptual mesh element length of zero. This shows that simulations to determine quantities sensitive to surface impedances can be successfully performed with codes such as NEC.

Key words – Wire grid modeling, method of moments, extrapolation, and surface impedance.

I. INTRODUCTION

A resonant cavity's quality factor, *Q*, is highly dependent on the surface impedance, R_s, of the cavity's interior conducting surface. Numerical simulation of well understood cavities can serve to investigate numerical techniques employed to model conductive surfaces and their impedances. Once shortcomings of a particular numerical modeling technique are determined, they can often be compensated for and hence result in more accurate simulation results. These techniques can then be applied with confidence to the simulation of more complicated resonant structures for which analytical solutions are not readily available. In this paper, the well known quality factor of cylindrical half-wave coaxial cavity resonators was investigated, to determine how well wire grid models can represent conductor surfaces in resonant cavity structures.

II. THEORETICAL BACKGROUND ON QUALITY FACTOR OF HALF-WAVE RESONANT COAXIAL CAVITIES

A basic definition of quality factor, *Q*, for a resonant structure is given in equation (1). For the case of an electromagnetic half-wave coaxial cavity resonator, the energy stored, E_S, can be calculated through equation (2, the integral over the cavity volume, *V*, of the magnetic-field intensity, *H*. The energy dissipated per cycle, E_D, is given by equation (3), the surface integral of the ohmic losses due to the surface current density J_s, over the interior cavity surface area, *A*. The *Q* of a resonant cavity is often normalized with respect to the wavelength, λ, and conductor skin depth, δ, as shown in equation (4), and is then referred to as the cavity form factor [1],

$$Q = \frac{2\pi \cdot E_S}{E_D} \tag{1}$$

$$E_S = \frac{\mu}{2}\int \left|\vec{H}\right|^2 \cdot dV\,, \tag{2}$$

$$E_D = \frac{\pi \cdot R_s}{\omega}\int \left|\vec{J}_s\right|^2 \cdot dA \quad \text{or} \quad E_D = \frac{\pi \cdot \delta \cdot \mu}{2}\int \left|\vec{H}_T\right|^2 \cdot dA\,, \tag{3}$$

$$Q\frac{\delta}{\lambda} = \frac{2}{\lambda}\frac{\int \left|\vec{H}\right|^2 \cdot dV}{\int \left|\vec{H}_T\right|^2 \cdot dA}. \tag{4}$$

Since the fields in a half-wave long resonant cavity are standing transverse electromagnetic (TEM) waves, the time average magnetic-field intensity, *H*, which is strictly in the ϕ-direction for this mode, is known to be of the form given in equation (5) where *C* is a constant and z_0 is the length of the cavity as shown in Fig. 1.

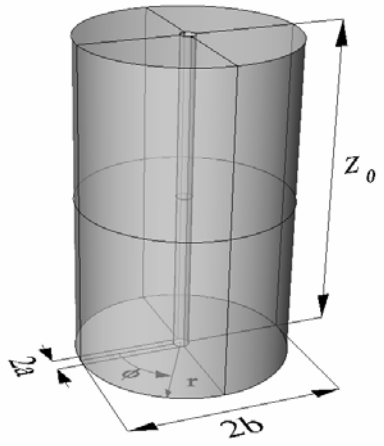

Fig. 1. Coaxial cavity geometry with inner radius, *a*, outer radius, *b,* and length, z_0.

$$\vec{H}(r,\phi,z) = C\frac{1}{r}\cdot Cos\left(\frac{\pi\cdot z}{z_0}\right)\cdot\hat{\phi}. \qquad (5)$$

Substituting *H* into equation (4) and evaluating, provides results shown in equation (6) for the form factor of a half-wave coaxial cavity [1]. Note that this quality factor is the unloaded quality factor, Q_u, which does not include losses due to a coupling structure or associated source impedance. If simulations of wire grid representations of such coaxial cavities result in quality factors predicted by theory, then the simulation technique must properly model conductive structures and their surface impedance losses with wire grids.

$$Q_u\frac{\delta}{\lambda} = \frac{\ln\left(\frac{b}{a}\right)}{z_0\cdot\left(\frac{1}{a}+\frac{1}{b}\right)+4\cdot\ln\left(\frac{b}{a}\right)} \qquad (6)$$

III. BACKGROUND ON CONDUCTIVE SURFACE MODELING BY WIRE GRIDS

Richmond pioneered modeling of conductive geometries using wire grid representations and this technique has become accepted radiation and scattering problems [2]. Rules of thumb have been developed for modeling conductive structures. A usual requirement for the wire grid models is that the grid element size be "small" with respect to a wavelength. Another commonly used rule is "the equal surface area rule", where the total surface area of the cylindrical wires comprising the grid is made to match the surface area of the conductive object being modeled [3-5]. It has been found that a rectangular wire grid, with the grid axes aligned to electromagnetic polarization, generally gives more accurate simulation results than other types of grids, including triangular grids [5]. A more elaborated set of rules for wire grid simulation of surfaces using the Numerical Electromagnetics Code (NEC) [6], a popular and well tested method of moments code, is discussed in Truman and Kubina [3]. However, these rules are only guidelines. According to Moore and Pizer, some simulations require the wire grid surface area to be up to five times larger than the object's actual surface area in order to match experimental results, so surface impedance seems to not be modeled well in these wire grid simulations [6].

IV. IMPLEMENTATION OF WIRE GRID MODELS FOR COAXIAL CAVITIES

To facilitate the construction of various simulation wire grid geometries for this study's simulations, a commercial computer aided design (CAD) program was employed. Each resulting cavity model mesh was exported to a text file in the open-Wavefront OBJ format [8]. This format specifies the mesh as a series of numbered vertices followed by a series of planar faces or patches with the vertices at the corners of these patches. This text file was then processed into a format compatible with NEC through custom written software. The process generated a wire segment for each edge of each mesh surface patch, while avoiding duplication amongst adjacent patches. The equal area rule was applied, in which the cylindrical surface area of a wire segment was chosen to be the average of the surface areas of the quadrilateral grid patches on either side of the wire. The wire mesh generated used equally sized, primarily square patches, and as such, polarization alignment of the mesh was not completely achieved at the shorted ends of the resonator. The equal area rule resulted in a total surface area of the grid elements of approximately twice the modeled conductor area.

V. MODEL FIELD EXCITATION AND SIMULATION

A small rectangular loop near the base of the cavity wire grid model provided the excitation to the model. This loop was added by manually editing the NEC geometry input file. The input files were then simulated using NEC2++ ver. 1.2.3, a PC implementation of NEC in the C++ programming language [9]. Approximate resonance peaks were found through iterative frequency sweeps. The coupling loop area and the loop's position were adjusted so that the simulation achieved reasonable coupling and the cavity Q could be reliably determined. Note that the effect of the coupling structure on Q was later removed from the data, and attention was focused on the unloaded quality factor, independent of the coupling structure.

A series of half-wave coaxial cavities were modeled to obtain the simulated impedance spectra. The inner conductor radius, a, and the cavity length, z, were held fixed arbitrarily, at 1 m and 12 m, respectively. The outer radius b was allowed to vary from 2 m to 6 m in increments of 0.5 m. Larger outer radii were not simulated, as 6 m is close to the upper limit for the TEM resonance mode [10]. Some sample cavity models are shown in Fig. 2.

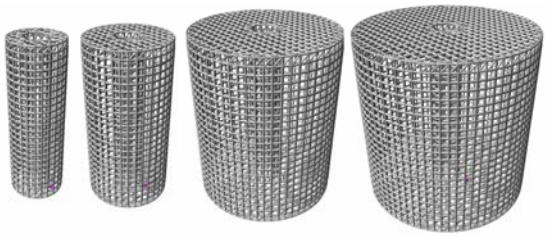

Fig. 2. Sample wire grid cavity models, a = 1 m, b = 2 m to 6 m, and z = 12 m.

VI. THEORETICAL, SIMULATION, AND EXPERIMENTAL RESULTS

Once simulations were complete, the simulated impedance spectra were used to determine the corresponding unloaded quality factors. The impedance spectra were transformed to reflection coefficients, as they would have been measured with a 50 Ω network analyzer. The loaded (by coupling loop) and unloaded quality factors were then determined by the half power frequency span about the resonance frequency. This was performed on the Smith chart, where the locus of the impedance is known to form a circle in the vicinity of the resonance frequency. A freely available piece of software readily performs these calculations from network the analyzer data. For references on the software and other methods of determining quality factors from impedance data, refer to Ginzton, Kaifez, and Hwan [11][13]. The resulting unloaded quality factors for the half-wave cavities were then normalized with respect to the skin depth, δ, and the wavelength, λ, and compared to theoretically calculated values, as given in equation (6). Several mesh edge lengths were simulated for each cavity. The edge length data was then extrapolated to a conceptual length of zero through a quadratic least squares fit of Q_u. For comparison purpose, experimental cavities (Fig. 3) with correspondingly scaled dimensions were constructed from brass and measured on a network analyzer. The measured data were processed identically to the simulated data to determine the normalized cavity form factors. The results are plotted in Fig. 4.

Fig. 3. Experimental cavity models, a = 1 in, b = 2 in to 6 in, and z = 12 in.

VII. DISCUSSION AND CONCLUSIONS

As shown in Fig. 4, mesh size has a considerable effect on the magnitude of the simulated form factors. However, the general shape of the simulated curves for each mesh element size agrees with theory and experiment. A large mesh size seems to result in erratic simulation results especially around b/a = 5.5 m, which is not reflected in the experimental data. These erratic results must therefore be numerical instabilities rather than excitation of higher resonance modes. As expected, finer mesh sizes result in more accurate and better behaved simulation results, but at the cost of additional computation time. The simulation error in absolute magnitude can be corrected by artificially shifting up the curves, which is equivalent to decreasing the conductivity of the wire grid elements. The required adjustments in conductivity for the 0.5 m and 0.375 m grids, is about 1/5 and 1/4, respectively, and seems to correlate well with Moore and Pizer's suggestion of a simulated area up to five times the actual area [6]. Alternatively, the simulation results for each b/a can be extrapolated to a conceptual mesh element length of zero. This then results in excellent agreement between

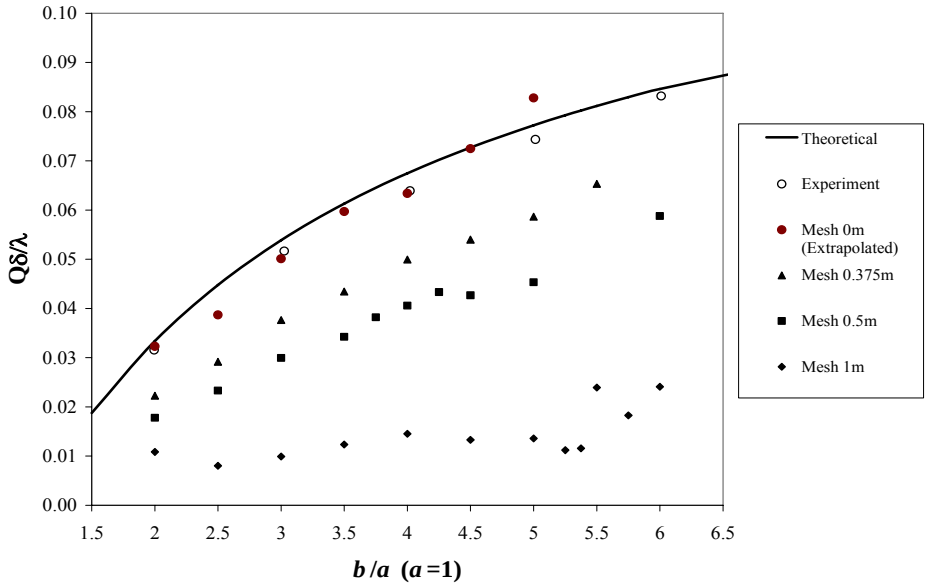

Fig. 4. Comparison of theoretical, simulated and experimental form factors.

experiment, theory and simulation. In practice, experimental data is expected to be slightly below theoretical, due to surface imperfections that lower the overall surface conductivity. Despite modeling errors, such as low level radiation leakage from meshed structures representing closed volumes and inaccurate absolute surface impedance modeling at larger mesh element sizes, trends in the simulation results are retained. This allows for meaningful comparison of other resonant geometries via simulation by using wire grid meshes with identical mesh parameters. As an alternative, the mesh element size can be varied and the results extrapolated to the limiting case of a zero length edge element. This will give quantitatively simulation results with much better accuracy. Wire grid modeling can be a valuable tool, not just for radiation and scattering problems, but even for problems that show sensitivity to surface impedance.

REFERENCES

[1] K. Henney, *Radio Engineering Handbook,* 5th ed., New York: McGraw-Hill, pp. 6.46-6.58, 1959.

[2] J. H. Richmond, "A wire-grid model for scattering by conductive bodies," *IEEE Transactions on Antennas and Propagation*, vol. AP-14, no. 6, pp. 782 - 786, Nov. 1966.

[3] C. W. Truman and S. J. Kubina, "Fields of complex surfaces using wire grid modeling," *IEEE Transactions on Magnetics*, vol. 27, no. 5, Sep. 1991.

[4] R. J. Paknys, "The near field of a wire grid model," *IEEE Transactions on Antennas and Propagation*, vol. 39, no. 7, July 1991.

[5] A. Rubinstein, F. Rachidi, and M. Rubenstein, "On wire-grid representation of solid metallic surfaces," *IEEE Transactions on Electromagnetic Compatibility*, vol. 47, no. 1, pp. 192-195, Feb. 2005.

[6] G. Burke and A. Poggio, *Numerical Electromagnetics Code (NEC) – Method of Moments*, NOSC TD 116, Jan. 1981.

[7] J. Moore and R. Pizer, *Moment Methods in Electromagnetics*, New York: Wiley, 1984, Secs. 1.1.2 and 6.4.

[8] Murray, D. James, and V. R. William, *Encyclopedia of Graphics File Formats*, 2nd, Sebastopol, CA, O'Reilly and Associates, April 1996.

[9] T. Molteno, S. Harris, and R. Sassolas, *"NEC2++", Alioth*, October 15th 2005, http://alioth.debian.org /projects/necpp/.

[10] T. Moreno, *Microwave Transmission Design Data*, New York: Dover Publications, 1948.

[11] D. Kaifez and E. J. Hwan, "Q-factor measurement with network analyzer," *IEEE Transactions on Microwave Theory and Techniques*, vol. 32, no. 7, July 1984.

[12] E. L. Ginzton, "Microwave Q measurements in the presence of coupling losses," *IEEE Transactions on Microwave Theory and Techniques*, vol. 6, pp. 383-389, Oct. 1958.

[13] D. Kaifez, "Graphical analysis of Q circuits," Correspondence in *IEEE Transactions on Microwave Theory and Techniques*, Sep. 1963.

2007 INSTITUTIONAL MEMBERS

AUSTRALIAN DEFENCE LIBRARY
Northcott Drive
Canberra, A.C.T. 2600 Australia

BAE SYSTEMS
W. Hanningfield Road
Technology Center Library
Great Baddow, Chelmsford
UK CM2 8HN

BEIJING BOOK COMPANY, INC
701 E Lindon Ave.
Linden, NJ 07036-2495

DARTMOUTH COLL-FELDBERG LIB
6193 Murdough Center
Hanover, NH 03755-3560

DSTO-DSTORL EDINBURGH
Jets AU/33851-99, PO Box 562
Milsons Point, NSW
Australia 1565

DTIC-OCP/LIBRARY
8725 John J. Kingman Rd. Ste 0944
Ft. Belvoir, VA 22060-6218

ELLEDIEMME SRL
C.P. 69 Poste S. Silvestro
Roma, Italy 00187

ELSEVIER
Bibliographic Databases
PO Box 2227
Amsterdam, Netherlands 1000 CE

ENGINEERING INFORMATION, INC
PO Box 543
Amsterdam, Netherlands 1000 Am

ETSE TELECOMUNICACION
Biblioteca, Campus Lagoas
Vigo, 36200 Spain

FGAN-FHR
Neuenahrerstrasse 20
Wachtberg, Germany 53343

FLORIDA INTERNATIONAL UNIV
10555 W. Flagler Street
Miami, FL 33174

GEORGIA TECH LIBRARY
225 North Avenue, NW
Atlanta, GA 30332-0001

HANYANG UNIVERSITY
Paiknam Academic Info. Ctr Library
17 Haengdang-Dong
Seongdong-Ku
Seoul, South Korea 133-791

HRL LABS, RESEARCH LIBRARY
3011 Malibu Canyon
Malibu, CA 90265

IEE INSPEC/Acquisitions Section
Michael Faraday House
6 Hills Way
Stevenage, Herts UK SG1 2AY

INSTITUTE FOR SCIENTIFIC INFO.
Publication Processing Dept.
3501 Market St.
Philadelphia, PA 19104-3302

IPS RADIO & SPACE SERVICES
PO Box 1386
Haymarket NSW Australia 1240

ISRAEL AIRCRAFT INDUSTRIES
Ben-Gurion Airport
70100 Israel

LEMA-EPFL
ELB-ECUBLEMS
Lausanne, Switzerland
CH-1020

LIBRARY – DRDC OTTAWA
3701 Carling Avenue
Ottawa, Ontario, Canada K1A OZ4

LIBRARY of CONGRESS
Reg. Of Copyrights
Attn: 40T Deposits
Washington DC, 20559

LINDA HALL LIBRARY
5109 Cherry Street
Kansas City, MO 64110-2498

MISSISSIPPI STATE UNIV LIBRARY
PO Box 9570Mississippi State, MS
39762

MIT LINCOLN LABORATORY
Periodicals Library
244 Wood Street
Lexington, MA 02420

NAVAL POSTGRADUATE SCHOOL
Attn:J. Rozdal/411 Dyer Rd./ Rm 111
Monterey, CA 93943-5101

NAVAL RESEARCH LABORATORY
Code 3516
4555 Overlook Avenue SW
Washington, DC 20375-5334

NDL KAGAKU
C/0 KWE-ACCESS
PO Box 300613 (JFK A/P)
Jamaica, NY 11430-0613

OHIO STATE UNIVERSITY
1320 Kinnear Road
Columbus, OH 43212

OVIEDO LIBRARY
PO BOX 830679
Birmingham, AL 35283

PENN STATE UNIVERSITY
126 Paterno Library
University Park, PA 16802-1808

PHILIPS RESEARCH LABORATORY
Cross Oak Lane, Stella Cox
Salfords, Redhill
UK RH1 5HA

RENTON TECH LIBRARY/BOEING
PO BOX 3707
SEATTLE, WA 98124-2207

SOUTHWEST RESEARCH INSTITUTE
6220 Culebra Road
San Antonio, TX 78238

SWETS INFORMATION SERVICES
160 Ninth Avenue, Suite A
Runnemede, NJ 08078

TECHNISCHE UNIV. DELFT
Mekelweg 4, Delft, Holland, 2628 CD
Netherlands

TELSTRA
TRL/M2/770 Blackburn Road
Clayton, Victoria, Australia 3168

TIB & UNIV. BIB. HANNOVER
DE/5100/G1/0001
Welfengarten 1B
Hannover, Germany 30167

TU DARMSTADT
Schlossgartenstrasse 8
Darmstadt, Hessen
Germany D-64289

UNIV OF CENTRAL FLORIDA LIB.
4000 Central Florida Boulevard
Orlando, FL 32816-8005

UNIV OF COLORADO LIBRARY
Campus Box 184
Boulder, CO 80309-0184

UNIVERSITY OF MISSISSIPPI
John Davis Williams Library
PO Box 1848
University, MS 38677-1848

UNIV OF MISSOURI-ROLLA LIB.
1870 Miner Circle
Rolla, MO 65409-0001

UNIV POL DE CARTAGENE
PO Box 830470
Birmingham, AL 35283

USAE ENG. RES. & DEV. CENTER
Attn: Library/Journals
72 Lyme Road
Hanover, NH 03755-1290

ACES COPYRIGHT FORM

This form is intended for original, previously unpublished manuscripts submitted to ACES periodicals and conference publications. The signed form, appropriately completed, MUST ACCOMPANY any paper in order to be published by ACES. PLEASE READ REVERSE SIDE OF THIS FORM FOR FURTHER DETAILS.

TITLE OF PAPER:

AUTHORS(S)

PUBLICATION TITLE/DATE:

RETURN FORM TO:

Dr. Atef Z. Elsherbeni
University of Mississippi
Dept. of Electrical Engineering
Anderson Hall Box 13
University, MS 38677 USA

PART A - COPYRIGHT TRANSFER FORM

(NOTE: Company or other forms may not be substituted for this form. U.S. Government employees whose work is not subject to copyright may so certify by signing Part B below. Authors whose work is subject to Crown Copyright may sign Part C overleaf).

The undersigned, desiring to publish the above paper in a publication of ACES, hereby transfer their copyrights in the above paper to The Applied Computational Electromagnetics Society (ACES). The undersigned hereby represents and warrants that the paper is original and that he/she is the author of the paper or otherwise has the power and authority to make and execute this assignment.

Returned Rights: In return for these rights, ACES hereby grants to the above authors, and the employers for whom the work was performed, royalty-free permission to:

1. Retain all proprietary rights other than copyright, such as patent rights.
2. Reuse all or portions of the above paper in other works.
3. Reproduce, or have reproduced, the above paper for the author's personal use or for internal company use provided that (a) the source and ACES copyright are indicated, (b) the copies are not used in a way that implies ACES endorsement of a product or service of an employer, and (c) the copies per se are not offered for sale.
4. Make limited distribution of all or portions of the above paper prior to publication.
5. In the case of work performed under U.S. Government contract, ACES grants the U.S. Government royalty-free permission to reproduce all or portions of the above paper, and to authorize others to do so, for U.S. Government purposes only.

ACES Obligations: In exercising its rights under copyright, ACES will make all reasonable efforts to act in the interests of the authors and employers as well as in its own interest. In particular, ACES REQUIRES that:

1. The consent of the first-named author be sought as a condition in granting re-publication permission to others.
2. The consent of the undersigned employer be obtained as a condition in granting permission to others to reuse all or portions of the paper for promotion or marketing purposes.

In the event the above paper is not accepted and published by ACES or is withdrawn by the author(s) before acceptance by ACES, this agreement becomes null and void.

AUTHORIZED SIGNATURE — TITLE (IF NOT AUTHOR)

EMPLOYER FOR WHOM WORK WAS PERFORMED — DATE FORM SIGNED

Part B - U.S. GOVERNMENT EMPLOYEE CERTIFICATION

(NOTE: if your work was performed under Government contract but you are not a Government employee, sign transfer form above and see item 5 under Returned Rights).

This certifies that all authors of the above paper are employees of the U.S. Government and performed this work as part of their employment and that the paper is therefor not subject to U.S. copyright protection.

AUTHORIZED SIGNATURE — TITLE (IF NOT AUTHOR)

NAME OF GOVERNMENT ORGANIZATION — DATE FORM SIGNED

PART C - CROWN COPYRIGHT

(NOTE: ACES recognizes and will honor Crown Copyright as it does U.S. Copyright. It is understood that, in asserting Crown Copyright, ACES in no way diminishes its rights as publisher. Sign only if *ALL* authors are subject to Crown Copyright).

This certifies that all authors of the above Paper are subject to Crown Copyright. (Appropriate documentation and instructions regarding form of Crown Copyright notice may be attached).

AUTHORIZED SIGNATURE TITLE OF SIGNEE

NAME OF GOVERNMENT BRANCH DATE FORM SIGNED

Information to Authors

ACES POLICY

ACES distributes its technical publications throughout the world, and it may be necessary to translate and abstract its publications, and articles contained therein, for inclusion in various compendiums and similar publications, etc. When an article is submitted for publication by ACES, acceptance of the article implies that ACES has the rights to do all of the things it normally does with such an article.

In connection with its publishing activities, it is the policy of ACES to own the copyrights in its technical publications, and to the contributions contained therein, in order to protect the interests of ACES, its authors and their employers, and at the same time to facilitate the appropriate re-use of this material by others.

The new United States copyright law requires that the transfer of copyrights in each contribution from the author to ACES be confirmed in writing. It is therefore necessary that you execute either Part A-Copyright Transfer Form or Part B-U.S. Government Employee Certification or Part C-Crown Copyright on this sheet and return it to the Managing Editor (or person who supplied this sheet) as promptly as possible.

CLEARANCE OF PAPERS

ACES must of necessity assume that materials presented at its meetings or submitted to its publications is properly available for general dissemination to the audiences these activities are organized to serve. It is the responsibility of the authors, not ACES, to determine whether disclosure of their material requires the prior consent of other parties and if so, to obtain it. Furthermore, ACES must assume that, if an author uses within his/her article previously published and/or copyrighted material that permission has been obtained for such use and that any required credit lines, copyright notices, etc. are duly noted.

AUTHOR/COMPANY RIGHTS

If you are employed and you prepared your paper as a part of your job, the rights to your paper initially rest with your employer. In that case, when you sign the copyright form, we assume you are authorized to do so by your employer and that your employer has consented to all of the terms and conditions of this form. If not, it should be signed by someone so authorized.

NOTE RE RETURNED RIGHTS: Just as ACES now requires a signed copyright transfer form in order to do "business as usual", it is the intent of this form to return rights to the author and employer so that they too may do "business as usual". If further clarification is required, please contact: The Managing Editor, R. W. Adler, Naval Postgraduate School, Code EC/AB, Monterey, CA, 93943, USA (831)656-2352.

Please note that, although authors are permitted to re-use all or portions of their ACES copyrighted material in other works, this does not include granting third party requests for reprinting, republishing, or other types of re-use.

JOINT AUTHORSHIP

For jointly authored papers, only one signature is required, but we assume all authors have been advised and have consented to the terms of this form.

U.S. GOVERNMENT EMPLOYEES

Authors who are U.S. Government employees are not required to sign the Copyright Transfer Form (Part A), but any co-authors outside the Government are.

Part B of the form is to be used instead of Part A only if all authors are U.S. Government employees and prepared the paper as part of their job.

NOTE RE GOVERNMENT CONTRACT WORK: Authors whose work was performed under a U.S. Government contract but who are not Government employees are required so sign Part A-Copyright Transfer Form. However, item 5 of the form returns reproduction rights to the U. S. Government when required, even though ACES copyright policy is in effect with respect to the reuse of material by the general public.

APPLIED COMPUTATIONAL ELECTROMAGNETICS SOCIETY JOURNAL
http://aces.ee.olemiss.edu

INFORMATION FOR AUTHORS

PUBLICATION CRITERIA

Each paper is required to manifest some relation to applied computational electromagnetics. **Papers may address general issues in applied computational electromagnetics, or they may focus on specific applications, techniques, codes, or computational issues.** While the following list is not exhaustive, each paper will generally relate to at least one of these areas:

1. **Code validation.** This is done using internal checks or experimental, analytical or other computational data. Measured data of potential utility to code validation efforts will also be considered for publication.

2. **Code performance analysis.** This usually involves identification of numerical accuracy or other limitations, solution convergence, numerical and physical modeling error, and parameter tradeoffs. However, it is also permissible to address issues such as ease-of-use, set-up time, run time, special outputs, or other special features.

3. **Computational studies of basic physics.** This involves using a code, algorithm, or computational technique to simulate reality in such a way that better, or new physical insight or understanding, is achieved.

4. **New computational techniques** or new applications for existing computational techniques or codes.

5. **"Tricks of the trade"** in selecting and applying codes and techniques.

6. **New codes, algorithms, code enhancement, and code fixes.** This category is self-explanatory, but includes significant changes to existing codes, such as applicability extensions, algorithm optimization, problem correction, limitation removal, or other performance improvement. **Note: Code (or algorithm) capability descriptions are not acceptable, unless they contain sufficient technical material to justify consideration.**

7. **Code input/output issues.** This normally involves innovations in input (such as input geometry standardization, automatic mesh generation, or computer-aided design) or in output (whether it be tabular, graphical, statistical, Fourier-transformed, or otherwise signal-processed). Material dealing with input/output database management, output interpretation, or other input/output issues will also be considered for publication.

8. **Computer hardware issues.** This is the category for analysis of hardware capabilities and limitations of various types of electromagnetics computational requirements. Vector and parallel computational techniques and implementation are of particular interest.

Applications of interest include, but are not limited to, antennas (and their electromagnetic environments), networks, static fields, radar cross section, inverse scattering, shielding, radiation hazards, biological effects, biomedical applications, electromagnetic pulse (EMP), electromagnetic interference (EMI), electromagnetic compatibility (EMC), power transmission, charge transport, dielectric, magnetic and nonlinear materials, microwave components, MEMS, RFID, and MMIC technologies, remote sensing and geometrical and physical optics, radar and communications systems, sensors, fiber optics, plasmas, particle accelerators, generators and motors, electromagnetic wave propagation, non-destructive evaluation, eddy currents, and inverse scattering.

Techniques of interest include but not limited to frequency-domain and time-domain techniques, integral equation and differential equation techniques, diffraction theories, physical and geometrical optics, method of moments, finite differences and finite element techniques, transmission line method, modal expansions, perturbation methods, and hybrid methods.

Where possible and appropriate, authors are required to provide statements of quantitative accuracy for measured and/or computed data. This issue is discussed in "Accuracy & Publication: Requiring, quantitative accuracy statements to accompany data," by E. K. Miller, *ACES Newsletter,* Vol. 9, No. 3, pp. 23-29, 1994, ISBN 1056-9170.

SUBMITTAL PROCEDURE

All submissions should be uploaded to ACES server through ACES web site (http://aces.ee.olemiss.edu) by using the upload button, journal section. Only pdf files are accepted for submission. The file size should not be larger than 5MB, otherwise permission from the Editor-in-Chief should be obtained first. Automated acknowledgment of the electronic submission, after the upload process is successfully completed, will be sent to the corresponding author only. It is the responsibility of the corresponding author to keep the remaining authors, if applicable, informed. Email submission is not accepted and will not be processed.

PAPER FORMAT (INITIAL SUBMISSION)

The preferred format for initial submission manuscripts is 12 point Times Roman font, single line spacing and single column format, with 1 inch for top, bottom, left, and right margins. Manuscripts should be prepared for standard 8.5x11 inch paper.

EDITORIAL REVIEW

In order to ensure an appropriate level of quality control, papers are peer reviewed. They are reviewed both for

technical correctness and for adherence to the listed guidelines regarding information content and format.

PAPER FORMAT (FINAL SUBMISSION)

Only camera-ready electronic files are accepted for publication. The term **"camera-ready" means that the material is neat, legible, reproducible, and in accordance with the final version format listed below.**

The following requirements are in effect for the final version of an ACES Journal paper:

1. The paper title should not be placed on a separate page. The title, author(s), abstract, and (space permitting) beginning of the paper itself should all be on the first page. The title, author(s), and author affiliations should be centered (center-justified) on the first page. The title should be of font size 16 and bolded, the author names should be of font size 12 and bolded, and the author affiliation should be of font size 12 (regular font, neither italic nor bolded).

2. An abstract is required. The abstract should be a brief summary of the work described in the paper. It should state the computer codes, computational techniques, and applications discussed in the paper (as applicable) and should otherwise be usable by technical abstracting and indexing services. The word "Abstract" has to be placed at the left margin of the paper, and should be bolded and italic. It also should be followed by a hyphen (—) with the main text of the abstract starting on the same line.

3. All section titles have to be centered and all the title letters should be written in caps. The section titles need to be numbered using roman numbering (I. II. ….)

4. Either British English or American English spellings may be used, provided that each word is spelled consistently throughout the paper.

5. Internal consistency of references format should be maintained. As a guideline for authors, we recommend that references be given using numerical numbering in the body of the paper (with numerical listing of all references at the end of the paper). The first letter of the authors' first name should be listed followed by a period, which in turn, followed by the authors' complete last name. Use a coma (,) to separate between the authors' names. Titles of papers or articles should be in quotation marks (" "), followed by the title of journal, which should be in italic font. The journal volume (vol.), issue number (no.), page numbering (pp.), month and year of publication should come after the journal title in the sequence listed here.

6. Internal consistency shall also be maintained for other elements of style, such as equation numbering. As a guideline for authors who have no other preference, we suggest that equation numbers be placed in parentheses at the right column margin.

7. The intent and meaning of all text must be clear. For authors who are not masters of the English language, the ACES Editorial Staff will provide assistance with grammar (subject to clarity of intent and meaning). However, this may delay the scheduled publication date.

8. Unused space should be minimized. Sections and subsections should not normally begin on a new page.

ACES reserves the right to edit any uploaded material, however, this is not generally done. It is the author(s) responsibility to provide acceptable camera-ready pdf files. Incompatible or incomplete pdf files will not be processed for publication, and authors will be requested to re-upload a revised acceptable version.

COPYRIGHTS AND RELEASES

Each primary author must sign a copyright form and obtain a release from his/her organization vesting the copyright with ACES. Copyright forms are available at ACES, web site (http://aces.ee.olemiss.edu). To shorten the review process time, the executed copyright form should be forwarded to the Editor-in-Chief immediately after the completion of the upload (electronic submission) process. Both the author and his/her organization are allowed to use the copyrighted material freely for their own private purposes.

Permission is granted to quote short passages and reproduce figures and tables from and ACES Journal issue provided the source is cited. Copies of ACES Journal articles may be made in accordance with usage permitted by Sections 107 or 108 of the U.S. Copyright Law. This consent does not extend to other kinds of copying, such as for general distribution, for advertising or promotional purposes, for creating new collective works, or for resale. The reproduction of multiple copies and the use of articles or extracts for commercial purposes require the consent of the author and specific permission from ACES. Institutional members are allowed to copy any ACES Journal issue for their internal distribution only.

PUBLICATION CHARGES

All authors are allowed for 8 printed pages per paper without charge. Mandatory page charges of $75 a page apply to all pages in excess of 8 printed pages. Authors are entitled to one, free of charge, copy of the journal issue in which their paper was published. Additional reprints are available for a nominal fee by submitting a request to the managing editor or ACES Secretary.

Authors are subject to fill out a one page over-page charge form and submit it online along with the copyright form before publication of their manuscript.

ACES Journal is abstracted in INSPEC, in Engineering Index, DTIC, Science Citation Index Expanded, the Research Alert, and to Current Contents/Engineering, Computing & Technology.